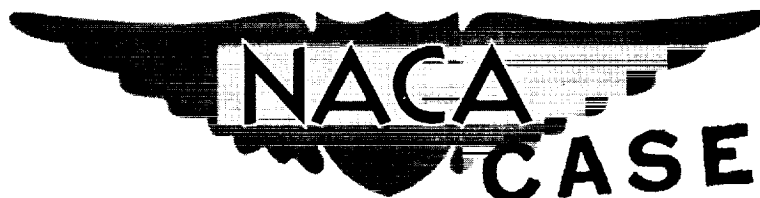


Sup SP-36

RM E56B03a

NACA RM E56B03a



CASE FILE COPY RESEARCH MEMORANDUM

AERODYNAMIC DESIGN OF AXIAL-FLOW COMPRESSORS

VOLUME II

By Members of the Compressor and Turbine Research Division

**Lewis Flight Propulsion Laboratory
Cleveland, Ohio**

**NATIONAL ADVISORY COMMITTEE
FOR AERONAUTICS
WASHINGTON**

August 1, 1956
Declassified September 3, 1958

1. The first part of the document discusses the importance of maintaining accurate records of all transactions and activities. It emphasizes the need for transparency and accountability in financial reporting.

2. The second part of the document outlines the various methods and techniques used to collect and analyze data. It includes a detailed description of the experimental procedures and the statistical analysis performed.

3383

AERODYNAMIC DESIGN OF AXIAL-FLOW COMPRESSORS

VOLUME II

By Members of the Compressor and Turbine Research Division
Lewis Flight Propulsion Laboratory
Cleveland, Ohio

Edited by
Irving A. Johnsen and Robert O. Bullock

TABLE OF CONTENTS

AERODYNAMIC DESIGN OF AXIAL-FLOW COMPRESSORS

VOLUME I

FOREWORD

CHAPTER

- I - OBJECTIVES AND SCOPE
- II - COMPRESSOR DESIGN REQUIREMENTS
- III - COMPRESSOR DESIGN SYSTEM
- IV - POTENTIAL FLOW IN TWO-DIMENSIONAL CASCADES
- V - VISCOUS FLOW IN TWO-DIMENSIONAL CASCADES

VOLUME II

CHAPTER

- VI - EXPERIMENTAL FLOW IN TWO-DIMENSIONAL CASCADES
- VII - BLADE-ELEMENT FLOW IN ANNULAR CASCADES
- VIII - DESIGN VELOCITY DISTRIBUTION IN MERIDIONAL PLANE
- IX - CHART PROCEDURES FOR DESIGN VELOCITY DISTRIBUTION
- X - PREDICTION OF OFF-DESIGN PERFORMANCE OF MULTISTAGE COMPRESSORS

VOLUME III

CHAPTER

- XI - COMPRESSOR STALL AND BLADE VIBRATION
- XII - COMPRESSOR SURGE
- XIII - COMPRESSOR OPERATION WITH ONE OR MORE BLADE ROWS STALLED
- XIV - THREE-DIMENSIONAL COMPRESSOR FLOW THEORY AND REAL FLOW EFFECTS
- XV - SECONDARY FLOWS AND THREE-DIMENSIONAL BOUNDARY-LAYER EFFECTS
- XVI - EFFECTS OF DESIGN AND MEASUREMENT ERRORS ON COMPRESSOR PERFORMANCE
- XVII - COMPRESSOR AND TURBINE MATCHING

3383

TABLE OF CONTENTS

VOLUME II

Chapter	Page
VI - EXPERIMENTAL FLOW IN TWO-DIMENSIONAL CASCADES, by Seymour Lieblein	1
SUMMARY	1
INTRODUCTION	1
SYMBOLS	3
PRELIMINARY CONSIDERATIONS	5
Description of Cascade	5
Performance Parameters	6
Data Selection	8
Two-dimensionality	8
Reynolds number and turbulence	8
Approach	9
INCIDENCE-ANGLE ANALYSIS	11
Preliminary Analysis	11
Data Correlations	12
Form of correlation	12
NACA 65-(A ₁₀)-series blades	13
C-Series circular-arc blades	14
Double-circular-arc blades	15
Other blades	15
Effect of blade maximum thickness	15
Effect of inlet Mach number	16
Summary	16
LOSS ANALYSIS	17
Preliminary Analysis	18
Data Correlations	20
Velocity diffusion based on local velocities	20
Velocity diffusion based on over-all velocities	21
Effect of blade maximum thickness	22
Effect of Reynolds number and turbulence	23
Effect of inlet Mach number	24
Summary	25

Chapter	Page
DEVIATION-ANGLE ANALYSIS	26
Preliminary Analysis	26
Data Correlations	28
Form of correlation	28
NACA 65-(A ₁₀)-series blades	29
C-Series circular-arc blades	30
Double-circular-arc blades	30
Comparison of rules	31
Effect of blade maximum thickness	32
Effect of Reynolds number	32
Effect of inlet Mach number	32
Variation with incidence angle	33
Summary	34
CONCLUDING REMARKS	35
REFERENCES	36
FIGURES	41
 VII - BLADE-ELEMENT FLOW IN ANNULAR CASCADES, By William H. Robbins, Robert J. Jackson, and Seymour Lieblein	 97
SUMMARY	97
INTRODUCTION	97
SYMBOLS	99
PRELIMINARY CONSIDERATIONS	101
Blade-Element Concept	101
Factors Affecting Blade-Element Performance	102
Incidence angle	102
Total-pressure loss	102
Deviation angle	103
Correlation Approach	104
Experimental Data Sources	106
INCIDENCE-ANGLE ANALYSIS	107
Method of Correlation	107
NACA 65-(A ₁₀)-series blades	107
Double-circular-arc blade	108
Summary Remarks	109

Chapter	Page
TOTAL-PRESSURE-LOSS ANALYSIS	110
Correlation of Data	110
Summary Remarks	111
DEVIATION-ANGLE ANALYSIS	111
Method of Correlation	112
NACA 65-(A ₁₀)-series blades	113
Double-circular-arc blade	114
Summary Remarks	114
APPLICATION TO DESIGN	115
Design Procedure	115
Summary Remarks	118
APPENDIX - EQUATIONS FOR BLADE-ELEMENT EFFICIENCY . . .	120
REFERENCES	124
TABLE I - DETAILS OF SINGLE-STAGE ROTORS AND STATORS . .	129
FIGURES	130
VIII - DESIGN VELOCITY DISTRIBUTION IN MERIDIONAL PLANE, by Charles C. Giamati, Jr., and Harold B. Finger	157
SUMMARY	157
INTRODUCTION	157
SYMBOLS	158
STATEMENT OF DESIGN PROBLEM	161
Specification of Compressor Performance and Configuration Requirements	161
Flow and Geometry Conditions to Be Determined	162
GENERAL EQUATIONS	163
Basic Assumptions	163
Simplified Flow Equations	164
SOLUTIONS OF EQUILIBRIUM EQUATIONS	164
Simple-Radial-Equilibrium Equation Neglecting Entropy Gradients	166
Simple-Radial-Equilibrium Equation Considering Radial Gradients of Entropy	167
Radial-Equilibrium Equation Considering Radial Accelerations	169

Chapter	Page
CONSIDERATION OF WALL BOUNDARY-LAYER EFFECTS	171
Correction for Weight-Flow Blockage Factor	175
Correction Factor for Stagnation-Temperature Rise	175
Correction Factor for Stagnation Pressure	176
Work-Done-Factor System	178
SELECTION OF DESIGN VARIABLES	179
Velocity Diagrams	179
Compressor-Inlet Conditions	180
Variation of Design Parameters through Compressor	181
Axial velocity	181
Diffusion factor	181
Efficiency	182
Boundary-layer characteristics	182
Physical Aspects	182
Off-Design Performance	183
APPLICATION OF EQUATIONS	183
Design Equations	183
General Determination of Axial Velocity Distribution	184
Method I	185
Inlet guide vanes	186
Rotor	186
Stator	187
Method II	188
Method III	188
Remarks	188
NUMERICAL EXAMPLE	189
CONCLUDING REMARKS	194
REFERENCES	195
TABLE I - DESIGN EQUATIONS	198
TABLE II - CALCULATION PROCEDURES	200
FIGURES	202
IX - CHART PROCEDURES FOR DESIGN VELOCITY DISTRIBUTION, by Arthur A. Medeiros and Betty Jane Hood	209
SUMMARY	209
INTRODUCTION	209

Chapter	Page
SYMBOLS	212
DESIGN EQUATIONS	214
FORMULATION OF CHARTS	216
Radial Equilibrium	216
Continuity	219
Energy Addition and Efficiency	222
Vector Relations	224
Diffusion Factor	224
EXAMPLE	226
COMPARISON OF CHART AND CALCULATED VALUES	235
REFERENCES	236
FIGURES	237
 X - PREDICTION OF OFF-DESIGN PERFORMANCE OF MULTISTAGE COMPRESSORS, By William H. Robbins and James F. Dugan, Jr.	 245
SUMMARY	245
INTRODUCTION	245
SYMBOLS	247
METHODS OF PREDICTING OFF-DESIGN PERFORMANCE	249
Blade-Element Method	249
Performance of inlet guide vanes	250
Rotor and stator analysis	251
Remarks on blade-element method	253
Stage-Stacking Method	254
Stage performance	254
Sources of stage performance	255
Stacking procedure	255
Remarks on stage-stacking method	257
Simplified Method	258
Background information	258
Calculation of compressor backbone	259
Calculation of stall-limit line	259
Constant-speed characteristics	259
Comments on reference point	260
Remarks on simplified method	262

Chapter	Page
CONCLUDING REMARKS	262
REFERENCES	263
TABLE I - EXPERIMENTAL COMPRESSOR DATA	265
FIGURES	266

CHAPTER VI

EXPERIMENTAL FLOW IN TWO-DIMENSIONAL CASCADES

By Seymour Lieblein

SUMMARY

Available experimental two-dimensional-cascade data for conventional compressor blade sections are correlated. The two-dimensional cascade and some of the principal aerodynamic factors involved in its operation are first briefly described. Then the data are analyzed by examining the variation of cascade performance at a reference incidence angle in the region of minimum loss. Variations of reference incidence angle, total-pressure loss, and deviation angle with cascade geometry, inlet Mach number, and Reynolds number are investigated.

From the analysis and the correlations of the available data, rules and relations are evolved for the prediction of the magnitude of the reference total-pressure loss and the reference deviation and incidence angles for conventional blade profiles. These relations are developed in simplified forms readily applicable to compressor design procedures.

INTRODUCTION

Because of the complexity and three-dimensional character of the flow in multistage axial-flow compressors, various simplified approaches have been adopted in the quest for accurate blade-design data. The prevailing approach has been to treat the flow across individual compressor blade sections as a two-dimensional flow. The use of two-dimensionally derived flow characteristics in compressor design has generally been satisfactory for conservative units (ch. III (ref. 1)).

In view of the limitations involved in the theoretical calculation of the flow about two-dimensional blade sections (chs. IV and V (ref. 1)), experimental investigations of two-dimensional cascades of blade sections were adopted as the principal source of blade-design data. Early experimental cascade results (e.g., refs. 2 to 4), however, were marked by a sensitivity to individual tunnel design and operation. This was largely a result of the failure to obtain true two-dimensional flow. Under these

3383

CG-1

circumstances, the correlation of isolated data was very difficult. Some efforts were made, however, to correlate limited experimental data for use in compressor design (e.g., ref. 5). The British, in particular, through the efforts primarily of Carter and Howell, appear to have made effective use of their early cascade investigations (refs. 6 to 9).

In recent years, the introduction of effective tunnel-wall boundary-layer removal for the establishment of true two-dimensional flow gave a substantial impetus to cascade analysis. In particular, the porous-wall technique of boundary-layer removal developed by the NACA (ref. 10) was a notable contribution. The use of effective tunnel boundary-layer control has resulted in more consistent systematic test data (refs. 11 to 14) and in more significant two-dimensional comparisons between theoretical and experimental performance (refs. 15 to 17). With the availability of a considerable amount of consistent data, it has become feasible to investigate the existence of general relations among the various cascade flow parameters. Such relations curtail the amount of future experimental data needed and also result in more effective use of the data currently available.

Inasmuch as the primary function of cascade information is to aid in the design of compressors, the present chapter expresses the existing cascade data in terms of parameters applicable to compressor design. Such expression not only facilitates the design of moderate compressors but also makes possible a rapid comparison of cascade data with data obtained from advanced high-speed compressor configurations. Since the bulk of the available cascade data has been obtained at low speed (Mach numbers of the order of 0.1), the question of applicability to such high-speed units is very significant. It is necessary to determine which flow parameters can or cannot be applied, to what extent the low-speed data are directly usable, and whether corrections can be developed in those areas where the low-speed data cannot be used directly.

In this chapter, the available cascade data obtained from a large number of tunnels are reworked in terms of what are believed to be significant parameters and, wherever possible, correlated in generalized forms. The performance parameters considered in the correlation are the outlet-air deviation angle and the cascade losses expressed in terms of blade-wake momentum thickness. The correlations are based on the variations of the performance parameters with cascade geometry (blade profile shape, solidity, chord angle) and inlet flow conditions. In view of the difficulties involved in establishing correlations over the complete range of operation of the cascade at various Mach number levels, the analysis is restricted to an examination of cascade performance at a reference incidence-angle location in the region of minimum loss.

The chapter is divided into four main sections: (1) a brief description of the two-dimensional cascade and of the parameters, concepts, and

data involved in the analysis, (2) an analysis of the variation of the reference incidence angle with cascade geometry and flow conditions, (3) an analysis of the variation of total-pressure loss at the reference incidence angle, and (4) an analysis of the variation of deviation angle at the reference incidence angle.

SYMBOLS

The following symbols are used in this chapter:

- A flow area
- b exponent in deviation-angle relation
- c chord length
- D diffusion factor (based on over-all velocities)
- D_l local diffusion factor (based on local velocities)
- d exponent in wake velocity-distribution relations
- f function
- H wake form factor, δ^*/θ^*
- i incidence angle, angle between inlet-air direction and tangent to blade mean camber line at leading edge, deg
- i_0 incidence angle of uncambered blade section, deg
- K_C compressibility correction factor in loss equation
- K_i correction factor in incidence-angle relation
- K_δ correction factor in deviation-angle relation
- M Mach number

3383

CG-1 back

m, m_c	factors in deviation-angle relation
n	slope factor in incidence-angle relation
P	total or stagnation pressure
p	static or stream pressure
Re_c	Reynolds number based on chord length
s	blade spacing
t	blade maximum thickness
V	air velocity
y	coordinate normal to axis
z	coordinate along axis
α	angle of attack, angle between inlet-air direction and blade chord, deg
β	air angle, angle between air velocity and axial direction, deg
γ^0	blade-chord angle, angle between blade chord and axial direction, deg
δ	wake full thickness
δ^*	wake displacement thickness
δ^0	deviation angle, angle between outlet-air direction and tangent to blade mean camber line at trailing edge, deg
δ_o^0	deviation angle of uncambered blade section, deg
θ^*	wake momentum-defect thickness
ρ	density
σ	solidity, ratio of chord to spacing
φ	blade camber angle, difference between angles of tangents to mean camber line at leading and trailing edges, deg

$\bar{\omega}$ total-pressure-loss coefficient

Subscripts:

av average

i.e. incompressible equation

inc incompressible

l lower surface

max maximum

ref reference

sh blade shape

t blade maximum thickness

u upper surface

z axial direction

θ tangential direction

0 free stream

1 station at cascade inlet

2 station at cascade exit (measuring station)

10 10 percent thick

PRELIMINARY CONSIDERATIONS

Description of Cascade

A schematic diagram of a low-speed two-dimensional-cascade tunnel is shown in figure 1 to illustrate the general tunnel layout. The principal components of the conventional tunnel are a blower, a diffuser section, a large settling chamber with honeycomb and screens to remove any swirl and to ensure a uniform velocity distribution, a contracting section to accelerate the flow, the cascade test section, and some form of outlet-air guidance. The test section contains a row or cascade of blades set in a mounting device that can be altered to obtain a range of air inlet angles (angle β_1 in figs. 1 and 2). Variations in blade angle of attack

are obtained either by rotating the blades on their individual mounting axes (i.e., by varying the blade-chord angle γ_0) while maintaining a fixed air angle or by keeping the blade-chord angle fixed and varying the air inlet angle by rotating the entire cascade. Outlet flow measurements are obtained from a traverse along the cascade usually between $\frac{1}{2}$ to $1\frac{1}{2}$ chord lengths behind the blade trailing edge at the blade mid-span. In the analysis, blade outlet refers to the cascade measuring station.

In most cases, some form of wall boundary-layer control in the cascade is provided by means of suction through slots or porous-wall surfaces. Examples of different tunnel designs or detailed information concerning design, construction, and operation of the two-dimensional-cascade tunnel can be obtained from references 10, 11, and 18 to 20.

Nomenclature and symbols designating cascade blade characteristics are given in figure 2. As in isolated-airfoil practice, cascade blade shapes are normally evolved by adding a basic thickness distribution to a mean camber line. The mean camber line (as indicated in fig. 2) represents the basic curvature of the profile. Some frequently used curvatures are the NACA (A_{10}) and related mean lines (refs. 11 and 13), the circular-arc mean line (ref. 6), and the parabolic-arc mean line (ref. 12). Two popular basic thickness distributions are the NACA 65-series thickness distribution (ref. 11) and the British C.4 thickness distribution (ref. 6). A high-speed profile has also been obtained from the construction of a circular-arc upper and lower surface (ref. 21); this profile is referred to as the double-circular-arc blade.

Performance Parameters

The performance of cascade blade sections has generally been presented as plots of the variation of air-turning angle, lift coefficient, and flow losses against blade angle of attack (or incidence angle) for a given cascade solidity and blade orientation. Blade orientation is expressed in terms of either fixed air inlet angle or fixed blade-chord angle. Flow losses have been expressed in terms of coefficients of the drag force and the defects in outlet total pressure or momentum. A recent investigation (ref. 22) demonstrates the significance of presenting cascade losses in terms of the thickness and form characteristics of the blade wakes.

In this analysis, the cascade loss parameters considered are the wake momentum-thickness ratio θ^*/c (ref. 22) and the total-pressure-loss coefficient $\bar{\omega}_1$, defined as the ratio of the average loss in total pressure across the blade to the inlet dynamic head. Cascade losses are considered

in terms of $\bar{\omega}_1$, since this parameter can be conveniently used for the determination of compressor blade-row efficiency and entropy gradients. The parameter θ^*/c represents the basic wake development of the blade profile and, as such, constitutes a significant parameter for correlation purposes. Values of θ^*/c were computed from the cascade loss data according to methods similar to those presented in reference 22. The diffusion factor D of reference 23 was used as a measure of the blade loading in the region of minimum loss.

In the present analysis, it was necessary to use a uniform nomenclature and consistent correlation technique for the various blade shapes considered. It was believed that this could best be accomplished by considering the approach characteristics of the blade in terms of air incidence angle i , the camber characteristics in terms of the camber angle ϕ , and the air-turning characteristics in terms of the deviation angle δ° (fig. 2). As indicated in figure 2, these angles are based on the tangents to the blade mean camber line at the leading and trailing edges. The use of the deviation angle, rather than the turning angle, as a measure of the air outlet direction has the advantage, for correlation purposes, of a generally small variation with incidence angle. Air-turning angle is related to the camber, incidence, and deviation angles by

$$\Delta\beta = \phi + i - \delta^\circ \quad (1)$$

Incidence angle is considered positive when it tends to increase the air-turning angle, and deviation angle is considered positive when it tends to decrease the air-turning angle (fig. 2).

The use of incidence and deviation angles requires a unique and reasonable definition of the blade mean-line angle at the leading and trailing edges, which may not be possible for some blade shapes. The principal difficulty in this respect is in the 65-(A₁₀)-series blades (ref. 11), whose mean-line slope is theoretically infinite at the leading and trailing edges. However, it is still possible to render these sections usable in the analysis by arbitrarily establishing an equivalent circular-arc mean camber line. As shown in figure 3, the equivalent circular-arc mean line is obtained by drawing a circular arc through the leading- and trailing-edge points and the point of maximum camber at the midchord position. Equivalent incidence, deviation, and camber angles can then be established from the equivalent circular-arc mean line as indicated in the figure. The relation between equivalent camber angle and isolated-airfoil lift coefficient of the NACA 65-(A₁₀)-series mean line is shown in figure 4.

A typical plot of the cascade performance parameters used in the analysis is shown in figure 5 for a conventional blade section at fixed solidity and air inlet angle.

Data Selection

In selecting data sources for use in the cascade performance correlations, it is necessary to consider the degree of two-dimensionality obtained in the tunnel and the magnitude of the test Reynolds number and turbulence level.

Two-dimensionality. - As indicated previously, test results for a given cascade geometry obtained from different tunnels may vary because of a failure to achieve true two-dimensional flow across the cascade. Distortions of the true two-dimensional flow are caused by the tunnel-wall boundary-layer growth and by nonuniform inlet and outlet flow distributions (refs. 10 and 18). In modern cascade practice, good flow two-dimensionality is obtained by the use of wall-boundary-layer control or large tunnel size in conjunction with a large number of blades, or both. Examples of cascade tunnels with good two-dimensionality are given by references 11 and 19.

The lack of good two-dimensionality in cascade testing affects primarily the air-turning angles and blade surface pressure distributions. Therefore, deviation-angle data were rejected when the two-dimensionality of the tunnel appeared questionable (usually the older and smaller tunnels). Practically all the cascade loss data were usable, however, since variations in the measured loss obtained from a given cascade geometry in different tunnels will generally be consistent with the measured diffusion levels (unless the blade span is less than about 1 or 2 inches and there is no extensive boundary-layer removal).

Reynolds number and turbulence. - For the same conditions of two-dimensionality and test-section Mach number, test results obtained from cascades of the same geometry may vary because of large differences in the magnitude of the blade-chord Reynolds number and the free-stream turbulence. Examples of the effect of Reynolds number and turbulence on the losses obtained from a given blade section at fixed incidence angle are presented in figure 6. Similar pronounced effects are observed on the deviation angle. As discussed in chapter V (ref. 1), the loss variation with Reynolds number is associated primarily with a local or complete separation of the laminar boundary layer on the blade surfaces. The data used in the correlation are restricted to values of blade-chord Reynolds number from about 2.0×10^5 to 2.5×10^5 in order to minimize the effects of different Reynolds numbers. Free-stream turbulence level was not generally determined in the various cascade tunnels.

In some cases (refs. 11 and 24, e.g.), in tunnels with low turbulence levels, marked local laminar-separation effects were observed in the range of Reynolds number selected for the correlation. Illustrative plots of the variation of total-pressure-loss coefficient with angle of attack for a cascade with local laminar separation are shown in figure 7. In such

instances, it was necessary to estimate the probable variation of loss (and deviation angle) in the absence of the local separation (as indicated in the figure) and use values obtained from the faired curves for the correlations.

The specific sources of data used in the analysis are indicated by the references listed for the various performance correlations. Details of the tunnel construction and operation and other pertinent information are given in the individual references.

Approach

In a correlation of two-dimensional-cascade data that is intended ultimately for use in compressor blade-element design, the variations of performance parameters should be established over a wide range of incidence angles. Experience shows (fig. 8) that the variation of loss with incidence angle for a given blade section changes markedly as the inlet Mach number is increased. Consequently, correlated low-speed blade performance at high and low incidence angles is not applicable at high Mach numbers. The low-speed-cascade performance is therefore considered at some reference point on the general loss-against-incidence-angle curve that exhibits the least variation in location and in magnitude of performance parameters as Mach number is increased.

The reference location herein is selected as the point of minimum loss on the curve of total-pressure loss against incidence angle. For conventional low-speed-cascade sections, the region of low-loss operation is generally flat, and it is difficult to establish precisely the value of incidence angle that corresponds to the minimum loss. For practical purposes, therefore, since the curves of loss coefficient against incidence angle are generally symmetrical, the reference minimum-loss location was established at the middle of the low-loss range of operation. Specifically, as shown in figure 9, the reference location is selected as the incidence angle at the midpoint of the range, where range is defined as the change in incidence angle corresponding to a rise in loss coefficient equal to the minimum value. Thus, for conventional cascade sections, the midrange reference location is considered coincident with the point of minimum loss. In addition to meeting the abovementioned requirement of small variation with inlet Mach number, the reference minimum-loss incidence angle (as compared with the optimum or nominal incidence settings of ref. 25 or the design incidence setting of ref. 11) requires the use of only the loss variation and also permits the use of the diffusion factor (applicable in region of minimum loss) as a measure of the blade loading.

At this point, it should be kept in mind that the reference minimum-loss incidence angle is not necessarily to be considered as a recommended design point for compressor application. The selection of the best

incidence angle for a particular blade element in a multistage-compressor design is a function of many considerations, such as the location of the blade row, the design Mach number, and the type and application of the design. In general, there is no one universal definition of design or best incidence angle. The cascade reference location is established primarily for purposes of analysis.

Of the many blade shapes currently in use in compressor design practice (i.e., NACA 65-series, C-series circular arc, parabolic arc, double circular arc), data sufficient to permit a reasonably complete and significant correlation have been published only for the 65-(A₁₀)-series blades of reference 11. Therefore, a basic correlation of the 65-(A₁₀)-series data had to be established first and the results used as a guide or foundation for determining the corresponding performance trends for the other blade shapes for which only limited data exist.

Since the ultimate objective of cascade tests is to provide information for designing compressors, it is desirable, of course, that the structure of the data correlations represent the compressor situation as closely as possible. Actually, a blade element in a compressor represents a blade section of fixed geometry (i.e., fixed profile form, solidity, and chord angle) with varying inlet-air angle. In two-dimensional-cascade practice, however, variations in incidence angle have been obtained by varying either the inlet-air angle or the blade-chord angle. The available systematic data for the NACA 65-(A₁₀)-series blades (ref. 11) have been obtained under conditions of fixed inlet-air angle and varying blade-chord angle. Since these data form the foundation of the analysis, it was necessary to establish the cascade performance correlations on the basis of fixed inlet-air angle. Examination of limited unpublished low-speed data indicate that, as illustrated in figure 10, the loss curve for constant air inlet angle generally falls somewhat to the right of the constant-chord-angle curve for fixed values of β_1 and γ^0 in the low-loss region of the curve. Values of minimum-loss incidence angle for fixed β_1 operation are indicated to be of the order of 1° or 2° greater than for fixed γ^0 operation. An approximate allowance for this difference is made in the use of reference-incidence-angle data from these two methods.

With the definition of reference incidence angle, performance parameters, and analytical approach established, the procedure is first to determine how the value of the reference minimum-loss incidence angle varies with cascade geometry and flow conditions for the available blade profiles. Then the variation of the performance parameters is determined at the reference location (as indicated in fig. 5) as geometry and flow are changed. Thus, the various factors involved can be appraised, and correlation curves and charts can be established for the available data. The analysis and correlation of cascade reference-point characteristics are presented in the following sections.

INCIDENCE-ANGLE ANALYSIS

Preliminary Analysis

In an effort to obtain a general empirical rule for the location of the reference minimum-loss incidence angle, it is first necessary to examine the principal influencing factors.

It is generally recognized that the low-loss region of incidence angle is identified with the absence of large velocity peaks (and subsequent decelerations) on either blade surface. For infinitely thin sections, steep velocity gradients are avoided when the front stagnation point is located at the leading edge. This condition has frequently been referred to as the condition of "impact-free entry." Weinig (ref. 26) used the criterion of stagnation-point location to establish the variation of "impact-free-entry" incidence angle for infinitely thin circular-arc sections from potential-flow theory. Results deduced from reference 26 are presented in figure 11(a). The minimum-loss incidence angle is negative for infinitely thin blades and decreases linearly with camber for fixed solidity and blade-chord angle.

While there is no definite corresponding incidence-angle theory for thick-nose blades with rounded leading edges, some equivalent results have been obtained based on the criterion that the location of the stagnation point in the leading-edge region of a thick blade is the controlling factor in the determination of the surface velocity distributions. Carter, in reference 9, showed semitheoretically on this basis that optimum incidence angle (angle at maximum lift-drag ratio) for a conventional 10-percent-thick circular-arc blade decreases with increasing camber angle. The results of reference 9 were followed by generalized plots of optimum incidence angle in reference 25, which showed, as in figure 11(a), that optimum incidence angle for a 10-percent-thick C-series blade varies with camber angle, solidity, and blade orientation. (In these references, blade orientation was expressed in terms of air outlet angle rather than blade-chord angle.) The plot for an outlet-air angle of 20° is shown in figure 11(b). Apparently, the greater the blade circulation, the lower in magnitude the minimum-loss incidence angle must be. It is reasonable to expect, therefore, that the trends of variation of minimum-loss incidence angle for conventional blade sections will be similar to those established by thin-airfoil theory.

A preliminary examination of experimental cascade data showed that the minimum-loss incidence angles of uncambered sections ($\phi = 0$) of conventional thicknesses were not zero, as indicated by theory for infinitely thin blades (fig. 11(a)), but always positive in value. The appearance of positive values of incidence angle for thick blades is attributed to the existence of velocity distributions at zero incidence angle that are not symmetrical on the two surfaces. Typical plots illustrating the high

3582

CG-2 back

velocities generally observed in the inlet region of the lower (pressure) surface of thick uncambered blades at zero incidence angle are shown in figure 12. Apparently, an increase in incidence angle from the zero value is necessary in order to reduce the lower-surface velocity to a more equitable distribution that results in a minimum of the over-all loss. This zero-camber thickness effect will appear only for blade-chord angles between 0° and 90° , since, as indicated by the highly simplified one-dimensional model of the blade passage flow in figure 13, the velocity distributions at these limit angles are symmetrical.

The effect of blade thickness blockage on "impact-free-entry" incidence angle for straight (uncambered) blades of constant chordwise thickness in incompressible two-dimensional flow is investigated in reference 27. The results of reference 27 are plotted in terms of the parameters used in this analysis in figure 14. It is reasonable to expect that similar trends of variations of zero-camber reference minimum-loss incidence angle will be obtained for compressor blade profiles.

On the basis of the preceding analysis, therefore, it is expected that, for low-speed-cascade flow, reference minimum-loss incidence angle will generally be positive at zero camber and decrease with increasing camber, depending on solidity and blade-chord angle. The available theory also indicates that the variation of reference incidence angle with camber at fixed solidity and chord angle might be essentially linear. If so, the variations could be expressed in terms of slope and intercept values, where the intercept value represents the magnitude of the incidence angle for the uncambered section (function of blade thickness, solidity, and blade-chord angle). Reference minimum-loss incidence angle may also vary with inlet Mach number and possibly with Reynolds number.

Data Correlations

Form of correlation. - Although preliminary theory indicates that blade-chord angle is the significant blade orientation parameter, it was necessary to establish the data correlations in terms of inlet-air angle, as mentioned previously. The observed cascade data were found to be represented satisfactorily by a linear variation of reference incidence angle with camber angle for fixed solidity and inlet-air angle. The variation of reference minimum-loss incidence angle can then be described in equation form as

$$i = i_0 + n\phi \quad (2)$$

where i_0 is the incidence angle for zero camber, and n is the slope of the incidence-angle variation with camber $(i - i_0)/\phi$.

Since the existence of a finite blade thickness is apparently the cause of the positive values of i_o , it is reasonable to assume that both the magnitude of the maximum thickness and the thickness distribution contribute to the effect. Therefore, since the 10-percent-thick 65-series blades of reference 11 are to be used as the basis for a generalized correlation of all conventional blade shapes, it is proposed that the zero-camber reference incidence angle be expressed in the form

$$i_o = (K_i)_{sh}(K_i)_t(i_o)_{10} \quad (3)$$

where $(i_o)_{10}$ represents the variation of zero-camber incidence angle for the 10-percent-thick 65-series thickness distribution, $(K_i)_t$ represents any correction necessary for maximum blade thicknesses other than 10 percent, and $(K_i)_{sh}$ represents any correction necessary for a blade shape with a thickness distribution different from that of the 65-series blades. (For a 10-percent-thick 65-series blade, $(K_i)_t = 1$ and $(K_i)_{sh} = 1$.)

The problem, therefore, is reduced to finding the values of n and i_o (through eq. (3)) as functions of the pertinent variables involved for the various blade profiles considered.

NACA 65-(A₁₀)-series blades. - From the extensive low-speed-cascade data for the 65-(A₁₀)-series blades (ref. 11), when expressed in terms of equivalent incidence and camber angles (figs. 3 and 4), plots of i_o and n can be deduced that adequately represented the minimum-loss-incidence-angle variations of the data. The deduced values of i_o and n as functions of solidity and inlet-air angle are given for these blades in figures 15 and 16. The subscript 10 in figure 15 indicates that the i_o values are for 10-percent maximum-thickness ratio. Values of intercept i_o and slope n were obtained by fitting a straight line to each data plot of reference incidence angle against camber angle for a fixed solidity and air inlet angle. The straight lines were selected so that both a satisfactory representation of the variation of the data points and a consistent variation of the resulting n and i_o values were obtained.

The deduced rule values and the observed data points compared in figure 17 indicate the effectiveness of the deduced representation. In several configurations, particularly for low cambers, the range of equivalent incidence angle covered in the tests was insufficient to permit an accurate determination of a minimum-loss value. Some of the scatter of the data may be due to the effects of local laminar separation in altering the range characteristics of the sections.

Although the cascade data in reference 11 include values of inlet-air angle from 30° to 70° and values of solidity from 0.5 to 1.5, the deduced variations in figures 15 and 16 are extrapolated to cover wider ranges of β_1 and σ . The extrapolation of i_0 to zero at $\beta_1 = 0$ is obvious. According to theory (fig. 11), the value of the slope term does not vanish at $\beta_1 = 0$. In figure 16, therefore, an arbitrary fairing of the curves down to nonzero values of n was adopted as indicated. Actually, it is not particularly critical to determine the exact value of the slope term at $\beta_1 = 0$ necessary to locate the reference incidence angle precisely, since, for such cases (inlet guide vanes and turbine nozzles), a wide low-loss range of operation is usually obtained. The solidity extrapolations were attempted because of the uniform variations of the data with solidity. However, caution should be exercised in any further extrapolation of the deduced variations.

C-Series circular-arc blades. - The various thickness distributions used in combination with the circular-arc mean line have been designated C.1, C.2, C.3, and so forth (refs. 25, 28, and 29). In general, the various C-series thickness distributions are fairly similar, and have their maximum thickness located at between 30 and 40 percent of the chord length. The 65-series and two of the more popular C-series thickness distributions (C.1 and C.4) are compared on an exaggerated scale in figure 18. (The 65-series profile shown is usually thickened near the trailing edge in actual blade construction.)

In view of the somewhat greater thickness blockage in the forward portions of the C-series blades (fig. 18), it may be that the minimum-loss incidence angles for zero camber for the C-series blades are somewhat greater than those for the 65-series profiles; that is, $(K_i)_{sh} > 1$. In the absence of any definitive cascade data, the value of $(K_i)_{sh}$ for the C-series profiles was arbitrarily taken to be 1.1. Observed minimum-loss incidence angles for an uncambered 10-percent-thick C.4 profile (obtained from ref. 30) are compared in figure 19 with values predicted from the deduced $(i_0)_{10}$ values for the 65-series blade (fig. 15 and eq. (3)) with an assumed value of $(K_i)_{sh} = 1.1$. (For 10-percent thickness, $(K_i)_t = 1$.)

In view of the similarity between the 65- (A_{10}) -series mean line and a true circular arc (fig. 3), the applicability of the slope values in figure 16 to the circular-arc mean line was investigated. For the recent cascade data obtained from tunnels having good boundary-layer control (refs. 15 and 31), a check calculation for the 10-percent-thick C.4 circular-arc blades using figures 15 and 16 with $(K_i)_{sh} = 1.1$ revealed good results. For the three configurations in reference 31 tested at constant β_1 ($\varphi = 30^\circ$), the agreement between observed and predicted

minimum-loss incidence angles was within 1° . For the one configuration in reference 15 tested at constant γ^0 ($\phi = 31^\circ$), the predicted value of minimum-loss incidence angle was 1.7° greater than the observed value. However, in view of the general 1° to 2° difference between fixed β_1 and fixed γ^0 operation (fig. 10), such a discrepancy is to be expected. On the basis of these limited data, it appears that the low-speed minimum-loss incidence angles for the C-series circular-arc blade can be obtained from the i_0 and n values of the 65-series blade with $(K_1)_{sh} = 1.1$.

Double-circular-arc blades. - The double-circular-arc blade is composed of circular-arc upper and lower surfaces. The arc for each surface is drawn between the point of maximum thickness at midchord and the tangent to the circles of the leading- and trailing-edge radii. The chordwise thickness distribution for the double-circular-arc profile with 1-percent leading- and trailing-edge radius is shown in figure 18. Lack of cascade data again prevents an accurate determination of a reference-incidence-angle rule for the double circular arc. Since the double-circular-arc blade is thinner than the 65-series blade in the inlet region, the zero-camber incidence angles for the double-circular-arc blade should be somewhat different from those of the 65-series section, with perhaps $(K_1)_{sh} \leq 1$. It can also be assumed, as before, that the slope-term values of figure 16 are valid for the double-circular-arc blade. From an examination of the available cascade data for the double-circular-arc blade ($\phi = 25^\circ$, $\sigma = 1.333$, ref. 21; and $\phi = 40^\circ$, $\sigma = 1.064$, ref. 28), it appears that the use of figures 15 and 16 with a value of $(K_1)_{sh} = 0.7$ in equations (2) and (3) results in a satisfactory comparison between predicted and observed values of reference incidence angle.

Other blades. - Similar procedures can be applied to establish reference incidence-angle correlations for other blade shapes. Cascade data are also available for the C-series parabolic-arc blades (refs. 12, 21, 30, 32, and 33) and the NACA 65-(A10)-series blade (ref. 13); but, in view of the limited use of these forms in current practice, no attempt was made at this time to deduce corresponding incidence-angle rules for these blades.

Effect of blade maximum thickness. - As indicated previously, some correction (expressed here in terms of $(K_1)_t$, eq. (3)) of the base values of $(i_0)_{10}$ obtained from the 10-percent-thick 65-series blades in figure 15 should exist for other values of blade maximum-thickness ratio. According to the theory of the zero-camber effect, $(K_1)_t$ should be zero for zero thickness and increase as maximum blade thickness is increased, with a value of 1.0 for a thickness ratio of 0.10. Although the very limited low-speed data obtained from blades of variable thickness ratio (refs. 34 and 35) were not completely definitive, it was possible to establish a preliminary thickness-correction factor for reference zero-camber incidence angle as indicated in figure 20 for use in conjunction with equation (3).

Effect of inlet Mach number. - The previous correlations of reference minimum-loss incidence angle have all been based on low-speed-cascade data. It appears from limited high-speed data, however, that minimum-loss incidence angle will vary with increasing inlet Mach number for certain blade shapes.

The variations of minimum-loss incidence angle with inlet Mach number are plotted for several blade shapes in figures 21 and 22. The extension of the test data points to lower values of inlet Mach number could not generally be made because of reduced Reynolds numbers or insufficient points to establish the reference location at the lower Mach numbers. In some instances, however, it was possible to obtain low-speed values of incidence angle from other sources.

The blades of figure 21 show essentially no variation of minimum-loss incidence angle with inlet Mach number, at least up to a Mach number of about 0.8. The blades of figure 22, however, evidence a marked increase in incidence angle with Mach number. The difference in the variation of minimum-loss incidence angle with Mach number in figures 21 and 22 is associated with the different way the general pattern of the loss variation changes with increasing Mach number for the two types of blades. For the thick-nose blades, as illustrated in figures 8(a) and (b), the loss coefficient increases with Mach number at both the high and low incidence angles; thus tending to maintain the same point of minimum loss. For the sharp-nose blade, as illustrated by figures 8(c) and (d), the increase in loss occurs primarily on the low-incidence-angle side; and a positive shifting of the minimum-loss incidence angle results. Data for other thick-nose sections in reference 33 show the rise in loss to occur at both ends of the curve, but plots of reference incidence angle against Mach number could not validly be made for these blades because of evidence of strong local laminar-separation effects.

Since the most obvious difference between the blades in figures 21 and 22 is the construction of the leading-edge region, the data suggest that blades with thick-nose inlet regions tend to show, for the range of inlet Mach number covered, essentially no Mach number effect on minimum-loss incidence angle, while blades with sharp leading edges will have a significant Mach number effect. The available data, however, are too limited to conclusively confirm this observation at this time. Furthermore, for the blades that do show a Mach number effect, the magnitude of the variation of reference incidence angle with Mach number is not currently predictable.

Summary

The analysis of blade-section reference minimum-loss incidence angle shows that the variation of the reference incidence angle with cascade

geometry at low speed can be established satisfactorily in terms of an intercept value i_0 and a slope value n as given by equation (2). Deduced values of i_0 and n were obtained as a function of β_1 and σ from the data for the 10-percent-thick 65-(A₁₀)-series blades of reference 11 as equivalent circular-arc sections (figs. 15 and 16). It was then shown that, as a first approach, the deduced values of $(i_0)_{10}$ and n in figures 15 and 16 could also be used to predict the reference incidence angles of the C-series and double-circular-arc blades by means of a correction $(K_i)_{sh}$ to the $(i_0)_{10}$ values of figure 15 (eq. (3)).

The procedure involved in estimating the low-speed reference minimum-loss incidence angle of a blade section is as follows: From known values of β_1 and σ , $(i_0)_{10}$ and n are selected from figures 15 and 16. The value of $(K_i)_t$ for the blade maximum-thickness ratio is obtained from figure 20, and the appropriate value of $(K_i)_{sh}$ is selected for the type of thickness distribution. For NACA 65-series blades, $(K_i)_{sh} = 1.0$; and it is proposed that $(K_i)_{sh}$ be taken as 1.1 for the C-series circular-arc blade and as 0.7 for the double-circular-arc blade. The value of i_0 is then computed from equation (3); and, finally, i is determined from the blade camber angle according to equation (2).

It should be noted that the values of $(K_i)_{sh}$ given for the circular-arc blades are rather tenuous values obtained from very limited data. The use of the proposed values is not critical for good accuracy; the values were included primarily for completeness as a reflection of the anticipated differences in the blade thickness blockage effects. Further experimental data will be necessary to establish the significance of such a correction. Also, a marked increase in reference minimum-loss incidence angle with Mach number is to be expected for sharp-nose blade sections. The magnitude of the Mach number correction for these blades is currently unpredictable.

LOSS ANALYSIS

With the location of the low-speed reference minimum-loss incidence angle established for several conventional blade sections, the magnitude of the losses occurring at this reference position (fig. 5) will now be investigated. Accordingly, the nature of the loss phenomena and the various factors influencing the magnitude of the loss over a range of blade configurations and flow conditions are first analyzed. The available experimental loss data are then examined to establish fundamental loss correlations in terms indicated by the analysis.

Preliminary Analysis

Two-dimensional-cascade losses arise primarily from the growth of boundary layer on the suction and pressure surfaces of the blades. These surface boundary layers come together at the blade trailing edge, where they combine to form the blade wake, as shown in figure 23. As a result of the formation of the surface boundary layers, a local defect in total pressure is created, and a certain mass-averaged loss in total pressure is determined in the wake of the section. The loss in total pressure is measured in terms of the total-pressure-loss coefficient $\bar{\omega}$, defined generally as the ratio of the mass-averaged loss in total pressure $\overline{\Delta P}$ across the blade row from inlet to outlet stations to some reference free-stream dynamic pressure $(P_0 - P_0)_{\text{ref}}$, or

$$\bar{\omega}_{\text{ref}} = \frac{\overline{\Delta P}}{(P_0 - P_0)_{\text{ref}}} \quad (4)$$

For incompressible flow, $P_0 - P_0$ is equal to the conventional free-stream dynamic pressure $\rho_0 V_0^2/2$. The total-pressure-loss coefficient is usually determined from consideration of the total-pressure variation across a blade spacing s (fig. 23).

A theoretical analysis of incompressible two-dimensional-cascade losses in reference 22 shows that the total-pressure-loss coefficient at the cascade-outlet measuring station (where the static pressure is essentially uniform across the blade spacing) is given by

$$\bar{\omega}_1 = 2 \left(\frac{\theta^*}{c} \right)_2 \frac{\sigma}{\cos \beta_2} \left(\frac{\cos \beta_1}{\cos \beta_2} \right)^2 \left\{ \frac{\frac{2H_2}{3H_2 - 1}}{\left[1 - \left(\frac{\theta^*}{c} \right)_2 \frac{\sigma H_2}{\cos \beta_2} \right]^3} \right\} \quad (5)$$

where $\bar{\omega}_1$ is the loss coefficient based on inlet dynamic head, θ^*/c is the ratio of wake momentum thickness to blade-chord length, σ is cascade solidity, β_2 is the air outlet angle, and H_2 is the wake form factor (displacement thickness divided by momentum thickness). The wake characteristics in equation (5) are expressed in terms of conventional thickness in a plane normal to the wake (i.e., normal to the outlet flow) at the measuring station. Definitions of wake characteristics and variations in velocity and pressure assumed by the analysis are given in reference 22. The analysis further indicates that the collection of terms within the braces is essentially secondary (since H_2 is generally \leq about 1.2 at the measuring station), with a magnitude of nearly 1 for conventional unstalled configurations. The principal determinants of the loss

in total pressure at the cascade measuring station are, therefore, the cascade geometry factors of solidity, air outlet and air inlet angles, and the aerodynamic factor of wake momentum-thickness ratio.

Since the wake is formed from a coalescing of the pressure- and suction-surface boundary layers, the wake momentum thickness naturally depends on the development of the blade surface boundary layers and also on the magnitude of the blade trailing-edge thickness. The results of references 22, 34, and 36 indicate, however, that the contribution of conventional blade trailing-edge thickness to the total loss is not generally large for compressor sections; the preliminary factor in the wake development is the blade surface boundary-layer growth. In general, it is known (ch. V (ref. 1), e.g.) that the boundary-layer growth on the surfaces of the blade is a function primarily of the following factors: (1) the surface velocity gradients (in both subsonic and supersonic flow), (2) the blade-chord Reynolds number, and (3) the free-stream turbulence level.

Experience has shown that blade surface velocity distributions that result in large amounts of diffusion in velocity tend to produce relatively thick blade boundary layers. The magnitude of the velocity diffusion in low-speed flow generally depends on the geometry of the blade section and its incidence angle. As Mach number is increased, however, compressibility exerts a further influence on the velocity diffusion of a given cascade geometry and orientation. If local supersonic velocities develop at high inlet Mach numbers, the velocity diffusion is altered by the formation of shock waves and the interaction of these shock waves with the blade surface boundary layers. The losses associated with local supersonic flow in a cascade are generally greater than for subsonic flow in the same cascade. The increases in loss are frequently referred to as shock losses.

Cascade-inlet Mach number also influences the magnitude of the subsonic diffusion for a fixed cascade. This Mach number effect is the conventional effect of compressibility on the blade velocity distributions in subsonic flow. Compressibility causes the maximum local velocity on the blade surface to increase at a faster rate than the inlet and outlet velocities. Accordingly, the magnitude of the surface diffusion from maximum velocity to outlet velocity becomes greater as inlet Mach number is increased. A further secondary influence of Mach number on losses is obtained because of an increase in losses associated with the eventual mixing of the wake with the surrounding free-stream flow (ref. 37).

On the basis of the foregoing considerations, therefore, it is expected that the principal factors upon which to base empirical cascade-wake-thickness correlations should be velocity diffusion, inlet Mach number, blade-chord Reynolds number, and, if possible, turbulence level.

3383

CG-3 back

Data Correlations

Velocity diffusion based on local velocities. - Recently, several investigations have been reported in references 22, 23, and 38 on the establishment of simplified diffusion parameters and the correlation of cascade losses in terms of these parameters. The general hypothesis of these diffusion correlations states that the wake thickness, and consequently the magnitude of the loss in total pressure, is proportional to the diffusion in velocity on the suction surface of the blade in the region of the minimum loss. This hypothesis is based on the consideration that the boundary layer on the suction surface of conventional compressor blade sections contributes the major share of the wake in these regions, and therefore the suction-surface velocity distribution becomes the governing factor in the determination of the loss. It was further established in these correlations that, for conventional velocity distributions, the diffusion in velocity can be expressed significantly as a parameter involving the difference between some function of the measured maximum suction-surface velocity V_{\max} and the outlet velocity V_2 .

Reference 38 presents an analysis of blade-loading limits for the 65-(A₁₀)10 blade section in terms of drag coefficient and a diffusion parameter given for incompressible flow by $(V_{\max}^2 - V_2^2)/V_{\max}^2$. Results of an unpublished analysis of cascade losses in terms of the momentum thickness of the blade wake (as suggested in ref. 22) indicate that a local diffusion parameter in the form given previously or in the form $(V_{\max} - V_2)/V_{\max}$ can satisfactorily correlate experimental cascade loss data. The term "local diffusion parameter" is used to indicate that a knowledge of the maximum local surface velocity is required. The correlation obtained between calculated wake momentum-thickness ratio θ^*/c and local diffusion factor given by

$$D_l = \frac{V_{\max} - V_2}{V_{\max}} \quad (6)$$

obtained for the NACA 65-(A₁₀)-series cascade sections of reference 11 at reference incidence angle is shown in figure 24. Values of wake momentum-thickness ratio for these data were computed from the reported wake coefficient values according to methods similar to those discussed in reference 22. Unfortunately, blade surface velocity-distribution data are not available for the determination of the diffusion factor for other conventional blade shapes.

The correlation of figure 24 indicates the general validity of the basic diffusion hypothesis. At high values of diffusion (greater than about 0.5), a separation of the suction-surface boundary layer is

suggested by the rapid rise in the momentum thickness. The indicated nonzero value of momentum thickness at zero diffusion represents the basic friction loss (surface shear stress) of the flow and also, to a smaller extent, the effect of the finite trailing-edge thickness. The correlation of figure 24 further indicates that wake momentum-thickness ratio at reference incidence angle can be estimated from the computed local diffusion factor for a wide range of solidities, cambers, and inlet-air angles. The loss relations of equation (5) and reference 22 can then be used to compute the resulting loss in the total pressure.

Velocity diffusion based on over-all velocities. - In order to include the cases of blade shapes for which velocity-distribution data are not available, a diffusion parameter has been established in reference 23 that does not require a specific knowledge of the peak local suction-surface velocity. Although originally derived for use in compressor design and analysis, the diffusion factor of reference 23 can also be applied in the analysis of cascade losses. The diffusion factor of reference 23 attempts, through several simplifying approximations, to express the local diffusion on the blade suction surface in terms of over-all (inlet or outlet) velocities or angles, quantities that are readily determined. The basis for the development of the over-all diffusion factor is presented in detail in reference 23 and is indicated briefly in figure 25. The diffusion factor is given by

$$D = \left(1 - \frac{V_2}{V_1}\right) + \frac{\Delta W_\theta}{2\sigma V_1} \quad (7)$$

which, for incompressible two-dimensional-cascade flow, becomes

$$D = \left(1 - \frac{\cos \beta_1}{\cos \beta_2}\right) + \frac{\cos \beta_1}{2\sigma} (\tan \beta_1 - \tan \beta_2) \quad (8)$$

As in the case of the local diffusion factor, the diffusion factor of equation (8) is restricted to the region of minimum loss.

Cascade total-pressure losses at reference minimum-loss incidence angle are presented in reference 23 as a function of diffusion factor for the blades of reference 11. In a further unpublished analysis, a composite plot of the variation of computed wake momentum-thickness ratio with D factor at reference minimum-loss incidence angle was obtained from the available systematic cascade data (refs. 11, 12, and 30) as shown in figure 26. Blade maximum thickness was 10 percent in all cases. A separation of the suction-surface boundary layer at high blade loading is indicated by the increased rise in the wake momentum thickness for values of diffusion factor greater than about 0.6.

For situations in which the determination of a wake momentum-thickness ratio cannot be made, a significant loss analysis may be obtained if a simplified total-pressure-loss parameter is used that closely approximates the wake thickness. Since the terms within the braces of equation (5) are generally secondary factors, a loss parameter of the

form $\bar{\omega}_1 \frac{\cos \beta_2}{2\sigma} \left(\frac{\cos \beta_2}{\cos \beta_1} \right)^2$ should constitute a more fundamental expres-

sion of the basic loss across a blade element than the loss coefficient alone. The effectiveness of the substitute loss parameter

$\bar{\omega}_1 \frac{\cos \beta_2}{2\sigma} \left(\frac{\cos \beta_2}{\cos \beta_1} \right)^2$ in correlating two-dimensional-cascade losses is

illustrated in figure 27(a) for all the data for the NACA 65-(A₁₀)-series blades of reference 11. (Total-pressure-loss coefficients were computed for the data from relations given in ref. 23.) A generalized correlation

can also be obtained in terms of $\bar{\omega}_1 \frac{\cos \beta_2}{2\sigma}$, as shown in figure 27(b), but its effectiveness as a separation indicator does not appear to be as good. Such generalized loss parameters are most effective if the wake form does not vary appreciably among the various data considered.

Effect of blade maximum thickness. - Since an increase in blade maximum-thickness ratio increases the magnitude of the surface velocities (and therefore the diffusion), higher values of wake momentum-thickness ratio would be expected for thicker blades. From an analysis of limited available data on varying blade maximum-thickness ratio (refs. 34 and 35), it appears that the effect of blade thickness on wake momentum-thickness ratio is not large for conventional cascade configurations. For example, for an increase in blade maximum-thickness ratio from 0.05 to 0.10, an increase in θ^*/c of about 0.003 at D of about 0.55 and an increase of about 0.002 at D of about 0.35 are indicated. The greater increase in wake θ^*/c at the higher diffusion level is understandable, since the rate of change of θ^*/c with D_1 increases with increasing diffusion (see fig. 24).

If blade surface velocity distributions can be determined, then the thickness effect will automatically be included in the evaluation of the resulting local diffusion factor. When an over-all diffusion factor such as equation (7) is used, variations in blade thickness are not reflected in the corresponding loss prediction. However, in view of the small observed effect and the scatter of the original θ^*/c against D correlation of figure 26, it is believed that a thickness correction is unwarranted for conventional thickness ranges. However, the analysis does indicate that, for high diffusion and high solidity levels, it may be advisable to maintain blade thickness as small as practicable in order to obtain the lowest loss at the reference condition.

Thus, the plots of figures 24, 26, and 27 show that, when diffusion factor and wake momentum-thickness ratio (or total-pressure-loss parameter) are used as the basic blade-loading and loss parameters, respectively, a generalized correlation of two-dimensional-cascade loss data is obtained. Although several assumptions and restrictions are involved in the use and calculation of these parameters, the basic diffusion approach constitutes a useful tool in cascade loss analysis. In particular, the diffusion analysis should be investigated over the complete range of incidence angle in an effort to determine generalized off-design loss information.

Effect of Reynolds number and turbulence. - The effect of blade-chord Reynolds number and turbulence level on the measured losses of cascade sections is discussed in the section on Data Selection, in chapter V (ref. 1), and in references 11, 15, 39. In all cases, the data reveal an increasing trend of loss coefficient with decreasing Reynolds number and turbulence. Examples of the variation of the total-pressure-loss coefficient with incidence angle for conventional compressor blade sections at two different values of Reynolds number are illustrated in figure 28. Loss variations with Reynolds number over a range of incidence angles for a given blade shape are shown in figure 29. A composite plot of the variation of total-pressure-loss coefficient at minimum loss with blade-chord Reynolds number for a large number of blade shapes is shown in figure 30. Identification data for the various blades included in the figure are given in the references. For the blades whose loss data are reported in terms of drag coefficient, conversion to total-pressure-loss coefficient was accomplished according to the cascade relations presented in reference 23. The effect of change in tunnel turbulence level through the introduction of screens is indicated for some of the blades.

It is apparent from the curves in figure 30 that it is currently impossible to establish any one value of limiting Reynolds number that will hold for all blade shapes. (The term limiting Reynolds number refers to the value of Reynolds number at which a large rise in loss is obtained.) On the basis of the available cascade data presented in figure 30, however, it appears that serious trouble in the minimum-loss region may be encountered at Reynolds numbers below about 2.5×10^5 . Carter in reference 9 places the limiting blade-chord Reynolds number based on outlet velocity at 1.5 to 2.0×10^5 . Considering that outlet Reynolds number is less than inlet Reynolds number for decelerating cascades, this quoted value is in effective agreement with the value of limiting Reynolds number deduced herein.

The desirability of conducting cascade investigations in the essentially flat range of the curve of loss coefficient against Reynolds number in order to enhance the correlation of data from various tunnels, as well as from the various configurations of a given tunnel, is indicated. Cascade operation in the flat range of Reynolds number may also yield a more significant comparison between observed and theoretically computed loss.

Reynolds number and turbulence level should always be defined in cascade investigations. Furthermore, the development of some effective Reynolds number (ch. V (ref. 1)) which attempts to combine the effects of both blade-chord Reynolds number and turbulence should be considered for use as the independent variable.

Effect of inlet Mach number. - In the previous correlations, attention was centered on the various factors affecting the loss of cascade blades for essentially incompressible or low Mach number flow. Tests of cascade sections at higher Mach number levels have been relatively few, primarily because of the large power requirements and operational difficulties of high-velocity tunnels. As a consequence, it has not been possible to establish any empirical correlations that will permit the estimation of Mach number effects for conventional blade sections. The limited available data indicate, however, that a marked rise in loss is eventually obtained as Mach number is increased.

A typical example of the variation of total-pressure-loss coefficient with inlet Mach number for a conventional cascade section at fixed incidence angle in the region of minimum loss is presented in figure 31(a). The inlet Mach number at which the sharp rise in loss occurs is referred to as the limiting Mach number. The variation of the wake profile downstream of the blade as Mach number is increased is shown in figure 31(b) to illustrate the general deterioration of the suction-surface flow. The flow deterioration is the result of a separation of the suction-surface boundary layer induced by shock-wave and boundary-layer interactions.

In view of the complex nature of the shock-wave development and its interaction effects, the estimation of the variation of minimum total-pressure loss with inlet Mach number for a given blade is currently impossible. At the moment, this pursuit must be primarily an experimental one. Schlieren photographs showing the formation of shocks in a cascade are presented in references 40 to 42, and detailed discussions of shock formations and high-speed performance of two-dimensional-cascade sections are treated in references 40 and 42 to 45. Cascade experience (refs. 21 and 40) and theory (refs. 42, 45, and 46) indicate that a location of the point of maximum thickness at about the 50-percent-chord position and a thinning of the blade leading and trailing edges are favorable for good high Mach number performance. The avoidance of a throat area within the blade passage is also indicated in order to minimize the effects of flow choking. Discussions of the choking problem are presented in references 35 and 44, and blade throat areas are given for several blade shapes in references 13 and 47 to 49. The effects of camber distribution on high Mach number performance are discussed extensively in the literature (refs. 13, 32, and 33). Results indicate that, for the range of blade shapes and Mach numbers normally covered, camber distribution does not have a large effect on maximum Mach number performance as obtained in the two-dimensional cascade.

Summary

From the foregoing correlations and considerations, the low-speed loss in total pressure of conventional two-dimensional-cascade sections can readily be estimated. If blade surface velocity distributions are available, the suction-surface local diffusion factor D_l is determined according to equation (6) and a value of θ^*/c is then selected from figure 24. In the absence of blade surface velocity data, the diffusion factor D is computed from over-all conditions by means of equation (7) and θ^*/c is selected from figure 26. With θ^*/c determined, the total-pressure-loss coefficient is computed according to equation (5) from the cascade geometry and a pertinent value of wake form factor H .

According to reference 22, for cascade measuring stations located more than about $1/2$ chord length downstream of the blade trailing edge, the value of H will generally be less than about 1.2. For practical purposes, it was indicated that a constant value of H of about 1.1 can be used over a wide range of cascade configurations and incidence angles for measuring stations located between $1/2$ to $1\frac{1}{2}$ chord lengths behind the trailing edge. Loss coefficients based on inlet dynamic head can then be determined, if desired, from equation (8). The estimation of losses based on the diffusion factor D can, for example, produce a value of solidity that results in the least computed loss coefficient for a given velocity diagram.

The accuracy of the results obtained from the prediction procedure outlined is subject to the limitations and approximations involved in the diffusion analysis and wake momentum-thickness correlations. Strictly speaking, the procedure gives essentially a band of probable loss values at the cascade measuring station about $1/2$ to $1\frac{1}{2}$ chord lengths downstream of the blade trailing edge for the reference incidence-angle setting and Reynolds numbers of about 2.5×10^5 and greater at low speed (up to about 0.3 inlet Mach number). It should also be noted at this point that the loss values obtained in this manner represent the low-speed profile loss of the cascade section. Such loss values are not generally representative of the losses of the section in a compressor blade row or in a high-speed cascade.

A corresponding loss-estimation technique for high Mach number flow is currently unavailable because of the unknown magnitude of the compressibility effect on the wake momentum-thickness ratio of a given cascade geometry. Furthermore, both the wake form factor H and the relation between θ^*/c and \bar{w} (given for incompressible flow by eq. (5)) vary with Mach number. For example, if the velocity variation in each leg of

3383

CG-4

the wake is assumed to vary according to the power relation

$$\frac{v}{v_0} = \left(\frac{y}{\delta}\right)^d \quad (9)$$

where δ is the thickness of the wake and d is some constant. then variations of H and θ^* and of the relation between θ^*/c and $\bar{\omega}$ with outlet free-stream Mach number can be established analytically to illustrate the nature of the compressibility effects.

Curves of the variation of the ratios of compressible to incompressible form factor H/H_{inc} and momentum thickness θ^*/θ_{inc}^* with outlet Mach number for various d values obtained from numerical integration of the wake parameters involved are shown in figures 32 and 33. Recently, the increasing trend of H with M_2 was substantiated experimentally at the NACA Lewis laboratory in an investigation of the wake characteristic of a turbine nozzle (unpublished data). Curves of the ratio of the integrated value of $\bar{\omega}$ obtained from a given value of θ^*/c in a compressible flow to the value of $\bar{\omega}$ computed from the same value of θ^*/c according to the incompressible relation of equation (5) are shown in figure 34. It should be noted that for compressible flow the denominator in the loss-coefficient definition (eq. (4)) is now given by $P - p$.

In summary, therefore, an accurate prediction of the variation of reference total-pressure loss with inlet Mach number for a given cascade blade is currently impossible. At the moment, this pursuit is primarily an experimental one. Families of curves of wake momentum thickness and form factor against diffusion factor are required (with appropriate definitions for subsonic or supersonic flow) as in figure 24 or 26 for a wide range of inlet Mach number. Analytically, a simple compressible relation is needed between θ^*/c and $\bar{\omega}$ as a function of Mach number.

DEVIATION-ANGLE ANALYSIS

Preliminary Analysis

The correct determination of the outlet flow direction of a cascade blade element presents a problem, because the air is not discharged at the angle of the blade mean line at the trailing edge, but at some angle δ^0 to it (fig. 2). Inasmuch as the flow deviation is an expression of the guidance capacity of the passage formed by adjacent blades, it is expected that the cascade geometry (camber, thickness, solidity, and chord angle) will be the principal influencing factor involved.

From cascade potential-flow theory (ref. 26, e.g.), it is found that the deviation angle increases with blade camber and chord angle and decreases with solidity. Weinig in reference 26 shows that the deviation angle varies linearly with camber for a given value of solidity and chord angle for infinitesimally thin blades at zero incidence. Furthermore, with deviation angle equal to zero at zero camber angle in this theory, it is possible to express the deviation angle as a ratio of the camber angle. Values of the ratio of deviation angle to camber angle for an infinitely thin circular-arc blade of small camber deduced from the theory of reference 26 are presented in figure 35 for a range of solidities and chord angles. The values in figure 35 are for the incidence angle for "impact-free entry" previously mentioned, which corresponds essentially to the condition of minimum loss.

The results of figure 35 show that, for a blade of zero thickness, the minimum-loss deviation angle is zero at zero camber angle. Analysis indicates, however, that this is not the case for blades of conventional thicknesses. A recent theoretical demonstration of the existence of a positive value of zero-camber deviation angle according to potential-flow calculations is given by Schlichting in reference 16. The computed variation of zero-camber deviation angle for a conventional 10-percent-thick profile at zero incidence angle as obtained in the reference is shown in figure 36.

It will be recalled from the discussion of the zero-camber minimum-loss incidence angle that, for the conventional staggered cascade ($0^\circ < \gamma^\circ < 90^\circ$) with finite blade thickness set at zero incidence angle, a greater magnitude of velocity occurs on the blade lower (concave) surface than on the upper (convex) surface (fig. 12). Such velocity distributions result in a negative blade circulation and, consequently (as indicated by the solid vectors in fig. 37), in a positive deviation angle. Furthermore, since the deviation angle increases slightly with increasing incidence angle ($d\delta^\circ/di$ is positive in potential cascade flow), positive values of deviation angle will likewise be obtained at the condition of minimum-loss incidence angle (as illustrated by the dashed vectors in fig. 37). Since the zero-camber deviation angle arises from essentially a thickness blockage effect, the characteristics of the variation of minimum-loss zero-camber deviation angle with cascade geometry would be expected to roughly parallel the variation of the minimum-loss zero-camber incidence angle in figure 15. The low-speed reference-deviation-angle correlations may, therefore, involve intercept values as in the case of the reference-incidence-angle correlations.

In addition to the cascade-geometry factors mentioned, the low-speed deviation angles can also be affected by Reynolds number, turbulence, and Mach number. The thickened surface boundary layers resulting from low levels of Reynolds number and turbulence tend to increase the deviation angle. Variations in inlet Mach number can affect the deviation angle of a fixed two-dimensional-cascade geometry because of the associated changes

in blade circulation, boundary-layer development, and outlet to inlet axial velocity ratio (compressibility effect on ρV_z).

Data Correlations

Form of correlation. - Examination of deviation-angle data at reference incidence angle reveals that the observed data can be satisfactorily represented by a linear variation of reference deviation angle with camber angle for fixed solidity and air inlet angle. The variation of reference deviation angle can then be expressed in equation form as

$$\delta^0 = \delta_0^0 + m\phi \quad (10)$$

where δ_0^0 is the reference deviation angle for zero camber, m is the slope of the deviation-angle variation with camber $(\delta^0 - \delta_0^0)/\phi$, and ϕ is the camber angle. As in the case of the analogous terms in the reference-incidence-angle relation (eq. (2)), δ_0^0 and m are functions of inlet-air angle and solidity.

The influence of solidity on the magnitude of the slope term m could also be directly included as a functional relation in equation (10), so that equation (10) could be expressed as

$$\frac{\delta^0 - \delta_0^0}{\phi} = \frac{m_{\sigma=1}}{\sigma^b} \quad (11)$$

where $m_{\sigma=1}$ represents the value of m (i.e., $(\delta^0 - \delta_0^0)/\phi$) at a solidity of 1, b is the solidity exponent (variable with air inlet angle), and the other terms are as before. It will be noted that equation (11) is similar in form to the frequently used deviation-angle rule for circular-arc blades originally established by Constant in reference 4 and later modified by Carter in reference 46. Carter's rule for the condition of nominal incidence angle is given by

$$\frac{\delta^0}{\phi} = \frac{m_c}{\sqrt{\sigma}} \quad (12)$$

in which m_c is a function of blade-chord angle. Values of m_c determined from theoretical considerations for circular-arc and parabolic-arc mean lines (ref. 46) are shown in figure 38. In the ensuing correlations, both forms of the deviation-angle relation (eqs. (10) and (11)) are used, since each has a particular advantage. Equation (10), with m plotted as a function of β_1 and σ , is easier to use for prediction, especially if the calculation of a required camber angle is involved. Equation (11) may be better for extrapolation and for comparison with Carter's rule.

As in the case for the zero-camber reference minimum-loss incidence angle, the zero-camber deviation angle can be represented as a function of blade thickness as

$$\delta_o^0 = (K_\delta)_{sh} (K_\delta)_t (\delta_o^0)_{10} \quad (13)$$

where $(\delta_o^0)_{10}$ represents the basic variation for the 10-percent-thick 65-series thickness distribution, $(K_\delta)_{sh}$ represents any correction necessary for a blade shape with a thickness distribution different from that of the 65-series blade, and $(K_\delta)_t$ represents any correction necessary for maximum blade thicknesses other than 10 percent. (For a 10-percent-thick 65-series blade, $(K_\delta)_t$ and $(K_\delta)_{sh}$ are equal to 1.) The problem, therefore, is reduced to finding the values of m , b , and δ_o^0 (through eq. (13)) as functions of the pertinent variables involved for the various blade shapes considered.

NACA 65-(A₁₀)-series blades. - From an examination of the plots of equivalent deviation angle against equivalent camber angle at reference minimum-loss incidence angle obtained from the cascade data, values of zero-camber deviation angle can be determined by extrapolation. The deduced plots of zero-camber deviation angle $(\delta_o^0)_{10}$ and slope term m as functions of solidity and air inlet angle are presented in figures 39 and 40 for these blades. The subscript 10 indicates that the δ_o^0 values are for 10-percent maximum-thickness ratio. Values of the intercept term δ_o^0 and the slope term m were obtained by fitting a straight line to each data plot of reference equivalent deviation angle against equivalent camber angle for a fixed solidity and air inlet angle. The straight lines were selected so that both a satisfactory representation of the variation of the data points and a consistent variation for the resulting δ_o^0 and m values were obtained. The extrapolation of the values of m to $\beta_1 = 0$ was guided by the data for the 65-(12A₁₀)10 blade at solidities of 1 and 1.5 reported in the cascade guide-vane investigation of reference 50 (for an aspect ratio of 1, as in ref. 11).

For the deviation-angle rule as given by equation (11), deduced values of $m_{\sigma=1}$ and exponent b as functions of inlet-air angle are presented in figures 41 and 42. The deduced rule values (eq. (10) or (11)) and the observed data points are compared in figure 43 to indicate the effectiveness of the deduced representations. The flagged symbols in the high-camber range in the figure represent blade configurations for which boundary-layer separation is indicated (D greater than about 0.62). In view of the higher loss levels for this condition, an increase in the magnitude of the deviation angle is to be expected compared with the values extrapolated from the smaller cambers for which a lower loss level existed.

C-Series circular-arc blades. - In view of the absence of systematic cascade data for the C-series circular-arc blade, an accurate determination of the rule constants cannot be made for this blade shape. However, a preliminary relation can be deduced on the basis of limited data. It appears that, for the uncambered C.4 section (refs. 12 and 30), if a value of $(K_\delta)_{sh}$ equal to 1.1 (as for the determination of i_0) is used, a satisfactory comparison between predicted and observed δ_0^0 values is obtained.

The characteristic number $m_{\sigma=1}$ in the deviation-angle design rule of equation (11) for a given blade mean line corresponds to the value of $(\delta^0 - \delta_0^0)/\phi$ at a solidity of unity. Cascade data for a C.4 circular-arc profile obtained from tunnels with good boundary-layer control are presented in references 15 and 31 for a solidity of 1.0 for $\beta_1 = 30^\circ, 42.5^\circ, 45^\circ$, and 60° . Values of $(\delta^0 - \delta_0^0)/\phi$ were computed for these blades according to the δ_0^0 variations of figure 39. A value of $m_{\sigma=1}$ for $\beta_1 = 0^\circ$ was obtained from the performance data of a free-stream circular-arc inlet guide vane presented in reference 51. These values of m are plotted in figure 44 against inlet-air angle, and the proposed variation of $m_{\sigma=1}$ for the circular-arc mean line is shown by the solid line.

In the absence of data covering a range of solidities, it was assumed that the solidity exponent b in the deviation-angle rule of equation (11) is independent of the profile shape and will therefore also be applicable for the circular-arc mean line. This assumption agrees with limited experimental data. The variation of ratio of deviation angle to camber angle obtained from constant-thickness circular-arc guide-vane sections of reference 52 ($\delta_0^0 = 0^\circ$ for guide vanes) over a wide range of solidities is shown in figure 45. A computed variation based on values of b and $m_{\sigma=1}$ obtained from figures 42 and 44, respectively, is shown in the figure by the solid line. A satisfactory agreement with these circular-arc data is thus demonstrated for the value of b obtained from the 65-series data. On the basis of these results, deduced curves of m against β_1 for a range of solidities (for use in conjunction with eq. (10)) were computed for the C-series circular-arc blade as indicated in figure 46.

Double-circular-arc blades. - Although limited data are available for the double-circular-arc blade (refs. 21 and 28), it was felt that these data could not be reliably utilized in the construction of a deviation-angle rule because of the questionable two-dimensionality of the respective test tunnels. However, since the C-series and the double-circular-arc blades differ only in thickness distribution, it is reasonable to expect that, as in the case of the reference-incidence-angle correlations, only the zero-camber deviation angles will be materially affected.

Therefore, the slope-term value m deduced for the C-series circular-arc blade (fig. 46) might also be used for the double-circular-arc blade, but the δ_o^o values may be different. An arbitrarily selected value of 0.7 for $(K_8)_{sh}$ in equation (13) (as for the reference-incidence-angle determination) is suggested for the double-circular-arc blade.

3383 Comparison of rules. - In view of the widespread use of Carter's rule (eq. (12)) with fig. 38) for predicting the deviation angle of circular-arc-mean-line blades, some results obtained from the use of Carter's rule were compared with the deduced rule of equation (11) with figures 39, 42, and 44. The principal difference between the two rules occurs in the blade orientation parameter used for the m variation and in the δ_o^o and b variations. The value of the solidity exponent of $1/2$ in equation (12) was originally obtained from limited data. Carter, in a later work, (ref. 9) proposes a variable solidity exponent and indicates values close to 1 for accelerating cascades and close to $1/2$ for decelerating cascades. The variation of b obtained from the NACA 65-(A₁₀)-series blades as equivalent circular arcs in figure 42 essentially confirms this trend. Actually, the deviation-angle rule in the form of equation (11) constitutes a modification of Carter's rule.

In addition to the basic differences between the rules in the magnitudes of the m , b , and δ_o^o values, it is noted that Carter's rule was originally developed for the condition of nominal incidence angle, whereas the modified rule pertains to the reference minimum-loss incidence angle. However, since Carter's rule has frequently been used over a wide range of reference angle in its application, both rules were evaluated, for simplicity, for the reference minimum-loss incidence angle.

An illustrative comparison of predicted reference deviation angle as obtained from Carter's rule and the modified rule for a 10-percent-thick, thick-nosed circular-arc blade is shown by the calculated results in figure 47 for ranges of camber angle, solidity, and inlet-air angle. Deviation angles in figure 47 were restricted to cascade configurations producing values of diffusion factor less than 0.6. Blade-chord angle for Carter's rule was computed from the equation

$$\gamma^o = \beta_1 - 1 - \frac{\phi}{2} \quad (14)$$

Reference incidence angle was determined from equations (2) and (3) and figures 15 and 16.

The plots of figure 47 show that, in practically all cases, the deviation angles given by the modified rule are somewhat greater in magnitude than those predicted by Carter's rule for the 10-percent-thick

blade. This is particularly true for the high inlet-air angles. Thus, greater camber angles are required for a given turning angle according to the modified rule. Differences are even less for the double-circular-arc blade, as indicated in figure 48, since the δ_0^0 values are smaller for these blades. However, it should be kept in mind that the magnitude of the factors in the modified rule are proposed values based on limited data. Further research is required to establish the modified rule on a firmer foundation.

Effect of blade maximum thickness. - Available data on the variation of reference deviation angle with blade maximum-thickness ratio obtained from cascade investigations of the 65-(12A₁₀) blade of reference 34 are shown in figure 49. The solid symbols representing the values of deviation angle at zero thickness were determined by subtracting the values of $(\delta_0^0)_{10}$ obtained from figure 39 from the measured value of deviation angle at 10-percent maximum thickness obtained from the data in figure 49. A very reasonable variation with thickness ratio, as indicated by the faired curves, is thus obtained for all three configurations. The increasing slope of the deviation-angle variation with increasing thickness ratio is believed due to some extent to the accompanying increase in wake losses.

Preliminary values of a correction factor for maximum-thickness ratio $(K_\delta)_t$ deduced from the data of figure 49 are shown in figure 50. In the absence of further data, it is proposed that this correction curve is also applicable to other conventional blade shapes.

Effect of Reynolds number. - In view of the large rise in loss as blade-chord Reynolds number is reduced (fig. 30), a corresponding rise in deviation angle (or decrease in turning angle) is to be expected. Experimental confirmation of the marked effect of Reynolds number on blade deviation angle at fixed incidence angle is illustrated in figure 51 for several compressor blade shapes. The variation of deviation angle with Reynolds number over a range of incidence angle is demonstrated in figure 52. In all cases the variation of the deviation or turning angle closely parallels the variation of the loss. Therefore, factors involved in the deviation-angle variation are the same as those for the loss behavior. Correspondingly, no Reynolds number correction factors that will be applicable for all blade configurations have been established. The deduced deviation-angle rule developed herein is applicable at a Reynolds number of about 2.5×10^5 and greater.

Effect of inlet Mach number. - Experimental variations of minimum-loss deviation angle with inlet Mach number are presented in figure 53 for two circular-arc blades. Further cascade data in terms of air-turning angle at fixed angle of attack are shown in figure 54 for two other

compressor blade shapes. (Inasmuch as the data in fig. 54 were obtained at constant angle of attack, the variation of turning angle is an inverse reflection of the variation of deviation angle.) The data of figures 53 and 54 indicate that deviation angle varies little with inlet Mach number up to the limiting value. As indicated in the Preliminary Analysis section (p. 27), the resultant Mach number effect for a given blade configuration will depend on the relative magnitude of the various factors involved. Apparently, the net effect is small up to the limiting value of inlet Mach number. Large increases in deviation angle can be expected, however, when the loss rises rapidly at the limiting Mach number because of the adverse effects of the shock formation. (The rise in deviation angle in the data is always associated with the sharp rise in loss.)

Variation with incidence angle. - Thus far, of necessity, the analysis has been conducted for flow conditions at only one reference position on the general curve of loss against incidence angle. Ultimately, of course, it is desired to predict flow variations over the entire range of incidence angle. The variation of deviation angle with incidence angle for a fixed geometry in the two-dimensional cascade is primarily a function of the change in the guidance capacity of the cascade arising from the change in orientation of the approaching flow (a potential-flow effect) and of the variation in the wake loss. Since no information is currently available on the effect of losses, attention is centered on deviation-angle variations in the region of low loss, where the trend of variation approaches that of the potential flow.

Examination of potential-flow theory (Weinig, ref. 26, e.g.) shows that a positive slope of deviation angle against incidence angle exists (i.e., deviation angle increases with incidence angle). Calculations based on the theory of Weinig reveal that the magnitude of the slope varies with solidity and blade-chord angle. The deviation-angle slope approaches zero for infinite solidity (deviation angle is essentially constant at high solidity) and increases as solidity is reduced. At constant solidity, the slope of deviation angle against incidence angle increases as the chord angle is increased. These trends indicate physically that the greater the initial guidance effect (high solidity and low blade angle), the less sensitive the deviation angle is to changes in incidence angle.

For analysis purposes, since the region of low loss is generally small, the variation of deviation angle with incidence angle for a given cascade geometry in the region of minimum loss can be represented as

$$\delta^0 = \delta_{\text{ref}}^0 + (i - i_{\text{ref}}) \left(\frac{d\delta^0}{di} \right)_{\text{ref}} \quad (15)$$

where $(d\delta^0/di)_{\text{ref}}$ represents the slope of the deviation-angle variation

at the reference incidence angle. An empirical determination of the magnitude of the slope of the variation of deviation angle with incidence angle was obtained from an analysis of the low-speed experimental data for the 65-(A₁₀)10 blades of reference 11. From the plot of deviation angle against incidence angle for each configuration (as in fig. 5, e.g.), the slope of the curve at the minimum-loss incidence angle was evaluated graphically. The deduced variation of reference slope magnitude $d\delta^0/di$ obtained from fairings of these values is presented in figure 55 as a function of solidity and inlet-air angle. Qualitative agreement with theory is strongly indicated by the data. Inasmuch as the phenomenon is essentially a guidance or channel effect, it is anticipated that the slope values of figure 55 will also be applicable for other conventional blade shapes. Thus, it is possible to predict the deviation angle at incidence angles other than the reference location within the low-loss range of operation from the use of equation (15) and figure 55.

Summary

The analysis of blade-section deviation angle shows that the variation of reference deviation angle with cascade geometry at low speed can be satisfactorily established in terms of an intercept value δ_0^0 and a slope value m as given by equation (10). The experimental data could also be expressed in terms of a rule similar in form to Carter's rule, as indicated by equation (11). Deduced values of δ_0^0 and m were obtained as a function of β_1 and σ from the data for the 10-percent-thick 65-(A₁₀)-series blades of reference 11 as equivalent circular arc (figs. 39 and 40). Rules for predicting the reference deviation angle of the C-series and double-circular-arc blades were also deduced based on the correlations for the 65-(A₁₀)-series blades and on limited data for the circular-arc blade (figs. 39 and 46).

The procedure involved in estimating the low-speed reference deviation angle of a blade section is as follows: From known values of β_1 and σ , $(\delta_0^0)_{10}$ is selected from figure 39, and m is selected from figure 40 for the 65-(A₁₀)-series blades or from figure 46 for circular-arc-mean-line blades. The value of $(K_\delta)_t$ for the blade maximum-thickness ratio is obtained from figure 50, and the approximate value of $(K_\delta)_{sh}$ is selected for the type of thickness distribution. For the 65-series blades, $(K_\delta)_{sh} = 1.0$, and it is proposed that $(K_\delta)_{sh}$ be taken as 1.1 for the C-series blades and as 0.7 for the double-circular-arc blade. The value of δ_0^0 is then computed from equation (13), and finally δ^0 is determined from the blade camber angle according to equation (10). As in the case of reference i_0 values, the use of the proposed values of $(K_\delta)_{sh}$ is not

critical for good accuracy in the final determination of δ^0 . Reference deviation angle can also be computed according to the rule in the form of equation (11) in conjunction with figures 41, 42, and 44.

The camber angle required to produce a given turning angle at the reference condition at low speed can readily be calculated by means of the preceding incidence-angle and deviation-angle correlations when the inlet-air angle and blade solidity are known. From equations (1), (2), and (10), the camber angle as a function of the turning, deviation, and incidence angle is

$$\phi = \frac{\Delta\beta - (i_o - \delta_o^0)}{1 - m + n} \quad (16)$$

or, in terms of the thickness corrections (eqs. (3) and (13)),

$$\phi = \frac{\Delta\beta - [(K_i)_{sh}(K_i)_t(i_o)_{10} - (K_\delta)_{sh}(K_\delta)_t(\delta_o^0)_{10}]}{1 - m + n} \quad (17)$$

For simplicity, since $(K_i)_{sh} = (K_\delta)_{sh} = K_{sh}$, equation (17) can be expressed in the form

$$\phi = \frac{\Delta\beta - K_{sh}\bar{K}_t [(i_o)_{10} - (\delta_o^0)_{10}]}{1 - m + n} \quad (18)$$

where \bar{K}_t represents some correction factor for blade thickness, such that

$$\bar{K}_t [(i_o)_{10} - (\delta_o^0)_{10}] \approx (K_i)_t(i_o)_{10} - (K_\delta)_t(\delta_o^0)_{10} \quad (19)$$

Curves of the values of $(i_o)_{10} - (\delta_o^0)_{10}$ as a function of β_1 and σ are given in figure 56; curves of the values of $1 - m + n$ as a function of β_1 and σ are given in figure 57(a) for the 65-(A₁₀)-series mean line and in figure 57(b) for the circular-arc mean line; and values of \bar{K}_t are plotted as a function of β_1 and t/c in figure 58. The use of the chart values of \bar{K}_t in equation (18) gives results within about 0.1° of the exact values given by equation (17). Required camber angle can thus be determined readily by equation (18) in conjunction with figures 56 to 58.

CONCLUDING REMARKS

The foregoing analysis has presented a correlation of available two-dimensional experimental cascade data in terms of parameters significant

3383

CG-5 back

in compressor design. The work essentially presents a summary of the state of experimental cascade research with regard to cascade performance at the reference incidence angle. Rules and procedures were evolved for the prediction of the magnitude of the reference total-pressure loss and the reference incidence and deviation angles in satisfactory agreement with existing cascade data. The rules may also be of help in reducing the necessary experimental effort in the accumulation of further cascade data.

However, the present analysis is incomplete. Many areas, such as the deviation-angle rule for the double-circular-arc blade, require further data to substantiate the correlations. Furthermore, additional information concerning the influence of high Mach number and off-design incidence angles of cascade performance is needed.

Finally, it is recognized that the performance of a given blade geometry in the compressor configuration will differ from the performance established in the two-dimensional cascade. These differences result from the effects of the various three-dimensional phenomena that occur in compressor blade rows. It is believed, however, that a firm foundation in two-dimensional-cascade flow constitutes an important step toward the complete understanding of the compressor flow. The extent to which cascade-flow performance can be successfully utilized in compressor design can only be established from further comparative evaluations. Such comparisons between observed compressor performance and predicted two-dimensional-cascade performance on the basis of the rules derived herein are presented in chapter VII.

REFERENCES

1. Compressor and Turbine Research Division: Aerodynamic Design of Axial-Flow Compressors. Vol. I. NACA RM E56B03, 1956.
2. Kantrowitz, Arthur, and Daum, Fred L.: Preliminary Experimental Investigation of Airfoils in Cascade. NACA WR L-231, 1942. (Supersedes NACA CB.)
3. Bogdonoff, Seymour M., and Bogdonoff, Harriet E.: Blade Design Data for Axial-Flow Fans and Compressors. NACA WR L-635, 1945. (Supersedes NACA ACR L5F07a.)
4. Constant, H.: Note on Performance of Cascades of Aerofoils. Note No. E.3696, British R.A.E., 1939.
5. Davis, Hunt: A Method of Correlating Axial-Flow-Compressor Cascade Data. A.S.M.E. Trans., vol. 70, no. 8, Nov. 1948, pp. 951-955.

6. Howell, A. R.: The Present Basis of Axial Flow Compressor Design. Pt. I - Cascade Theory and Performance. R. & M. No. 2095, British A.R.C., June 1942.
7. Howell, A. R., and Carter, A. D. S.: Fluid Flow through Cascades of Aerofoils. Rep. No. R.6, British N.G.T.E., Sept. 1946.
8. Carter, A. D. S., and Hounsell, A. F.: General Performance Data for Aerofoils Having C.1, C.2, or C.4 Base Profiles on Circular Arc Camber Lines. Memo. No. M.62, British N.G.T.E., Aug. 1949.
9. Carter, A. D. S.: The Low Speed Performance of Related Aerofoils in Cascade. Rep. No. R.55, British N.G.T.E., Sept. 1949. (See also C.P. No. 29, British M.O.S., Sept. 1949.)
10. Erwin, John R., and Emery, James C.: Effect of Tunnel Configuration and Testing Technique on Cascade Performance. NACA Rep. 1016, 1951. (Supersedes NACA TN 2028.)
11. Herrig, L. Joseph, Emery, James C., and Erwin, John R.: Systematic Two-Dimensional Cascade Tests of NACA 65-Series Compressor Blades at Low Speeds. NACA RM L51G31, 1951.
12. Fletcher, P. J.: Low Speed Tests on Compressor Cascades of Parabolic Cambered Aerofoils. Pt. II - Pitch/Chord Ratio = 0.75. Memo. No. M.159, British N.G.T.E., Nov. 1952.
13. Erwin, John R., Savage, Melvyn, and Emery, James C.: Two-Dimensional Low-Speed Cascade Investigation of NACA Compressor Blade Sections Having a Systematic Variation in Mean-Line Loading. NACA RM L53I30b, 1953.
14. Felix, A. Richard: Summary of 65-Series Compressor-Blade Low-Speed Cascade Data by Use of the Carpet-Plotting Technique. NACA RM L54H18a, 1954.
15. Blight, F. G., and Howard, W.: Tests on Four Airfoil Cascades. Pt. I - Deflection, Drag, and Velocity Distribution. Rep. E.74, Dept. Supply, Aero. Res. Lab., Melbourne (Australia), July 1952.
16. Schlichting, Herman: Problems and Results of Investigations on Cascade Flow. Jour. Aero. Sci., vol. 21, no. 3, Mar. 1954, pp. 163-178.
17. Katzoff, S., and Hannah, Margery E.: Further Comparisons of Theoretical and Experimental Lift and Pressure Distributions on Airfoils in Cascade at Low-Subsonic Speed. NACA TN 2391, 1951.

18. Carter, A. D. S., Andrews, S. J., and Shaw, H.: Some Fluid Dynamic Research Techniques. Proc. Inst. Mech. Eng. (London), vol. 163, 1950, pp. 249-263.
19. Blight, F. G., Howard, W., and McCallum, H.: The Design and Performance of a Low-Speed Cascade Tunnel. Eng. Note 133, Aero. Lab., Fishermen's Bend, Melbourne (Australia), June 1949.
20. Briggs, William B.: Effect of Mach Number on the Flow and Application of Compressibility Corrections in a Two-Dimensional Subsonic-Transonic Compressor Cascade Having Varied Porous-Wall Suction at the Blade Tips. NACA TN 2649, 1952.
21. Andrews, S. J.: Tests Related to the Effect of Profile Shape and Camber Line on Compressor Cascade Performance. Rep. No. R.60, British N.G.T.E., Oct. 1949.
22. Lieblein, Seymour, and Roudebush, William H.: Theoretical Loss Relations for Low-Speed Two-Dimensional-Cascade Flow. NACA TN 3662, 1956.
23. Lieblein, Seymour, Schwenk, Francis C., and Broderick, Robert L.: Diffusion Factor for Estimating Losses and Limiting Blade Loadings in Axial-Flow-Compressor Blade Elements. NACA RM E53D01, 1953.
24. Korbacher, G. K.: A Test on a Compressor Cascade of Aerofoils Having Their Position of Maximum Thickness 40% of the Chord from the Leading Edge and a Pitch/Chord Ratio of 0.75. Memo. No. M.89, British N.G.T.E., June 1950.
25. Jeffs, R. A., Hounsell, A. F., and Adams, R. G.: Further Performance Data for Aerofoils Having C.1, C.2, or C.4 Base Profiles on Circular Arc Camber Lines. Memo. No. M.139, British N.G.T.E., Dec. 1951.
26. Weinig, Fritz: The Flow Around the Blades of Turbomachines. Johann Ambrosius Barth (Leipzig), 1935.
27. Stanitz, John D.: Effect of Blade-Thickness Taper on Axial-Velocity Distribution at the Leading Edge of an Entrance Rotor-Blade Row with Axial Inlet, and the Influence of This Distribution on Alignment of the Rotor Blade for Zero Angle of Attack. NACA TN 2986, 1953.
28. Howell, A. R.: A Note on Compressor Base Aerofoils C.1, C.2, C.3, C.4, C.5, and Aerofoils Made Up of Circular Arcs. Memo. No. M.1011, Power Jets (Res. and Dev.), Ltd., Sept. 1944.
29. Hughes, Hazel P.: Base Profiles C.7. Memo. M.1210, British N.G.T.E., May 1946.

23

30. Fletcher, P. J.: Low Speed Tests on Compressor Cascades of Parabolic Cambered Aerofoils. Pt. I - Pitch/Chord Ratio = 1.0. Memo. No. M.81, British N.G.T.E., Mar. 1950.
31. Felix, A. Richard, and Emery, James C.: A Comparison of Typical National Gas Turbine Establishment and NACA Axial-Flow Compressor Blade Sections in Cascade at Low Speed. NACA RM L53B26a, 1953.
32. Andrews, S. J., Andrews, Patricia M., and Baines, Margaret: A Comparison between Two Compressor Cascades Using C.4 Profile on Parabolic and Circular Arc Camber Lines. Memo. No. M.6, British N.G.T.E., Sept. 1946.
33. Carter, A. D. S.: Some Tests on Compressor Cascades of Related Aerofoils Having Different Positions of Maximum Camber. Rep. No. R.47, British N.G.T.E., Dec. 1948.
34. Herrig, L. Joseph, Emery, James C., and Erwin, John R.: Effect of Section Thickness and Trailing-Edge Radius on the Performance of NACA 65-Series Compressor Blades in Cascade at Low Speeds. NACA RM L51J16, 1951.
35. Bailey, W., and Jefferson, J. L.: Compressibility Effects on Cascades of Low Cambered Compressor Blades. Rep. No. E.3972, British R.A.E., May 1943.
36. Reeman, J., and Simonis, E. A.: The Effect of Trailing Edge Thickness on Blade Loss. Tech. Note No. 116, British R.A.E., Mar. 1943.
37. Stewart, Warner L.: Investigation of Compressible Flow Mixing Losses Obtained Downstream of a Blade Row. NACA RM E54I20, 1954.
38. Savage, Melvyn: Analysis of Aerodynamic Blade-Loading-Limit Parameters for NACA 65-(C₁₀A₁₀)10 Compressor-Blade Sections at Low Speeds. NACA RM L54LO2a, 1955.
39. Lawson, T. V.: An Investigation into the Effect of Reynolds Number on a Cascade of Blades with Parabolic Arc Camber Lines. Memo. No. M.195, British N.G.T.E., Nov. 1953.
40. Todd, K. W.: An Experimental Study of Three-Dimensional High-Speed Air Conditions in a Cascade of Axial-Flow Compressor Blades. R. & M. No. 2792, British A.R.C., Oct. 1949.
41. Bogdonoff, Seymour M.: N.A.C.A. Cascade Data for the Blade Design of High-Performance Axial-Flow Compressors. Jour. Aero. Sci., vol. 15, no. 2, Feb. 1948, pp. 89-95.

42. Klapproth, John F.: General Considerations of Mach Number Effects on Compressor-Blade Design. NACA RM E53L23a, 1954.
43. Savage, Melvyn, Felix, A. Richard, and Emery, James C.: High-Speed Cascade Tests of a Blade Section Designed for Typical Hub Conditions of High-Flow Transonic Rotors. NACA RM L55F07, 1955.
44. Carter, A. D. S., and Hughes, Hazel P.: A Note on the High Speed Performance of Compressor Cascades. Memo. No. M.42, British N.G.T.E., Dec. 1948.
45. Staniforth, R.: A Note on Compressor Operation at Transonic Relative Inlet Mach Numbers. Memo. M.224, British N.G.T.E., July 1954.
46. Carter, A. D. S., and Hughes, Hazel P.: A Theoretical Investigation into the Effect of Profile Shape on the Performance of Aerofoils in Cascade. R. & M. No. 2384, British A.R.C., Mar. 1946.
47. Carter, A. D. S.: Throat Areas of Compressor Blade Cascades Derived for the Base Aerofoil C.4. Memo. No. M.1025, Power Jets, Ltd., Oct. 1944.
48. Hughes, Hazel P.: Throat Areas for the Parabolic Arc Cambered Aerofoil C.4 in Cascade. Memo. No. M.157, British N.G.T.E., Aug. 1952.
49. Wright, Linwood C., and Schwind, Richard: Throat-Area Determination for a Cascade of Double-Circular-Arc Blades. NACA RM E55H25a, 1955.
50. Dunavant, James C.: Cascade Investigation of a Related Series of 6-Percent-Thick Guide-Vane Profiles and Design Charts. NACA RM L54I02, 1954.
51. Alsworth, Charles C., and Iura, Toru: Theoretical and Experimental Investigations of Axial Flow Compressors. Pt. 3 - Progress Report on Loss Measurements in Vortex Blading. Mech. Eng. Lab., C.I.T., July 1951. (Navy Contract N6-ORI-102, Task Order IV.)
52. Mankuta, Harry, and Guentert, Donald C.: Some Effects of Solidity on Turning through Constant-Thickness Circular-Arc Guide Vanes in Axial Annular Flow. NACA RM E51E07, 1951.
53. Korbacher, G. K.: A Test on a Compressor Cascade of Aerofoils Having Their Position of Maximum Thickness 40% of the Chord and a Position of Maximum Camber of 45% of the Chord from the Leading Edge. Memo. No. M.80, British N.G.T.E., Mar. 1950.
54. Wilson, Robert E.: Turbulent Boundary-Layer Characteristics at Supersonic Speeds - Theory and Experiment. Jour. Aero. Sci., vol. 17, no. 9, Sept. 1950, pp. 585-594.

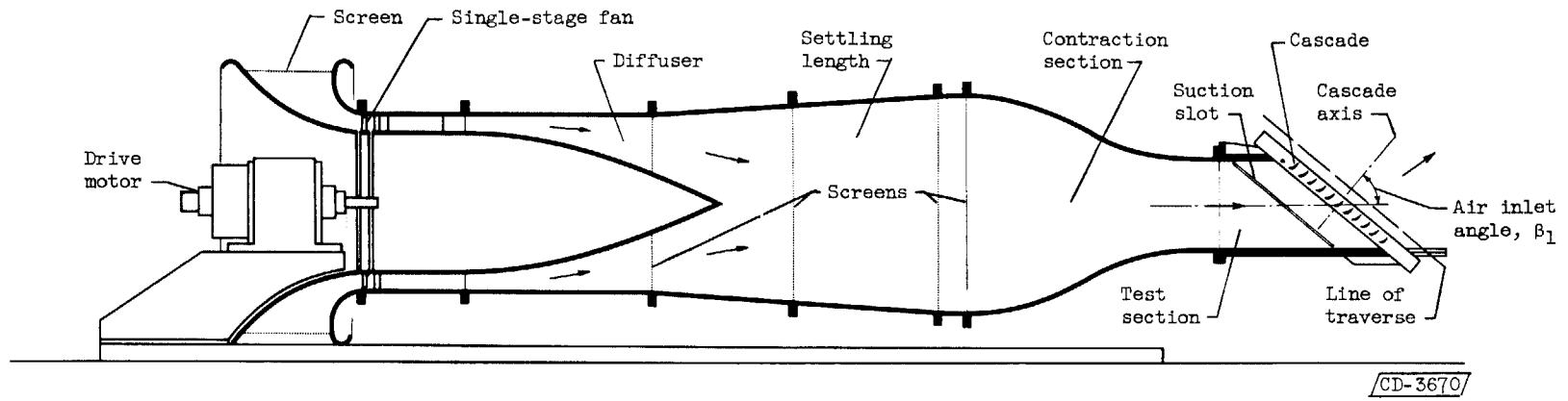
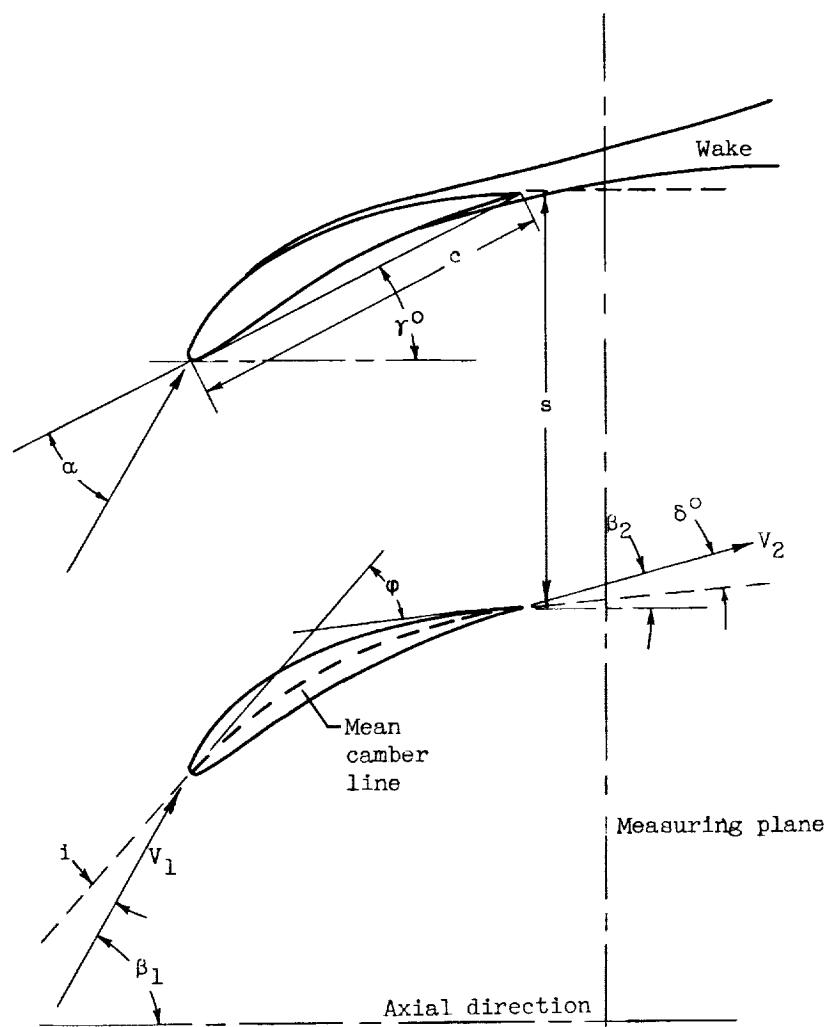


Figure 1. - Layout of conventional low-speed cascade tunnel (ref. 18).



- c blade chord
- i incidence angle, angle between tangent to mean camber line at leading edge and inlet-air velocity
- s blade spacing
- V_1 inlet-air velocity
- V_2 outlet-air velocity
- α angle of attack, angle between chord and inlet-air velocity
- β_1 inlet-air angle, angle between inlet-air velocity and axial direction
- β_2 outlet-air angle, angle between outlet-air velocity and axial direction
- $\Delta\beta$ air-turning angle, $\beta_1 - \beta_2$
- γ^o blade-chord angle, angle between chord and axial direction
- δ^o deviation angle, angle between tangent to mean camber line at trailing edge and outlet-air velocity
- σ solidity, ratio of chord to spacing, c/s
- ϕ blade camber angle, difference between angles of tangents to mean camber line at leading and trailing edges

Figure 2. - Nomenclature for cascade blade.

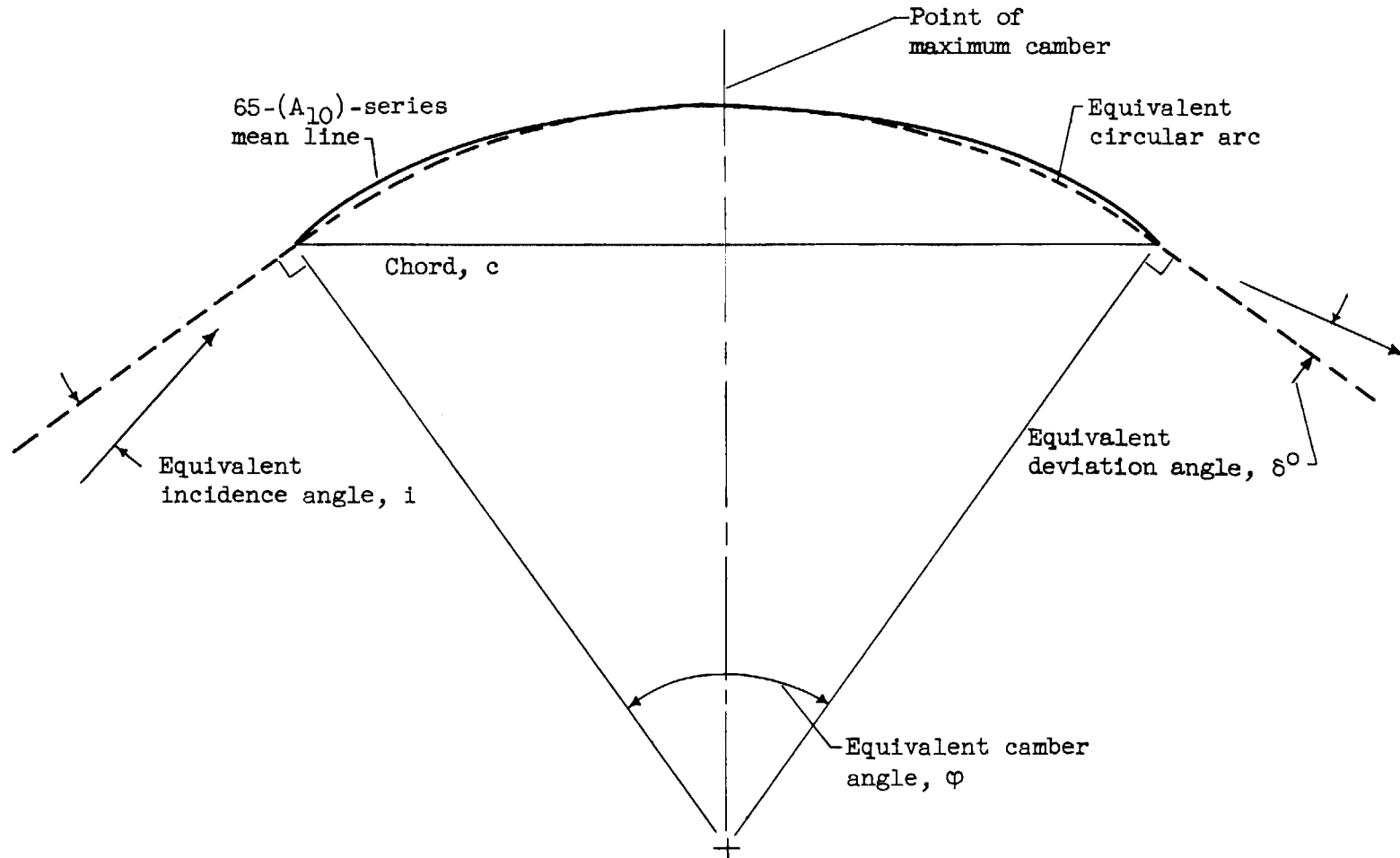


Figure 3. - Equivalent circular-arc mean line for NACA 65-(A₁₀)-series blades.

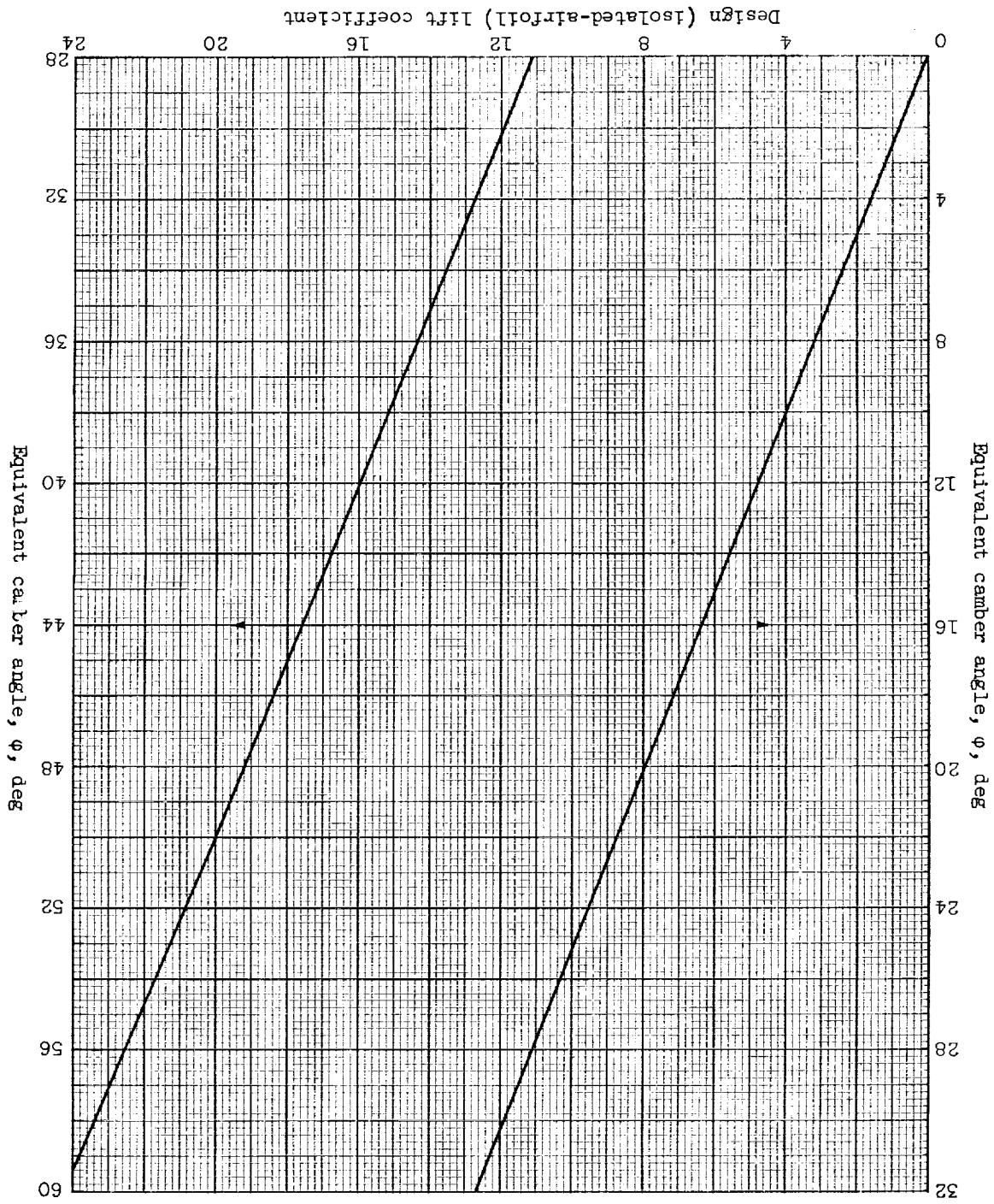


Figure 4. - Equivalent camber angles for NACA 65- $(C_{l0}A_{10})$ mean camber line as equivalent circular arc (Fig. 3).

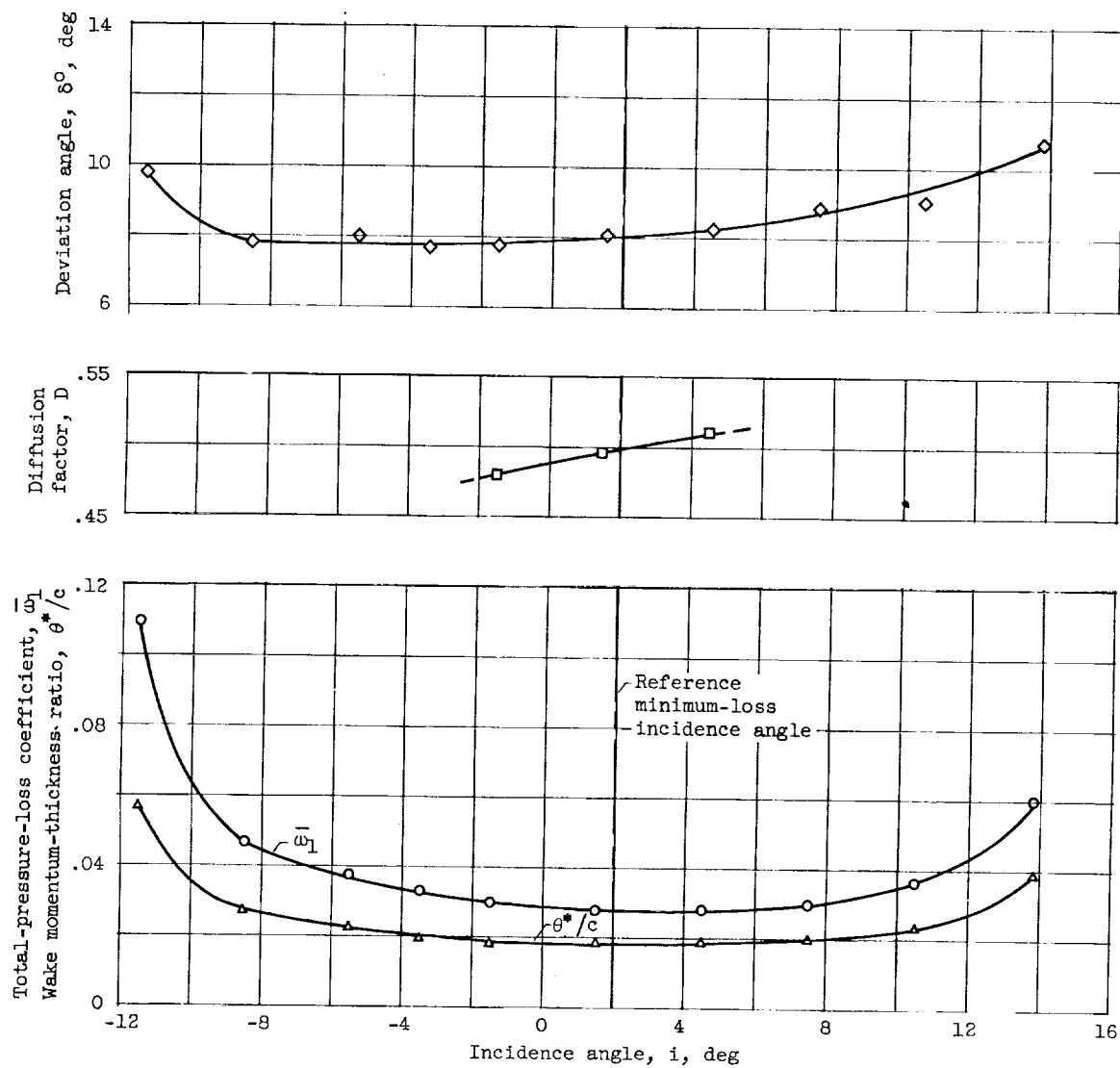
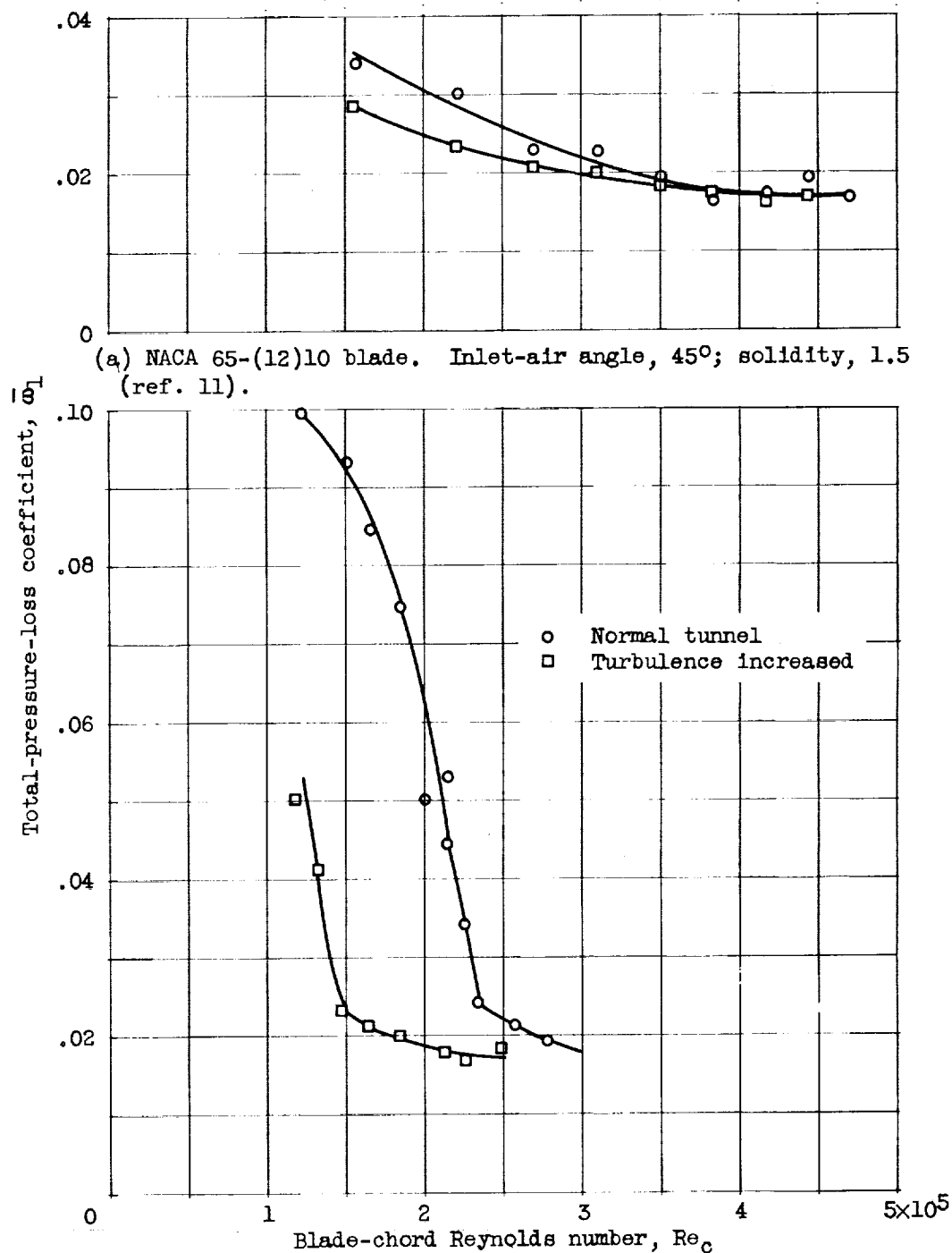


Figure 5. - Illustration of basic performance parameters for cascade analysis. Data obtained from conventional blade geometry in low-speed two-dimensional tunnel.



(a) NACA 65-(12)10 blade. Inlet-air angle, 45° ; solidity, 1.5 (ref. 11).

(b) Lighthill blade, 50 percent laminar flow. Inlet-air angle, 45.5° ; solidity, 1.0 (ref. 15).

Figure 6. - Effect of blade-chord Reynolds number and free-stream turbulence on minimum-loss coefficient of cascade blade section in two-dimensional tunnel.

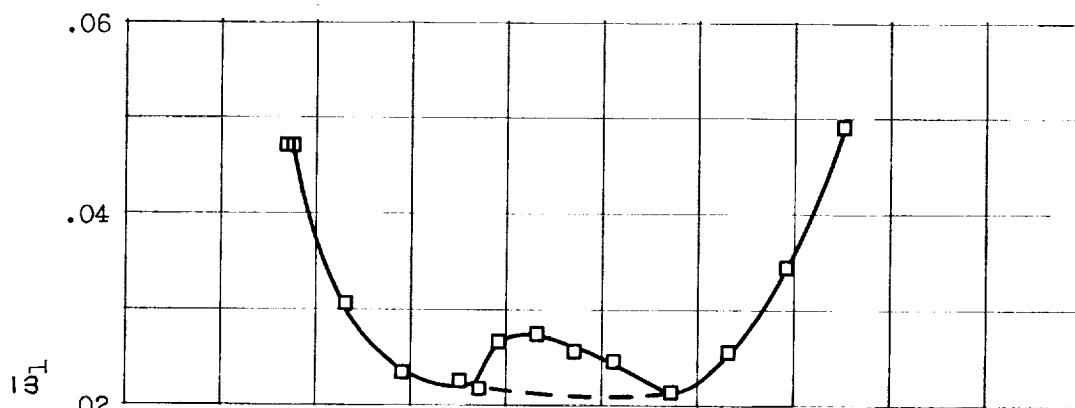
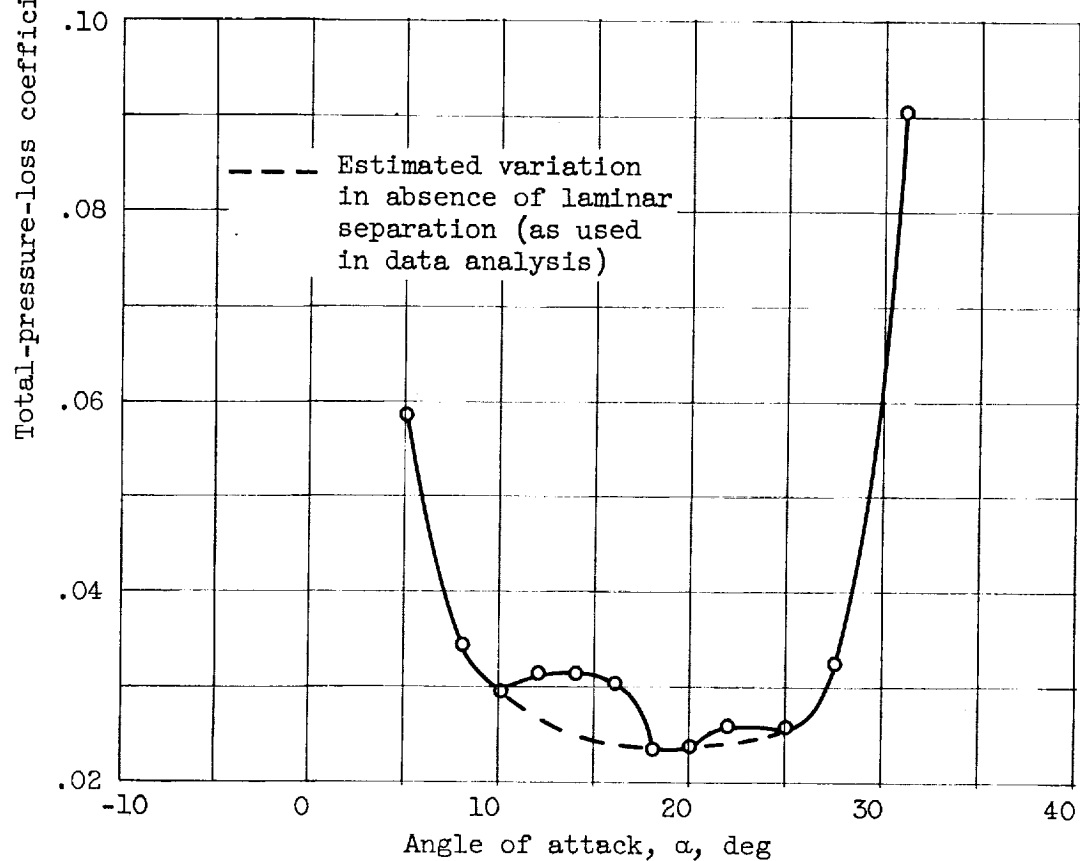
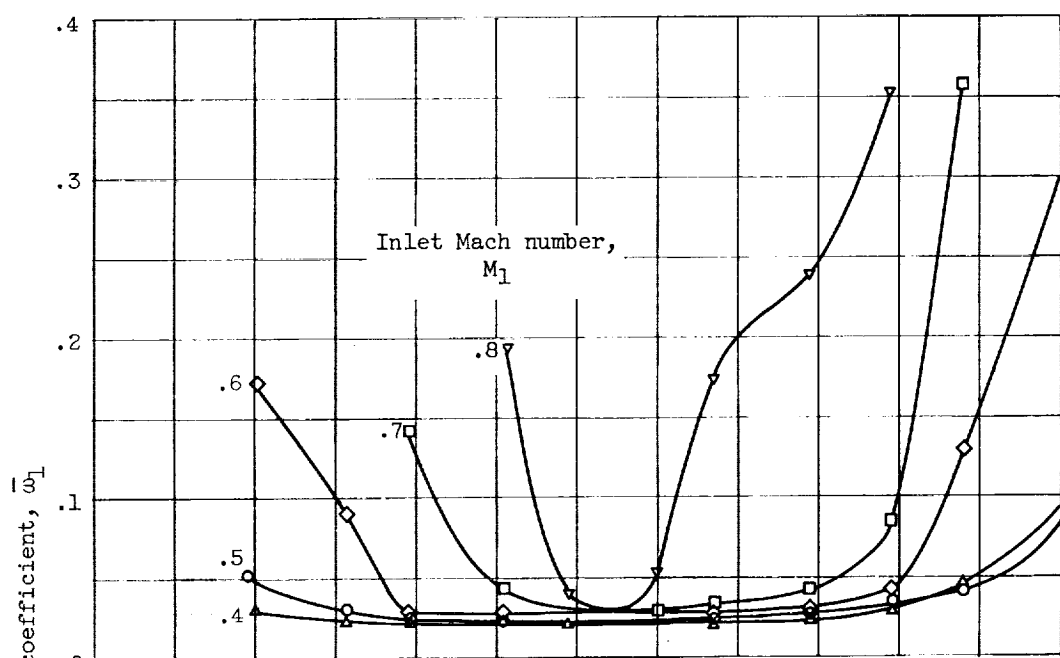
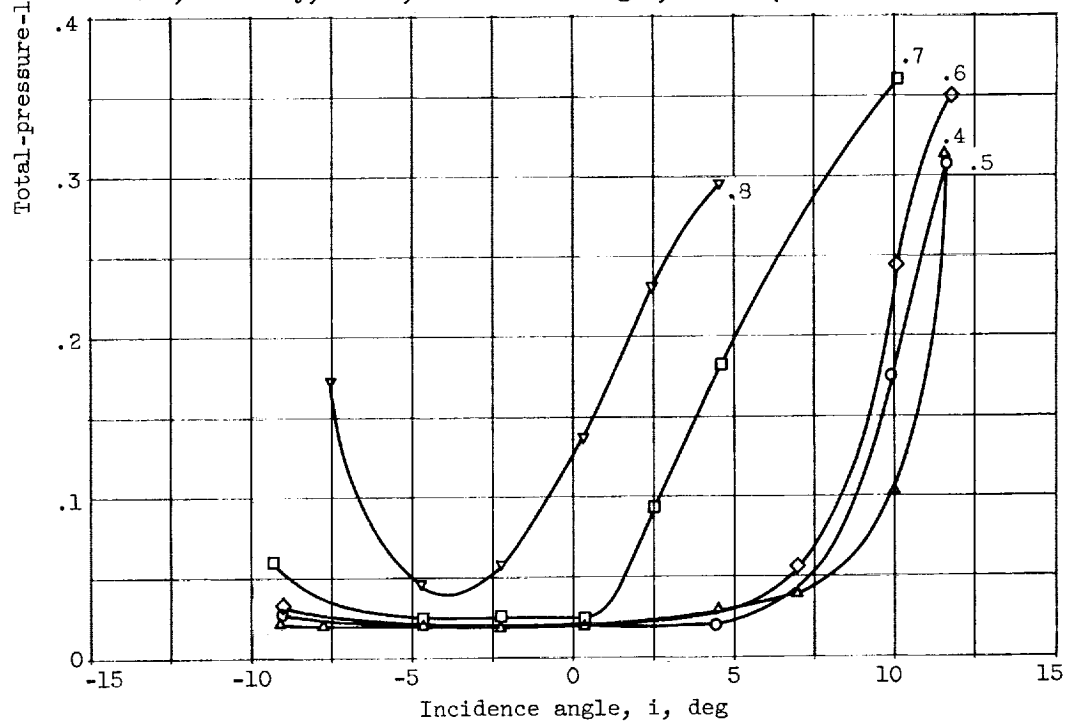
(a) NACA 65-810 blade. Inlet-air angle, 30° .(b) NACA 65-(12)10 blade. Inlet-air angle, 45° .

Figure 7. - Loss characteristics of cascade blade with local laminar separation. Solidity, 1.5; blade-chord Reynolds number, 2.45×10^5 (ref. 11).

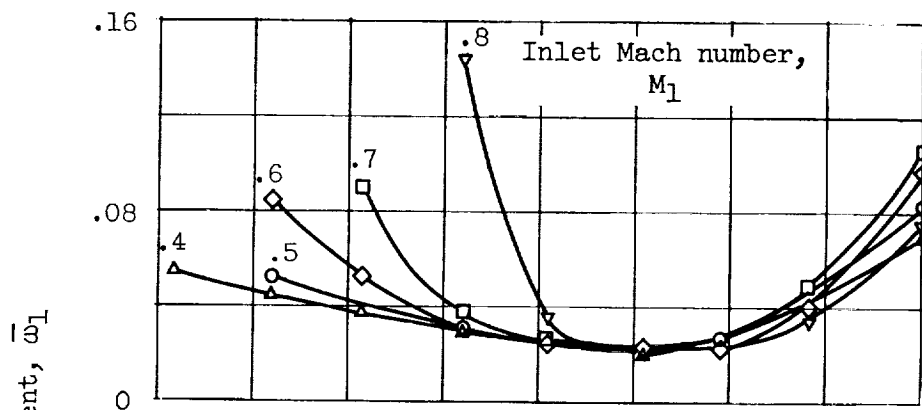


(a) C.4 Circular-arc blade. Camber angle, 25° ; maximum-thickness ratio, 0.10; solidity, 1.333; blade-chord angle, 42.5° (ref. 21).

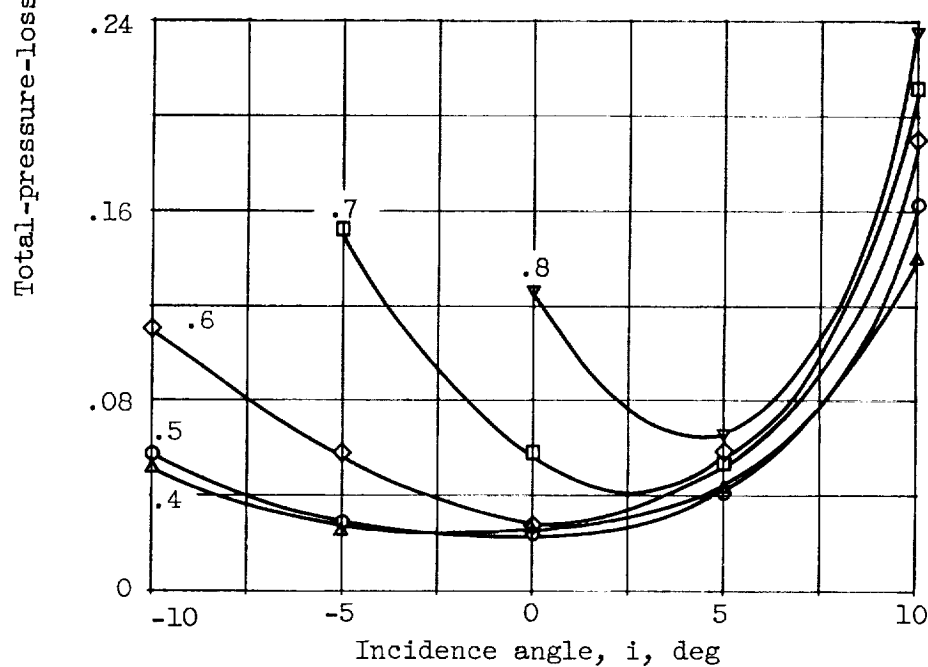


(b) C.4 Parabolic-arc blade. Camber angle, 25° ; maximum-thickness ratio, 0.10; solidity, 1.333; blade-chord angle, 37.6° (ref. 21).

Figure 8. - Effect of inlet Mach number on loss characteristics of cascade blade sections.



(c) Double-circular-arc blade. Camber angle, 25° ; maximum-thickness ratio, 0.105; solidity, 1.333; blade-chord angle, 42.5° (ref. 21).



(d) Sharp-nose blade. Camber angle, 27.5° ; maximum-thickness ratio, 0.08; solidity, 1.15; blade-chord angle, 30° (ref. 40).

Figure 8. - Concluded. Effect of inlet Mach number on loss characteristics of cascade blade sections.

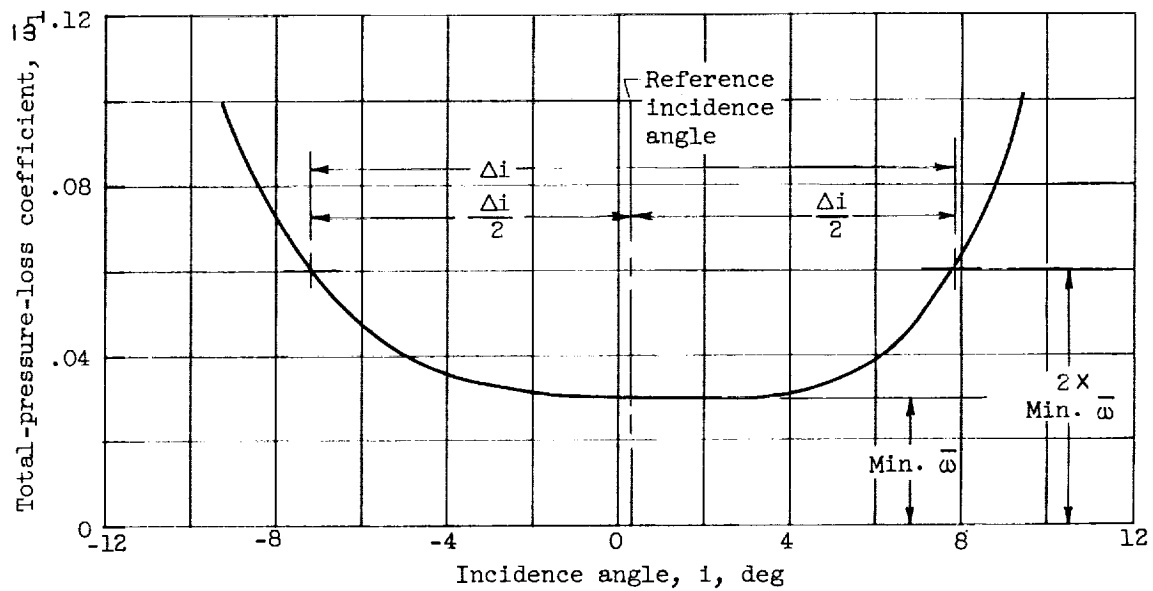


Figure 9. - Definition of reference minimum-loss incidence angle.

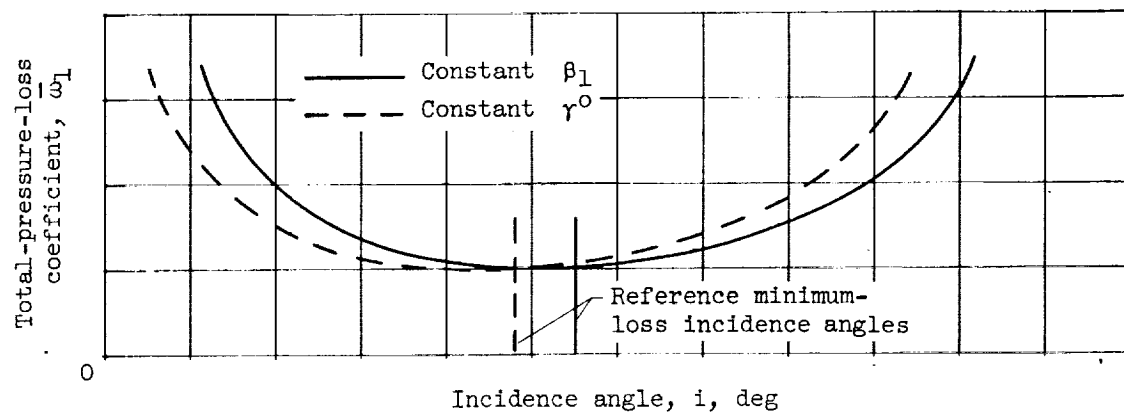
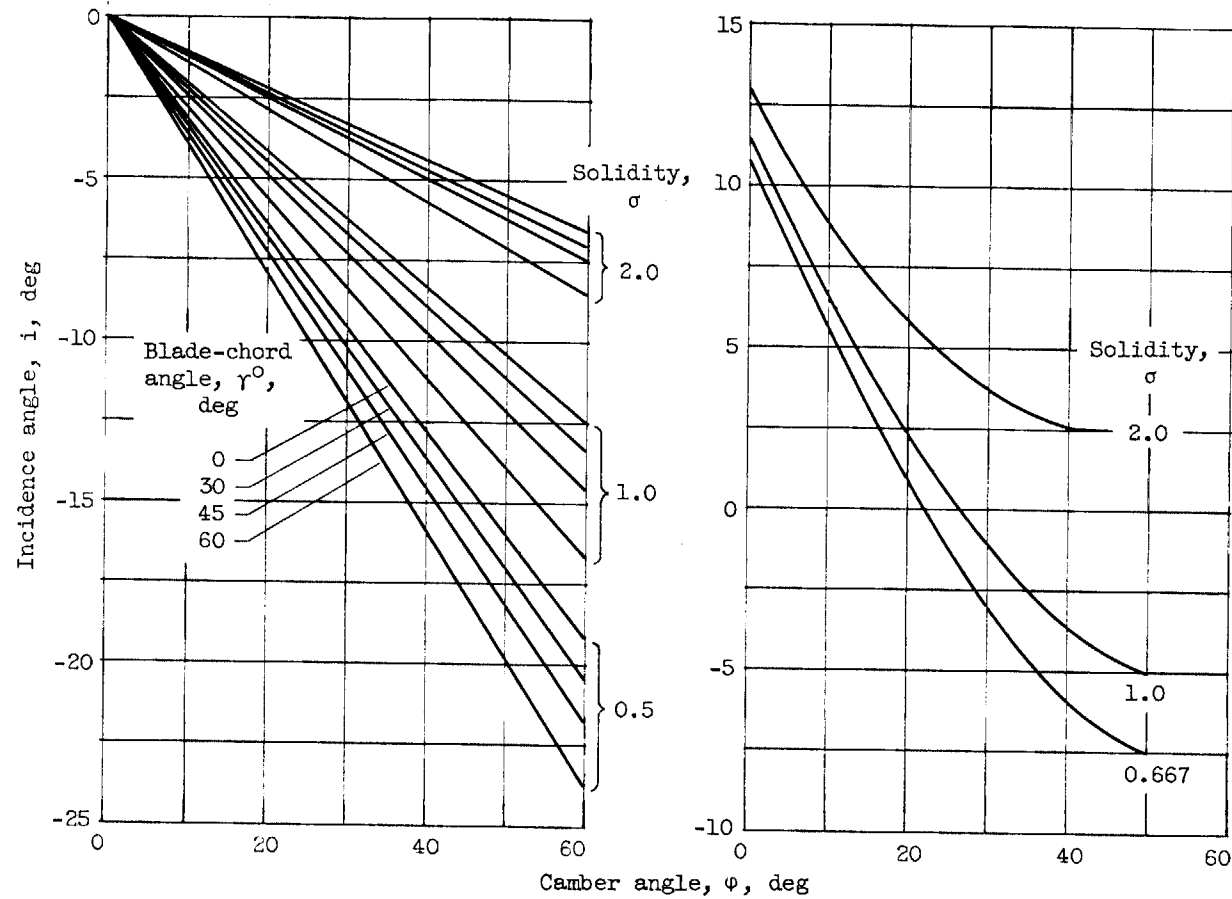


Figure 10. - Qualitative comparison of cascade range characteristics at constant blade-chord angle and constant inlet-air angle (for same value of β_1 in region of minimum loss).



(a) "Impact-free-entry" incidence angle for infinitely thin blades according to potential theory of Weinig (ref. 26).

(b) "Optimum" incidence angle for 10-percent-thick C-series profiles according to semitheoretical developments of Carter et al. (refs. 25 and 9). Outlet-air angle, 20° .

Figure 11. - Variation of reference incidence angle for circular-arc-mean-line blades obtained from theoretical or semitheoretical investigations.

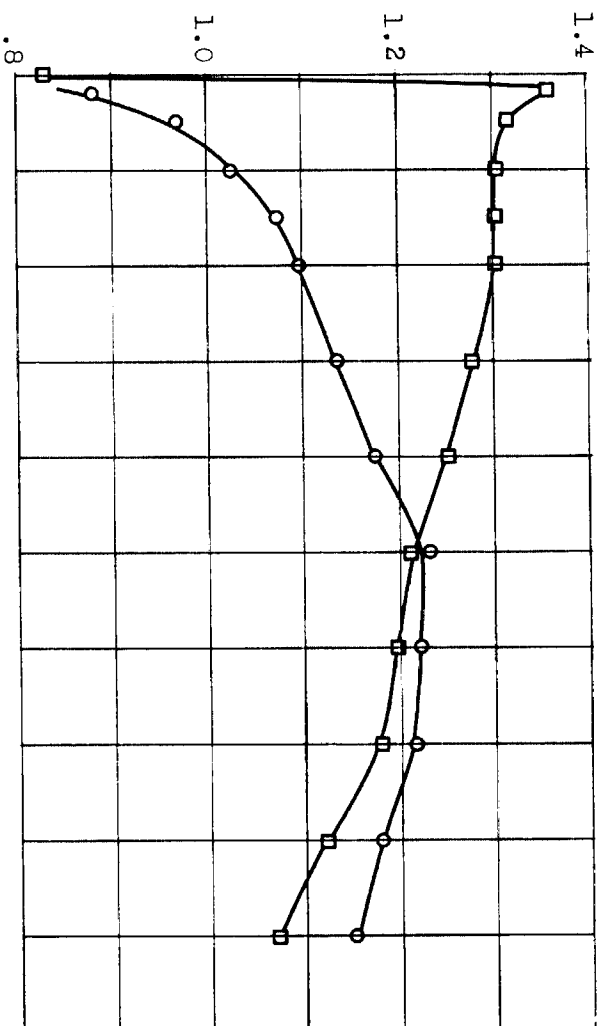
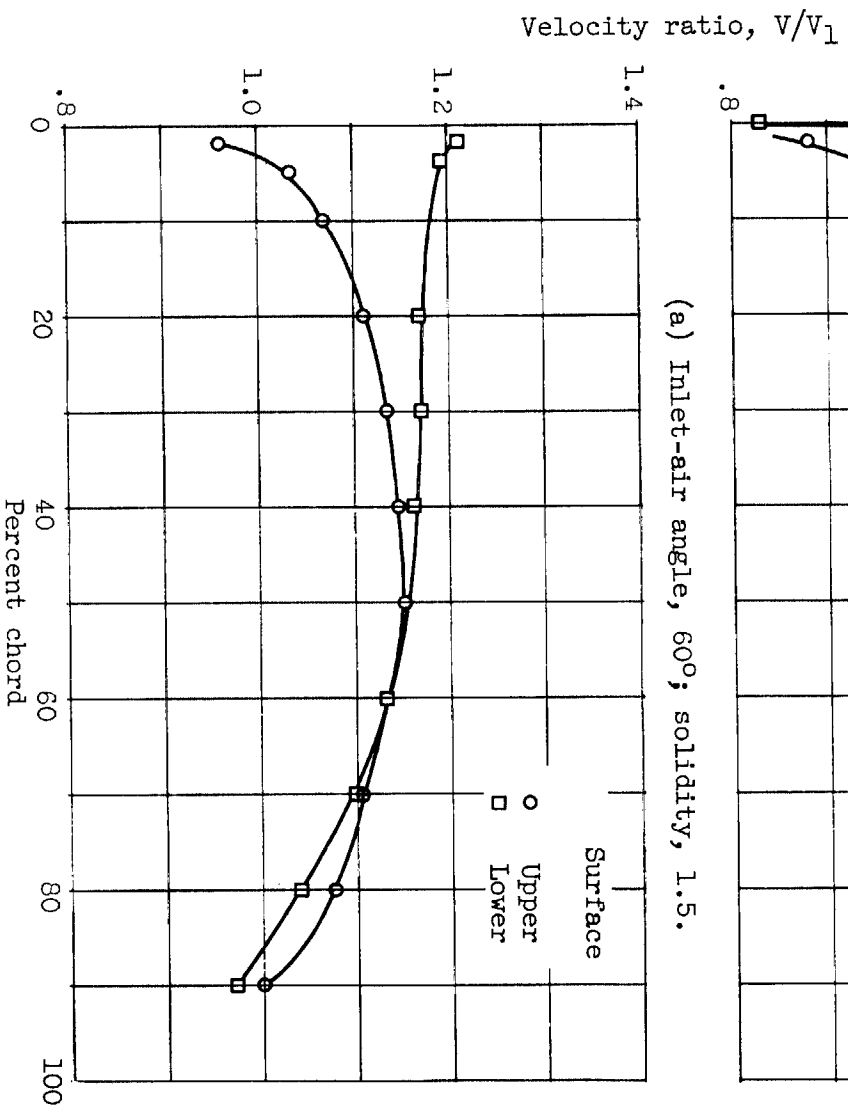
(a) Inlet-air angle, 60° ; solidity, 1.5.(b) Inlet-air angle, 30° ; solidity, 1.0.

Figure 12. - Illustration of velocity distribution for uncambered blade of conventional thickness at zero incidence angle. Data for 65-(0)10 blade of reference 11.

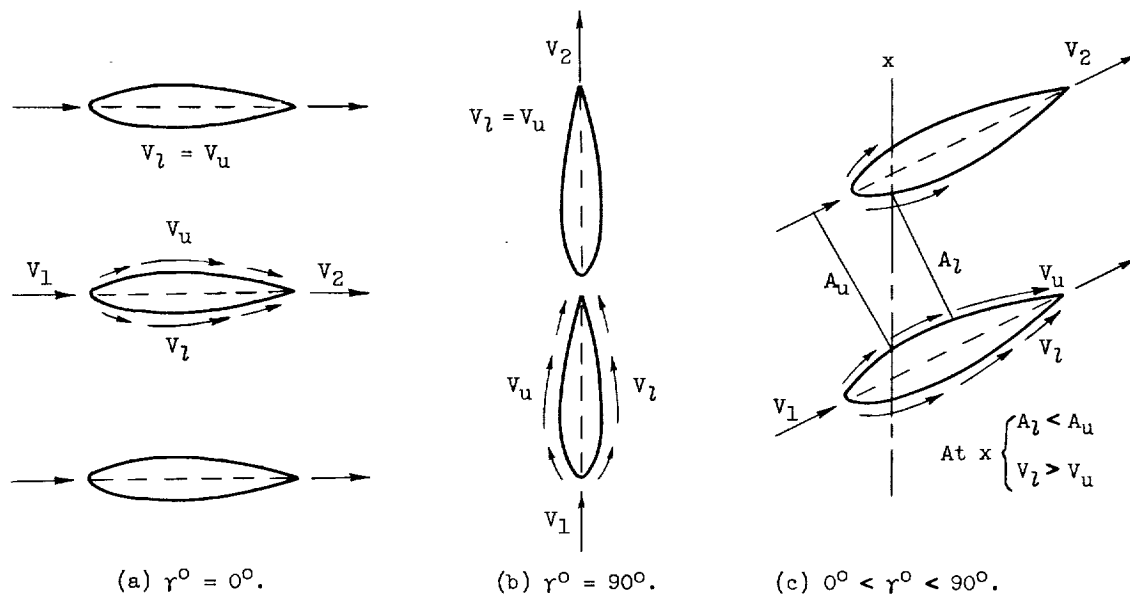


Figure 13. - Effect of blade thickness on surface velocity at zero incidence angle for uncambered airfoil section according to simplified one-dimensional model.

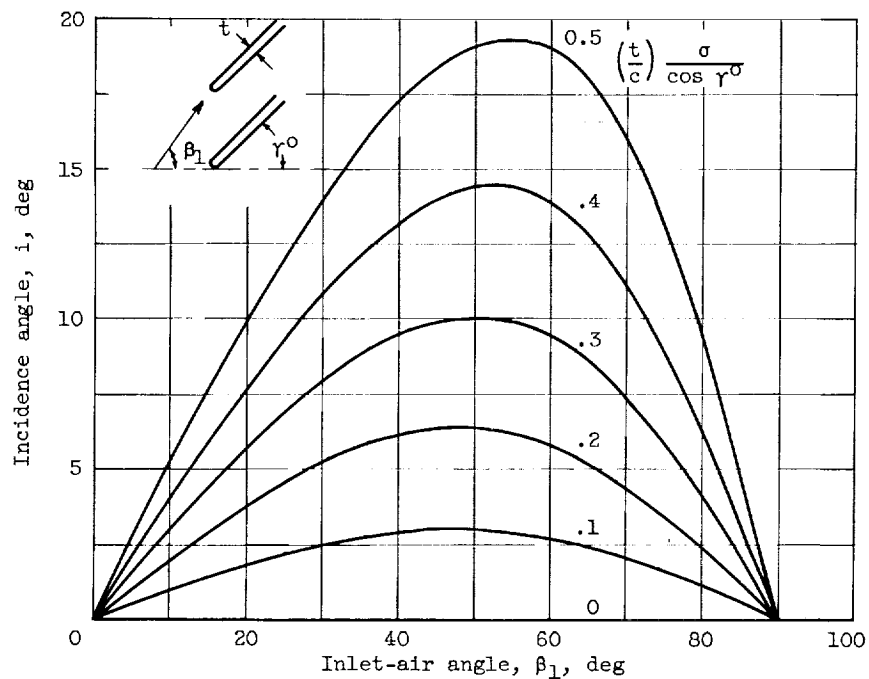


Figure 14. - Theoretical variation of "impact-free-entry" incidence angle for constant-thickness uncambered sections according to developments of reference 27.

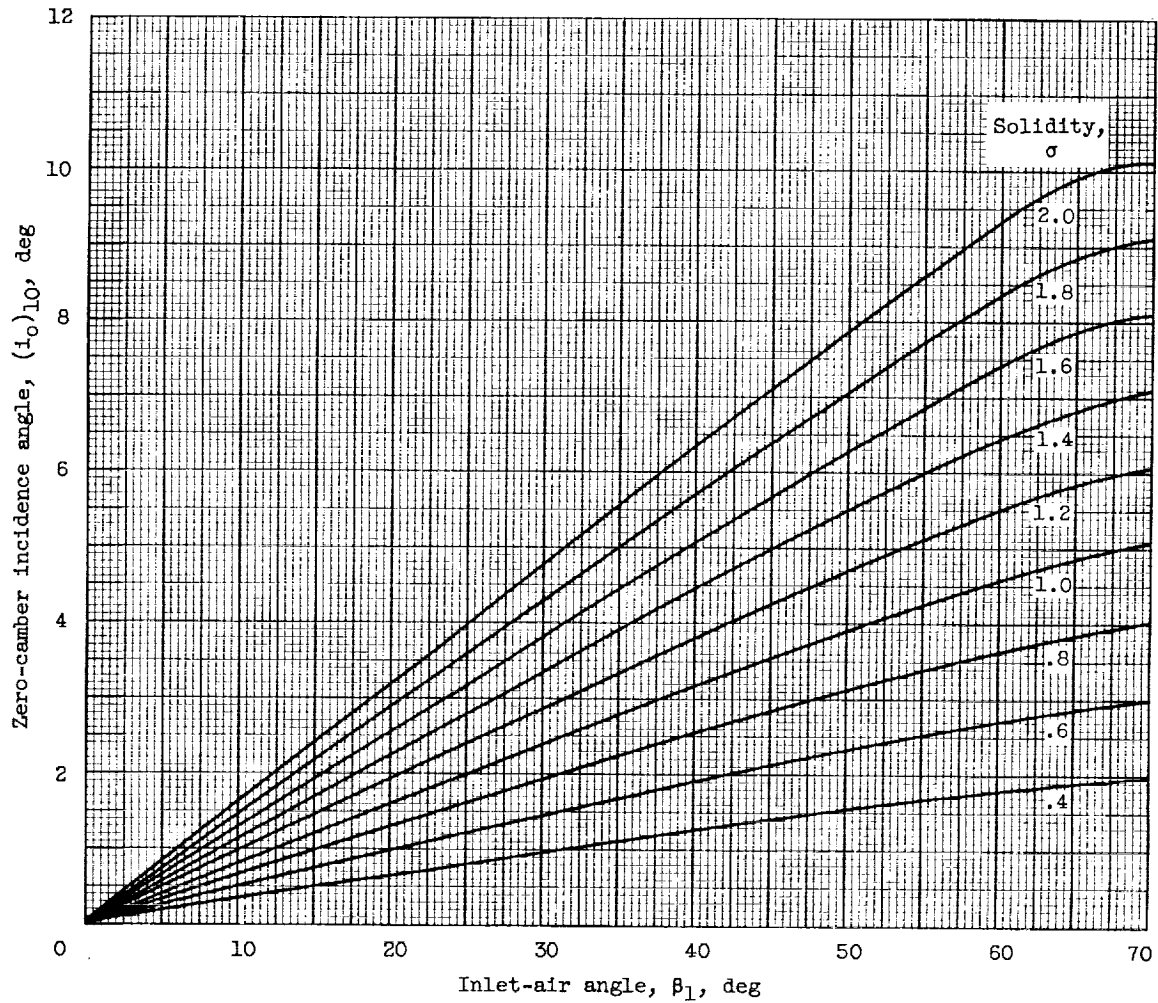


Figure 15. - Reference minimum-loss incidence angle for zero camber deduced from low-speed-cascade data of 10-percent-thick NACA 65-(A_{10})-series blades (ref. 11).

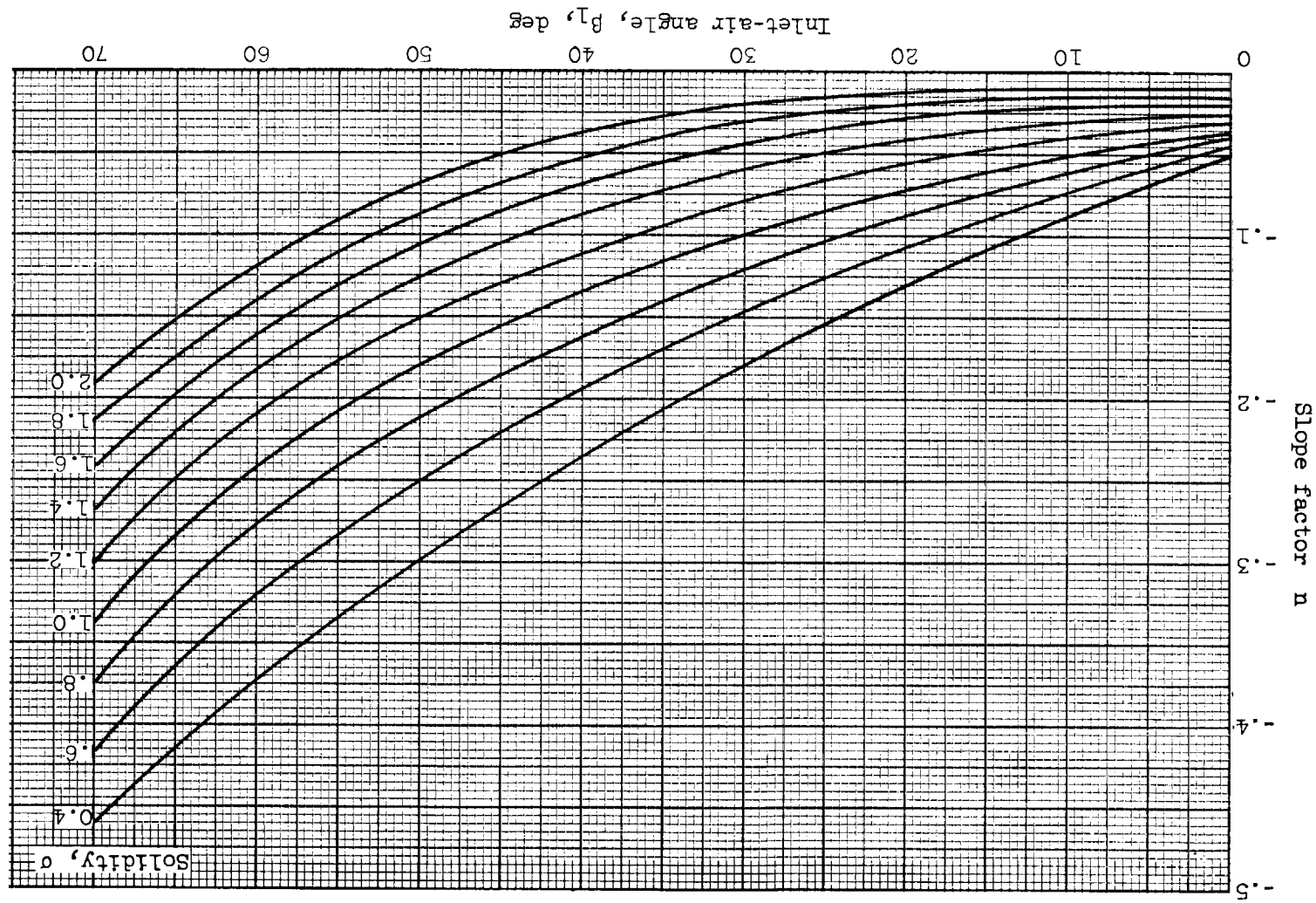
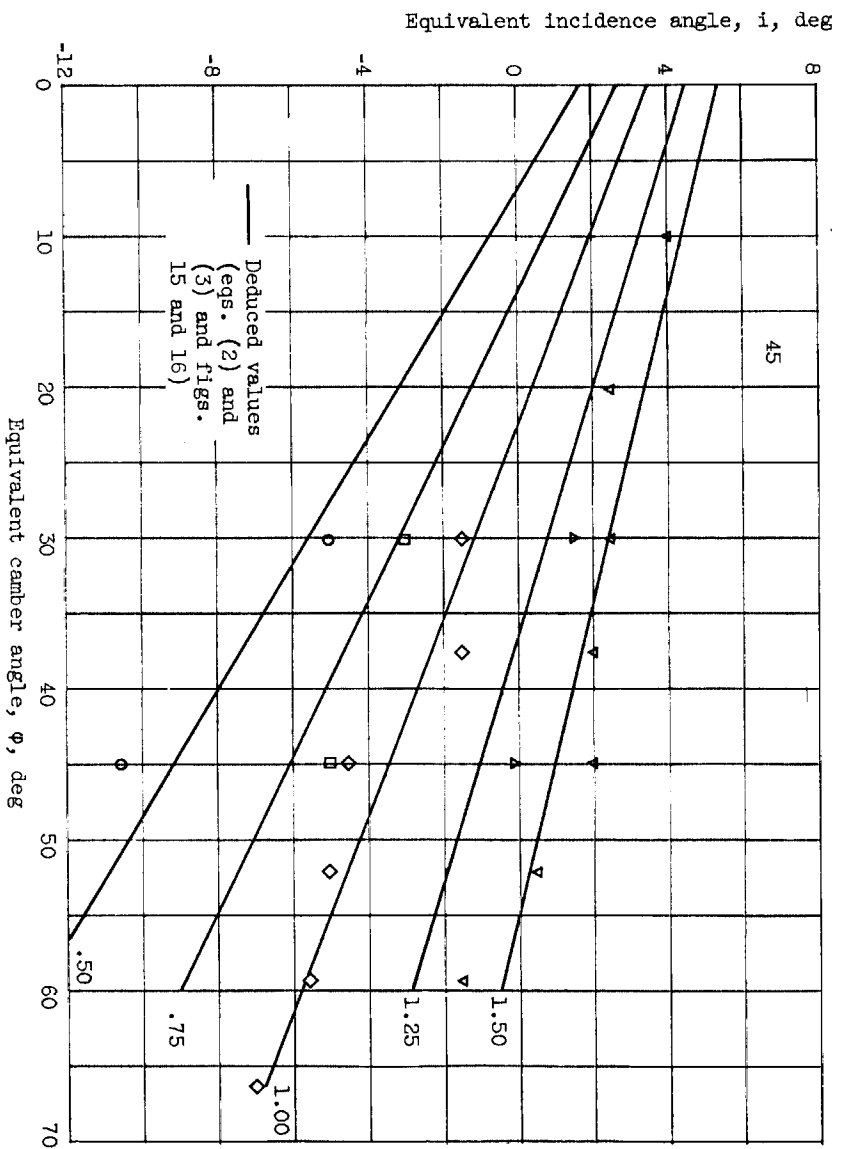
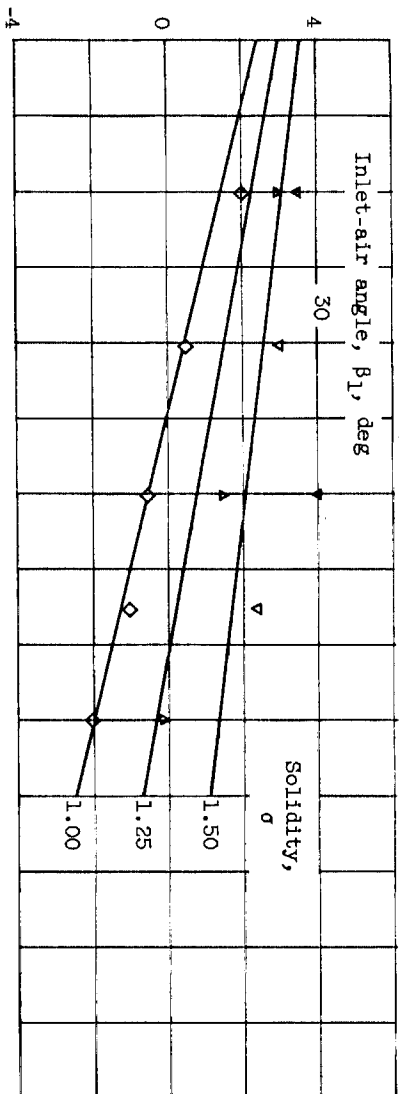
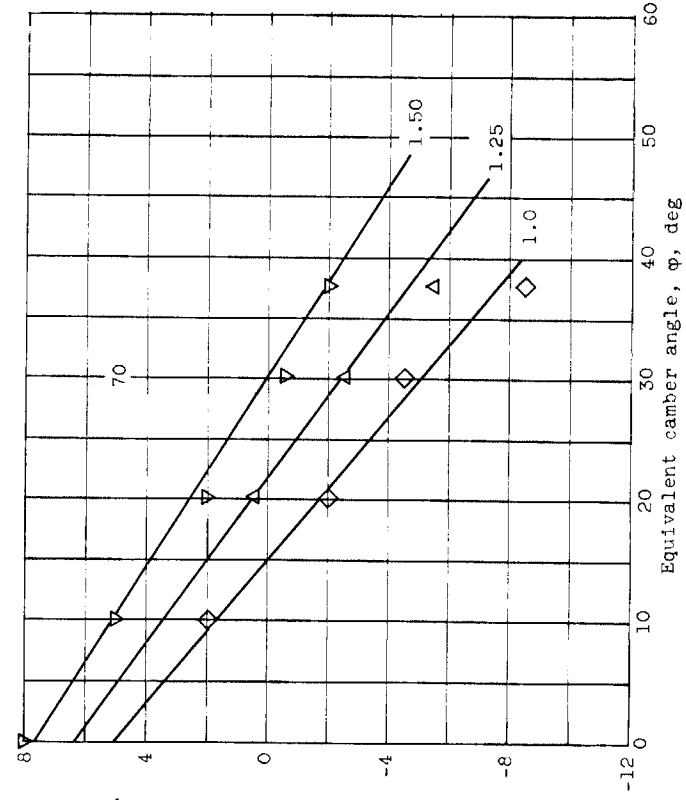
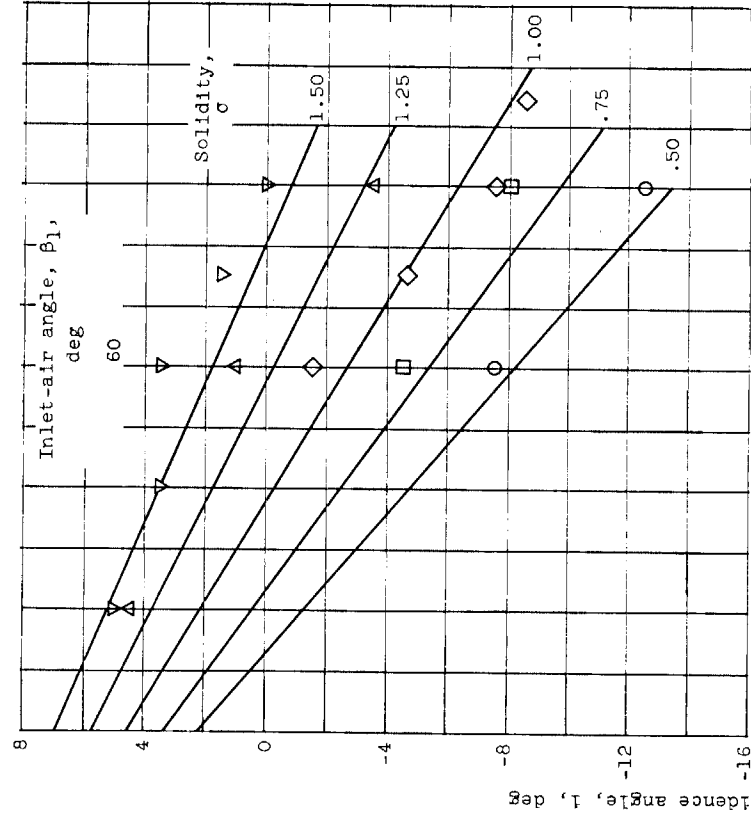


Figure 16. - Reference minimum-loss-incidence-angle slope factor deduced from low-speed cascade data for NACA 65-(A₁₀)-series blades as equivalent circular arcs.



(a) Inlet-air angles of 30° and 45°.

Figure 17. - Comparison of data values and deduced rule values of reference minimum-loss incidence angle for 65-(A_{10})10 blades as equivalent circular arc (ref. 11).



(b) Inlet-air angles of 60° and 70° .

Figure 17. - Concluded. Comparison of data values and deduced rule values of reference minimum-loss incidence angle for 65-(A₁₀)10 blades as equivalent circular arc (ref. 11).

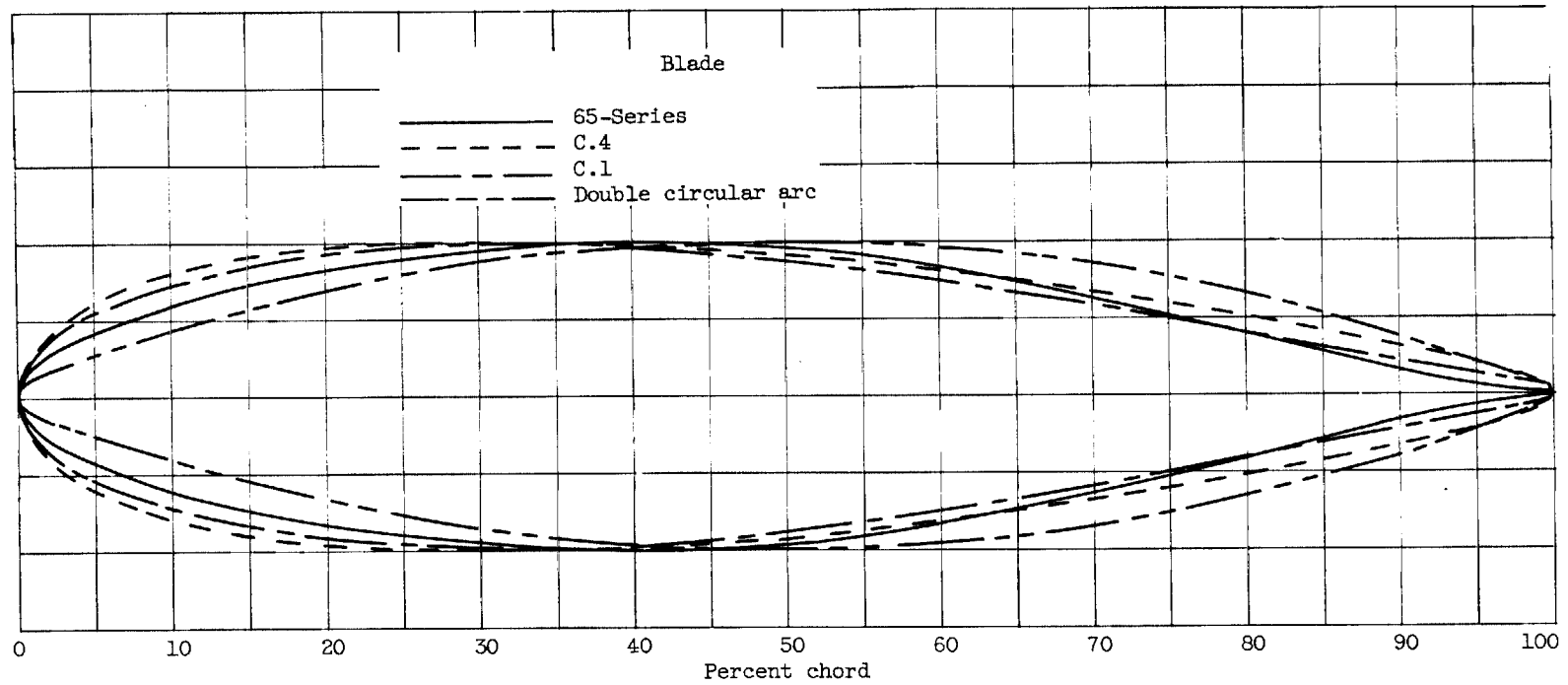


Figure 18. - Comparison of basic thickness distributions for conventional compressor blade sections.

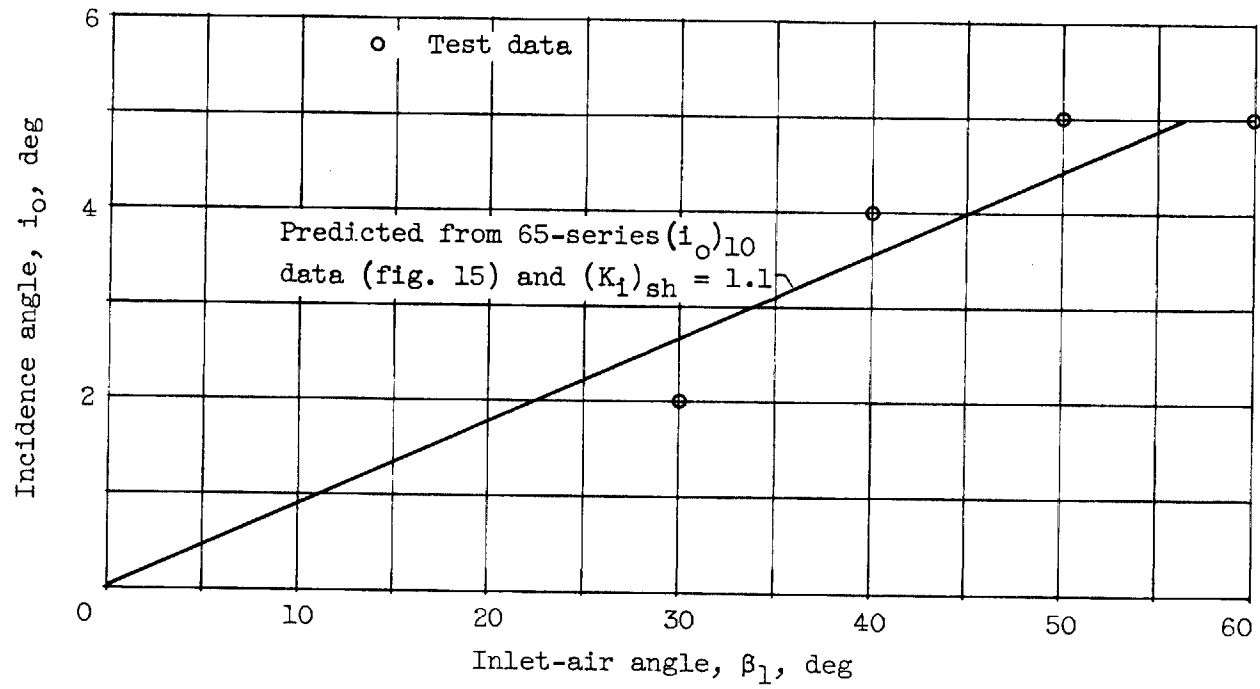


Figure 19. - Zero-camber minimum-loss incidence angle for 10-percent-thick C.4 profile. Solidity, 1.0 (ref. 30).

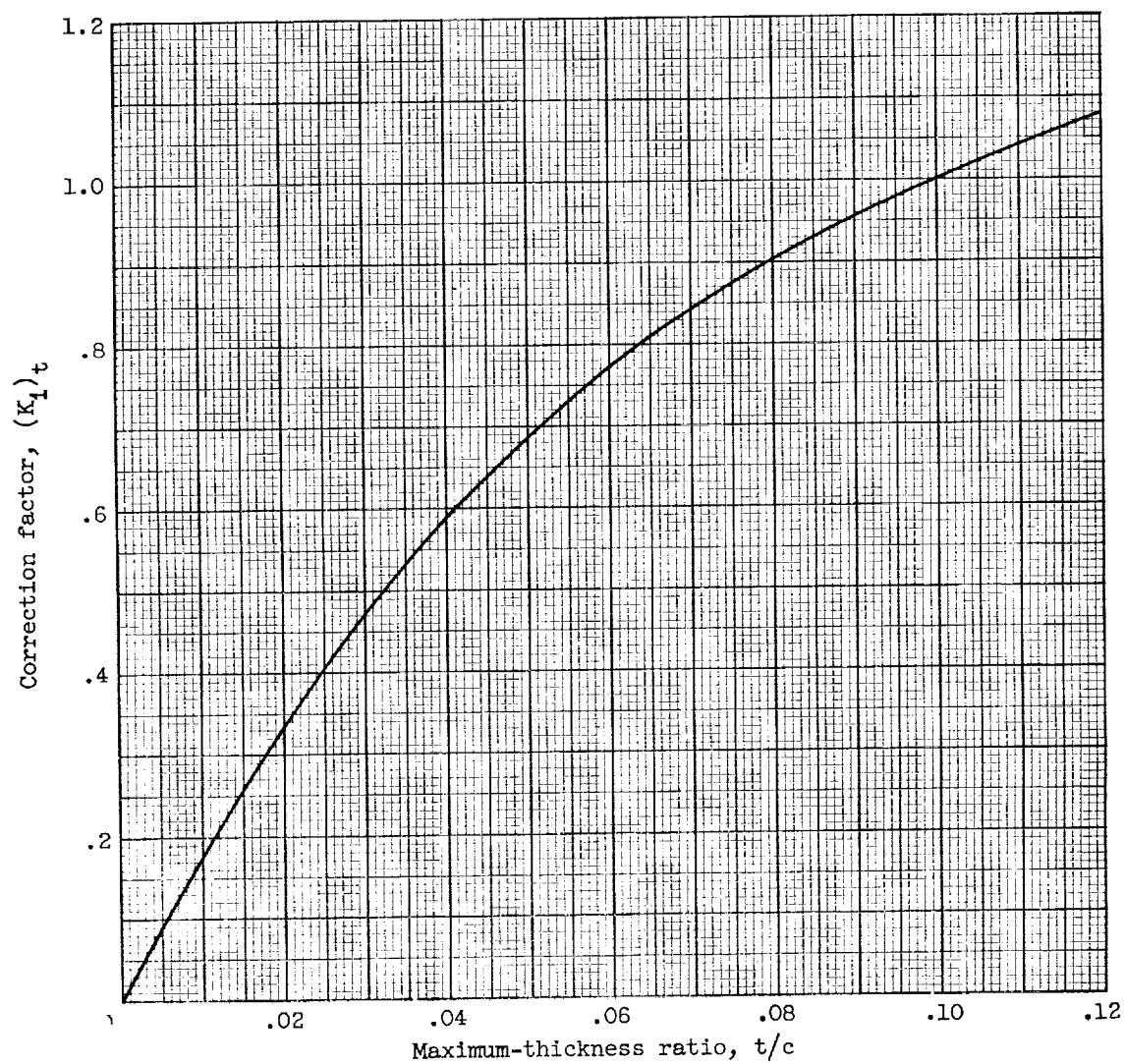


Figure 20. - Deduced blade maximum-thickness correction for zero-camber reference minimum-loss incidence angle (eq. (3)).

3383

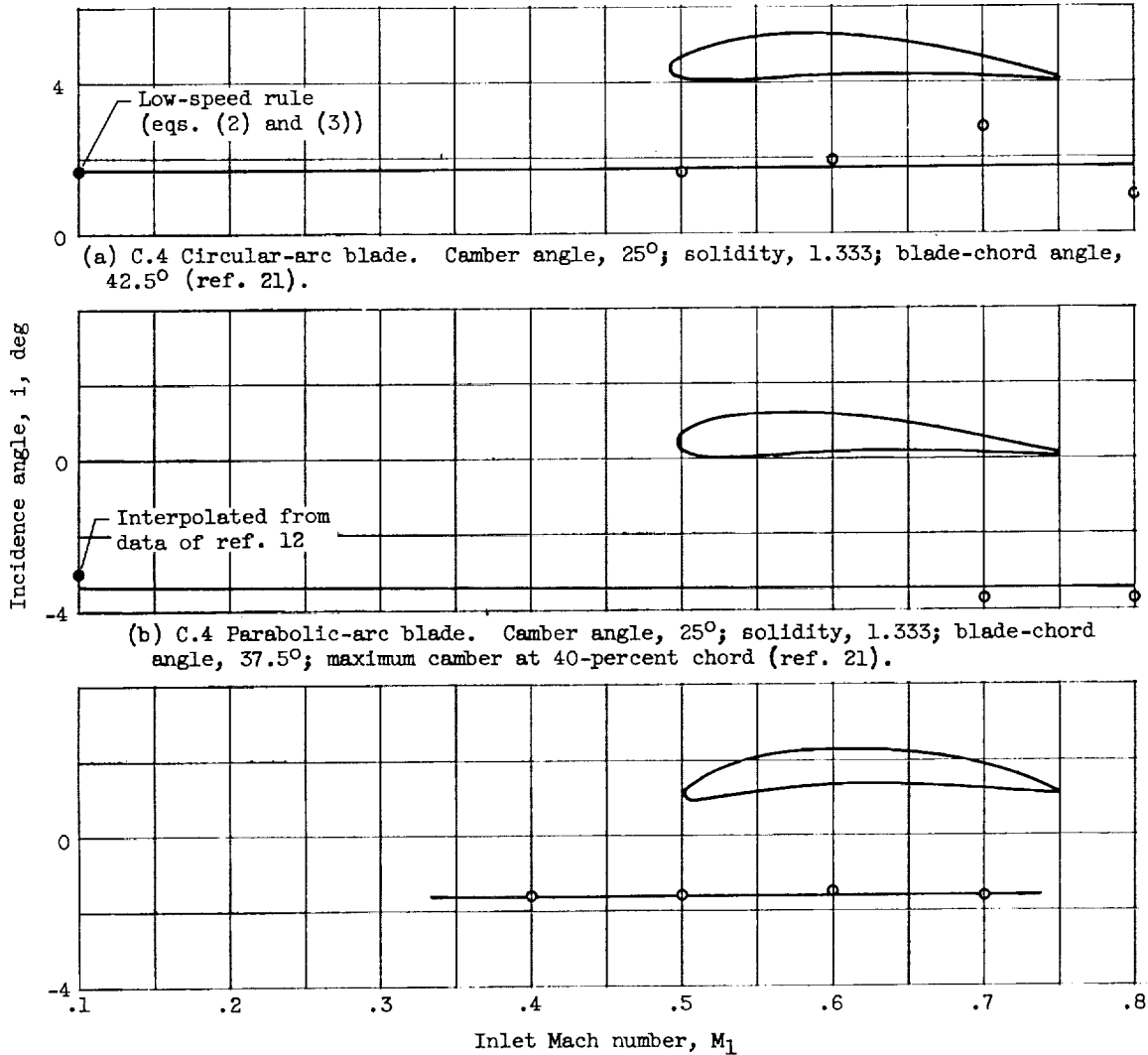


Figure 21. - Variation of reference minimum-loss incidence angle with inlet Mach number for thick-nose sections. Maximum-thickness ratio, 0.10.

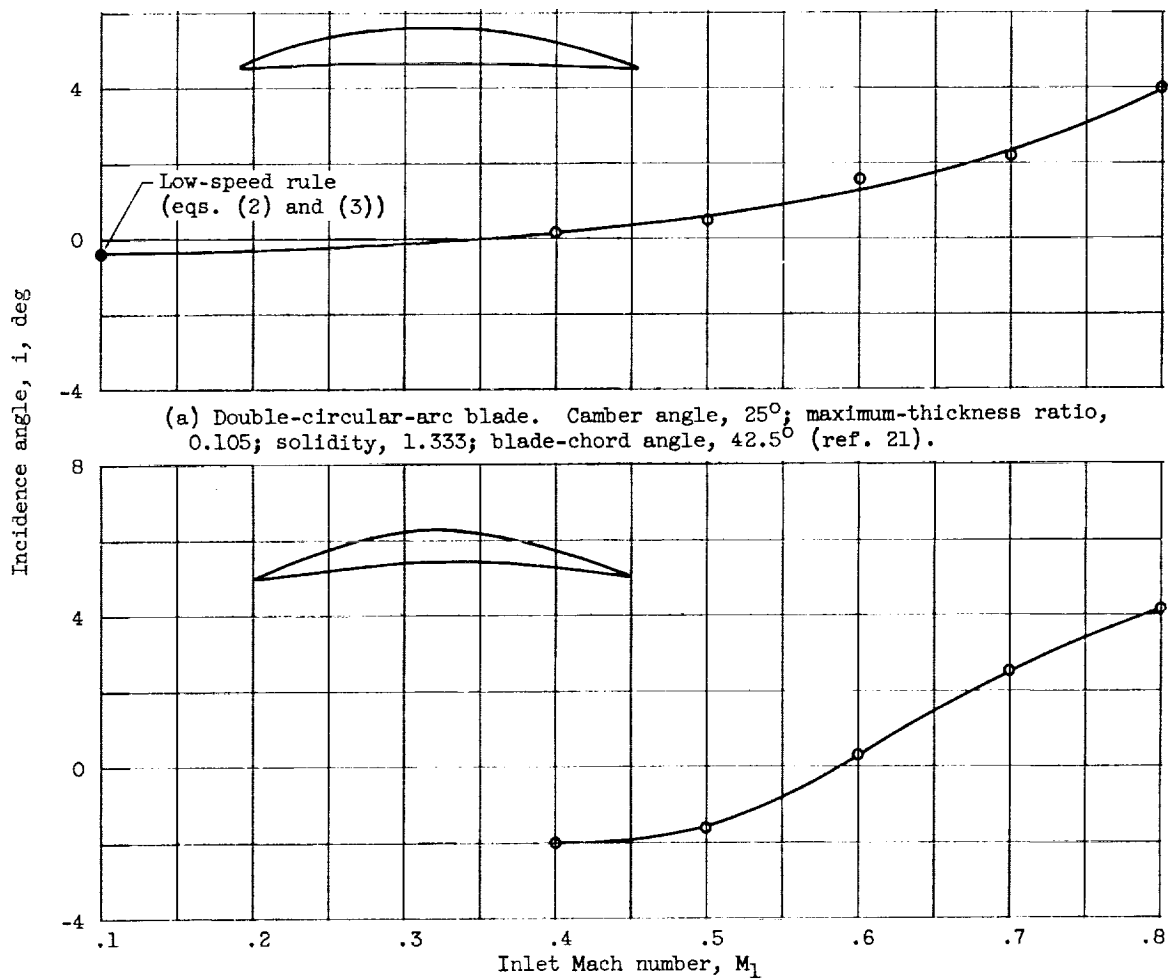


Figure 22. - Variation of reference minimum-loss incidence angle with inlet Mach number for sharp-nose sections.

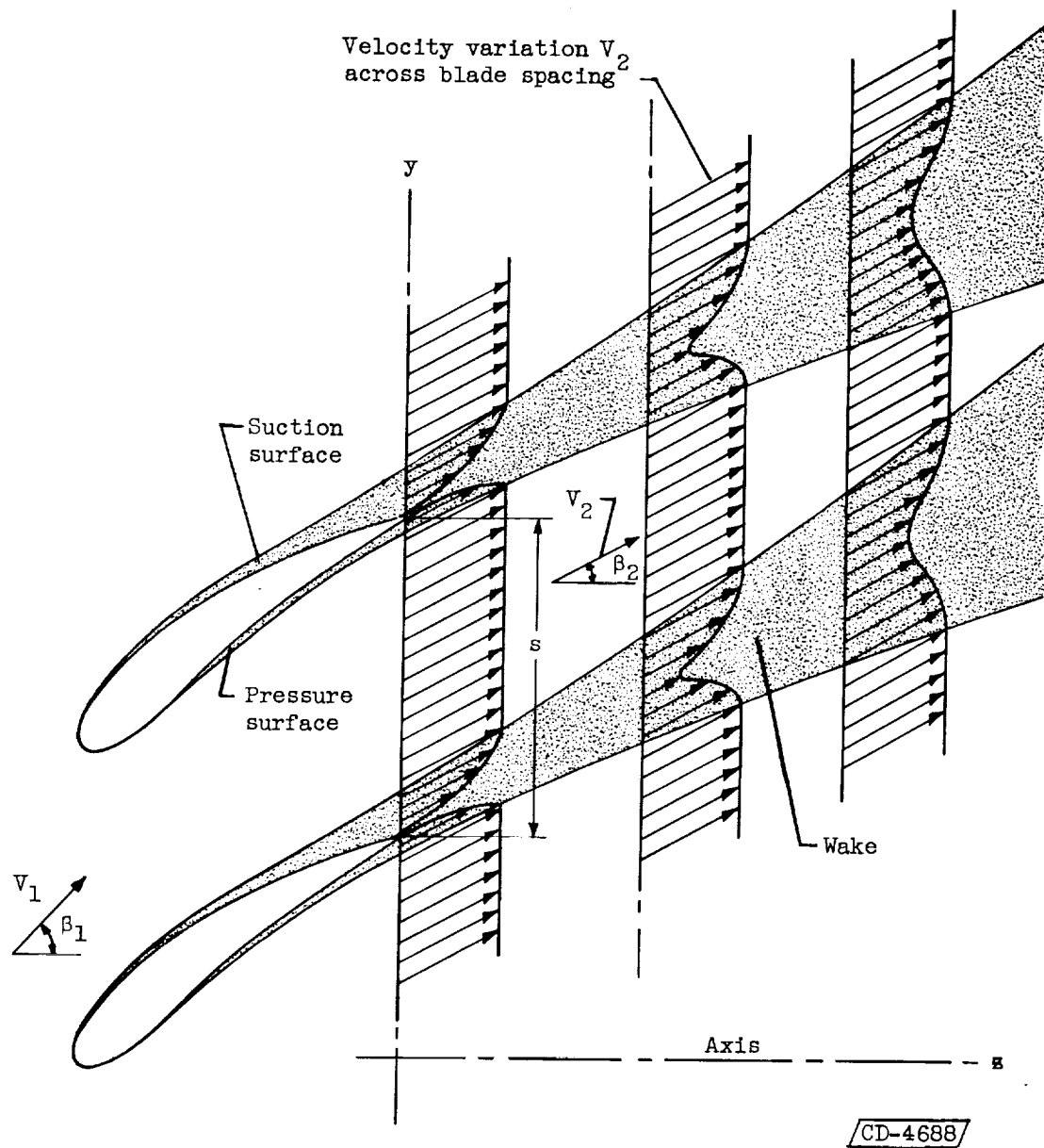


Figure 23. - Schematic representation of development of surface boundary layers and wake in flow about cascade blade sections.

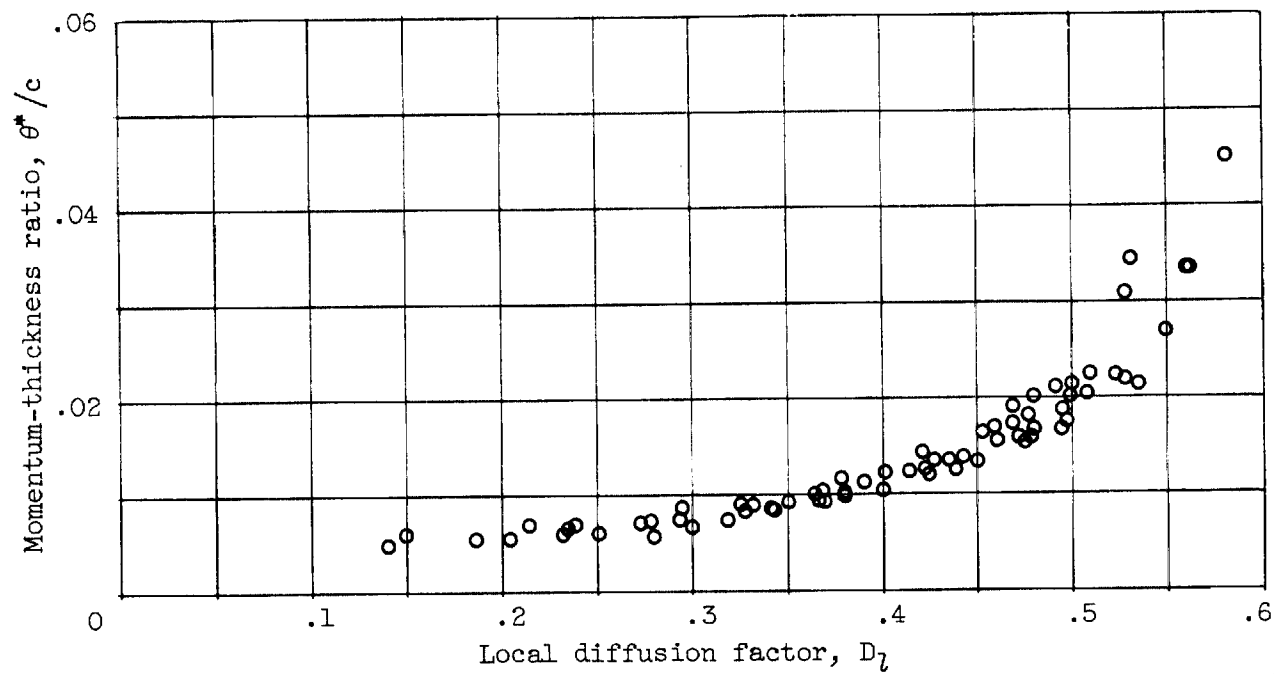
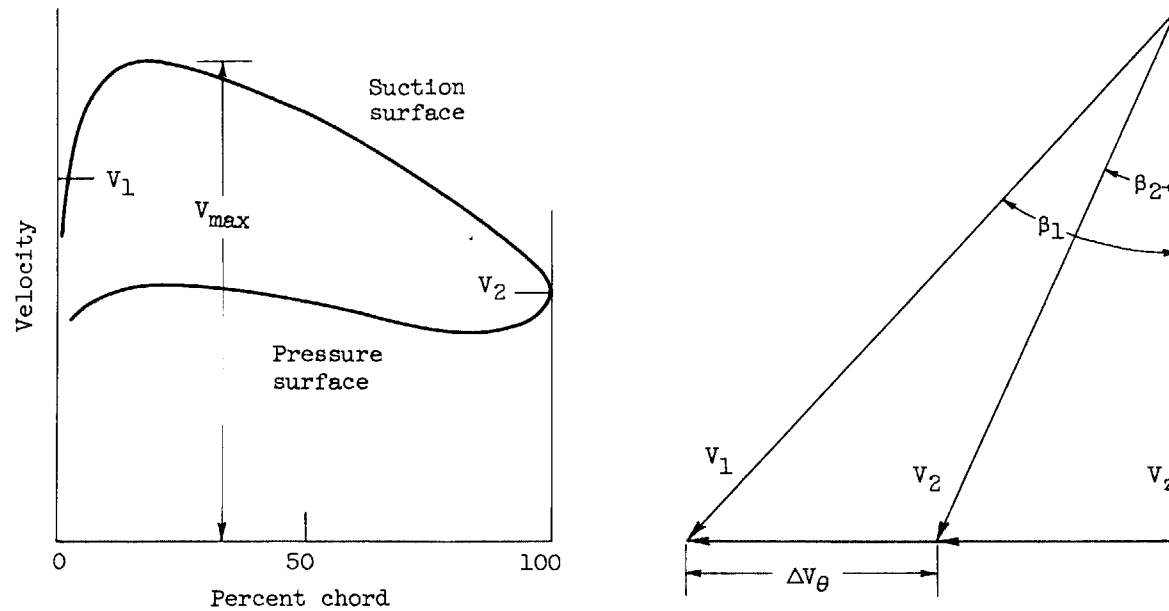


Figure 24. - Variation of computed wake momentum-thickness ratio with local diffusion factor at reference incidence angle for low-speed-cascade data of NACA 65-(A₁₀)10 blades (ref. 11).



$$D = \frac{V_{\max} - V_2}{V_{av}} = \frac{V_{\max} - V_2}{V_1}; \quad V_{\max} = V_1 + f \left(\frac{\Delta V_\theta}{\sigma} \right)$$

$$\text{Thus, } D = \left(1 - \frac{V_2}{V_1} \right) + \frac{\Delta V_\theta}{2\sigma V_1} \quad (\text{eq. (7)})$$

$$\text{For two-dimensional flow, with } V_{z,1} = V_{z,2}, \quad D = \left(1 - \frac{\cos \beta_1}{\cos \beta_2} \right) + \frac{\cos \beta_1}{2\sigma} (\tan \beta_1 - \tan \beta_2) \quad (\text{eq. (8)})$$

Figure 25. - Basis of development of diffusion factor for cascade flow from reference 23.

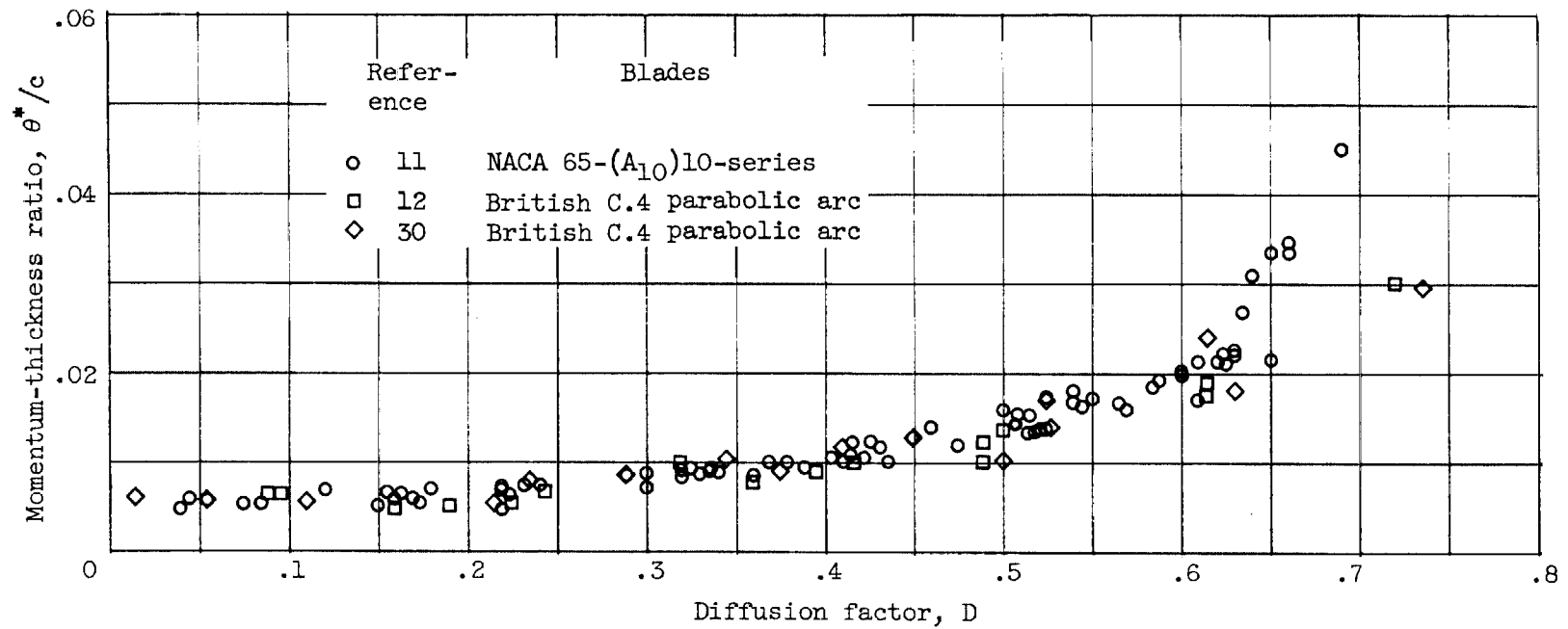


Figure 26. - Variation of computed wake momentum-thickness ratio with over-all diffusion factor at reference incidence angle for low-speed systematic cascade data of references 11, 12, and 30. Blade maximum-thickness ratio, 0.10; Reynolds number, -2.5×10^5 .

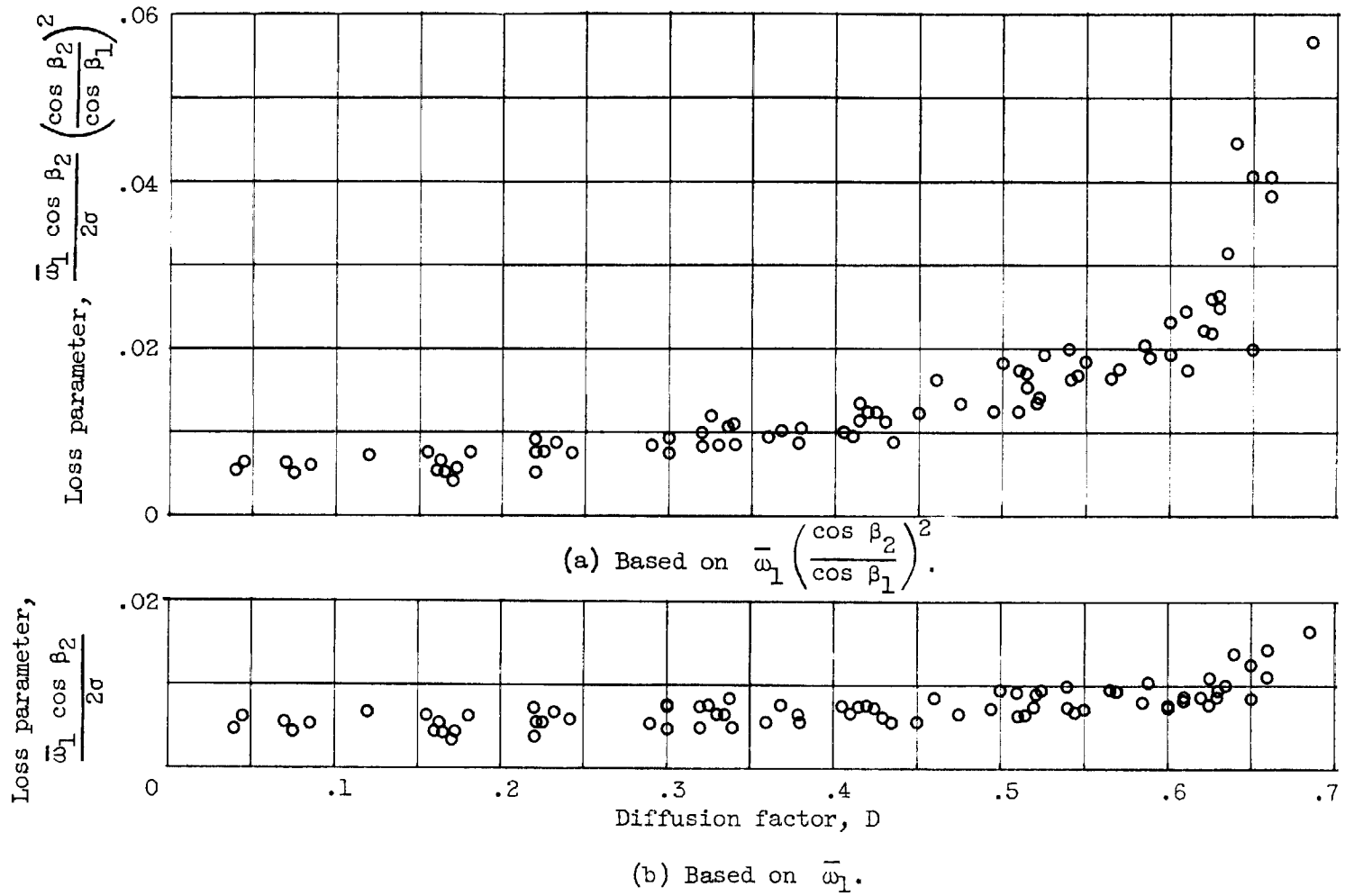
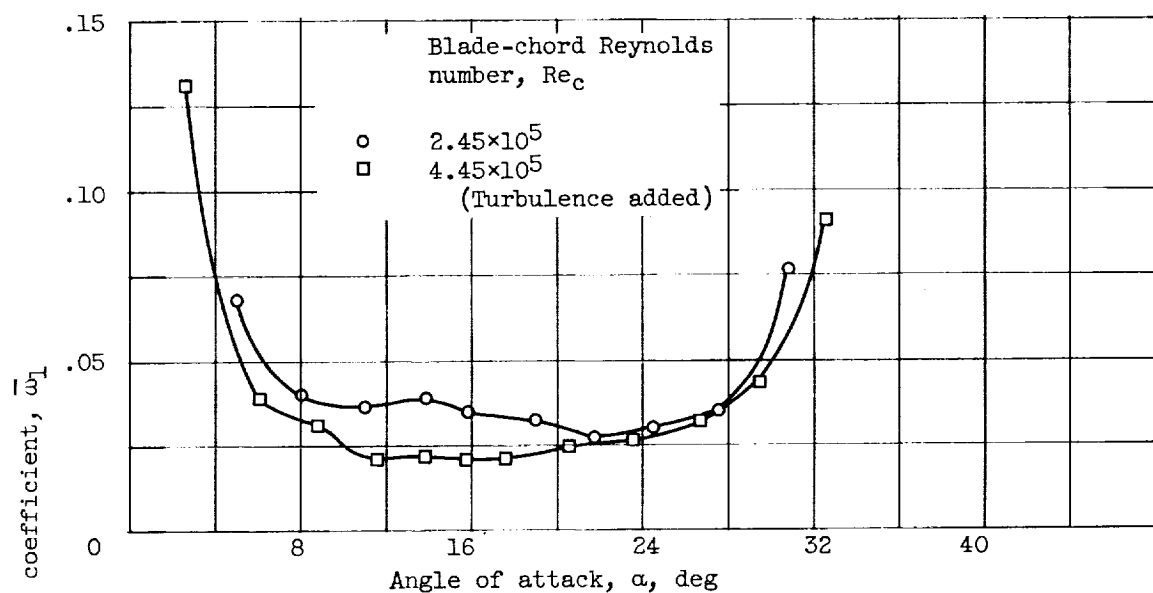
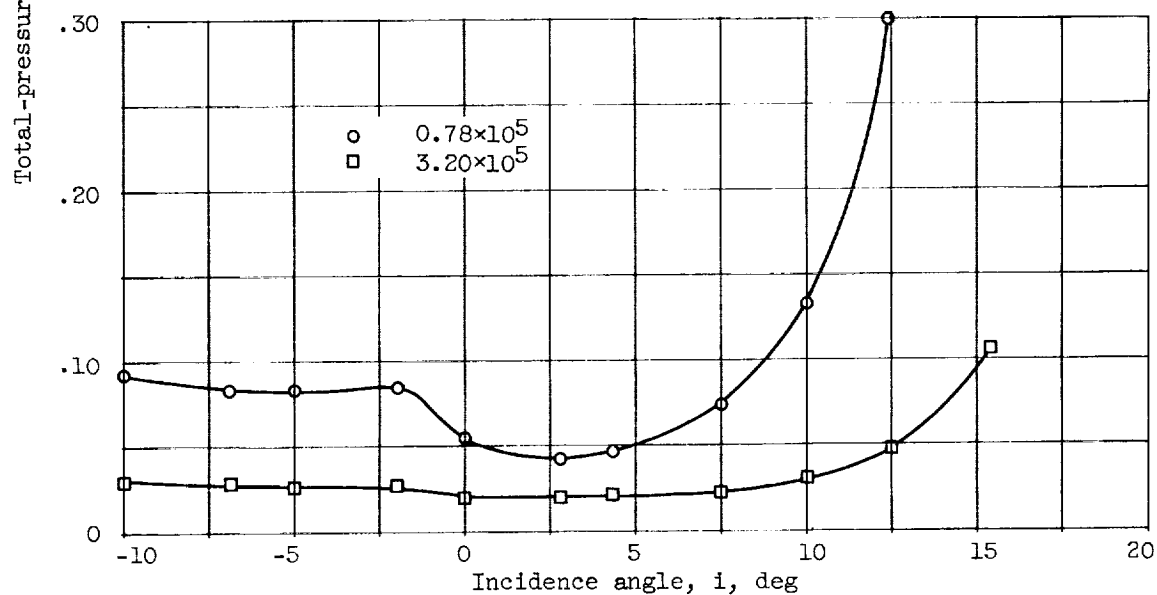


Figure 27. - Variation of loss parameter with diffusion factor at reference minimum-loss incidence angle computed from low-speed-cascade data of NACA 65-(A₁₀)10 cascade blades (ref. 11).



(a) 65-Series blade 65-(12)10. Solidity, 1.5; inlet-air angle, 45° (ref. 11).



(b) Circular-arc blade 10C4/25C50. Solidity, 1.333; blade-chord angle, 42.5° (ref. 21).

Figure 28. - Effect of Reynolds number on variation of loss with incidence angle.

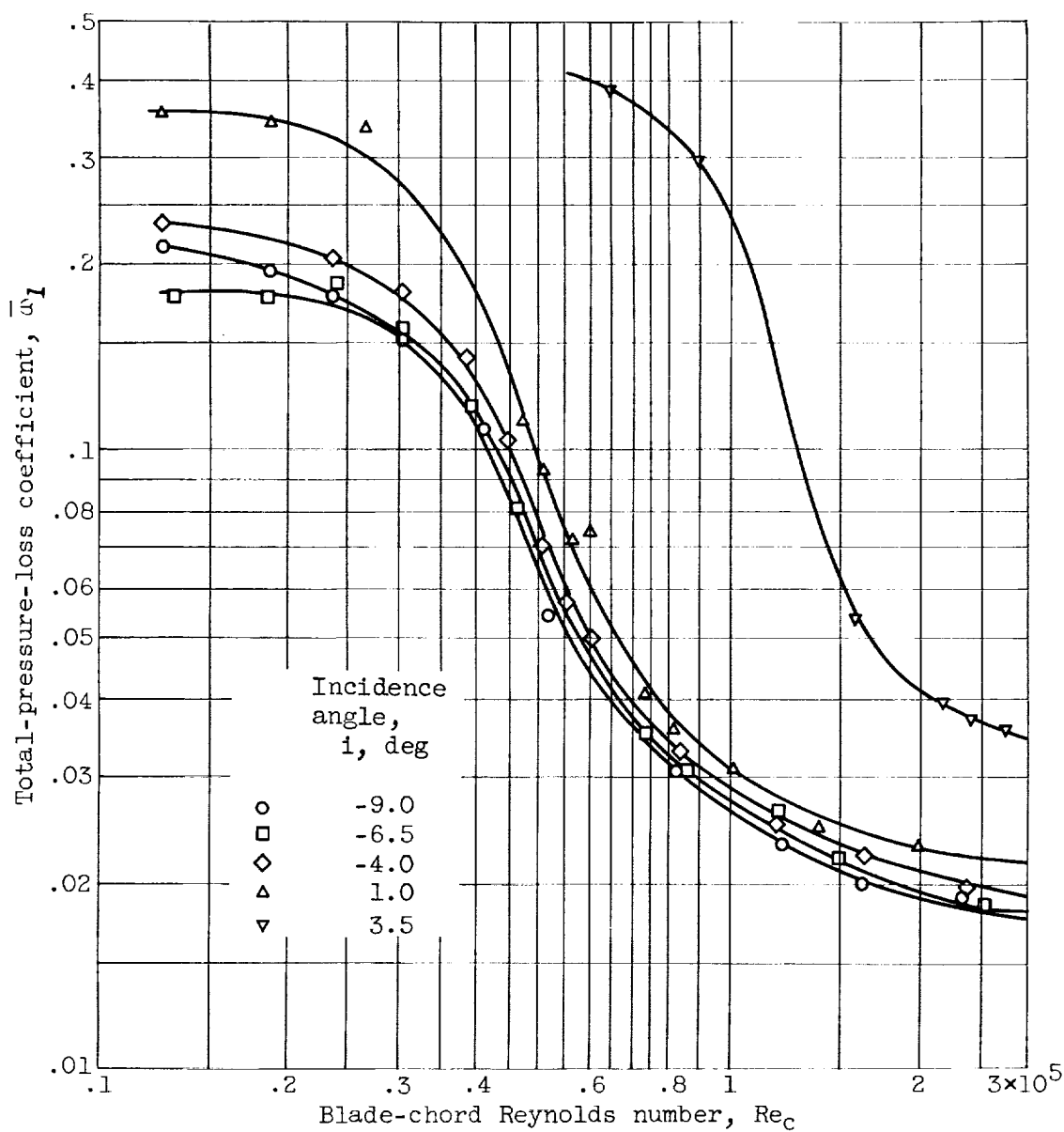


Figure 29. - Variation of total-pressure-loss coefficient with blade-chord Reynolds number for parabolic-arc blade 10C4/40 P40. Inlet-air angle, 28° to 40° ; solidity, 1.333 (ref. 39).

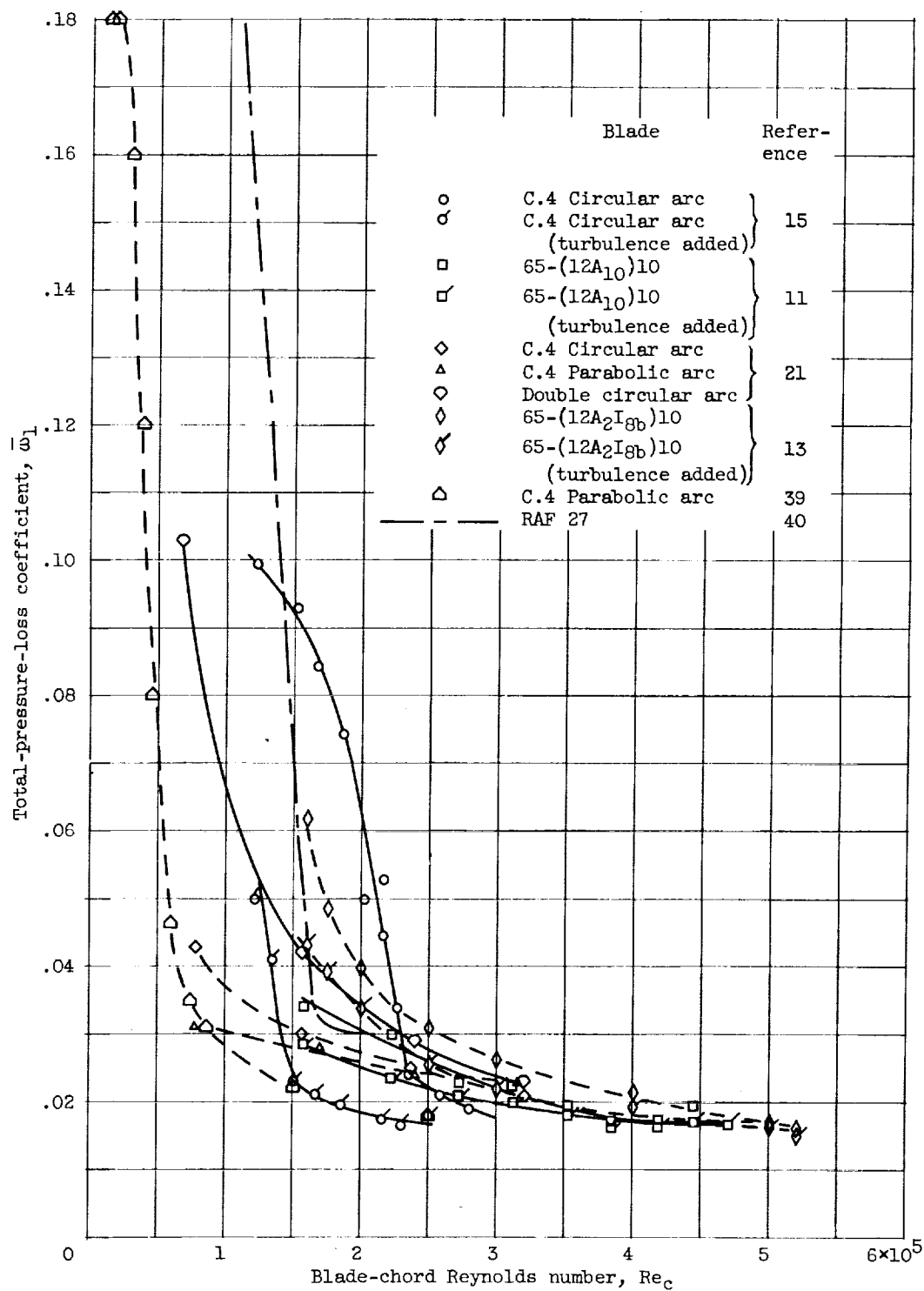
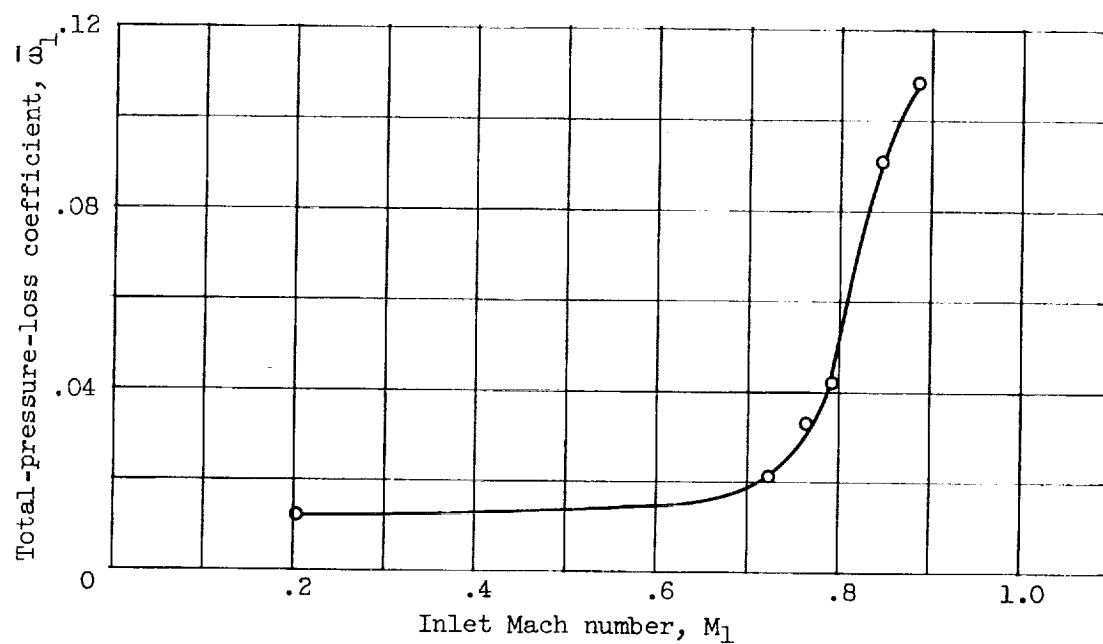
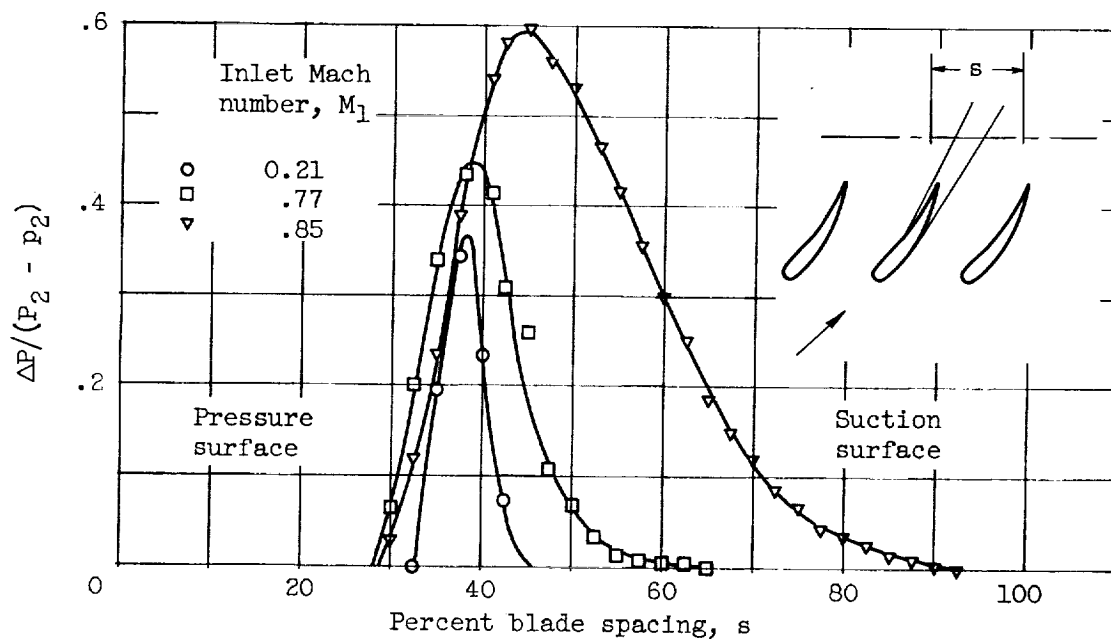


Figure 30. - Composite plot of loss coefficient against blade-chord Reynolds number in region of minimum loss for two-dimensional-cascade blade sections at low speed.



(a) Total-pressure-loss coefficient.



(b) Blade wake.

Figure 31. - Variation of cascade blade loss with inlet Mach number for NACA 65-(12A₁₀)₁₀ blade in region of minimum loss (ref. 20).

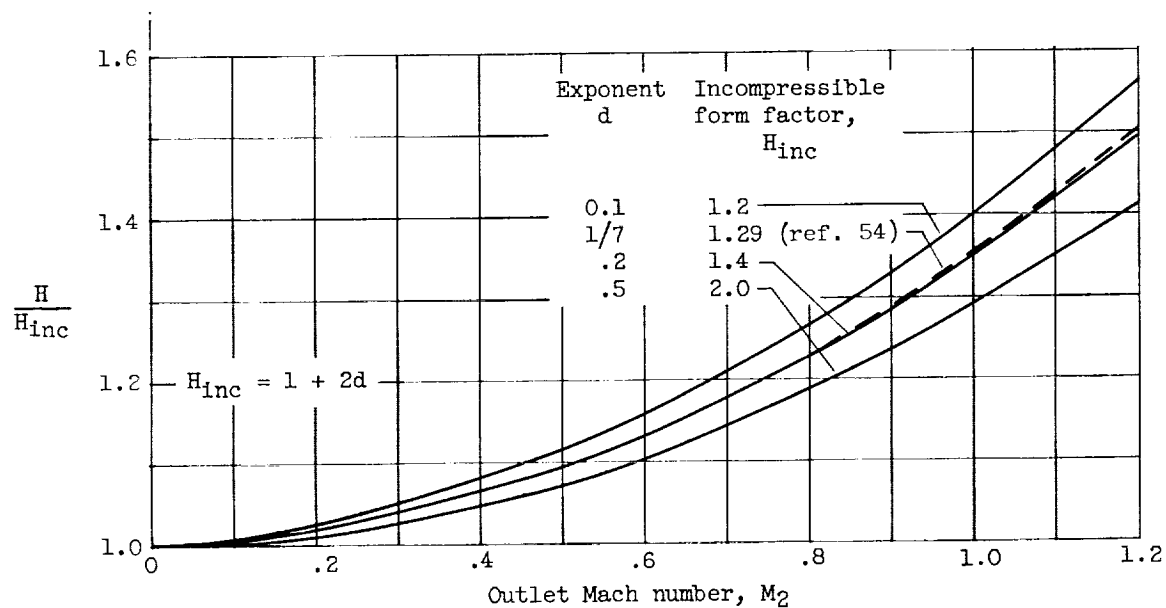


Figure 32. - Ratio of compressible to incompressible form factor for constant value of exponent in power velocity distribution.

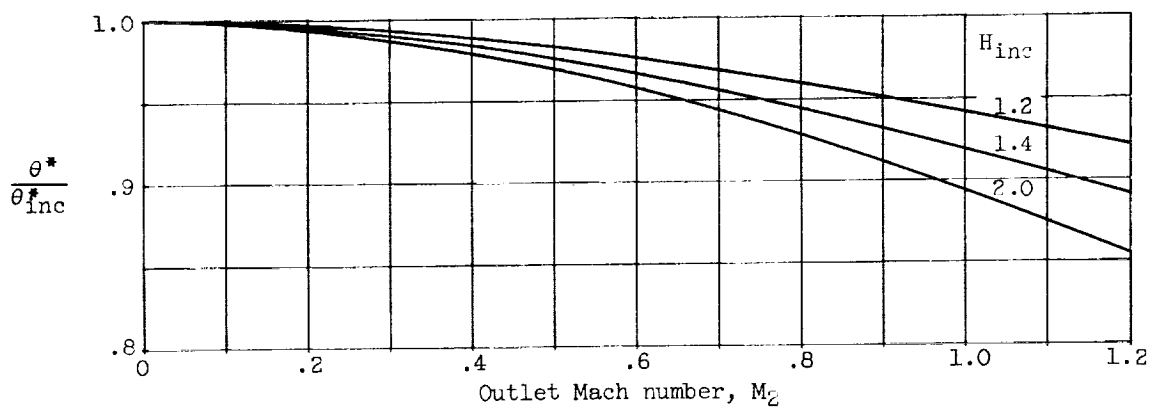


Figure 33. - Ratio of compressible to incompressible momentum thickness for constant full thickness and exponent for power velocity distribution.

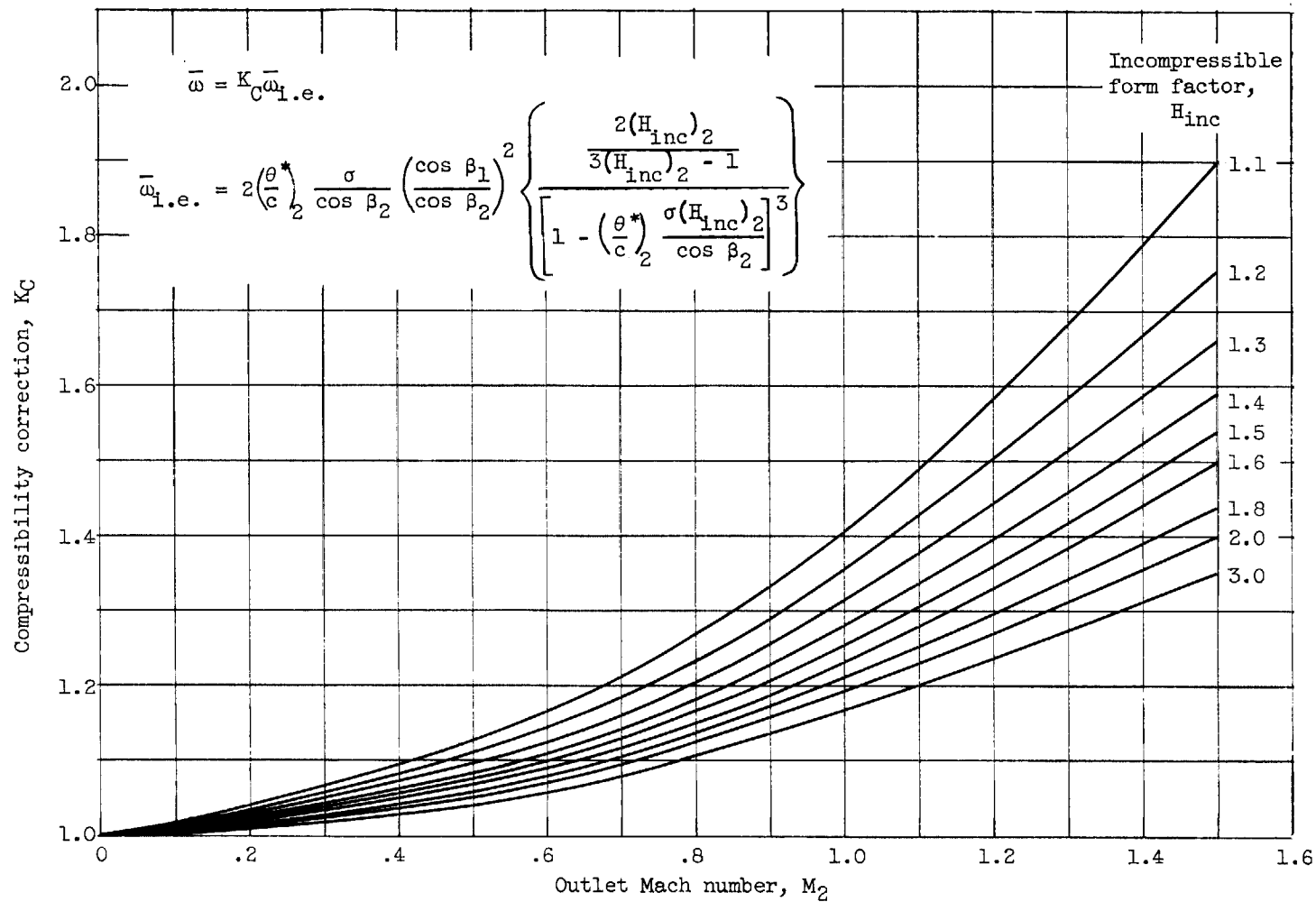


Figure 34. - Correction factor K_C for calculation of total-pressure-loss coefficient for compressible flow on basis of incompressible equation (5) as determined from model wake form with power velocity profile.

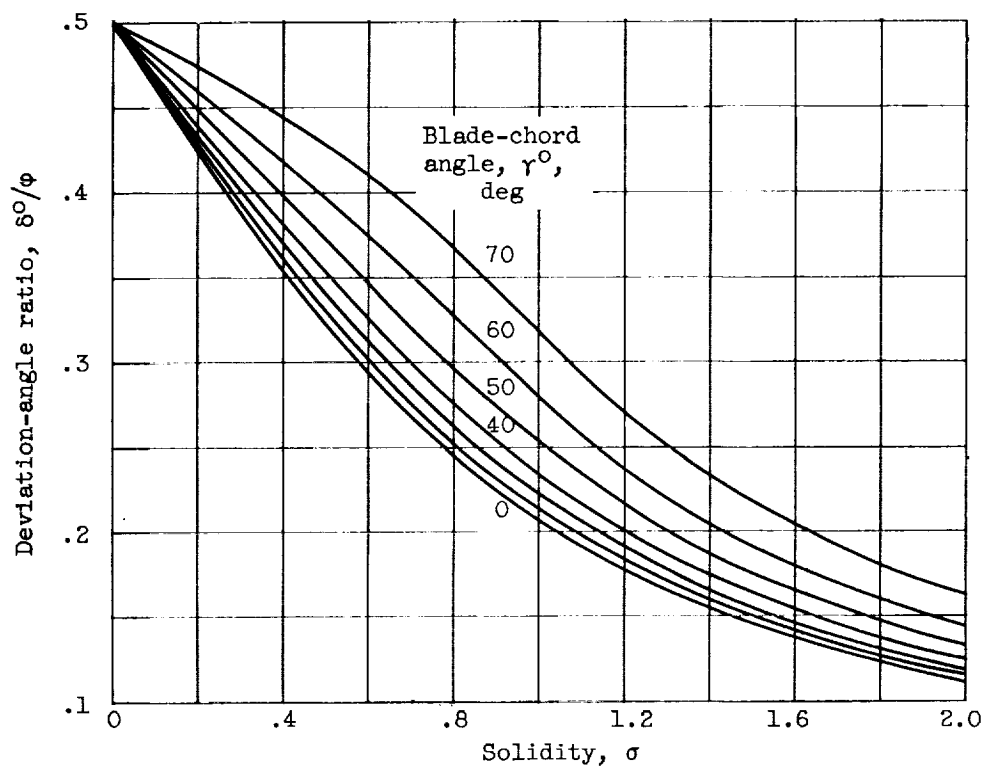


Figure 35. - Theoretical variation of deviation-angle ratio for infinitely thin circular-arc sections at "impact-free-entry" incidence angle according to potential theory of reference 26.

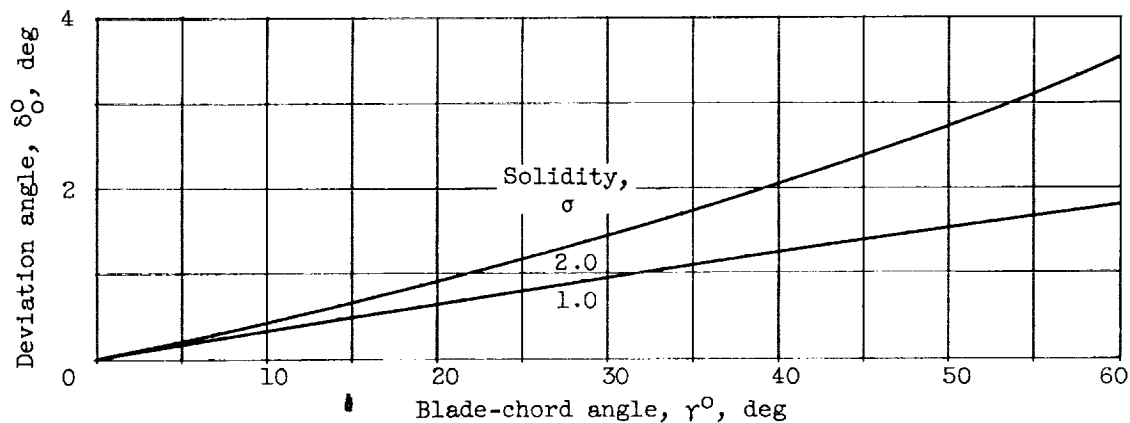


Figure 36. - Theoretical variation of deviation angle for conventional uncambered 10-percent-thick blade section at zero incidence angle as presented in reference 16.

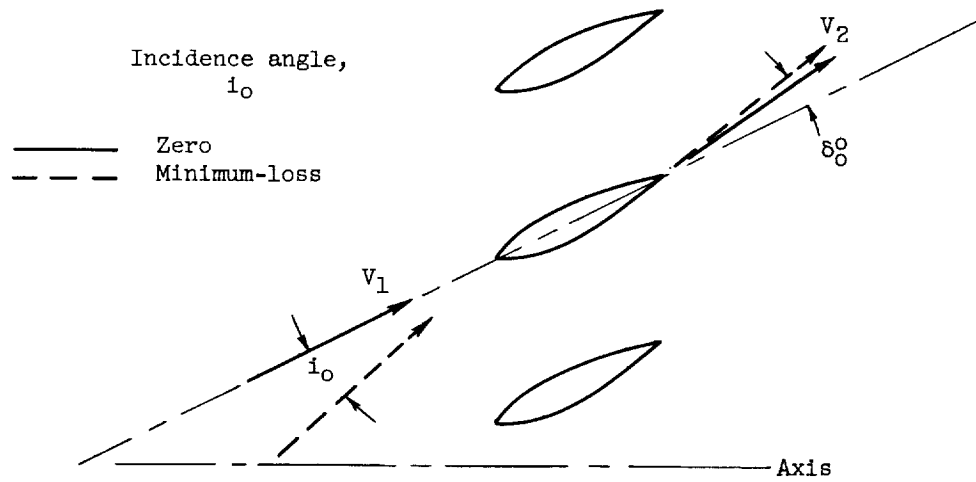


Figure 37. - Outlet flow direction for cascade of staggered uncambered blades.

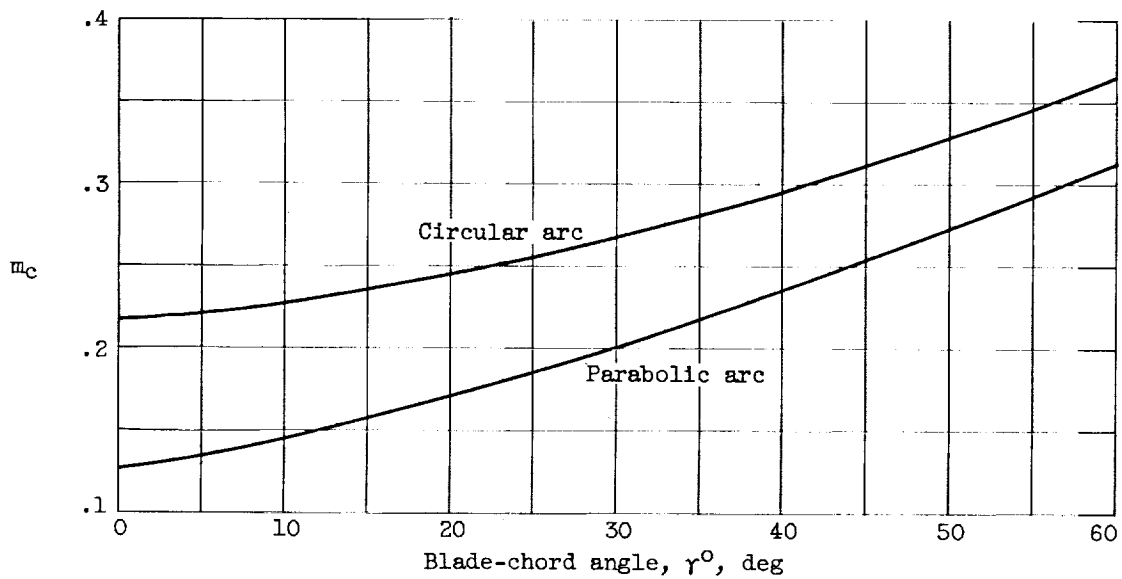


Figure 38. - Variation of factor m_c in Carter's deviation-angle rule (ref. 46).

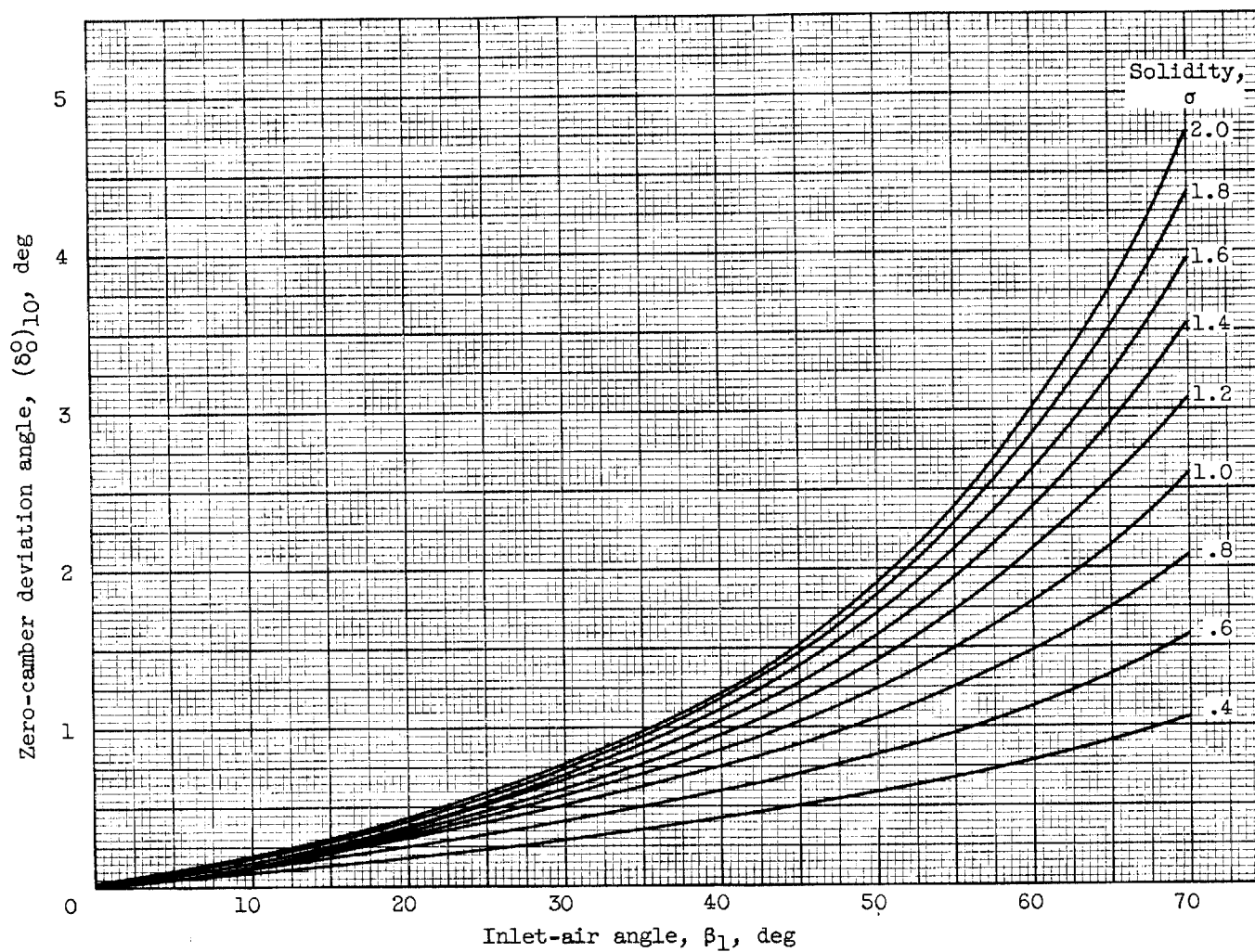


Figure 39. - Zero-camber deviation angle at reference minimum-loss incidence angle deduced from low-speed-cascade data for 10-percent-thick NACA 65-(A_{10})-series blades (ref. 11).

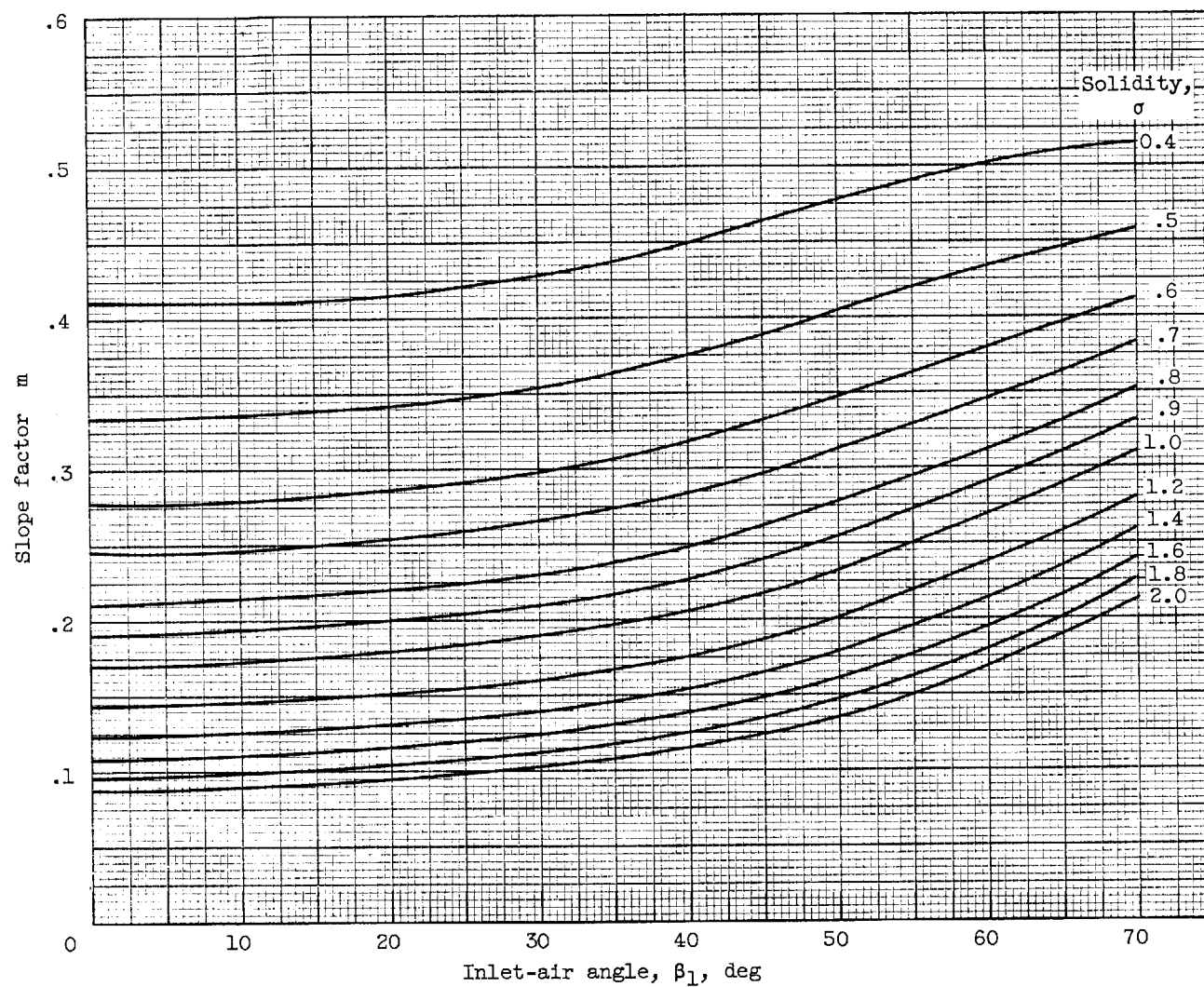


Figure 40. - Deduced variation of slope factor m in deviation-angle rule for NACA 65-(A_{10})-series blades as equivalent circular arc.

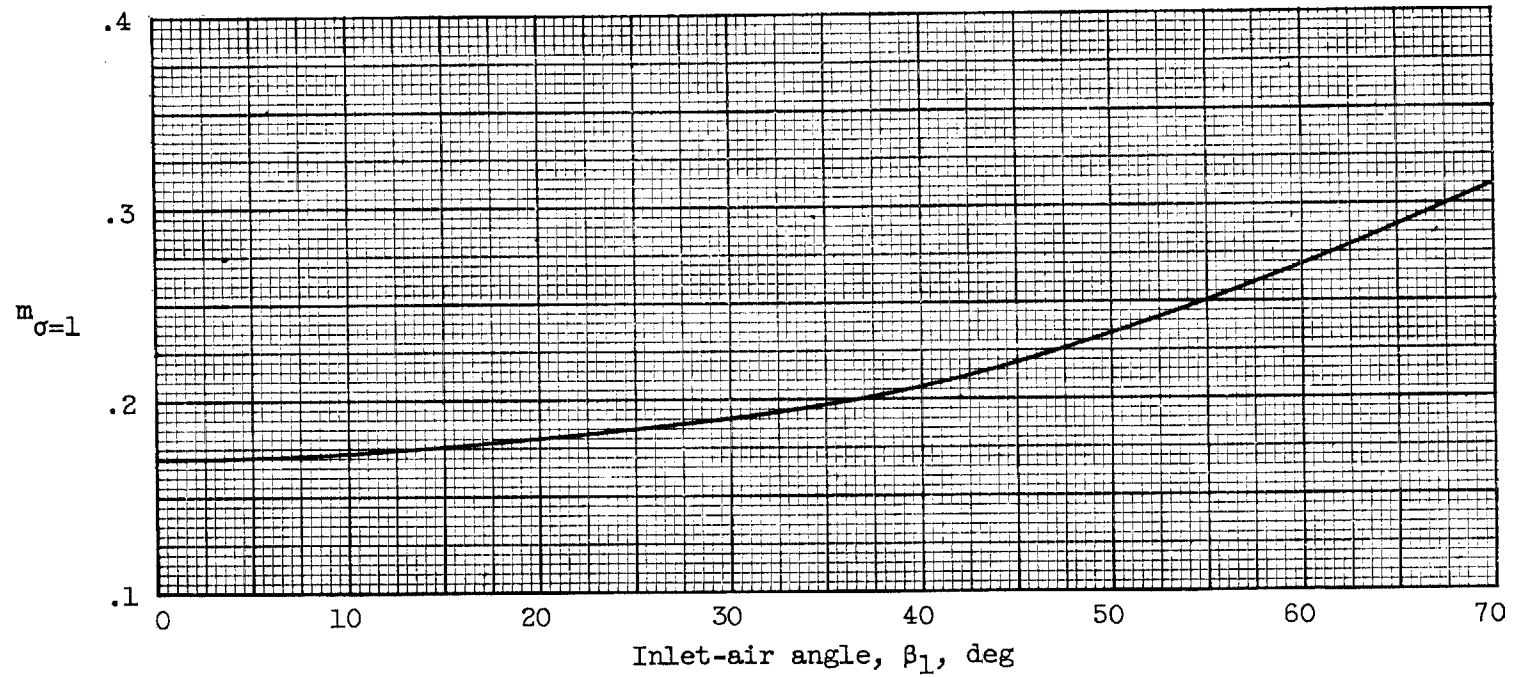


Figure 41. - Value of $m_{\sigma=1}$ in deviation-angle rule for 65-(A₁₀)-series blades as equivalent circular arcs (deduced from data of ref. 11).

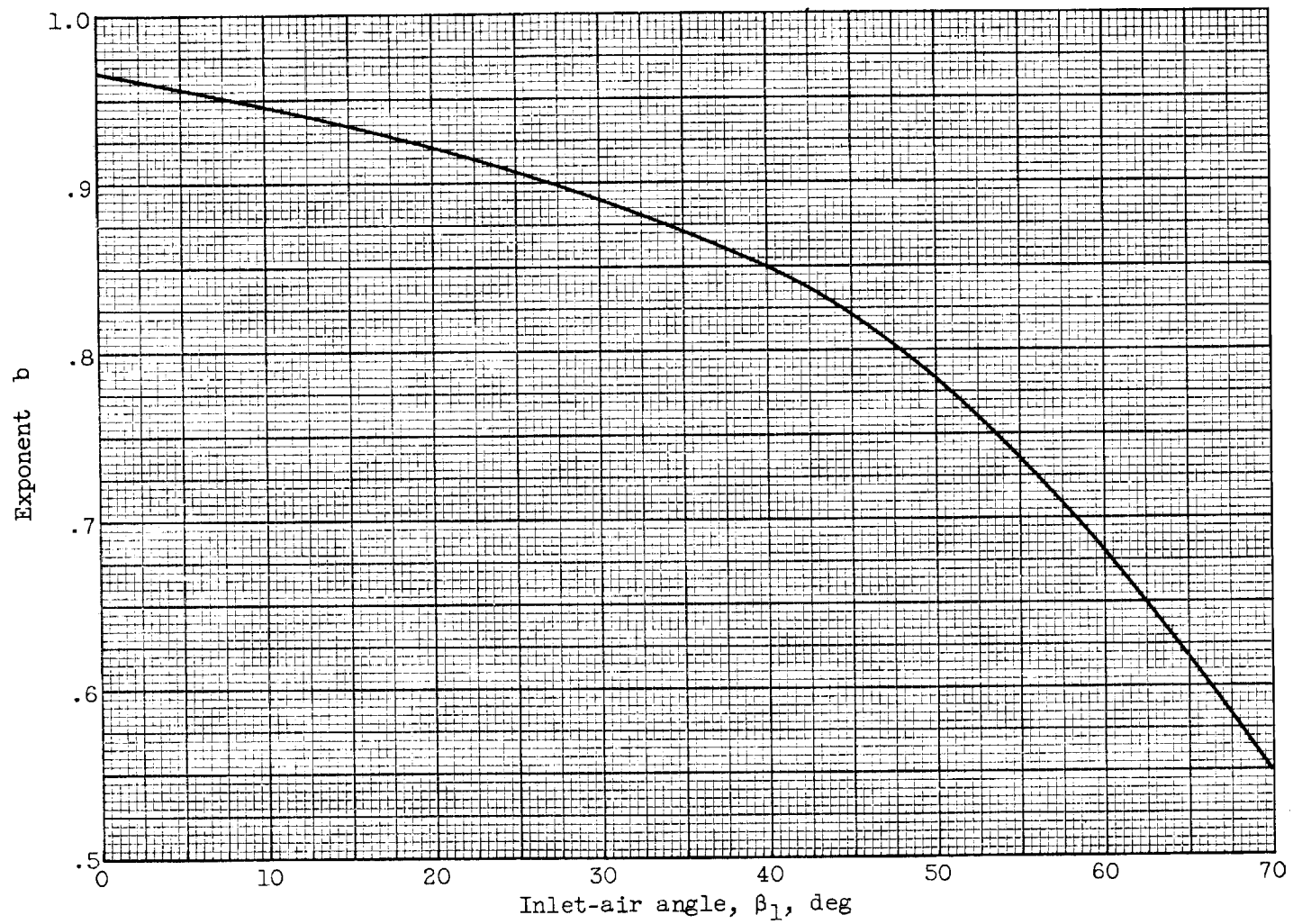


Figure 42. - Value of solidity exponent b in deviation-angle rule (eq. (11))
(deduced from data for 65-(A₁₀)-series blades in ref. 11).

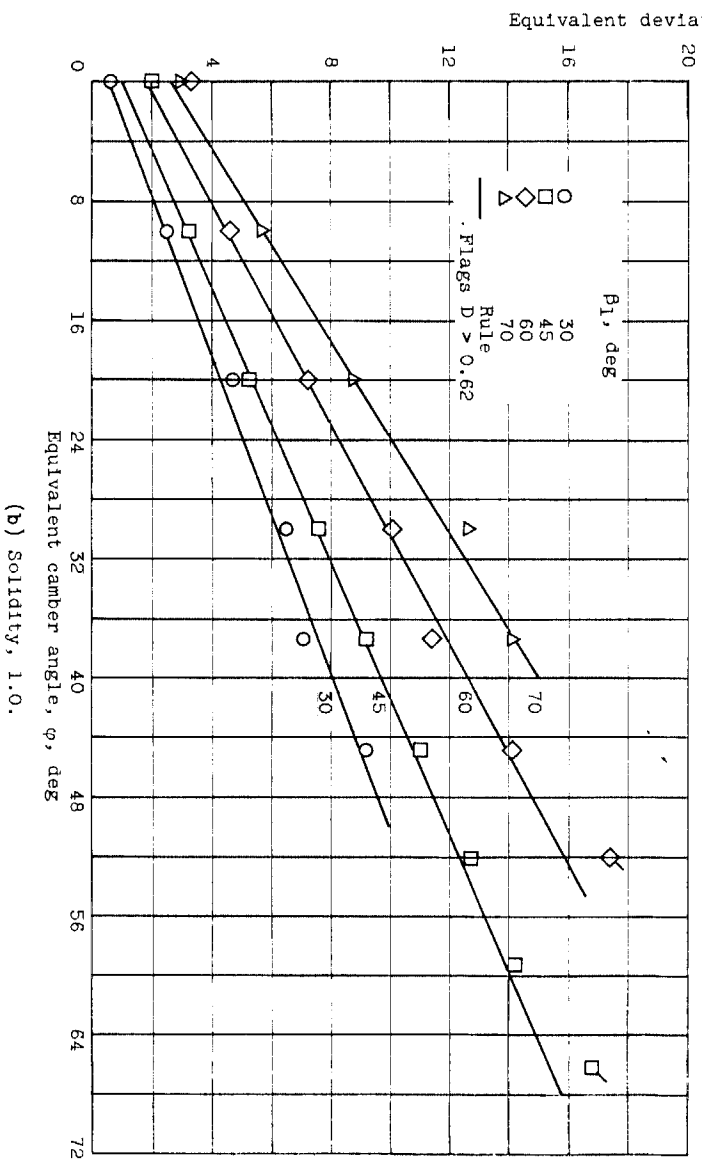
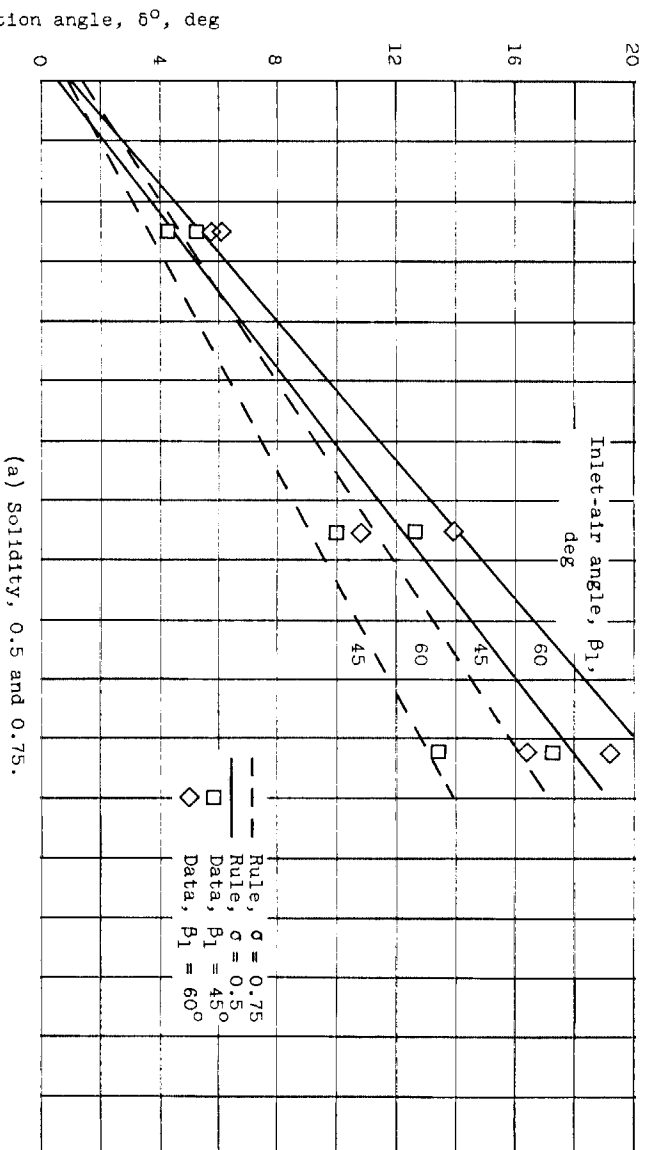
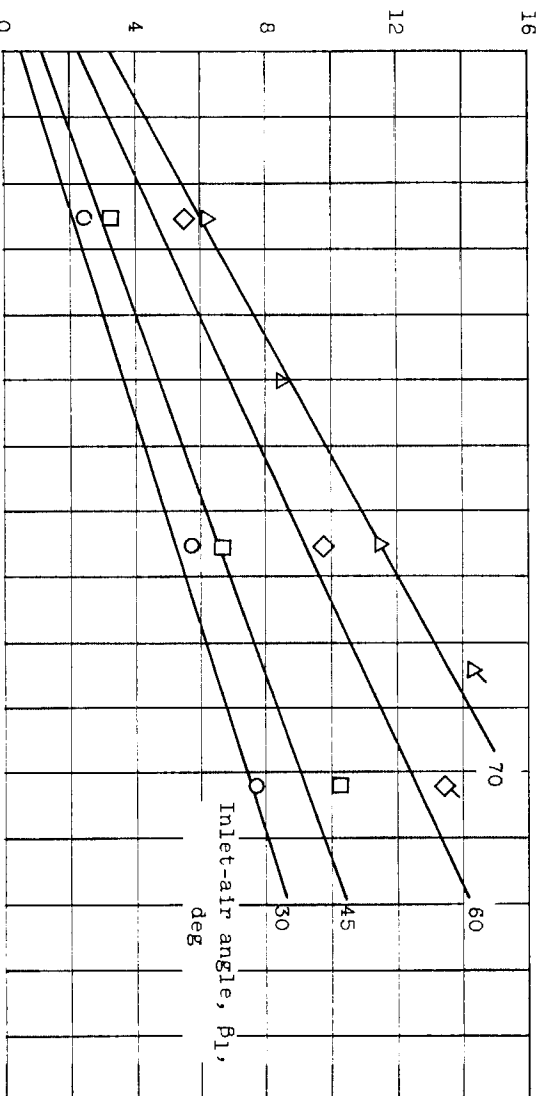


Figure 43. - Comparison between data values and deduced rule values of reference minimum-loss deviation angle for NACA 65-(A10)10-series blades as equivalent circular arcs (data from ref. 11).



CG-11

3383

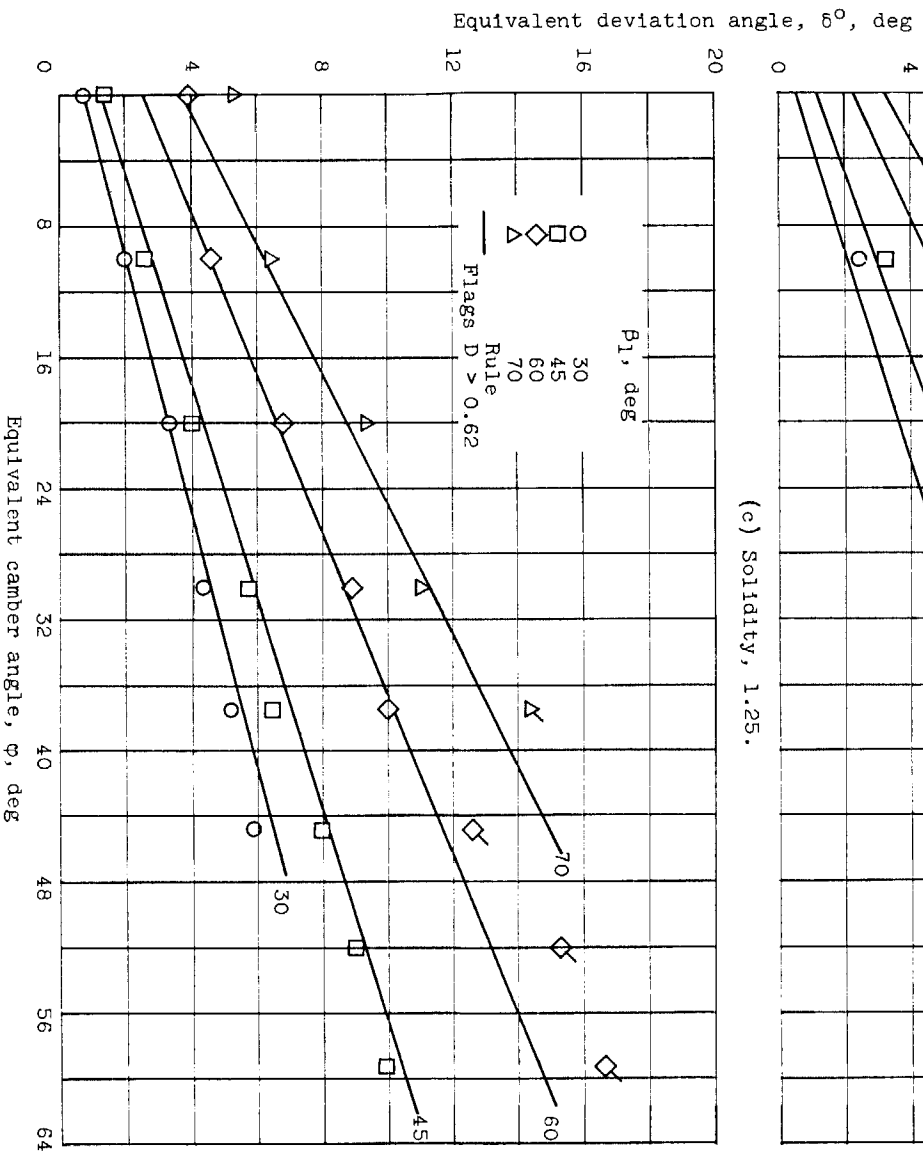


Figure 43. - Concluded. Comparison between data values and deduced rule values of reference minimum-loss deviation angle for NACA 65-(A10)10-series blades as equivalent circular arcs (data from ref. 11).

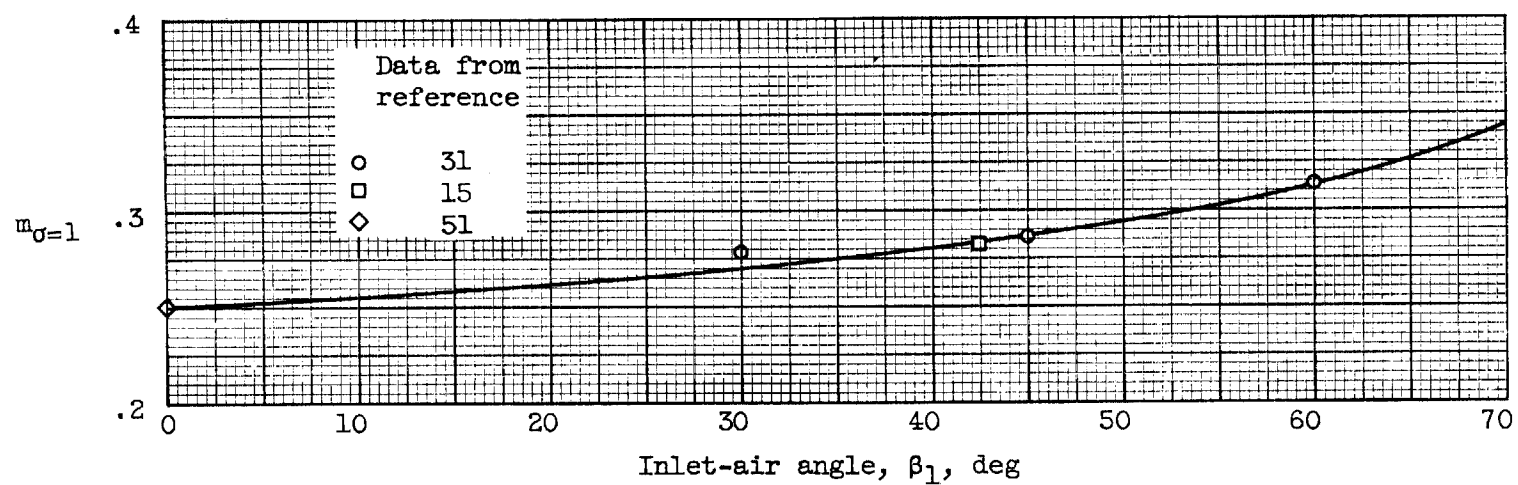


Figure 44. - Deduced values of $m_{\sigma=1}$ for circular-arc mean line.

3383

CG-11 back

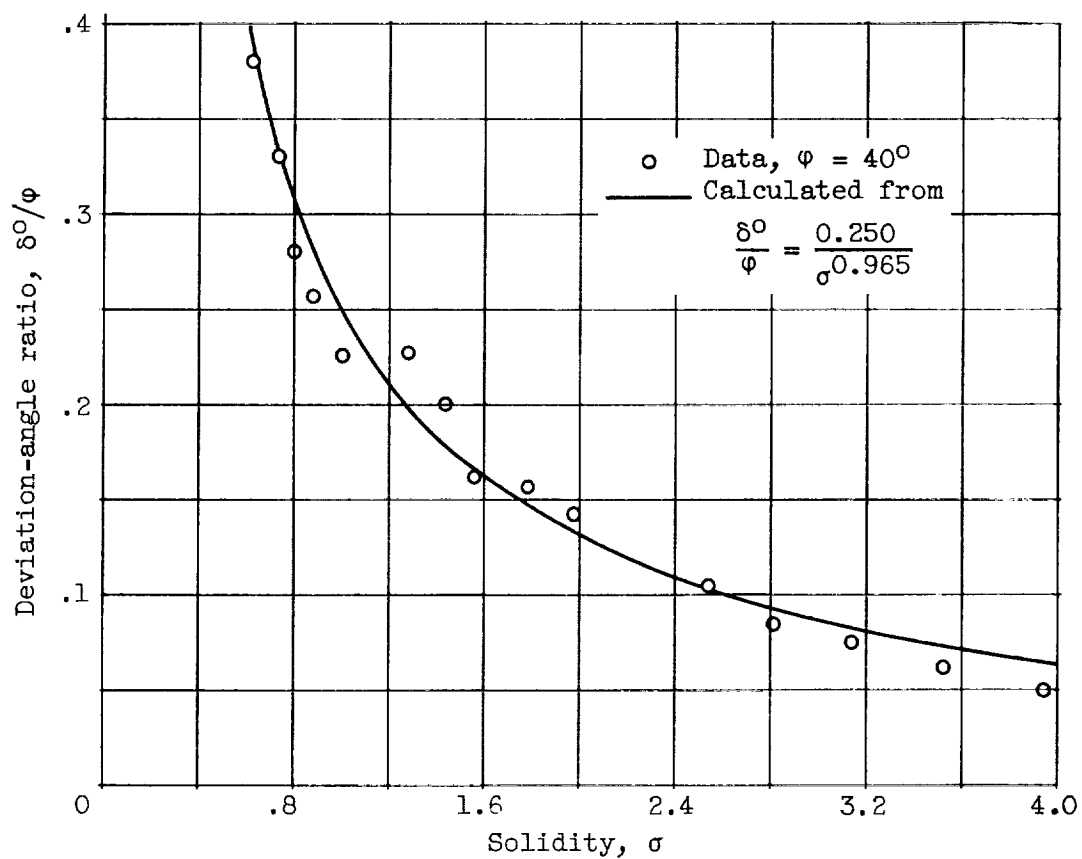


Figure 45. - Comparison of experimental deviation-angle ratio and rule values using solidity exponent given by figure 42. Data for circular-arc inlet guide vanes in annular cascade (ref. 52).

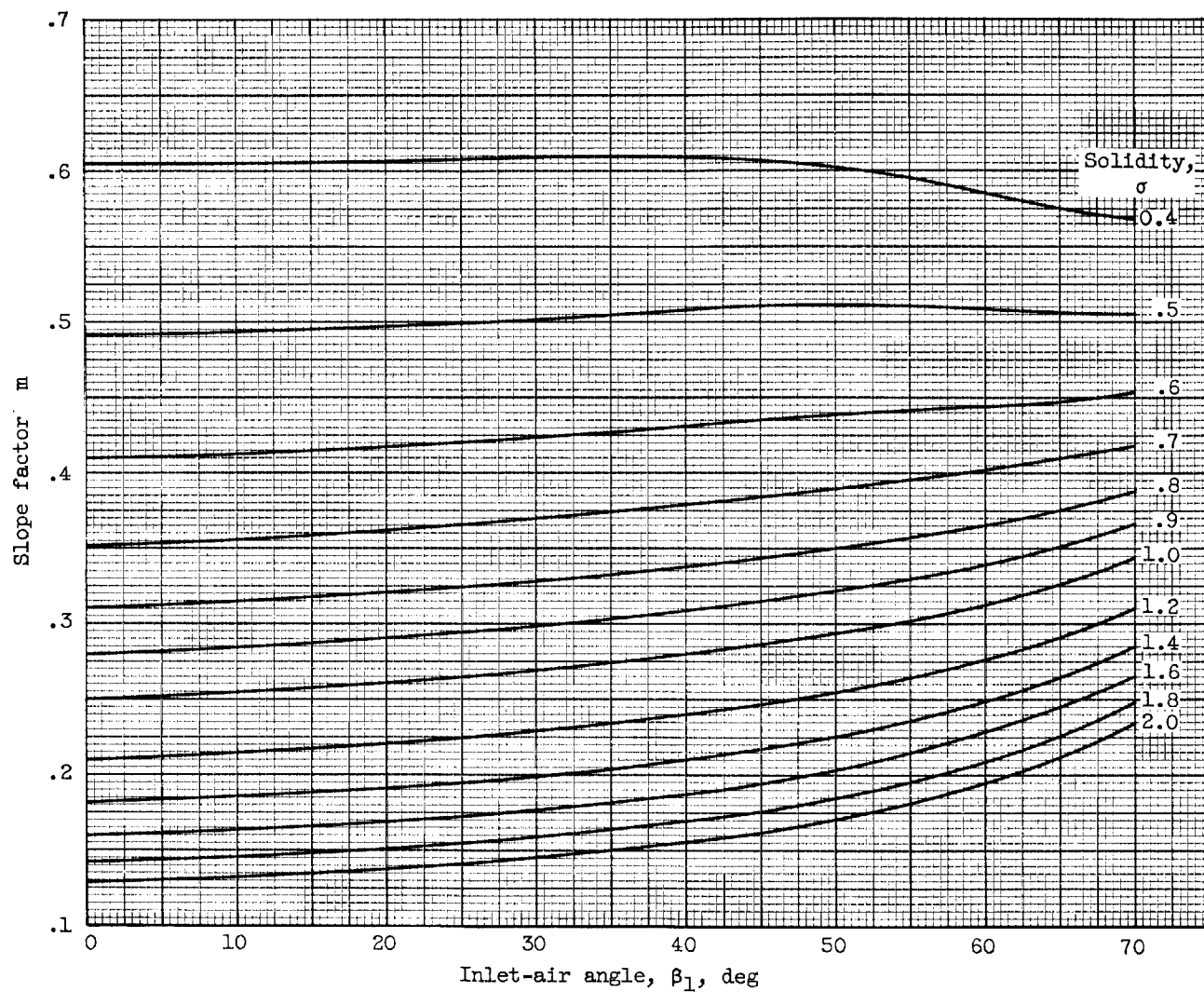


Figure 46. - Deduced variation of slope factor m in deviation-angle rule (eq. (10)) for circular-arc-mean-line blades.

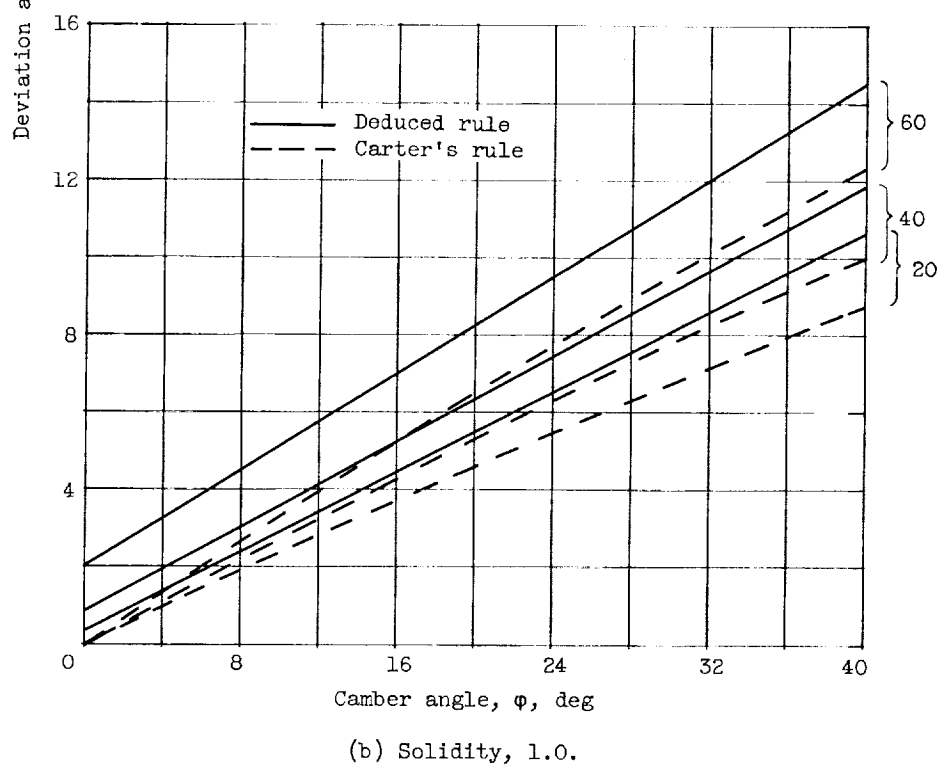
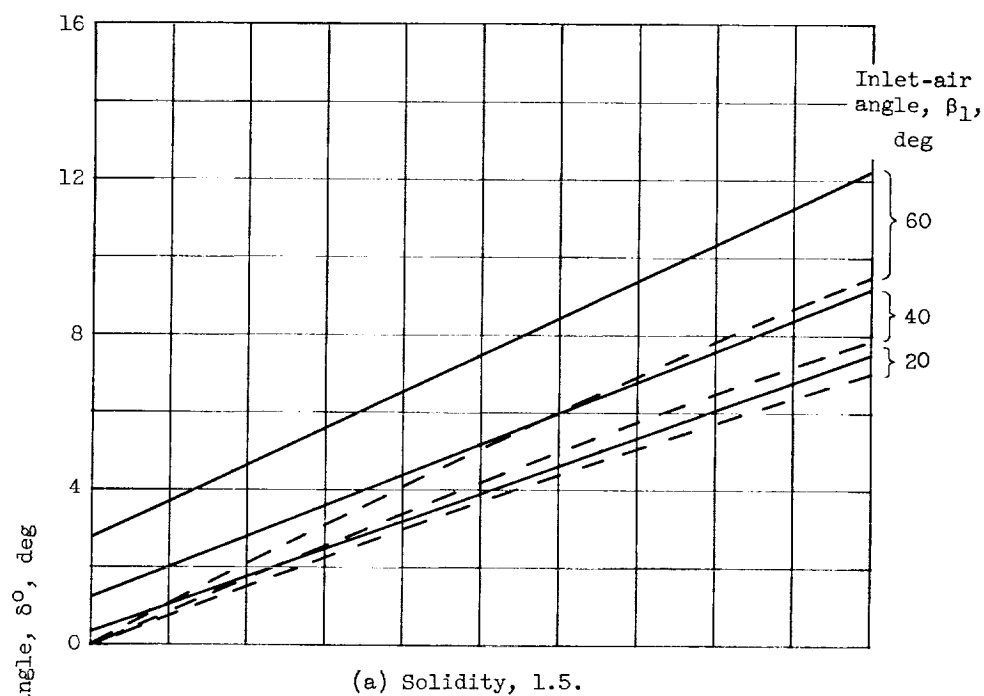


Figure 47. - Comparison of calculated reference deviation angles according to Carter's rule and deduced modified rule for 10-percent-thick, thick-nose circular-arc blades.

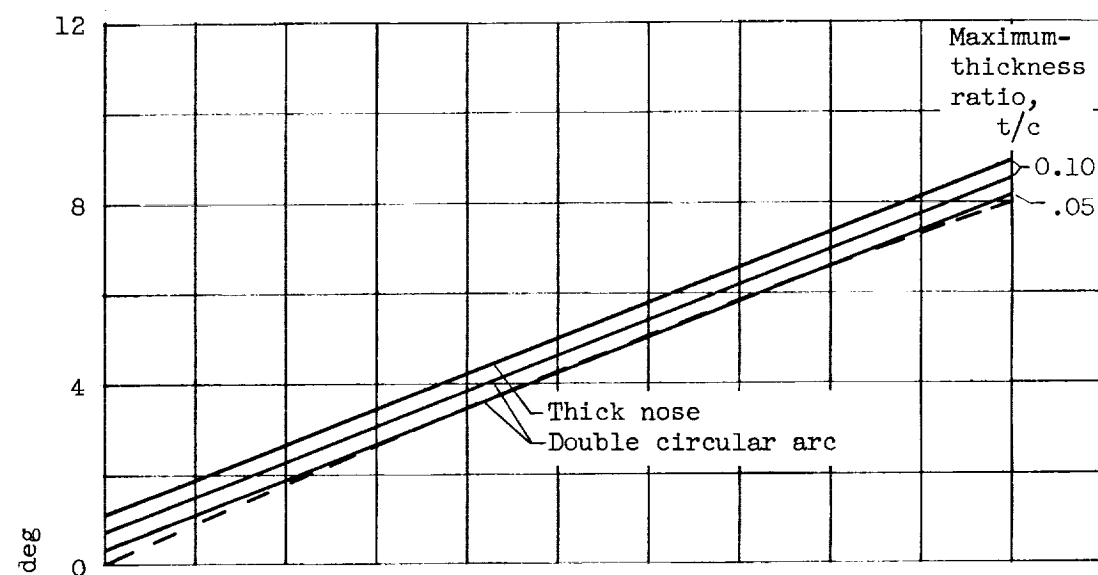
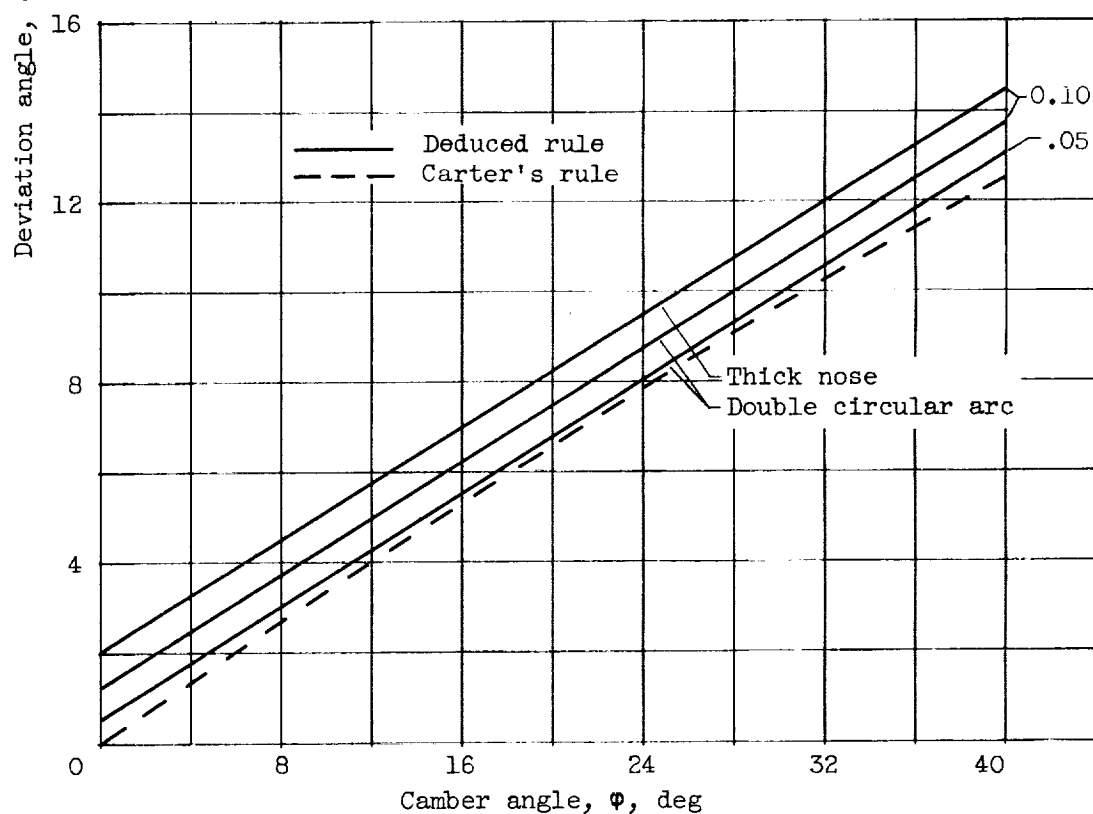
(a) Solidity, 1.5; inlet-air angle, 40° .(b) Solidity, 1.0; inlet-air angle, 60° .

Figure 48. - Comparison of calculated reference deviation angles according to Carter's rule and deduced modified rule for circular-arc blades of different thickness.

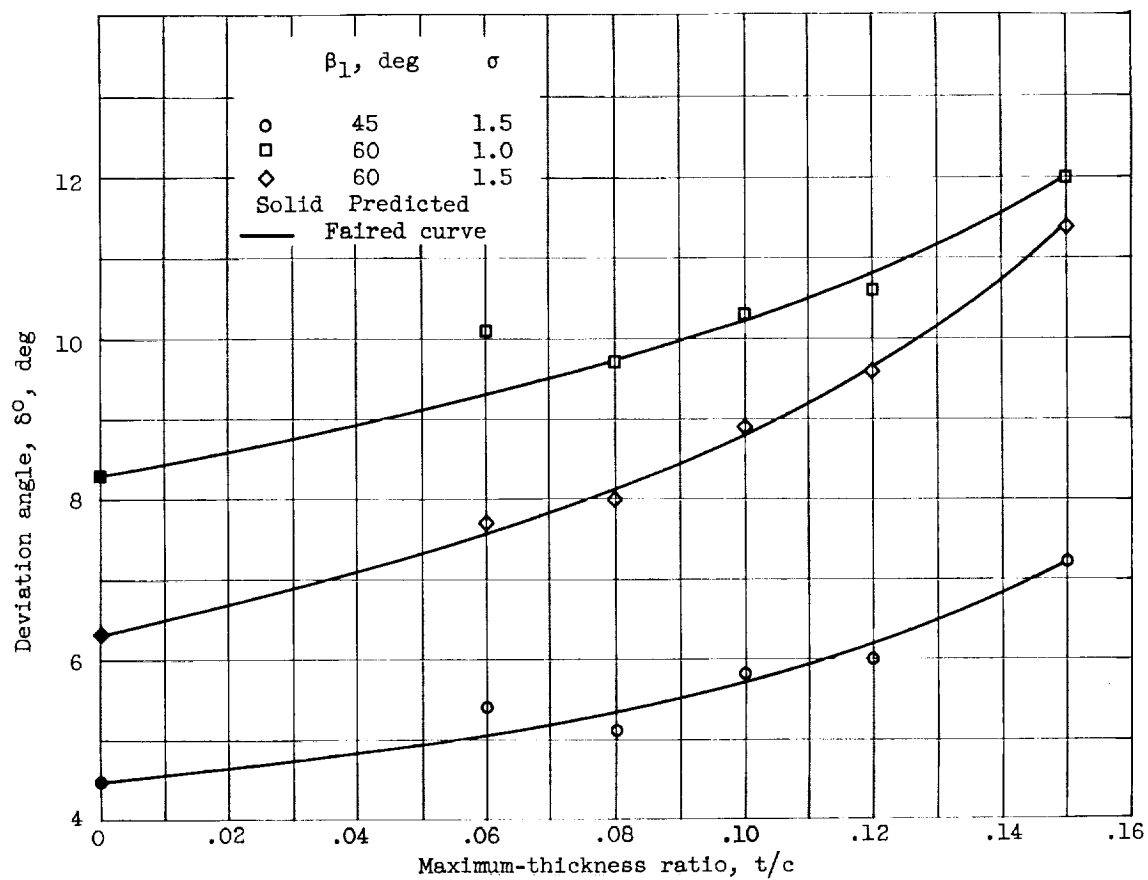


Figure 49. - Variation of deviation angle with blade maximum-thickness ratio for NACA 65-(12A₁₀) blade in region of minimum loss (data from ref. 34).

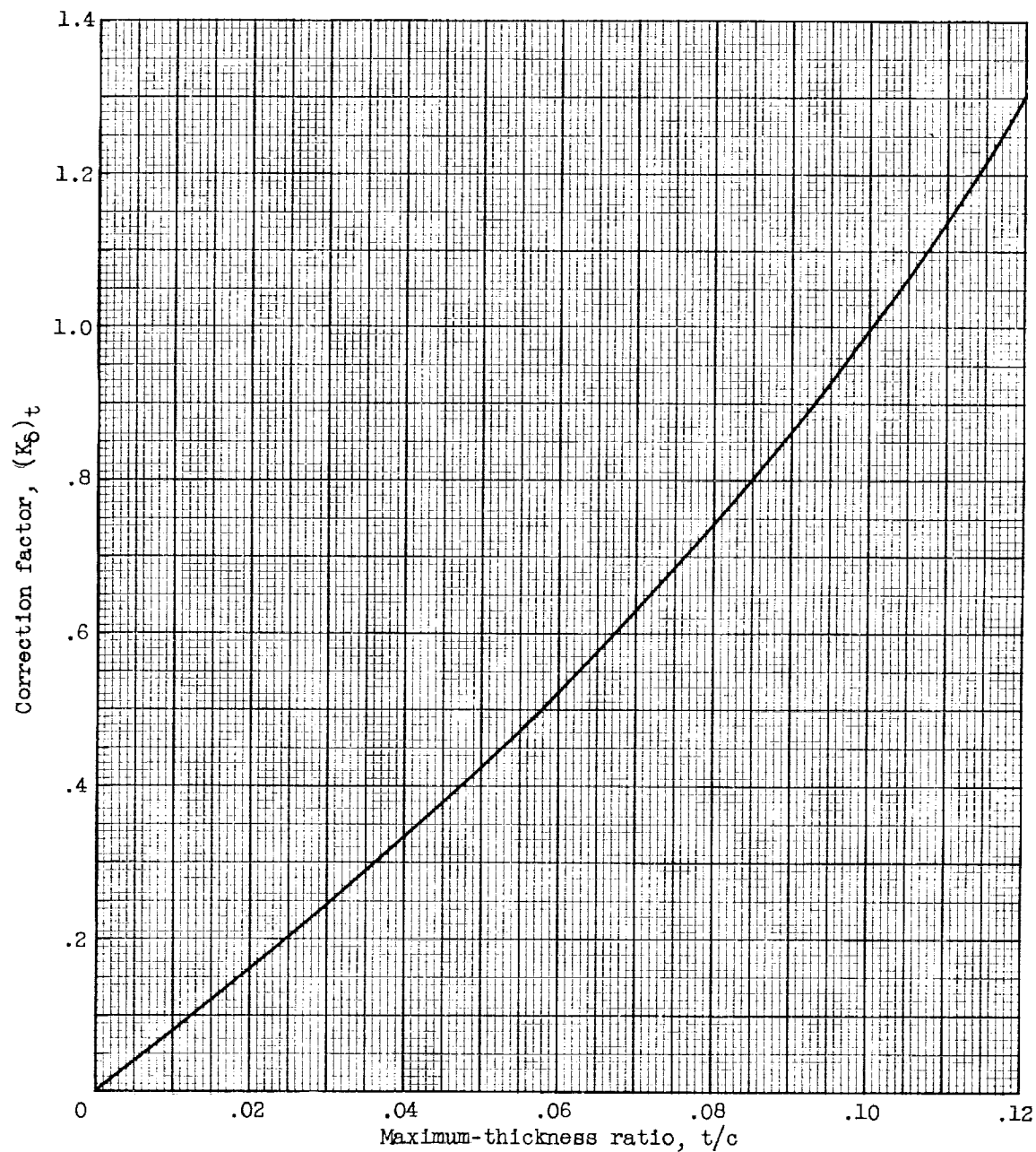


Figure 50. - Deduced maximum-thickness correction for zero-camber reference minimum-loss deviation angle (eq. (13)).

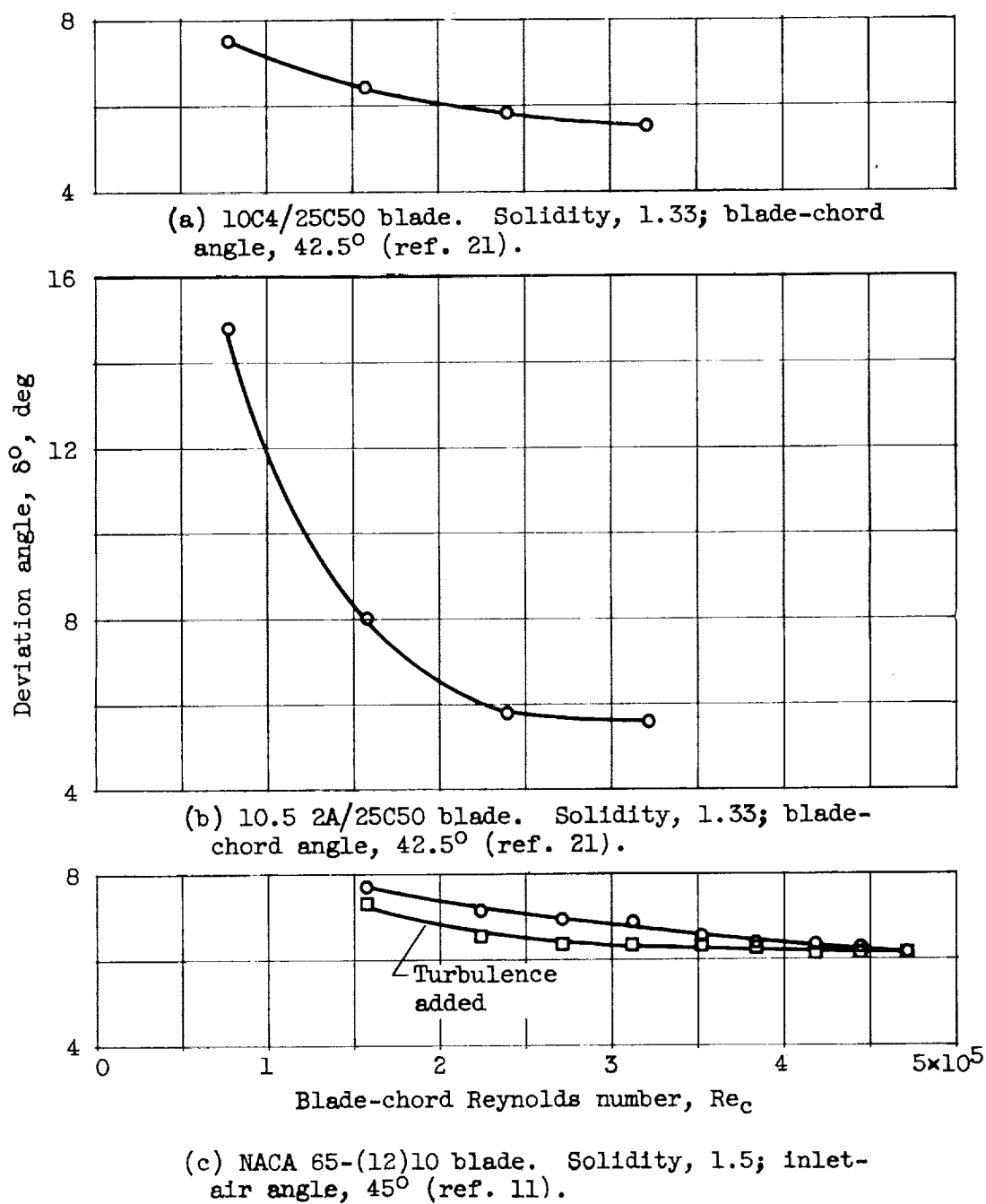


Figure 51. - Illustrative variations of reference deviation angle with Reynolds number.

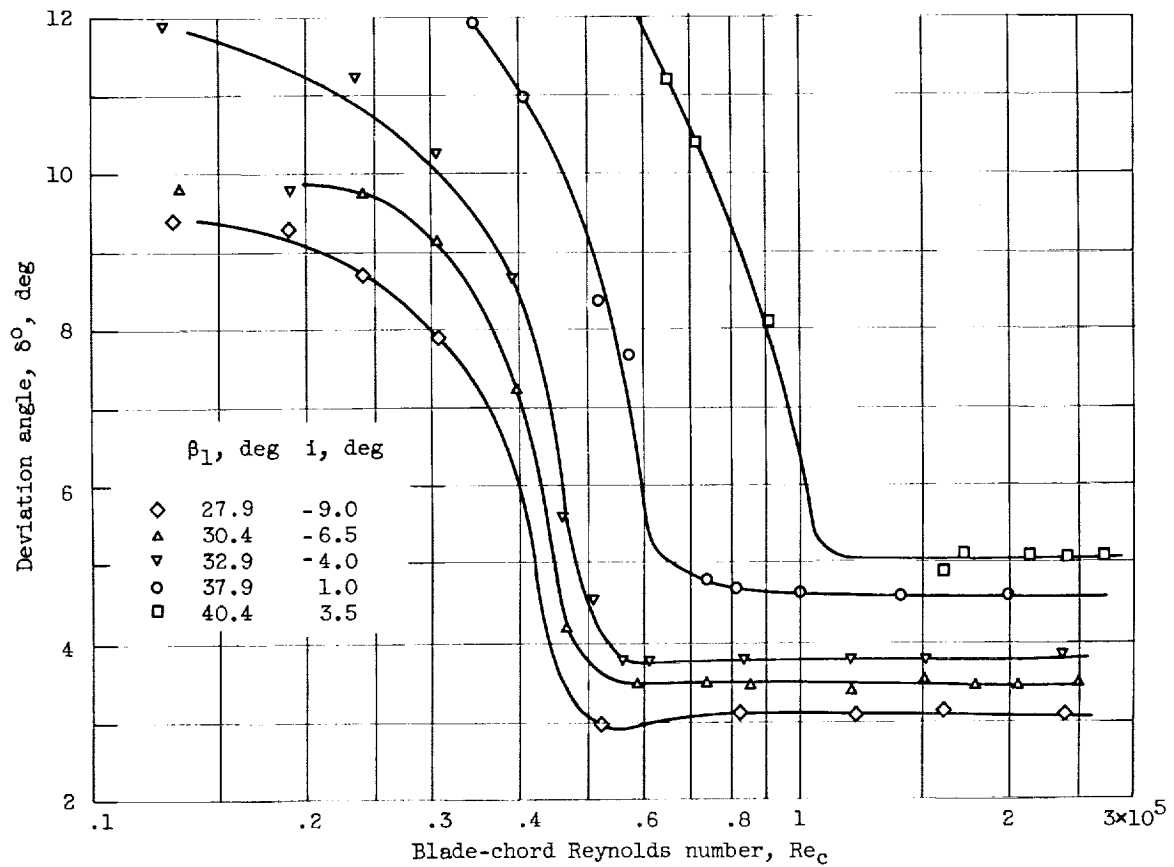


Figure 52. - Variation of deviation angle with Reynolds number for 10C4/40 P40 blade. Solidity, 1.33 (ref. 39).

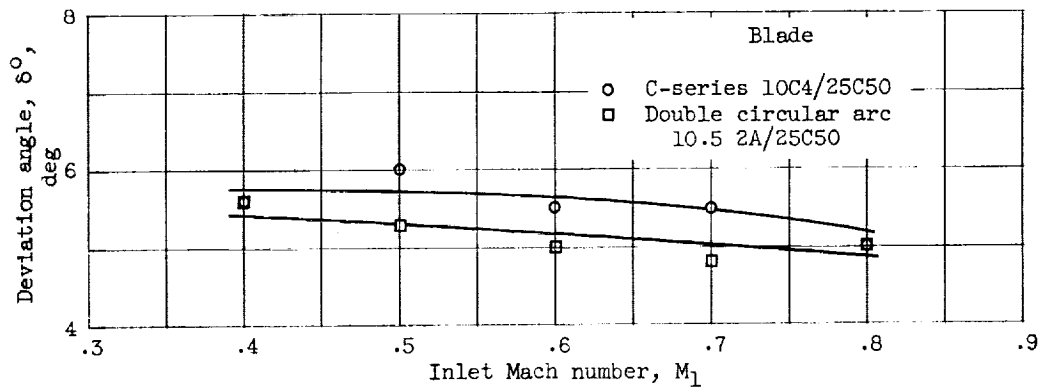
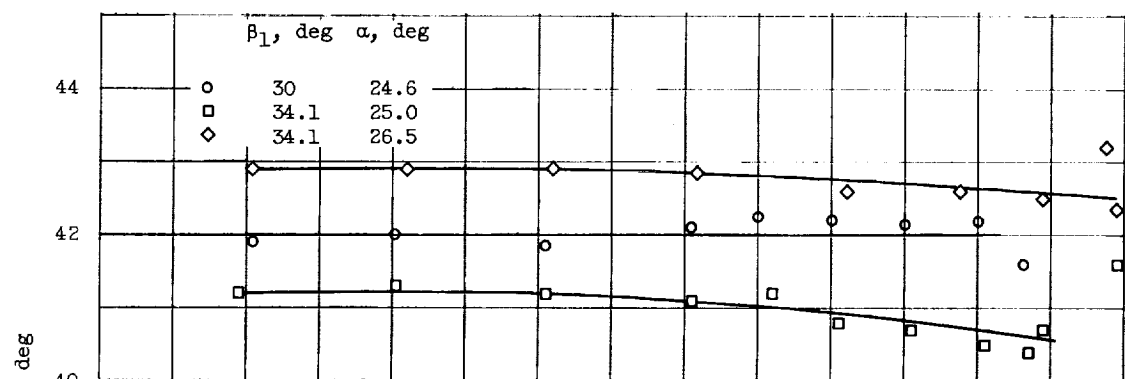
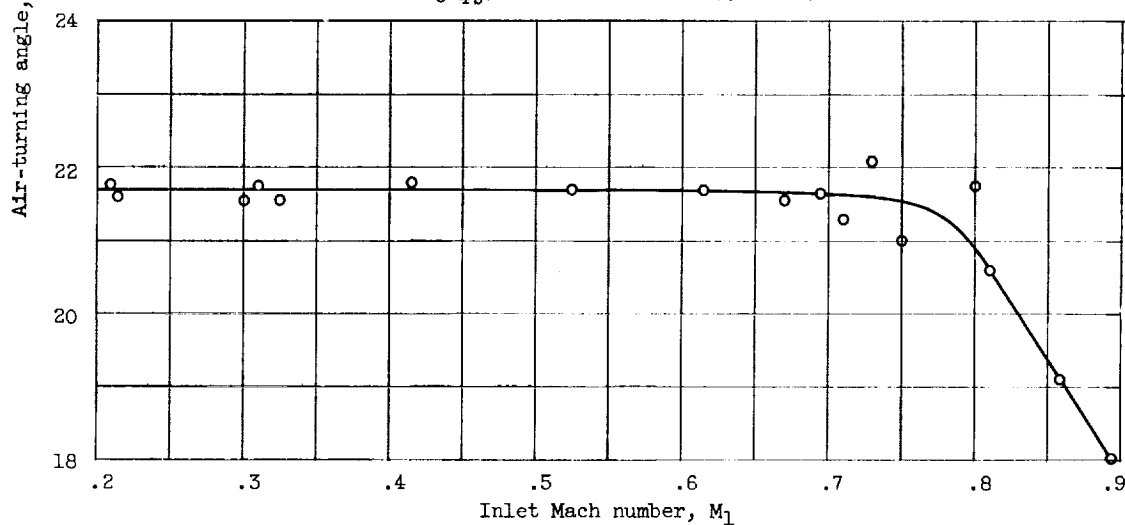


Figure 53. - Variation of reference deviation angle with inlet Mach number for circular-arc blades. Solidity, 1.333; blade-chord angle, 42.5° (ref. 21).



(a) T1(18A₆I_{4b})08 blade. Solidity, 1.5 (ref. 43).



(b) 65-(12A₁₀)10 blade. Solidity, 1.0; inlet-air angle, 45° ; angle of attack, 16.5° (ref. 20).

Figure 54. - Variation of air-turning angle with inlet Mach number in region of minimum loss.

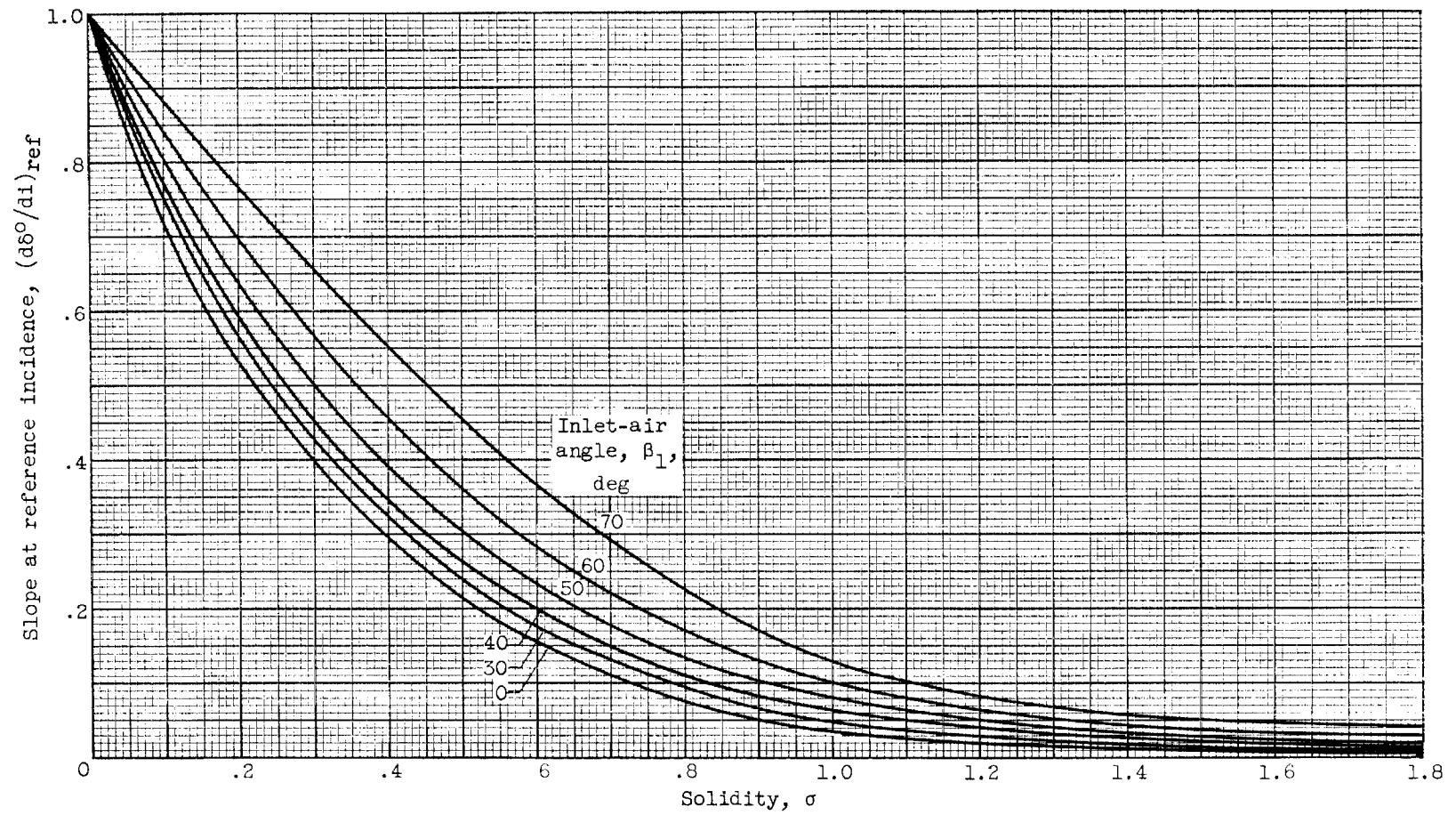


Figure 55. - Deviation-angle slope $d\delta^\circ/di$ at reference incidence angle deduced from low-speed data for NACA 65-(A₁₀)10 blades (ref. 11).

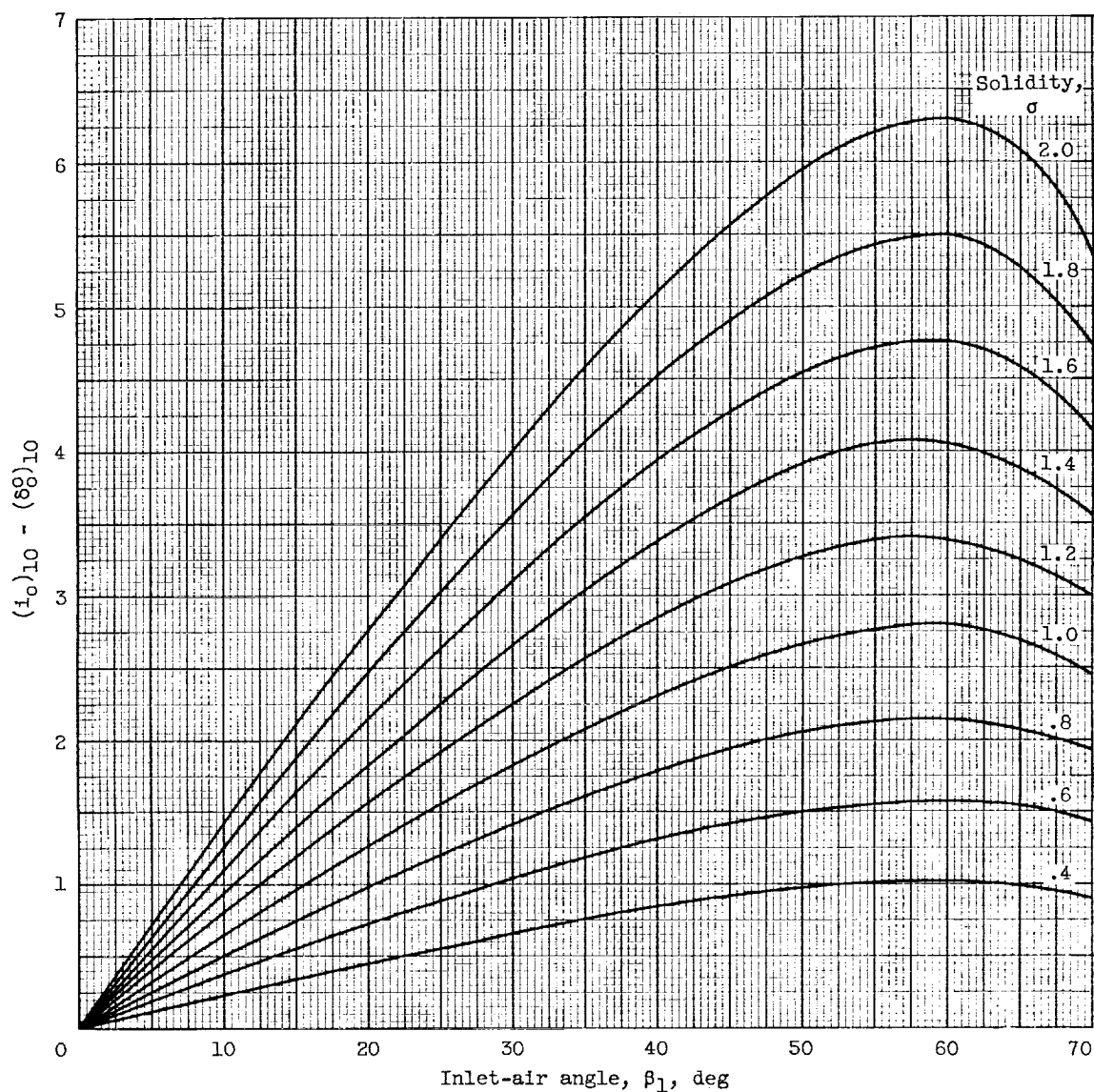
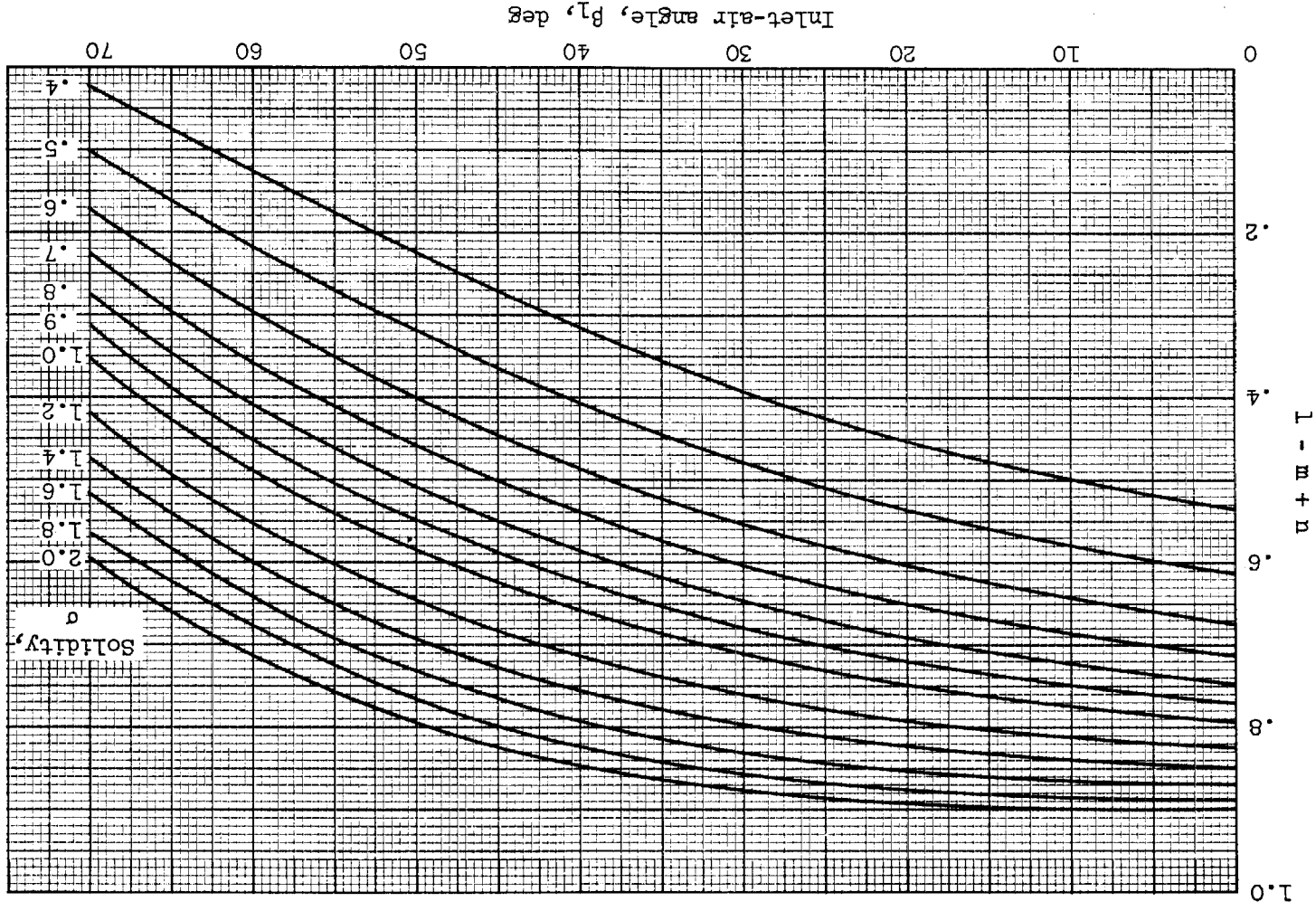
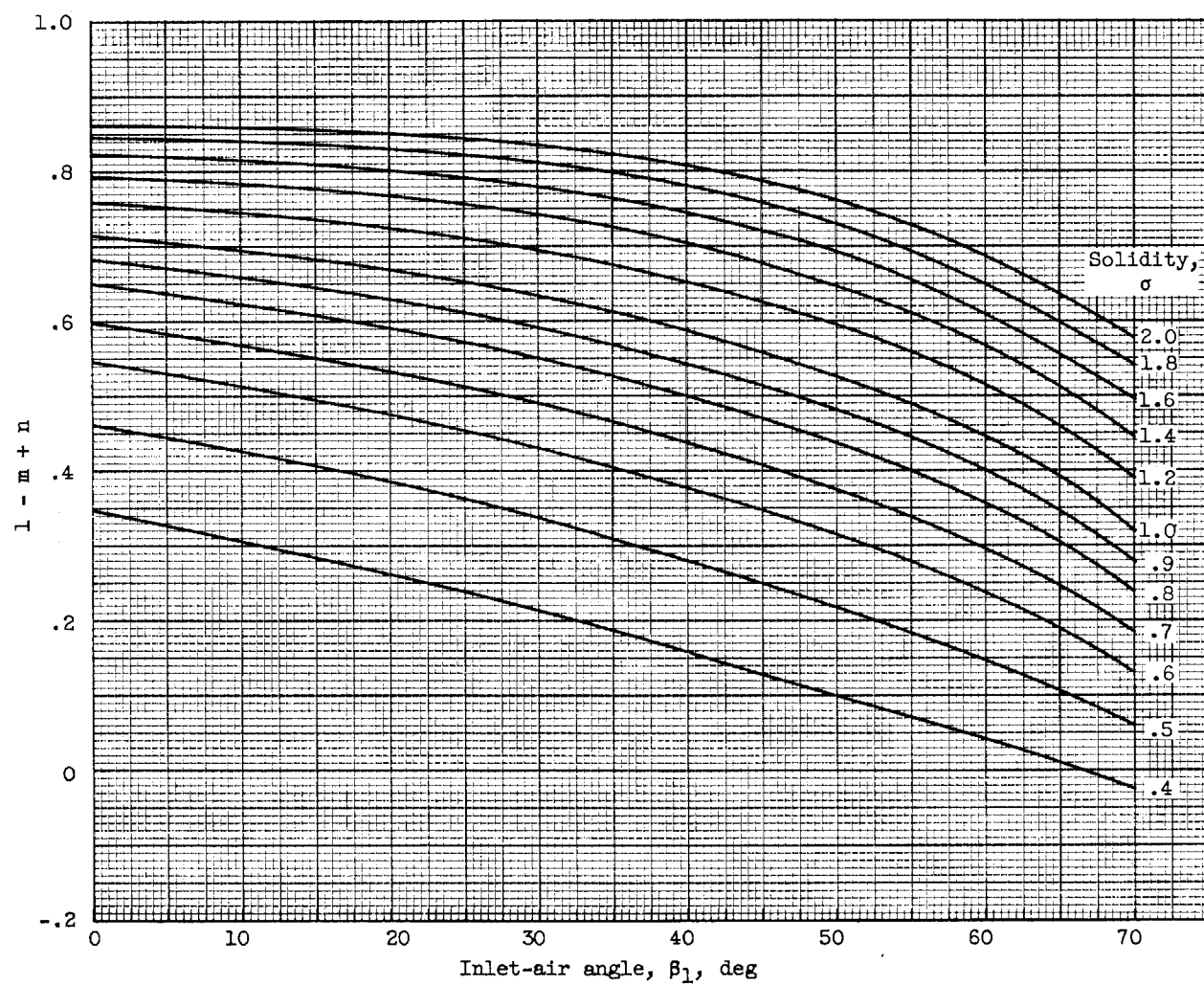


Figure 56. - Variation of $(i_o)_{10} - (s_o^o)_{10}$ with inlet-air angle and solidity (eq. (18)).



(a) NACA 65-(A₁₀)-series blades as equivalent circular arc (eq. 18)).
 Figure 57. - Variation of $l - m + n$.



(b) Circular-arc-mean-line blades (eq. (18)).

Figure 57. - Concluded. Variation of $l - m + n$.

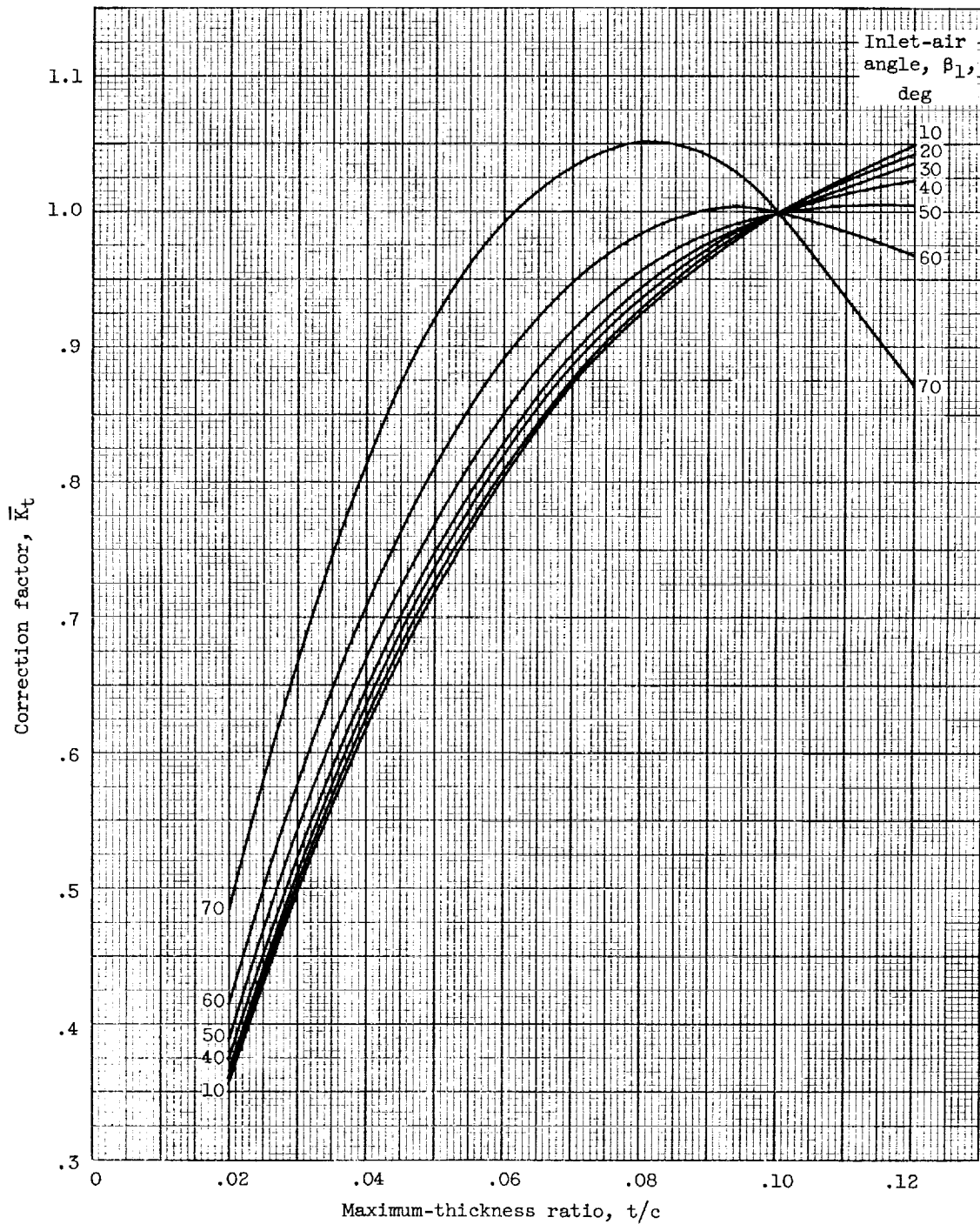


Figure 58. - Variation of thickness-correction factor \bar{K}_t for camber calculation (eq. (18)).

CHAPTER VII

BLADE-ELEMENT FLOW IN ANNULAR CASCADES

By William H. Robbins, Robert J. Jackson, and Seymour Lieblein

SUMMARY

A blade-element analysis is made of annular-cascade data obtained primarily from single-stage-compressor test installations. The parameters that describe blade-element flow (total-pressure loss, incidence angle, and deviation angle) are discussed with reference to the many variables affecting these parameters. The blade-element data are correlated over a fairly wide range of inlet Mach number and cascade geometry. Two blade shapes are considered in detail, the 65-(A₁₀)-series profile and the double-circular-arc airfoil. Compressor data at three radial positions near the tip, mean, and hub are correlated at minimum-loss incidence angle. Curves of loss, incidence angle, and deviation angle are presented for rotor and stator blade elements. These correlation curves are presented in such a manner that they are directly related to the low-speed two-dimensional-cascade results. As far as possible, physical explanations of the flow phenomena are presented. In addition, a calculation procedure is given to illustrate how the correlation curves could be utilized in compressor design.

INTRODUCTION

Axial-flow-compressor research has generally been directed toward the solution of either compressor design or compressor analysis problems. In the design problem, the compressor-inlet and -outlet conditions are given, and the compressor geometry must be determined to satisfy these conditions. In contrast, for the analysis problem the inlet conditions and compressor are specified, and the outlet conditions are desired. (The analysis problem is sometimes referred to as the "direct compressor problem.")

There are two phases of the axial-flow-compressor design problem. In the first phase it is necessary to prescribe desirable velocity distributions at each radius of the compressor that will ultimately fulfill the design requirements. A discussion of the velocity-diagram

phase of the compressor design procedure is given in chapter VIII. Secondly, proper blade sections are selected at each radial position and stacked in proper relation to each other to establish the design velocity diagrams at each radius. In order to satisfy the design requirements successfully, accurate blade-row design data are needed. Successful analysis of a compressor (the analysis problem) also depends upon accurate blade-row data, not only at the design point but also over a wide range of flow conditions (ch. X).

In general, compressor designers have relied primarily on three sources of blading information: (1) theoretical (potential-flow) solutions of the flow past airfoil cascades, (2) low-speed two-dimensional-cascade data, and (3) three-dimensional annular-cascade data. Potential-flow solutions have been used to a limited extent. In order to handle the complex mathematics involved in the theoretical solutions, it is necessary to make simplifying assumptions concerning the flow field. Among the most important of these is the assumption of a two-dimensional flow field with no losses. Unfortunately, in some cases these assumptions lead to invalid results unless experimental correction factors are applied to the computed results. These solutions are reviewed in chapter IV (ref. 1).

A considerable amount of blade design data has been obtained from low Mach number experimental two-dimensional cascades. A rather complete study of the cascade work that has been done to date is presented in chapter VI, which correlates cascade data at minimum-loss incidence angle for a wide range of inlet conditions and blade loadings. Low-speed two-dimensional-cascade data have been applied successfully in many compressor designs. However, with the design trends toward higher Mach numbers and higher blade loadings, these cascade results have not always been completely adequate for describing the compressor flow conditions, particularly in regions of the compressor where three-dimensional-flow effects predominate.

Because of such effects, it becomes essential that blade-element data be obtained in a three-dimensional-compressor environment. These three-dimensional-cascade data (obtained primarily from single-stage compressors) may then be used to supplement and correct the theoretical solutions and the two-dimensional-cascade information. Some success has been obtained in correlating annular-cascade data with the theory and the two-dimensional-cascade results (refs. 2 to 6); however, the range of variables covered in these investigations is not nearly complete.

The purpose of this chapter is to correlate and summarize the available compressor data on a blade-element basis for comparison with the two-dimensional-cascade data of chapter VI. An attempt is made to indicate the regions of a compressor where low-speed two-dimensional-cascade data can be applied to compressors and also to indicate the regions where cascade results must be modified for successful application to compressor

design. Two blade sections are considered in detail, the NACA 65-(A₁₀)-series blade and the double-circular-arc airfoil section. Particular emphasis is placed on obtaining incidence-angle, deviation-angle, and loss correlations at minimum loss for blade elements near the hub, mean, and tip radii of both rotor and stator blades. Empirical correction factors that can be applied to the two-dimensional-cascade design rules are given, and application of the design rules and correction factors to compressor design is illustrated.

SYMBOLS

The following symbols are used in this chapter:

a_a	speed of sound based on stagnation conditions, ft/sec
b	exponent in deviation-angle relation (eq. (4)), function of inlet-air angle
c	chord length, in.
D	diffusion factor
i	incidence angle, angle between inlet-air direction and tangent to blade mean camber line at leading edge, deg
K_1	correction factor in incidence-angle relation, function of blade maximum-thickness ratio and thickness distribution
K_δ	correction factor in deviation-angle relation, function of blade maximum-thickness ratio and thickness distribution
M	Mach number
m	factor in deviation-angle relation at $\sigma = 1$ (eq. (4)), function of inlet-air angle
m_c	factor in deviation-angle relation (eq. (6)), function of blade-chord angle
n	slope factor in incidence-angle relation (eq. (3)), function of inlet-air angle and solidity
P	total or stagnation pressure, lb/sq ft
p	static or stream pressure, lb/sq ft
r	radius

s	blade spacing, in.
T	total or stagnation temperature
t	blade maximum thickness, in.
V	air velocity, ft/sec
β	air angle, angle between air velocity and axial direction, deg
γ	ratio of specific heats
γ°	blade-chord angle, angle between blade chord and axial direction, deg
δ°	deviation angle, angle between outlet-air direction and tangent to blade mean camber line at trailing edge, deg
η	efficiency
θ^*	boundary-layer momentum thickness, in.
σ	solidity, ratio of chord to spacing
ϕ	blade camber angle, difference between angles of tangents to mean camber line at leading and trailing edges, deg
ω	angular velocity of rotor, radians/sec
$\bar{\omega}$	total-pressure-loss coefficient

Subscripts:

ad	adiabatic
C	compressor
GV	inlet guide vanes
h	hub
id	ideal
m	mean

min minimum
o zero camber
R rotor
S stator
ST stage
t tip
z axial direction
 θ tangential direction
1 station at inlet to blade row or stage
2 station at exit of blade row or stage
2-D low-speed two-dimensional cascade
10 blade maximum-thickness-to-chord ratio of 10 percent

Superscript:

' relative to rotor

PRELIMINARY CONSIDERATIONS

Blade-Element Concept

In current design practice, the flow distribution at the outlet of compressor blade rows is determined from the flow characteristics of the individual blade sections or elements. The blade-element approach to compressor design is discussed in detail in chapter III (ref. 1) and reference 7. To review briefly, axial-flow-compressor blades are evolved from a process of radial stacking of individual airfoil shapes called blade elements. The blade elements are assumed to be along surfaces of revolution generated by rotating a streamline about the compressor axis; this stream surface of revolution may be approximated by an equivalent cone (fig. 1). Each element along the height of the blade is designed to direct the flow of air in a certain direction as required by the design velocity diagram of the blade row. The basic parameters defining the flow about a blade element are indicated in figure 2. Stated simply, blade-element flow is described by the variations of the loss in total pressure across the blade row and of the air-turning angle with the incidence angle (or angle of attack).

Factors Affecting Blade-Element Performance

The flow about a given blade element in a compressor configuration is different from that in a two-dimensional cascade because of three-dimensional effects in compressor blade rows. These three-dimensional effects influence the magnitude of the design incidence angle, the loss in total pressure, and the deviation angle.

Incidence angle. - In the low-speed two-dimensional cascade, the minimum-loss incidence angle depends on the blade geometry (camber, solidity, and blade thickness), the inlet-air angle, and inlet Mach number (ch. VI). In compressor operation, several additional factors can alter the minimum-loss incidence angle for a given element geometry - for example, differences in testing procedure. In compressor operation, incidence angle, inlet-air angle, and inlet Mach number vary simultaneously; in contrast, cascades are often operated with fixed inlet-air angle and inlet Mach number. Some net difference in the range characteristics and, therefore, the location of the point of minimum loss between cascade operation at constant inlet-air angle and compressor test operation (with varying inlet-air angle) may be obtained.

In addition to these blade-element considerations, of course, there are sources of difference arising from compressor three-dimensional effects. For example, radial variations of minimum-loss incidence angle that are not consistent with the trends predicted from cascade blade-element considerations have been observed in compressor rotors (refs. 8 and 9). Apparently, radial position may also be a factor in determining compressor minimum-loss incidence angle.

Total-pressure loss. - In the two-dimensional cascade, the magnitude of the loss in total pressure across the blade element is determined from the growth of the blade surface boundary layers (profile loss). In the actual compressor, the loss in total pressure is determined not only by the profile loss, but also by the losses induced by the three-dimensional nature of the flow. These three-dimensional losses result from secondary motions and disturbances generated by the casing wall boundary layers, from blade tip clearance, from radial gradients of total energy, and from interactions of adjacent blade rows. The compressor loss picture is further complicated by the tendency of boundary-layer fluid on the compressor blade surfaces and in the blade wake to be displaced radially. As a consequence of this phenomenon, the loss measured downstream of a given blade element may not necessarily reflect the actual loss generated at that element, but something more or less, depending on the radial location of the element.

3390

It is expected, therefore, that the factors influencing the magnitude of the blade-element loss in the compressor will include the factors affecting the profile loss (blade surface velocity distribution, inlet Mach number, blade-chord Reynolds number, free-stream turbulence, and blade surface finish) and the factors affecting the three-dimensional losses. Investigations of compressor blade-element losses based on surface velocity distribution, as expressed in terms of diffusion factors, are presented in references 10 and 11. The essentially secondary effects of blade surface finish and trailing-edge thickness on compressor loss are investigated in references 12 and 13. Results of tests of blade-element performance (ref. 14 and ch. V (ref. 1)) and over-all performance (refs. 15 and 16) at varying Reynolds numbers indicate that there is no significant variation in loss for Reynolds numbers above approximately 2.5×10^5 . (Since most of the compressor data used in this analysis are for Reynolds numbers greater than 2.5×10^5 , no Reynolds number effects are believed to exist for the data.) Some variations of compressor loss with inlet Mach number have been established in references 8, 17, and 18. These results, however, are not complete indications of Mach number effects (shock losses), since the corresponding variations of blade diffusion with Mach number are not identified. An attempt to separate the variation of diffusion and shock losses with Mach number by means of an analysis based on the diffusion factor of reference 10 is presented in references 9 and 19.

Although some aspects of the compressor three-dimensional-flow phenomena are known (chs. XIV and XV (ref. 20)), the specific factors or parameters affecting compressor three-dimensional losses have not been established for analysis purposes. At present, the three-dimensional loss can be treated only on a gross basis as a difference between the total measured loss and the predicted profile loss.

Deviation angle. - In the two-dimensional cascade the minimum-loss deviation angle varies primarily with the blade geometry and the inlet-air angle. Experience with compressor operation indicates that blade-element minimum-loss deviation angle is also sensitive to three-dimensional effects. The two principal compressor effects are secondary flows and changes in axial velocity across the blade element. Secondary flows are treated in chapter XV (ref. 20) and in reference 21. Corrections are established in reference 21 for the effect of secondary flows on the outlet angles of compressor inlet guide vanes. At present, however, rotor and stator secondary-flow effects can be treated only on a gross basis.

The effects of changes in axial velocity ratio on the turning angles of a fixed blade-element geometry are conclusively demonstrated in the rotor investigations of reference 4. There are several origins of varying axial velocity ratio across a compressor blade element: (1) contraction of the annulus area across the blade row, (2) compressibility, which

varies axial velocity ratio for a fixed annulus area, and (3) differences in the radial gradient of axial velocity at blade-row inlet and outlet, which can arise from the effects of radial-pressure equilibrium (ch. VIII). Although several attempts have been made to establish corrections for the effect of change in axial velocity ratio on deviation angle (refs. 4 and 22), these proposed correction techniques have not been universally successful. The principal difficulty involved in the axial velocity corrections is the inability to determine the corresponding changes in blade circulation (i.e., tangential velocity). Values of axial velocity ratio were identified for the deviation-angle data presented, although no attempt was made to apply any corrections.

Some of the secondary factors influencing deviation angle, such as inlet Mach number and Reynolds number, are investigated in references 4, 8, and 17. These results indicate that the variations of deviation angle with Mach number and Reynolds number are small for the range of data considered in this survey.

Correlation Approach

In this chapter, annular-cascade data are compared with the two-dimensional-cascade correlations of minimum-loss incidence angle, total-pressure loss, and deviation angle of chapter VI. In this way, compressor investigations serve as both a verification and an extension of the two-dimensional-cascade data. Two-dimensional-cascade data correlations and rules, in conjunction with correction factors deduced from the three-dimensional data, can then be used for compressor design and analysis.

With this approach in mind, all available single-stage data were collected, computed, and plotted in a form considered convenient for correlation. The blade and performance parameters used in the analysis are similar to those used in the two-dimensional-cascade correlations of chapter VI. Camber angle, incidence angle, and deviation angle (fig. 2) are used to define the blade camber, air approach, and air leaving directions, respectively. These angles are based on tangents to blade mean camber line at the leading and trailing edges. As in chapter VI, the NACA 65-(A₁₀)-series blades are considered in terms of the equivalent circular-arc camber line (figs. 3 and 4 of ch. VI, pp. 43-44).

Loss in total pressure across the blade element is expressed in terms of the loss parameter $\bar{\omega}' \cos \beta_2'/2\sigma$, where the relative total-pressure-loss coefficient $\bar{\omega}'$ is defined as the mass-averaged defect in

relative total pressure divided by the pressure equivalent of the inlet velocity head:

$$\bar{\omega}' = \frac{P'_{2,id} - P'_2}{P'_1 - p_1} \quad (1)$$

For stationary blade rows, or no change in streamline radius across the rotor, the numerator of equation (1) becomes the decrease in relative total pressure across the blade row from inlet to outlet. The relative total-pressure-loss coefficient was computed from stationary measurements of total pressure and total temperature and from the computed relative inlet Mach number according to reference 10. The total-pressure-loss parameter $\bar{\omega}' \cos \beta'_2/2\sigma$, as indicated in chapter VI, can be used as a significant parameter for correlating blade losses.

The diffusion factor, which is used as a blade-loading parameter, is defined in reference 10 for no change in radius as follows:

$$D = \left(1 - \frac{V'_2}{V'_1}\right) + \frac{V'_{\theta,1} - V'_{\theta,2}}{2\sigma V'_1} \quad (2)$$

A typical example of the plotted performance parameters for a rotor blade row is shown in figure 3. The data represent the variations of the flow at fixed rotational speed. Plots for stator blade rows show similar trends of variation. As in chapter VI, a reference point was established as the incidence angle for minimum loss (fig. 4(a)), and the blade-element flow was analyzed at this reference point. In cases where minimum-loss incidence was not clearly defined, the reference point was taken as the mean incidence of the incidence-angle range for which values of $\bar{\omega}$ at the end points are twice the minimum value (fig. 4(b)). In some instances, near the compressor tip the loss-against-incidence-angle curve increased continuously from a minimum value of loss parameter at the open-throttle point. In presenting data for these cases several points near the minimum-loss value are plotted.

One of the primary objectives of this analysis is to determine differences in blade-element performance with compressor radial position. Therefore, three radial positions along the blade span (near the hub, mean radius, and tip) of each blade row are considered. The radial positions at the hub and tip are approximately 10 to 15 percent of the passage height away from the inner and outer walls, respectively, which are outside the wall boundary-layer region in all cases. The analysis is directed toward correlating the loss and deviation-angle data at reference incidence angle and determining the variation of reference incidence angle with blade geometry and Mach number at the three radial positions.

Experimental Data Sources

There are three sources of three-dimensional-cascade blade-element data: stationary annular-cascade tunnel investigations, multistage-compressor investigations, and single-stage or single-blade-row compressor investigations. A relatively small amount of data has been accumulated from blade-row investigations conducted in stationary annular-cascade tunnels. Tunnels of this type have been used primarily for inlet-guide-vane investigations. Typical examples of annular-cascade tunnel investigations are reported in references 14 and 23. Numerous multistage-compressor investigations have been conducted both in this country and abroad. Unfortunately, the data obtained from these investigations are too limited to permit the construction of individual blade-row-element performance curves similar to those illustrated in figure 3.

The data used in this investigation were obtained primarily from investigations of single rotor rows or of single-stage compressors. A typical single-stage-compressor test installation is shown in figure 5. This particular compressor consists of a row of inlet guide vanes, a rotor blade row driven by a variable-speed motor, and a stator blade row. A discharge throttle is installed in the outlet system to vary the compressor back pressure. In this manner, the compressor mass-flow rate can be controlled. In an installation such as this, compressor performance over a range of speeds and mass flows can be obtained simply. In many cases, test rigs similar to figure 5 have been operated with only guide vanes and rotors or with rotors alone.

Many phases of compressor research have been conducted in single-stage-compressor test rigs; and, in reporting these phases, complete blade-element results are not usually presented. Therefore, it was necessary to collect available original data and rework them in terms of the parameters of the analysis. Since only NACA original data were available in blade-element form, the data analysis is based mainly on single-stage-compressor investigations conducted at the Lewis laboratory. The measurements taken and the instrumentation used vary somewhat from compressor to compressor; in most cases, however, it is possible from the available data to reconstruct complete experimental velocity diagrams and to determine the blade-element performance. Radial survey measurements were made after each blade row. Normally, total pressure, static pressure, total temperature, and air direction were measured. The pressure- and temperature-measuring devices were calibrated for the effect of Mach number.

Most of the compressor investigations that were adaptable to this analysis were conducted on NACA 65-(A₁₀)-series airfoil shapes and double-circular-arc airfoils. Therefore, the analysis is concerned solely with these airfoils. The 65-(A₁₀)-series airfoil has been used extensively in subsonic compressors; and the double-circular-arc airfoil, which is a relatively simple airfoil shape, has been used effectively in transonic compressors. Details of the characteristics of the various blade rows

used in this analysis are summarized in table I, and details of the instrumentation, calculation procedure, and accuracy of measurement are given in the listed references.

INCIDENCE-ANGLE ANALYSIS

Method of Correlation

In correlating blade-element reference-incidence-angle data, measured values of incidence angle are compared with values of reference incidence angle predicted for the geometry of the blade element according to the low-speed two-dimensional-cascade correlations of chapter VI. In chapter VI, the low-speed two-dimensional reference incidence angle is expressed in terms of the blade geometry as

$$i_{2-D} = K_i(i_o)_{10} + n\phi \quad (3)$$

where K_i is a function of blade thickness distribution and maximum-thickness ratio, $(i_o)_{10}$ is the zero-camber incidence angle for the 10-percent-thick airfoil section (function of air inlet angle β_1' and solidity σ), and n is equal to $[(i - i_o)/\phi]_{2-D}$ (also a function of β_1' and σ). Values of K_i , $(i_o)_{10}$, and n for the circular-arc and 65-(A₁₀)-series blade are repeated in figures 6 to 8 for convenience.

The comparisons between measured blade-element reference incidence angle i_C and predicted two-dimensional incidence angle i_{2-D} are expressed in terms of the difference $(i_C - i_{2-D})$. Thus, a value of zero of the difference parameter corresponds to an equivalence of the two incidence angles. In view of the established tendency of the reference incidence angle to increase somewhat with inlet Mach number (ch. VI), it was thought desirable to plot the variation of the difference parameter $(i_C - i_{2-D})$ against relative inlet Mach number for the three radial positions at hub, mean, and tip.

NACA 65-(A₁₀)-series blades. - The results of the comparison between compressor and two-dimensional-cascade reference incidence angles for the NACA 65-(A₁₀)-series blades are presented in figure 9 for hub-, mean-, and tip-radius regions. Both rotor and stator data are presented; the stator data being represented by the solid points. Different values of incidence angle for a given symbol represent different compressor tip speeds. As might be expected in a correlation of this type involving data from different test installations and instrumentations, the data are somewhat scattered, particularly in the hub and tip regions. It has

3390

CG-14 back

not been possible in these instances to evaluate the significance or origin of the scatter. (In compressor investigations, instrumentation inaccuracy generally contributes heavily to the data scatter, especially at hub and tip.) Nevertheless, the results of the comparison are indicative of the trends involved, and it is possible to make some general observations.

For the rotor mean-radius region, where three-dimensional disturbances are most likely a minimum, the rotor minimum-loss incidence angles are, on the average, about 1° smaller than the corresponding cascade-predicted values. This difference may be a reflection of some of the compressor influences discussed previously. The data also indicate that no essential variation of reference incidence angle with relative inlet Mach number exists up to values of M_1 of about 0.8. The 65-(A₁₀)-series blade, having a thick-nose profile, apparently exhibits the same approximate constancy of minimum-loss incidence angle with Mach number as indicated for the British thick-nose C-series profile in the cascade comparisons of chapter VI.

At the rotor tip, the compressor reference incidence angles are from 0° to 4° less than the predicted cascade values. As in the case of the rotor mean radius, no essential variation with inlet Mach number is observed in the range of data covered. The lower values of rotor reference incidence angle were generally the result of a change in the form of the variations of loss against incidence angle in the rotor, as illustrated in figure 10. The change in form may be explained on the basis of a probable increase in rotor tip three-dimensional losses (centrifuging of blade boundary layer, tip-clearance disturbances, etc.) with increasing incidence angle.

At the rotor hub, the situation is somewhat confused by the wide range of data. A tendency of the compressor incidence angles to be somewhat larger than the corresponding cascade values with an average value of about 1° or 2° is indicated.

For the stator mean-radius and hub regions, close agreement between compressor and cascade incidence angles is indicated for the range of Mach numbers covered (to about 0.7). Considerable scatter exists in the stator data at the compressor tip; therefore, no definite conclusions can be made concerning the variations of incidence angle.

Double-circular-arc blade. - The results of the double-circular-arc airfoil correlation are presented in figure 11, where compressor reference incidence angle minus low-speed-cascade-rule incidence angle (eq. (3)) is plotted against relative inlet Mach number for the hub, mean, and tip radial positions for both rotors and stators. The dashed curve represents the variation obtained with a 25° -camber double-circular-arc blade in high-speed two-dimensional cascade (ch. VI).

3390 It is immediately apparent that rotor reference incidence angle at all radial positions increases with increasing Mach number. The data indicate that the magnitude of the increase in reference incidence angle with Mach number is larger at the hub than at the tip. The hub data points in figure 11 were obtained from blade elements of relatively high camber. Both potential-flow and low-speed-cascade results indicate that this type of configuration is associated with a negative value of reference incidence angle. As inlet Mach number is increased, the increase in incidence angle in the positive direction must be fairly large in order to avoid high losses associated with blade-row choking. In contrast, at the compressor tip, since the blade cambers are generally lower (see table I), the low-speed incidence angle is higher and the required rate of change of incidence angle with increasing Mach number is not as large. Unfortunately, low Mach number data were not available to permit extrapolation of the rotor incidence-angle variations to zero Mach number (level of cascade correlation). However, it is believed that there will be very little change in the rotor incidence angle for values of Mach number below about 0.4 to 0.5. Extrapolated values of rotor reference incidence angle at zero Mach number appear to be of the order of 0.5° at the hub, 1.5° at the mean radius, and 2.5° at the tip below cascade-rule values.

The double-circular-arc blade element in the compressor rotor exhibits the same general incidence-angle characteristic with Mach number that was observed for sharp-nosed blade sections in the high-speed two-dimensional cascade (ch. VI). As indicated in chapter VI, the increase in reference incidence angle with Mach number is associated with the tendency of the range of the blade to be reduced only on the low-incidence side of the loss curve as Mach number is increased.

The rotor data for the double-circular-arc section, like those for the 65-(A₁₀)-series blades, are comparable to the cascade variations at the mean radius, somewhat higher at the hub at the higher Mach numbers, and noticeably lower at the tip. Apparently, the same type of three-dimensional phenomenon occurs at the tip for both blade shapes.

The available double-circular-arc stator data are too meager for any conclusions.

Summary Remarks

The variation of reference incidence angle for 65-(A₁₀)-series and double-circular-arc blade sections has been presented. No Mach number effect on reference incidence angle was observed for the 65-(A₁₀)-series blades for the range of Mach numbers considered. In contrast, the double-circular-arc blade sections exhibit a pronounced variation of reference incidence angle over the range of Mach number investigated. Significant

differences between the two-dimensional-cascade data and the rotor data were observed at the compressor tip. In contrast, at the mean radius and hub, the differences in two-dimensional-cascade data and rotor data were relatively small, even though the flow field was three-dimensional.

Additional data are required to determine the variation of stator reference incidence angle, particularly for the double-circular-arc airfoil sections. Also, no information has been presented concerning the allowable incidence-angle range for efficient (low-loss) operation and the variation of this range with inlet Mach number. Investigations of these phases of compressor research are very essential to fill gaps in the compressor design and analysis procedures and warrant attention in future research programs.

TOTAL-PRESSURE-LOSS ANALYSIS

Correlation of Data

For two-dimensional-cascade data obtained at low Mach numbers, the values of total-pressure-loss parameter $\bar{w} \cos \beta_2 / 2\sigma$ plotted against diffusion factor (eq. (2)) form essentially a single curve for all cascade configurations. The diffusion-factor correlation of loss parameter was applied to data obtained over a range of Mach numbers from single-stage axial-flow compressors of various geometries and design Mach numbers. Values of total-pressure-loss parameter calculated from single-stage-compressor data are plotted against diffusion factor for the hub, mean, and tip measuring stations in figure 12. Each symbol represents the value of diffusion factor and loss parameter at reference incidence angle at a given tip speed. Also plotted as a dashed curve is the corresponding correlation presented in chapter VI for the low-speed two-dimensional-cascade data. The data of figure 12, which were obtained from the rotor and stator configurations summarized in table I, represent both 65-(A₁₀)-series and circular-arc blade sections. The plots of figure 12 essentially represent an elaboration of the loss-diffusion correlations of reference 10.

The most important impression obtained from the rotor data plots is the wide scatter and increasing loss trend with diffusion factor at the rotor tip, while no discernible trend of variation is obtained at the rotor hub and mean radii. For the rotor hub and mean radii, it can be assumed that the rotor blade-element loss parameter follows the cascade variation but at a higher average magnitude. Unfortunately, the range of diffusion factor that could be covered in the compressor tests was not sufficient to determine whether a marked rise in loss is obtained for values of diffusion factor greater than about 0.6 (as in the cascade).

It is apparent from the loss trend and data scatter at the rotor tip that a different loss phenomenon is occurring in the tip region. It is recognized that a part of the scatter is due to the general instrumentation inaccuracy in the highly turbulent tip regions. In view of the usually large radial gradients of loss existing in the blade tip region, small variations in positioning radial survey probes can cause noticeable differences in the computed results. Nevertheless, it is obvious that factors other than the blade-element diffusion are influencing the tip loss. The specific three-dimensional factors or origins involved in the loss rise at the tip are not currently known. The principal conclusion reached from the plot is that the likelihood of a rising loss trend on the rotor tip exists for values of diffusion factor greater than about 0.35.

The stator losses at all radial positions in figure 12 appear to be somewhat higher than those of the two-dimensional cascade, particularly at the higher values of diffusion factor.

Summary Remarks

Rotor and stator blade-element loss data were correlated by means of the diffusion factor. The losses for stator and rotor blade elements at hub and mean radii were somewhat higher than those for the two-dimensional cascade over the range of diffusion factor investigated. At the rotor tip, the losses were considerably higher at values of diffusion factor above approximately 0.35.

The foregoing blade-element loss analysis is clearly incomplete. The need for additional work is indicated for such purposes as evaluating the origin and magnitude of the tip-region losses. The loading limits for rotors at other than the tip region and for stators at all blade elements have not been determined, because, for the available data, the diffusion factors at reference incidence do not extend to sufficiently high values. Single-stage investigations are needed over the critical range of Reynolds number to determine the effect of Reynolds number on the blade-element loss. It is desirable to isolate the effects of velocity diffusion and shock waves on the loss at high Mach number operation. The loss correlations presented should also be extended so that the data are applicable over a range of incidence angle. This would be of extreme value in the compressor analysis problem.

DEVIATION-ANGLE ANALYSIS

In addition to design information concerning blade-element losses and incidence angle, it is, of course, desirable to have a rather complete picture of the air deviation-angle characteristics of axial-flow-compressor blade elements. Therefore, the two-dimensional-cascade correlation results are reviewed and supplemented with annular-cascade data in this section.

Method of Correlation

As in the analysis of reference incidence angle, the correlation of blade-element deviation angle at reference incidence is presented in terms of a comparison between measured blade-element deviation angle and deviation angle predicted for the element according to the low-speed two-dimensional-cascade correlations of chapter VI. In chapter VI, the low-speed two-dimensional-cascade deviation angle at reference incidence angle is expressed in terms of blade geometry as

$$\delta_{2-D}^0 = K_\delta (\delta_0^0)_{10} + \frac{m}{\sigma^b} \phi \quad (4)$$

where K_δ is a function of maximum-thickness-to-chord ratio and thickness distribution, $(\delta_0^0)_{10}$ is the zero-camber deviation angle for the 10-percent-thick airfoil section (function of β_1' and σ), m is a function of β_1' for the different basic camber distributions, and b is an exponent that is also a function of β_1' .

As was shown previously, the reference incidence angle of the compressor blade element may differ somewhat from the corresponding two-dimensional reference incidence angle. Inasmuch as deviation angle will vary with changing reference incidence angle for a given blade geometry (depending on solidity), the two-dimensional deviation angles were corrected to the reference incidence angles of the compressor blade elements. The corrected deviation angle, as suggested in chapter VI, is given by

$$\delta_{2-D}^0 = K_\delta (\delta_0^0)_{10} + \frac{m}{\sigma^b} \phi + (i_C - i_{2-D}) \left(\frac{d\delta^0}{di} \right)_{2-D} \quad (5)$$

where $(d\delta^0/di)_{2-D}$ is the slope of the two-dimensional variation of deviation angle with incidence angle at reference incidence. Values of K_δ , $(\delta_0^0)_{10}$, m , b , and $(d\delta^0/di)_{2-D}$ for the circular-arc and 65-(A₁₀)-series blade are repeated in figures 13 to 17 for convenience.

Deviation-angle comparisons for the double-circular-arc blade were also made on the basis of Carter's rule for cascade blades (ref. 24):

$$\delta_{2-D}^0 = \frac{m_c}{\sigma^{0.5}} \phi \quad (6)$$

where m_c is a factor that is a function of blade-chord angle (fig. 18).

Carter's rule, which has been used extensively in the design of circular-arc blades, was used as the basis for the more elaborate rule of equation (4). In the calculations, Carter's rule was applied directly to the compressor reference incidence angles.

The comparisons between measured blade-element reference deviation angle δ_C^0 and predicted two-dimensional deviation angle δ_{2-D}^0 are expressed in terms of the difference parameter $(\delta_C^0 - \delta_{2-D}^0)$ against relative inlet Mach number for the three radial positions at hub, tip, and mean radius.

NACA 65-(A₁₀)-series blades. - Curves of compressor deviation angle minus cascade-rule deviation angle (eq. (5)) for the 65-(A₁₀)-series airfoil for both rotors and stators are plotted against relative inlet Mach number for the hub, mean, and tip radial positions in figure 19(a). All values of deviation angle correspond to those at compressor reference incidence angle. As in the case of the incidence-angle and loss correlations, there is considerable scatter of data, particularly in the hub and tip regions. Some of the scatter is believed due to the effects of three-dimensional flows and changes in axial velocity ratio across the element, but perhaps the most important factors are instrumentation differences and errors. It is generally recognized that it is difficult to measure compressor air angles with an accuracy better than about $\pm 1^\circ$ to 1.5° . The correlations must therefore be evaluated on an average or trend basis.

The correlation of rotor data in the mean-radius region is fairly good; axial velocity ratio varied between about 0.9 to 1.10. On the average, the rotor mean-radius deviation angles are about 0.5° less than the cascade values. These results agree with previous experience (refs. 4 and 5), which indicated rotor turning angles approximately 1° greater (i.e., deviation angles 1° less) than the two-dimensional-cascade results. If data points for the rotor tip having axial velocity ratios less than 0.8 are neglected, the average deviation angle is about 0.5° less than the cascade value. Axial velocity ratio for the tip-region unflagged data varied between 0.8 and 1.05. For the hub, on the average, the blade-element deviation angles were about 1.0° greater than the corresponding two-dimensional values. Hub axial velocity ratios varied between 1.0 and 1.3. As in the two-dimensional cascade (ch. VI), no Mach number effect on deviation angle is indicated over the range of Mach number investigated for all three regions.

For the stator mean-radius ($V_{z,2}/V_{z,1} = 1.0$ to 1.1) and hub-radius ($V_{z,2}/V_{z,1} = 0.85$ to 1.05) regions, the average deviation angles are both about 1.0° lower than the corresponding two-dimensional values. At the stator tip, the average blade-element value is indicated to be about 4° less than the two-dimensional value. However, these data all have high

axial velocity ratios (from 1.1 to 1.5). It is expected that, on the basis of constant axial velocity, the probable average blade-element deviation angles at the stator tip might be several degrees closer to the two-dimensional values. (Increasing axial velocity ratio at essentially constant circulation for the stator tends to decrease deviation angle.) As in the case of the rotor, no essential variation of deviation angle with Mach number is detected for the stator within the range of Mach numbers investigated.

Double-circular-arc blade. - Blade-element and two-dimensional-cascade deviation angles (eq. (5)) obtained for the double-circular-arc blade are compared in figure 19(b). The scatter of data is generally less than for the 65-(A₁₀)-series blades, partly because of the generally more accurate measurements taken in these investigations (all are more recent than the data of fig. 19(a)).

On the average, at the lower Mach numbers the blade-element deviation angles were about 1.5° less than the two-dimensional values at the tip, 1.0° greater at the hub, and equal to the two-dimensional values at the mean region. Ranges of axial velocity ratio covered for the data were 0.85 to 1.05 at the tip, 0.95 to 1.5 at the hub, and 0.90 to 1.15 at the mean radius. A slightly increasing trend of variation with inlet Mach number may be indicated at the mean radius and possibly also at the hub.

The double-circular-arc stator data available (solid symbols) are too limited to permit any reliable conclusions to be drawn. It appears, however, that at the stator mean radius, the blade-element deviation angles may be about 0.5° less than the two-dimensional-cascade values. This is essentially the same trend observed for the 65-(A₁₀)-series stators at mean radius in figure 19(a). Blade-element deviation angles appear to be greater at the tip and smaller at the hub than the two-dimensional values. Ranges of axial velocity ratio were 1.0 to 1.25 at the tip, 0.95 to 1.27 at the mean radius, and 0.9 to 1.30 at the hub.

Blade-element deviation angles and two-dimensional values predicted by Carter's rule (eq. (6)) are compared in figure 20. Inasmuch as Carter's rule results in values of two-dimensional deviation angle between 0.5° to 1.0° smaller than obtained from the modified rule of equation (5) for the range of blade-element geometries included in the data, the agreement with the blade-element data remains quite good.

Summary Remarks

From the comparisons of measured and predicted reference deviation angles for the NACA 65-(A₁₀)-series and double-circular-arc blades, it was found that the rules derived from two-dimensional-cascade data can

satisfactorily predict the compressor reference blade-element deviation angle in the rotor and stator mean-radius regions for the blade configurations presented. Larger differences between rule and measured values were observed in the hub and tip regions. These differences can be attributed to the effects of three-dimensional flow, differences in axial velocity ratio, and measurement inaccuracy. As in the cascade, essentially constant deviation angle with Mach number was indicated for the Mach number range covered. Additional stator blade-element data, particularly for the double-circular-arc blade, are required to establish the stator correlations more firmly.

APPLICATION TO DESIGN

Design Procedure

The foregoing correlations provide a means of establishing the reference incidence angle and estimating the corresponding deviation angle and total-pressure loss for rotor and stator blade elements of compressor designs similar to those covered in the analysis. This is accomplished by establishing deduced curves of compressor blade-element incidence-angle and deviation-angle corrections for the low-speed two-dimensional-cascade rules of chapter VI. Reference incidence and deviation angles for the compressor blade element are then given by

$$i_C = i_{2-D} + (i_C - i_{2-D}) \quad (7)$$

and

$$\delta_C^0 = \delta_{2-D}^0 + (\delta_C^0 - \delta_{2-D}^0) \quad (8)$$

where i_{2-D} and δ_{2-D}^0 are given by equations (3) and by (5) or (6), respectively. Curves of incidence-angle and deviation-angle corrections deduced from the rotor blade-element data of figures 9, 11, 19, and 20 are shown as functions of relative inlet Mach number for several radial positions along the blade height in figures 21 and 22. The curves in figures 21 and 22 are faired average values of the data spread and, strictly speaking, represent bands of values. In view of the very limited data available, compressor correction curves could not reliably be established for the stator deviation and incidence angles.

Establishing single deduced blade-element loss curves at reference incidence angle is a difficult task because of the scatter of the experimental data, especially in the rotor tip region. Nevertheless, for completeness in order to illustrate the prediction procedures, curves of average total-pressure-loss parameter as a function of diffusion parameter

3390

CG-15 part

obtained from the data of figure 12 are shown in figure 23 for rotor and stator. The shaded portion in the figure indicates the possible band of values obtainable at the rotor tip.

The procedure involved in determining blade-element camber angle and efficiency at reference incidence angle for a compressor design based on the blade-row velocity diagram and the foregoing correlation curves is now indicated. The desired blade-element turning angle $(\beta'_1 - \beta'_2)$ and relative inlet Mach number M'_1 are obtained from the design velocity diagram. Camber and turning angles are related by the equation

$$\phi = \beta'_1 - \beta'_2 + \delta^0 - i \quad (9)$$

Compressor blade-element incidence (eqs. (3) and (7)) and deviation (eqs. (5) and (8)) angles are given by

$$i_C = K_i(i_o)_{10} + n\phi + (i_C - i_{2-D}) \quad (10)$$

$$\delta_C^0 = K_\delta(\delta_o^0)_{10} + \frac{m}{\sigma b} \phi + (i_C - i_{2-D}) \left(\frac{d\delta^0}{di} \right)_{2-D} + (\delta_C^0 - \delta_{2-D}^0) \quad (11)$$

Substitution of equations (10) and (11) into equation (9) and rearrangement of terms yield:

$$\phi = \frac{(\beta'_1 - \beta'_2) + (\delta_C^0 - \delta_{2-D}^0) - (i_C - i_{2-D}) \left[1.0 - \left(\frac{d\delta^0}{di} \right)_{2-D} \right] - K_i(i_o)_{10} + K_\delta(\delta_o^0)_{10}}{1 - \frac{m}{\sigma b} + n} \quad (12)$$

All terms on the right side of equation (12) can be determined from the velocity-diagram properties, the specified blade shape and thickness, and the specified solidity. After the camber angle is determined, the incidence and deviation angles can be calculated from equations (10) and (11). Rotor blade-element loss parameter is estimated from the velocity-diagram diffusion factor and the curves of figure 12. The total-pressure-loss coefficient $\bar{\omega}'$ is then readily obtained from the blade-element solidity and relative air outlet angle. Blade-element efficiencies for the rotor and complete stage can be computed by means of the techniques and equations presented in the appendix. If the change in radius across the blade row can be assumed small, blade-element efficiency can be determined through the use of figures 24 to 26 from the selected values of $\bar{\omega}'$ and the values of M'_1 and absolute total-pressure ratio or total-temperature ratio obtained from the velocity diagram.

The foregoing procedure can best be illustrated by a numerical example. Suppose the following specified rotor design values represent typical values at 10 percent of the passage height from the compressor tip:

$$\left. \begin{array}{l} \beta_1' = 56.9^\circ \\ \beta_1' - \beta_2' = 10.9^\circ \\ M_1' = 1.1 \\ D = 0.35 \\ \frac{T_2}{T_1} = 1.091 \end{array} \right\} \begin{array}{l} \text{obtained from velocity-diagram} \\ \text{calculations (ch. VIII)} \end{array}$$

$$\left. \begin{array}{l} \sigma = 1.0 \\ t/c = 0.06 \end{array} \right\} \text{assumed values}$$

The problem is to find the camber, incidence, and deviation angles and the total-pressure-loss coefficient for a double-circular-arc airfoil section that will establish the velocity-diagram values.

(1) From the value of M_1' and figures 21(b) and 22(b),

$$i_C - i_{2-D} = 4.0^\circ \quad \delta_C^\circ - \delta_{2-D}^\circ = -1.5^\circ$$

(2) From the values of β_1' , σ , and t/c and figures 6 to 8 and 13 to 17,

$$K_i = 0.54 \quad (i_o)_{10} = 4.4^\circ \quad n = -0.22 \quad K_\delta = 0.37$$

$$(\delta_o^\circ)_{10} = 1.6^\circ \quad m = 0.305 \quad b = 0.714 \quad \left(\frac{d\delta^\circ}{di} \right)_{2-D} = 0.095$$

(3) When the values of steps (1) and (2) are substituted in equation (12), the value of blade camber $\varphi = 8.4^\circ$.

(4) From equations (10) and (11), $i_C = 4.5$ and $\delta_C^\circ = 2.0$.

(5) For calculation of the total-pressure-loss coefficient, the diffusion factor (0.35) and figure 23(a) yield a value of (0.025) for the loss parameter $(\bar{\omega}' \cos \beta_2')/2\sigma$, and

$$\beta_2' = \beta_1' - (\beta_1' - \beta_2') = 56.9 - 10.9 = 46.0^\circ$$

$$\cos \beta_2' = 0.6947$$

Therefore,

$$\bar{\omega}' = \left(\frac{\bar{\omega}' \cos \beta_2'}{2\sigma} \right) \frac{2\sigma}{\cos \beta_2'} = \frac{0.025 \times 2}{0.6947} = 0.072$$

(6) For a negligible change in radius across the blade element, the following values can be found from figures 24 and 25:

$$\frac{P_2'}{P_1'} = 0.962 \quad \eta_{ad} = 0.87 \quad \frac{P_2}{P_1} = 1.31$$

The preceding example has been carried out for a typical transonic rotor blade section. A similar procedure can be used for stator blade sections when adequate blade-element data become available.

Summary Remarks

The foregoing procedures and data apply only to the reference point (i.e., the point of minimum loss) on the general loss-against-incidence-angle variation for a given blade element. The reference minimum-loss incidence angle, which was established primarily for purposes of analysis, is not necessarily to be considered as a recommended design point for compressor application. The selection of the best incidence angle for a particular blade element in a multistage-compressor design is a function of many considerations, such as the location of the blade row, the design Mach number, and the type and application of the design. However, at transonic inlet Mach number levels, the point of minimum loss may very well constitute a desired design setting.

At any rate, the establishment of flow angles and blade geometry at the reference incidence angle can serve as an anchor point for the determination of conditions at other incidence-angle settings. For deviation-angle and loss variations over the complete range of incidence angles, reference can be made to available cascade data. Such low-speed cascade data exist for the NACA 65-(A₁₀)-series blades (ref. 25).

3390 It is recognized that many qualifications and limitations exist in the use of the foregoing design procedure and correlation data. For best results, the application of the deduced variations should be restricted to the range of blade geometries (camber, solidity, etc.) and flow conditions (inlet Mach number, Reynolds number, axial velocity ratio, etc.) considered in the analysis. In some cases for compressor designs with very low turning angle, the calculated camber angle may be negative. For these cases it is recommended that a zero-camber blade section be chosen and the incidence angle selected to satisfy the turning-angle requirements. The data used in the analysis were obtained for the most part from typical experimental inlet stages with essentially uniform inlet flow. Nevertheless, such data have been used successfully in the design of the latter stages of multistage compressors. It should also be remembered that the single curves appearing in the deduced variations represent essentially average or representative values of the experimental data spread. Also, in some cases, particularly for the stator, the available data are rather limited to establish reliable correlations. Considerable work must yet be done to place the design curves on a firmer and wider basis. The design procedures established and trends of variation determined from the data, however, should prove useful in compressor blade-element design.

APPENDIX

EQUATIONS FOR BLADE-ELEMENT EFFICIENCY

By definition, for a complete stage consisting of inlet guide vanes, rotor, and stator, the adiabatic temperature-rise efficiency of the flow along a stream surface is given by

$$\eta_{ad,ST} = \frac{\left(\frac{P_2}{P_1}\right)_{ST}^{\frac{\gamma-1}{\gamma}} - 1}{\left(\frac{T_2}{T_1}\right)_{ST} - 1} = \frac{\left[\left(\frac{P_2}{P_1}\right)_{GV} \left(\frac{P_2}{P_1}\right)_R \left(\frac{P_2}{P_1}\right)_S\right]^{\frac{\gamma-1}{\gamma}} - 1}{\left(\frac{T_2}{T_1}\right)_R - 1} \quad (A1)$$

From the developments of reference 26 (eq. (B8) in the reference), the absolute total-pressure ratio across a blade row P_2/P_1 can be related to the relative total-pressure ratio across the blade row P'_2/P'_1 according to the relation

$$\frac{P_2}{P_1} = \frac{\left(\frac{P'_2}{P'_1}\right)}{\left(\frac{P'_2}{P'_1}\right)_{id}} \left(\frac{T_2}{T_1}\right)^{\frac{\gamma}{\gamma-1}} \quad (A2)$$

where $(P'_2/P'_1)_{id}$ is the ideal (no loss) relative total-pressure ratio.

The relative total pressure is also referred to as the blade-row recovery factor. For stationary blade rows, (i.e., inlet guide vanes and stators), $(P'_2/P'_1)_{id}$ is equal to 1.0. For rotors, the ideal relative total-pressure ratio (eq. (B4) of ref. 10) is given by

$$\left(\frac{P'_2}{P'_1}\right)_{id} = \left\{ 1 + \frac{\gamma-1}{2} M_T^2 \left[1 - \left(\frac{r_1}{r_2}\right)^2 \right] \right\}^{\frac{\gamma}{\gamma-1}} \quad (A3)$$

in which M_T is equal to the ratio of the outlet element wheel speed to the inlet relative stagnation velocity of sound ($\omega r_2/a'_{a,1}$), and (r_1/r_2)

is the ratio of inlet to outlet radius of the streamline across the blade element. (For a flow at constant radius (cylindrical flow), $(P_2'/P_1')_{id}$ is equal to 1.0.) Thus, from equations (A1) and (A2),

$$\eta_{ad,ST} = \frac{\left[\left(\frac{P_2'}{P_1'} \right)_{GV} \frac{\left(\frac{P_2'}{P_1'} \right)_R}{\left(\frac{P_2'}{P_1'} \right)_{R,id}} - \left(\frac{T_2}{T_1} \right)_R^{\frac{\gamma}{\gamma-1}} \left(\frac{P_2'}{P_1'} \right)_S \right]^{\frac{\gamma-1}{\gamma}} - 1}{\left(\frac{T_2}{T_1} \right)_R - 1} \quad (A4)$$

For the rotor alone, the blade-element efficiency is given by

$$\eta_{ad,R} = \frac{\left[\frac{\left(\frac{P_2'}{P_1'} \right)_R}{\left(\frac{P_2'}{P_1'} \right)_{R,id}} \left(\frac{T_2}{T_1} \right)^{\frac{\gamma}{\gamma-1}} \right]^{\frac{\gamma-1}{\gamma}} - 1}{\left(\frac{T_2}{T_1} \right)_R - 1} \quad (A5)$$

From equation (B3) of reference 10, the loss coefficient of the rotating blade row (based on inlet dynamic pressure) is given by

$$\bar{\omega}' = \left(\frac{P_2'}{P_1'} \right)_{id} \left\{ \frac{1 - \frac{\left(\frac{P_2'}{P_1'} \right)}{\left(\frac{P_2'}{P_1'} \right)_{id}}}{1 - \left[\frac{1}{1 + \frac{\gamma-1}{2} (M_1')^2} \right]^{\frac{\gamma}{\gamma-1}}} \right\} \quad (A6)$$

For any blade element, then, from equation (A6),

$$\frac{P_2'}{P_1'} = \left(\frac{P_2'}{P_1'} \right)_{id} - \bar{\omega}' \left\{ 1 - \left[\frac{1}{1 + \frac{\gamma-1}{2} (M_1')^2} \right]^{\frac{\gamma}{\gamma-1}} \right\} \quad (A7)$$

The relations presented in equations (A4), (A5), and (A7) indicate that four quantities are required for the determination of the blade-element efficiency across the rotor or stage: the rotor absolute total-temperature ratio, the relative total-pressure-loss coefficient (based on inlet dynamic pressure), the relative inlet Mach number, and the ideal relative total-pressure ratio. Thus, the blade-element efficiencies for a given stage velocity diagram can be calculated if the loss coefficients of the blade elements in the various blade rows can be estimated.

For simplicity in the efficiency-estimation procedure, effects of changes in radius across the blade row can be assumed small (i.e., $r_1 = r_2$), so that the ideal relative pressure ratio is equal to unity. Then, equations (A4), (A5), and (A7) become, respectively,

$$\eta_{ad,ST} = \frac{\left[\left(\frac{P_2'}{P_1'} \right)_{GV} \left(\frac{P_2'}{P_1'} \right)_R \left(\frac{T_2}{T_1} \right)_R^{\frac{\gamma}{\gamma-1}} \left(\frac{P_2'}{P_1'} \right)_S \right]^{\frac{\gamma-1}{\gamma}} - 1}{\left(\frac{T_2}{T_1} \right)_R - 1} \quad (A8)$$

$$\eta_{ad,R} = \frac{\left[\left(\frac{P_2'}{P_1'} \right)_R \left(\frac{T_2}{T_1} \right)_R^{\frac{\gamma}{\gamma-1}} \right]^{\frac{\gamma-1}{\gamma}} - 1}{\left(\frac{T_2}{T_1} \right)_R - 1} \quad (A9)$$

and

$$\frac{P'_2}{P'_1} = 1 - \bar{\omega}' \left\{ 1 - \left[\frac{1}{1 + \frac{\gamma-1}{2} (M'_1)^2} \right]^{\frac{\gamma}{\gamma-1}} \right\} \quad (A10)$$

For purposes of rapid calculation and preliminary estimates, the efficiency relations are expressed in chart form in figures 24 to 26. The relation among relative recovery factor, blade-element loss coefficient, and inlet Mach number (eq. (A10)) is presented in figure 24. A chart for determining rotor blade-element efficiency from relative recovery factor and absolute total-temperature ratio (eq. (A9)) is given in figure 25. Lines of constant rotor absolute total-pressure ratio are also included in the figure. Figure 26 presents the ratio of stage efficiency to rotor efficiency for various stator or guide-vane recovery factors. The ratio of stage efficiency to rotor efficiency is obtained from equation (A1) in terms of rotor absolute total-pressure ratio as

$$\frac{\eta_{ad,ST}}{\eta_{ad,R}} = \frac{\left[\left(\frac{P_2}{P_1} \right)_R \left(\frac{P_2}{P_1} \right)_{GV} \left(\frac{P_2}{P_1} \right)_S \right]^{\frac{\gamma-1}{\gamma}} - 1}{\left(\frac{P_2}{P_1} \right)_R^{\frac{\gamma-1}{\gamma}} - 1} \quad (A11)$$

The charts are used as follows: For known or estimated values of rotor total-pressure-loss coefficient $\bar{\omega}'$ and relative inlet Mach number M'_1 of the element, the corresponding value of relative recovery factor P'_2/P'_1 is determined from figure 24. From the value of rotor-element absolute total-temperature ratio T_2/T_1 (obtained from calculations of the design velocity diagram) and the value of (P'_2/P'_1) obtained from figure 24, the rotor-element efficiency is determined from figure 25. Rotor absolute total-pressure ratio can also be determined from the dashed lines in figure 25.

If inlet guide vanes and stators are present, the respective recovery factors of each blade row are first obtained from figure 24. The product of the two recovery factors is then calculated and used in conjunction with the rotor absolute total-pressure ratio in figure 26 to determine the ratio of stage efficiency to rotor efficiency. A simple multiplication then yields the magnitude of the stage efficiency along the element stream surface.

227

CG-16 back

The charts can also be used to determine gross or mass-averaged efficiencies through the use of over-all loss terms. Furthermore, the charts can be used for the rapid determination of relative total-pressure-loss coefficient from known values of efficiency, pressure ratio, and inlet Mach number on an element or gross basis.

REFERENCES

1. Compressor and Turbine Research Division: Aerodynamic Design of Axial-Flow Compressors. Vol. I. NACA RM E56B03, 1956.
2. Bowen, John T., Sabersky, Rolf H., and Rannie, W. Duncan: Theoretical and Experimental Investigations of Axial Flow Compressors, Pt. 2. Mech. Eng. Lab., C.I.T., July 1949. (Navy Contract N6-ORI-102, Task Order IV.)
3. Alsworth, Charles C., and Iura, Toru: Theoretical and Experimental Investigations of Axial Flow Compressors. Pt. 3 - Progress Report on Loss Measurements in Vortex Blading. Mech. Eng. Lab., C.I.T., July 1951. (Navy Contract N6-ORI-102, Task Order IV.)
4. Schulze, Wallace M., Erwin, John R., and Ashby, George C., Jr.: NACA 65-Series Compressor Rotor Performance with Varying Annulus-Area Ratio, Solidity, Blade Angle, and Reynolds Number and Comparison with Cascade Results. NACA RM L52L17, 1953.
5. Ashby, George C., Jr.: Comparison of Low-Speed Rotor and Cascade Performance for Medium-Camber NACA 65- $(C_{l_0} A_{l_0})_{10}$ Compressor-Blade Sections over a Wide Range of Rotor Blade-Setting Angles at Solidities of 1.0 and 0.5. NACA RM L54I13, 1954.
6. Andrews, S. J., and Ogden, H.: A Detailed Experimental Comparison of Blades Designed for Free Vortex Flow and Equivalent Untwisted Constant Section Blades. Rep. No. R.123, British N.G.T.E., Aug. 1952.
7. Lieblein, Seymour: Review of High-Performance Axial-Flow-Compressor Blade-Element Theory. NACA RM E53L22, 1954.
8. Savage, Melvyn, Erwin, John R., and Whitley, Robert P.: Investigation of an Axial-Flow Compressor Rotor Having NACA High-Speed Blade Sections (A_2I_{8b} Series) at Mean Radius Relative Inlet Mach Numbers Up to 1.13. NACA RM L53G02, 1953.

330

9. Schwenk, Francis C., Lieblein, Seymour, and Lewis, George W., Jr.: Experimental Investigation of an Axial-Flow Compressor Inlet Stage Operating at Transonic Relative Inlet Mach Numbers. III - Blade-Row Performance of Stage with Transonic Rotor and Subsonic Stator at Corrected Tip Speeds of 800 and 1000 Feet Per Second. NACA RM E53G17, 1953.
10. Lieblein, Seymour, Schwenk, Francis C., and Broderick, Robert L.: Diffusion Factor for Estimating Losses and Limiting Blade Loadings in Axial-Flow-Compressor Blade Elements. NACA RM E53D01, 1953.
11. Savage, Melvyn: Analysis of Aerodynamic Blade-Loading-Limit Parameters for NACA 65-(C_l₀A₁₀)10 Compressor-Blade Sections at Low Speeds. NACA RM L54L02a, 1955.
12. Moses, Jason J., and Serovy, George K.: Effect of Blade-Surface Finish on Performance of a Single-Stage Axial-Flow Compressor. NACA RM E51C09, 1951.
13. Moses, J. J., and Serovy, G. K.: Some Effects of Blade Trailing-Edge Thickness on Performance of a Single-Stage Axial-Flow Compressor. NACA RM E51F28, 1951.
14. Thurston, Sidney, and Brunk, Ralph E.: Performance of a Cascade in an Annular Vortex-Generating Tunnel over a Range of Reynolds Numbers. NACA RM E51G30, 1951.
15. Wallner, Lewis E., and Fleming, William A.: Reynolds Number Effect on Axial-Flow Compressor Performance. NACA RM E9G11, 1949.
16. Mühlemann, E. (John Perl, trans.): Experimental Investigations on an Axial Blower Stage. Lockheed Aircraft Corp., Burbank (Calif.).
17. Dugan, Paul D., Mahoney, John J., and Benser, William A.: Effect of Mach Number on Performance of an Axial-Flow Compressor Rotor-Blade Row. NACA RM E8D29, 1948.
18. Voit, Charles H., Guentert, Donald C., and Dugan, James F.: Effect of Mach Number on Over-All Performance of Single-Stage Axial-Flow Compressor Designed for High Pressure Ratio. NACA RM E50D26, 1950.
19. Robbins, William H., and Glaser, Frederick W.: Investigation of an Axial-Flow-Compressor Rotor with Circular-Arc Blades Operating Up to a Rotor-Inlet Relative Mach Number of 1.22. NACA RM E53D24, 1953.

20. Compressor and Turbine Research Division: Aerodynamic Design of Axial-Flow Compressors. Vol. III. NACA RM E56B03b, 1956.
21. Lieblein, Seymour, and Ackley, Richard H.: Secondary Flows in Annular Cascades and Effects on Flow in Inlet Guide Vanes. NACA RM E51G27, 1951.
22. Erwin, John R., and Emery, James C.: Effect of Tunnel Configuration and Testing Technique on Cascade Performance. NACA Rep. 1016, 1951. (Supersedes NACA TN 2028.)
23. Mankuta, Harry, and Guentert, Donald C.: Some Effects of Solidity on Turning through Constant-Thickness Circular-Arc Guide Vanes in Axial Annular Flow. NACA RM E51E07, 1951.
24. Carter, A. D. S., and Hughes, Hazel P.: A Theoretical Investigation into the Effect of Profile Shape on the Performance of Aerofoils in Cascade. R. & M. No. 2384, British A.R.C., Mar. 1946.
25. Felix, A. Richard: Summary of 65-Series Compressor-Blade Low-Speed Cascade Data by Use of the Carpet-Plotting Technique. NACA RM L54H18a, 1954.
26. Howell, A. R.: Design of Axial Compressors. War Emergency Issue No. 12 pub. by Inst. Mech. Eng. (London), 1945. (Reprinted in U. S. by A.S.M.E., Jan. 1947, pp. 452-462.)
27. Jackson, Robert J.: Effects on the Weight-Flow Range and Efficiency of a Typical Axial-Flow Compressor Inlet Stage That Result from the Use of a Decreased Blade Camber or Decreased Guide-Vane Turning. NACA RM E52G02, 1952.
28. Jackson, Robert J.: Analysis of Performance of Four Symmetrical-Diagram-Type Subsonic Inlet-Stage Axial-Flow Compressors. NACA RM E53K03, 1954.
29. Mahoney, John J., Dugan, Paul D., Budinger, Raymond E., and Goelzer, H. Fred: Investigation of Blade-Row Flow Distributions in Axial-Flow-Compressor Stage Consisting of Guide Vanes and Rotor-Blade Row. NACA RM E50G12, 1950.
30. Standahar, Raymond M., and Serovy, George K.: Some Effects of Changing Solidity by Varying the Number of Blades on Performance of an Axial-Flow Compressor Stage. NACA RM E52A31, 1952.

- 3390
31. Serovy, George K., Robbins, William H., and Glaser, Frederick W.: Experimental Investigation of a 0.4 Hub-Tip Diameter Ratio Axial-Flow Compressor Inlet Stage at Transonic Inlet Relative Mach Numbers. I - Rotor Design and Over-All Performance at Tip Speeds from 60 to 100 Percent of Design. NACA RM E53I11, 1953.
 32. Tysl, Edward R., Schwenk, Francis C., and Watkins, Thomas B.: Experimental Investigation of a Transonic Compressor Rotor with a 1.5-Inch Chord Length and an Aspect Ratio of 3.0. I - Design, Over-All Performance, and Rotating-Stall Characteristics. NACA RM E54L31, 1955.
 33. Lewis, George W., Jr., Schwenk, Francis C., and Serovy, George K.: Experimental Investigation of a Transonic Axial-Flow-Compressor Rotor with Double-Circular-Arc Airfoil Blade Sections. I - Design, Over-All Performance, and Stall Characteristics. NACA RM E53L21a, 1954.
 34. Sandercock, Donald M., Lieblein, Seymour, and Schwenk, Francis C.: Experimental Investigation of an Axial-Flow Compressor Inlet Stage Operating at Transonic Relative Inlet Mach Numbers. IV - Stage and Blade-Row Performance of Stage with Axial-Discharge Stators. NACA RM E54C26, 1954.

TABLE I. - DETAILS OF SINGLE-STAGE ROTORS AND STATORS

Blade row	Description	Outer diameter, in.	Hub-tip ratio	Rotor tip speed, ft/sec	Inlet Mach number, M_1	Camber angle, ϕ , deg		Chord, c, in.		Solidity, σ		Blade-chord angle, γ° , deg		Blade maximum thickness-chord ratio, t/c		Reference
						Hub	Tip	Hub	Tip	Hub	Tip	Hub	Tip	Hub	Tip	
65-Series blade section																
1	Rotor	14	0.5	552,828,994 1104,1214	0.30-0.75	19.9	15.3	1.31	1.31	1.010	0.590	30.8	56.4	10	10	27
2	Stator	14	.55	552,1104	.26- .73	30.1	30.1	1.31	1.31	.996	.620	19.5	45.9	10	10	28
3	Rotor	30	.80	504,672,840	.36- .70	30.1	30.1	2.90	2.90	1.08	.906	28.8	45.9	10	10	29
4	Rotor	14	.50	1104,1214	.60- .80	30.1	30.1	1.31	1.31	1.010	.590	21.1	56.0	10	10	28
5	Rotor	14	.50	557,743	.39- .72	30.1	30.1	1.31	1.31	.962	.608	15.2	32.0	10	10	28
6	Stator	14	.52	371,557,743	.22- .66	30.1	30.1	1.31	1.31	.993	.631	16.2	32.2	10	10	28
7	Rotor	14	.50	546	.35- .56	40.0	23.9	1.31	1.31	.955	.600	21.0	58.0	10	10	27
8	Rotor	14	.50	552,828,1104	.30- .86	40.0	23.9	1.31	1.31	.955	.600	21.0	58.0	10	10	27
9	Rotor	14	.50	552,828,1104 1214	.30- .76	40.0	23.9	1.31	1.31	.955	.600	21.0	58.0	10	10	27
10	Stator	14	.53	412,617,823	.25- .74	30.1	30.1	1.31	1.31	.970	.587	15.1	39.6	10	10	28
11	Rotor	14	.80	669,753,836	.52- .75	45.2	34.1	1.35	1.35	.823	.692	21.4	35.4	6	6	30
12	Rotor	14	.80	669,753,836	.49- .75	45.2	34.1	1.35	1.35	1.12	.943	21.4	35.4	6	6	30
13	Rotor	14	.80	669,753,836	.49- .75	45.2	34.1	1.35	1.35	1.69	1.35	21.4	35.4	6	6	30
14	Rotor	14	.80	600,736,874	.50- .92	30.3	19.4	1.46	1.82	1.20	1.20	42.5	48.8	10	8	13
Circular-arc blade section																
15	Rotor	14	0.4	600,800,1000 1050	0.33-1.06	40.3	11.4	2.00	2.00	1.778	0.963	12.1	46.7	8	5	31
16	Rotor	18	.5	600,700,800 900,1000	.38-1.07	28.3	7	1.5	1.5	1.63	1.03	23.6	46.3	10	6	32
17	Rotor	14	.5	600,800,900 1000	.37-1.17	29.4	13.7	2.09	2.32	1.28	1.04	23.0	44.1	8	5	33
18	Rotor	14	.5	800,900	.55-1.12	29.4	13.7	2.09	2.32	.85	.66	23.0	44.1	8	5	33
19	Rotor	14	.5	800,900,1000 1120	.50-1.22	23.1	4.3	1.50	1.50	1.40	.825	17.4	51.3	10	5	19
20	Rotor	14	.5	800,900,1000 1120	.4 - .82	23.1	4.3	1.50	1.50	1.40	.825	17.4	51.3	10	5	19
21	Stator	17.36	.62	600,800,900	.41- .63	52.0	52.0	3.25	3.25	1.64	1.07	10.0	10.0	7	7	34
22	Stator	17.36	.60	800,1000	.53- .66	20.6	20.0	2.66	3.23	1.45	1.08	34.0	28.0	8	6	9

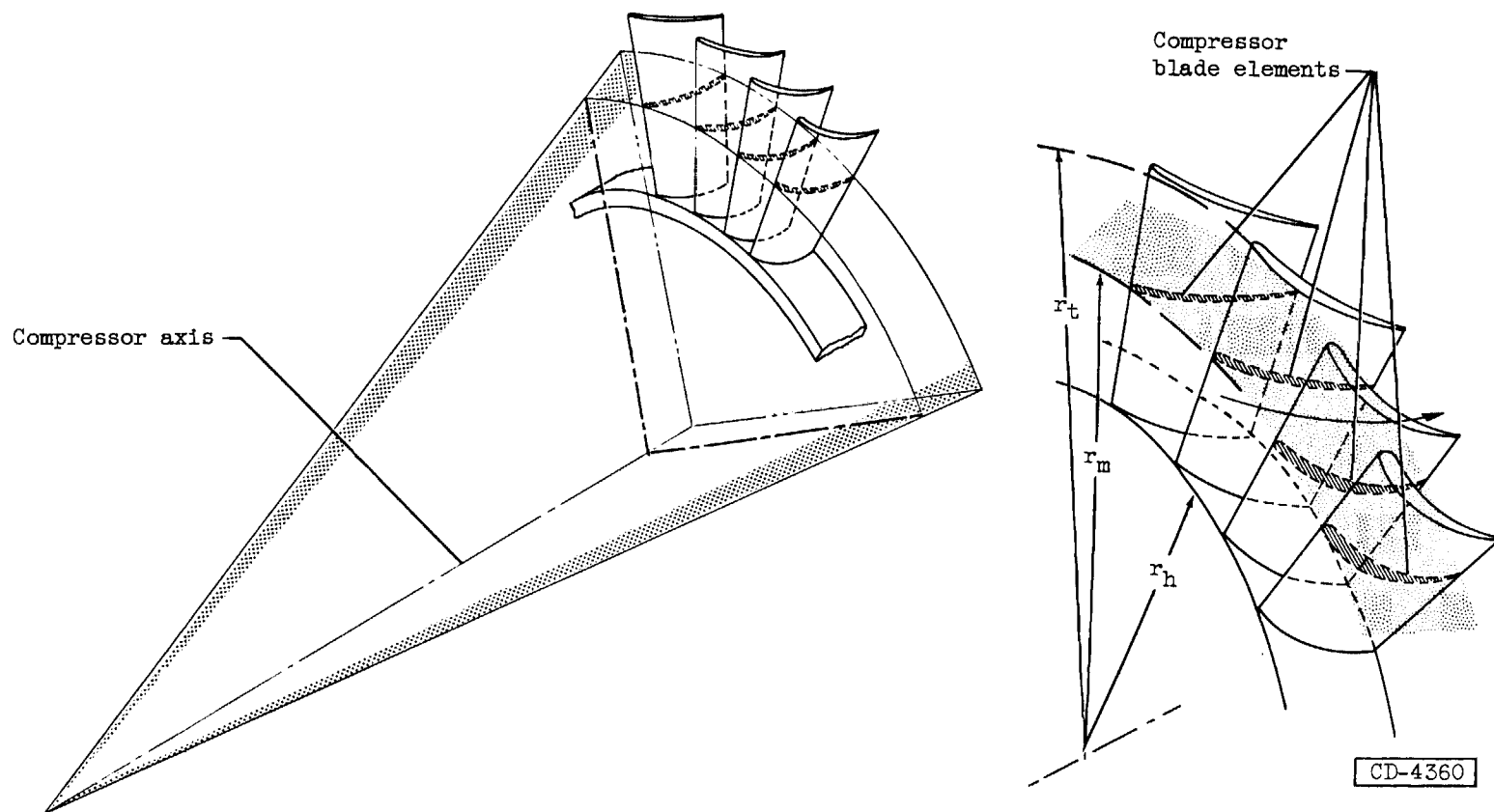


Figure 1. - Compressor blade elements shown along conical surface of revolution about compressor axis.

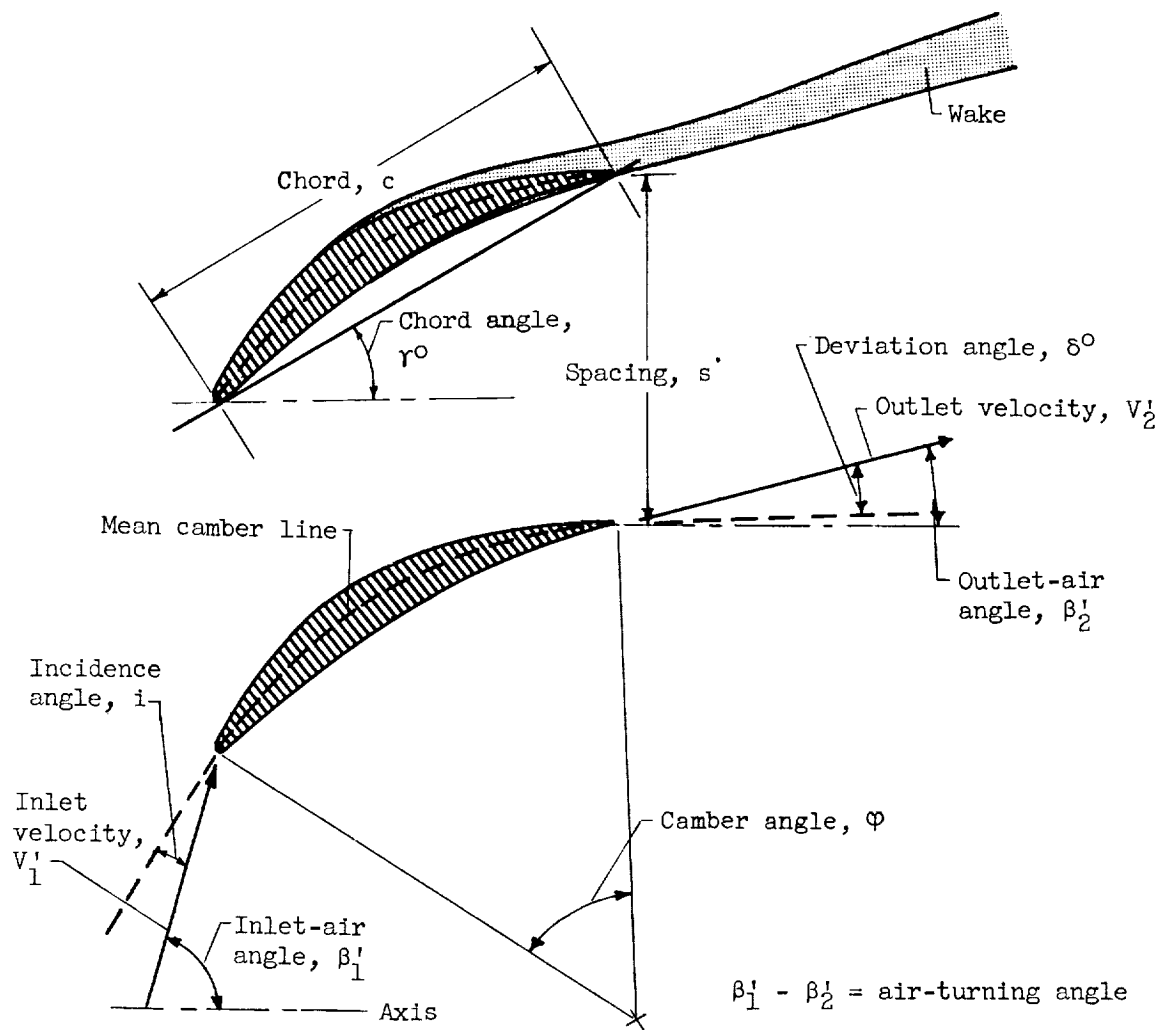


Figure 2. - Blade-element properties.

3390

CG-17 back

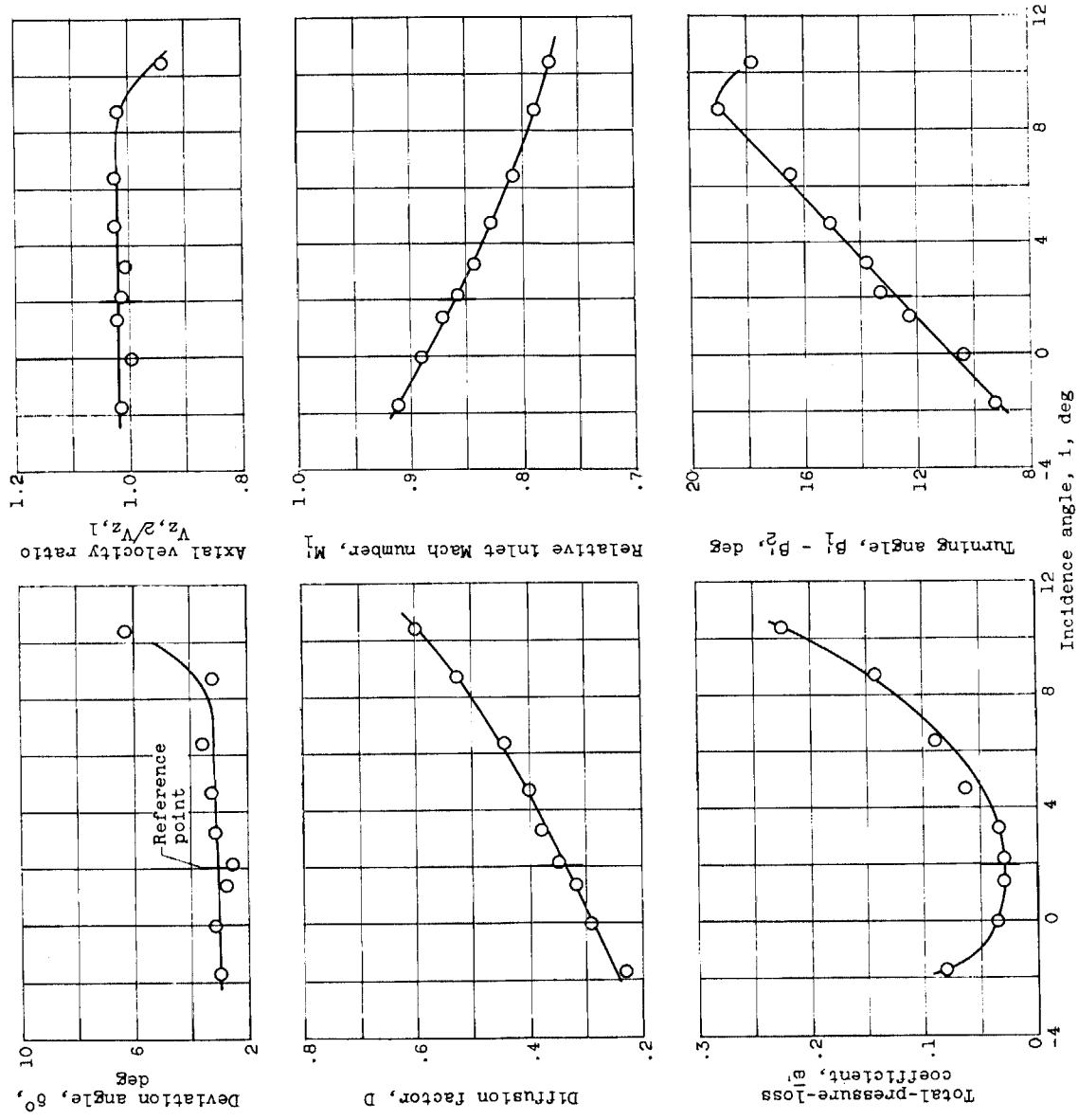


Figure 3. - Example of typical variation of blade-element performance parameters with incidence angle. Transonic rotor with double-circular-arc blade sections at tip speed of 800 feet per second; data for blade row 17 (table I) at tip position (ref. 33).

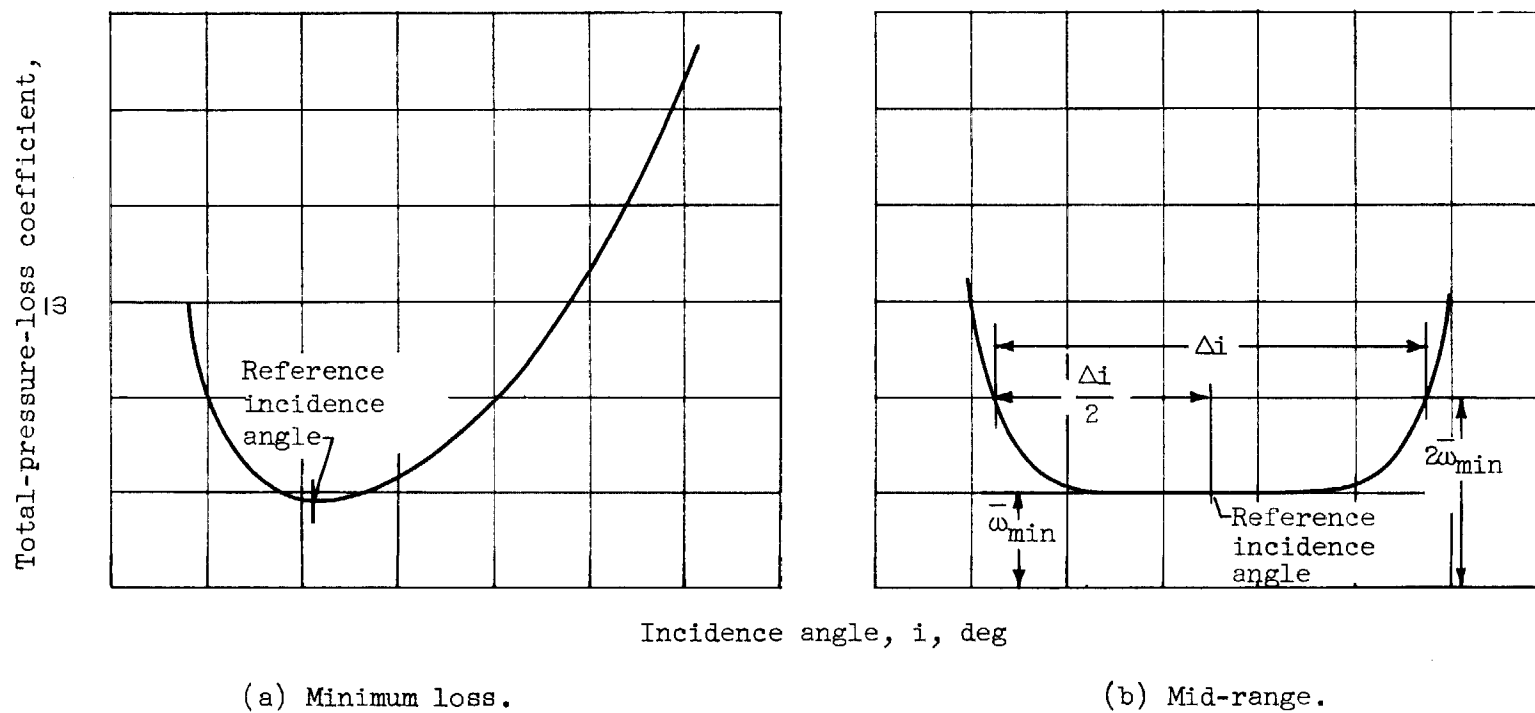


Figure 4. - Definitions of reference incidence angle.

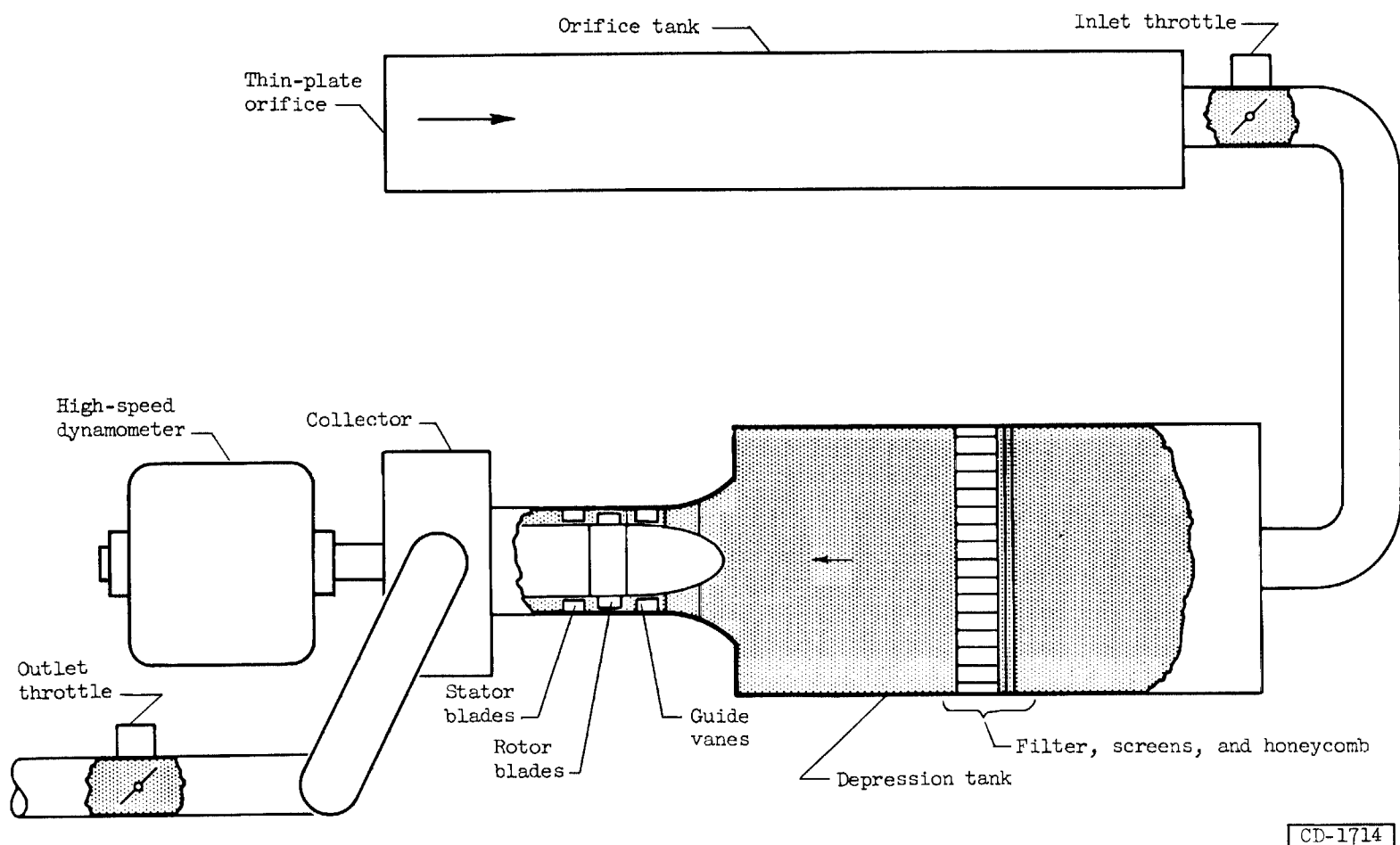


Figure 5. - Schematic diagram of single-stage-compressor test installation.

CD-1714

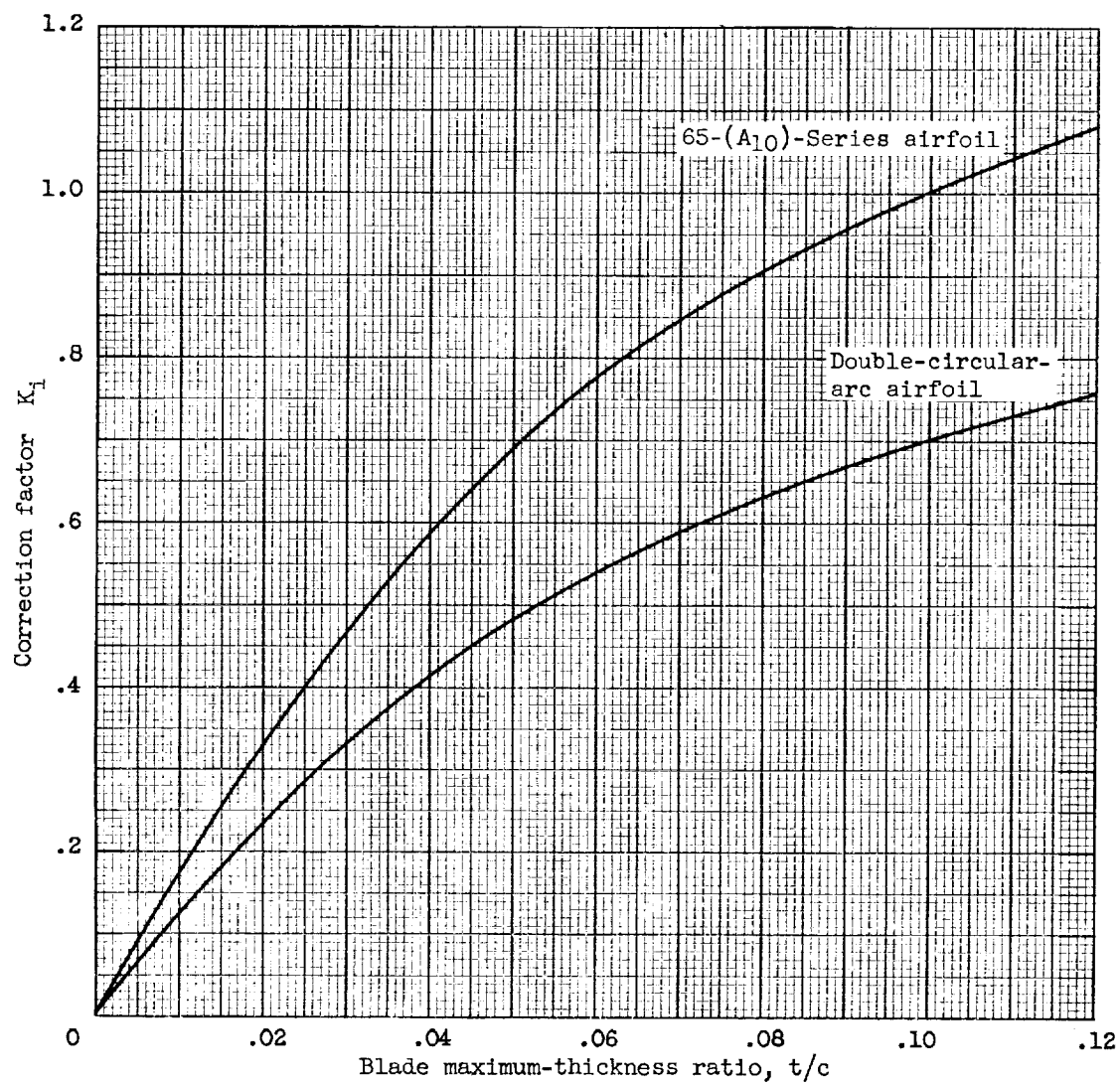


Figure 6. - Thickness correction for zero-camber reference incidence angle (ch. VI).

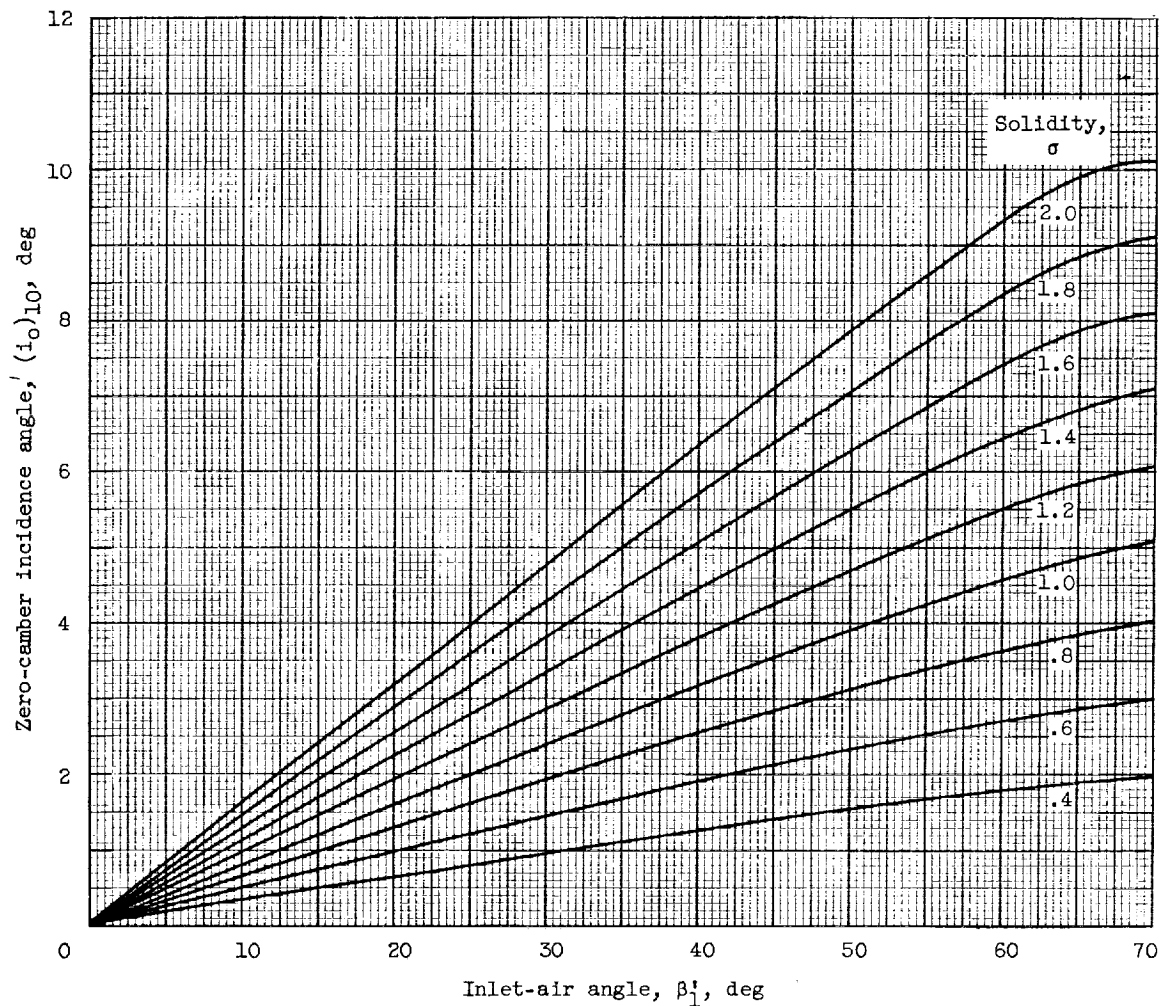


Figure 7. - Zero-camber reference incidence angle for NACA 65-(A₁₀)-series and true circular-arc blades of 10-percent maximum-thickness ratio (ch. VI).

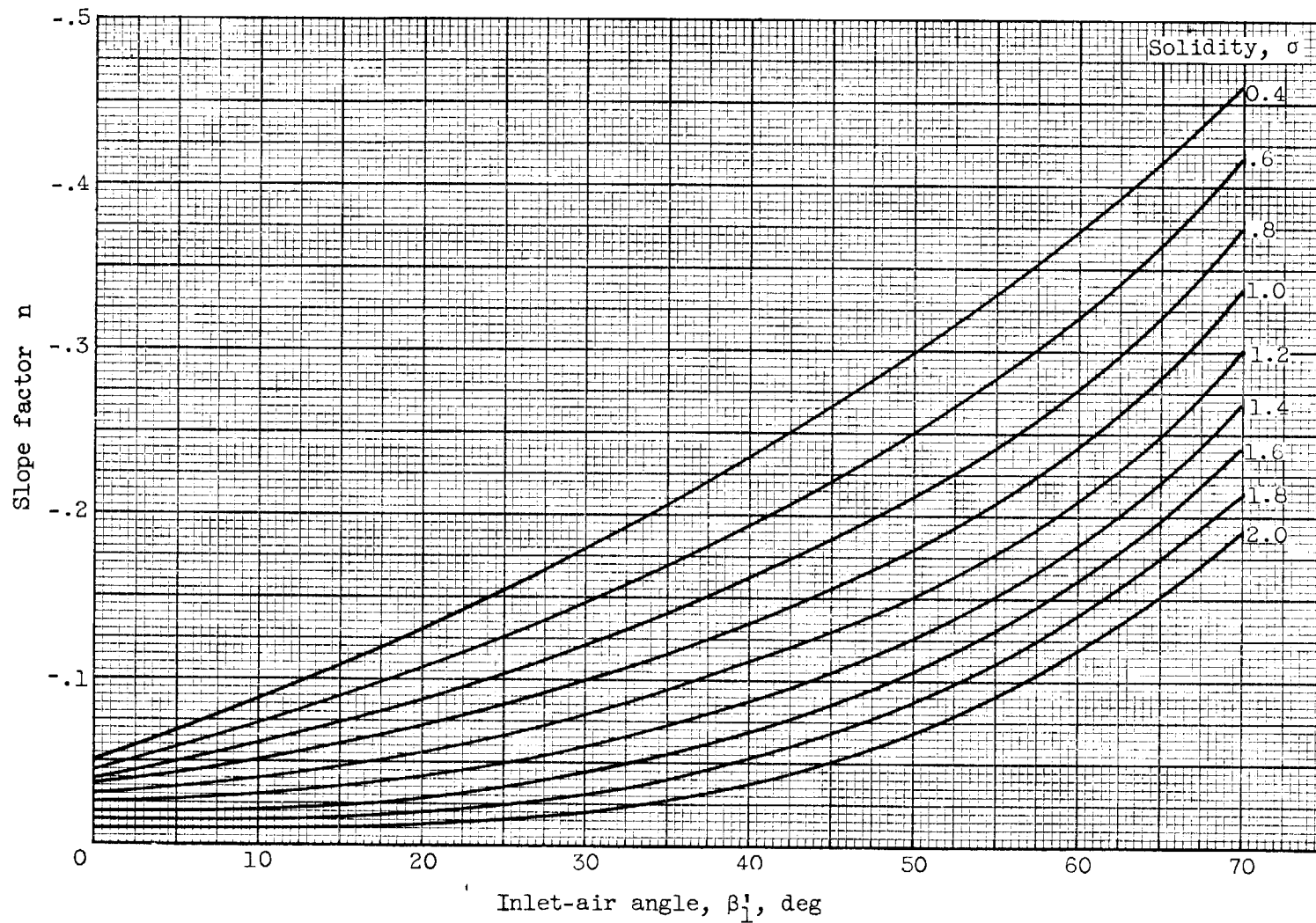


Figure 8. - Reference-incidence-angle slope factor for NACA 65-(A₁₀)-series blades as equivalent circular arcs and for true circular-arc blades (ch. VI).

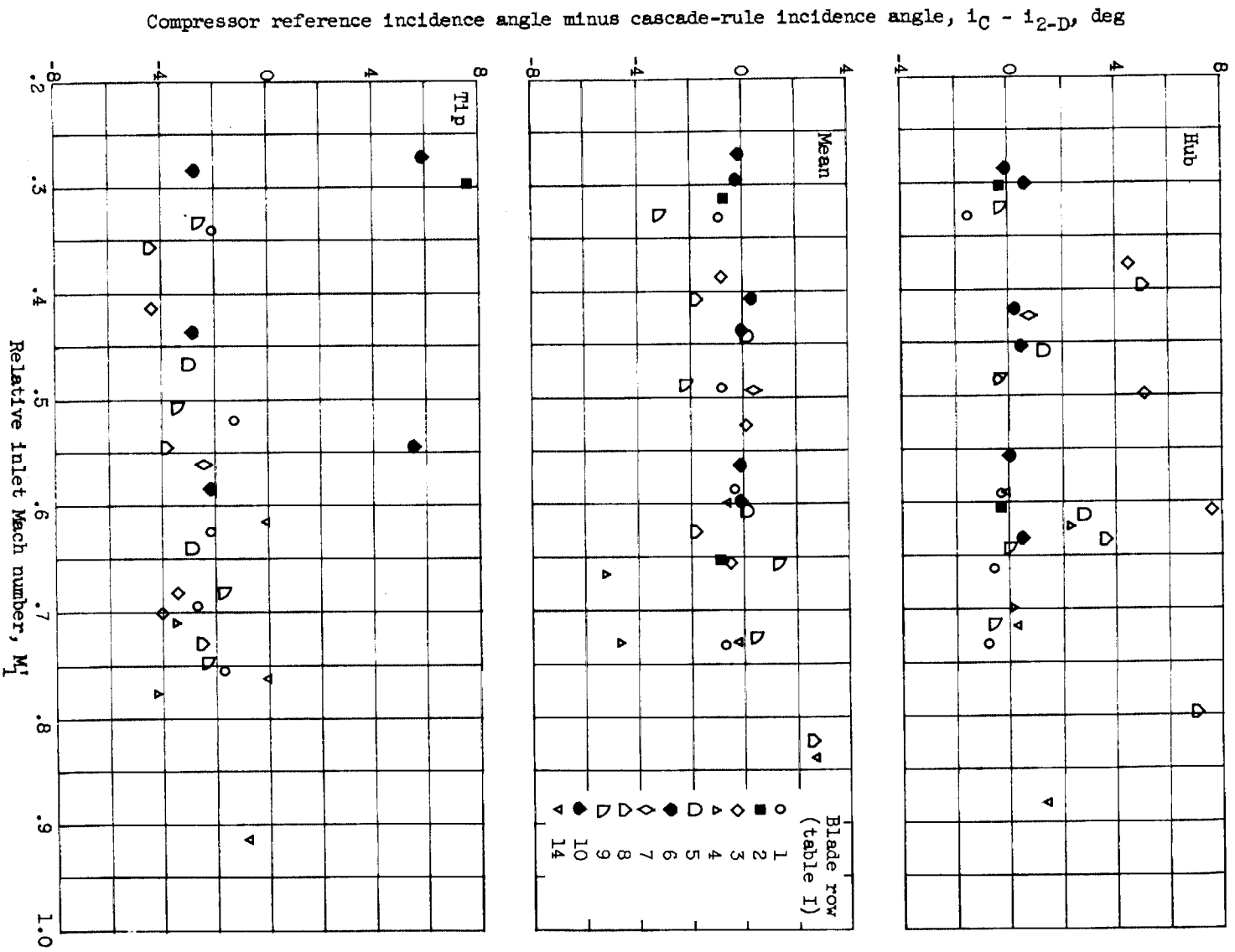


Figure 9. - Variation of compressor reference incidence angle minus two-dimensional-cascade-rule incidence angle with relative inlet Mach number for NACA 65-(A₁₀)-series blade section.

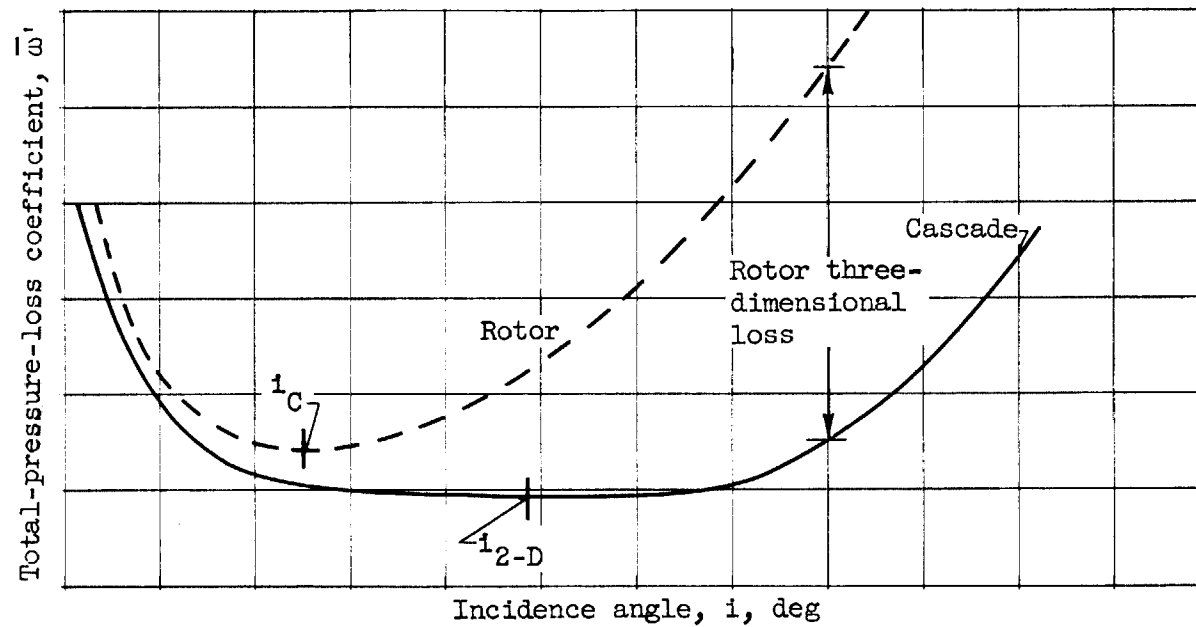


Figure 10. - Typical variation of loss with incidence angle for rotor blade element near tip and in two-dimensional cascade for same blade geometry and inlet Mach number.

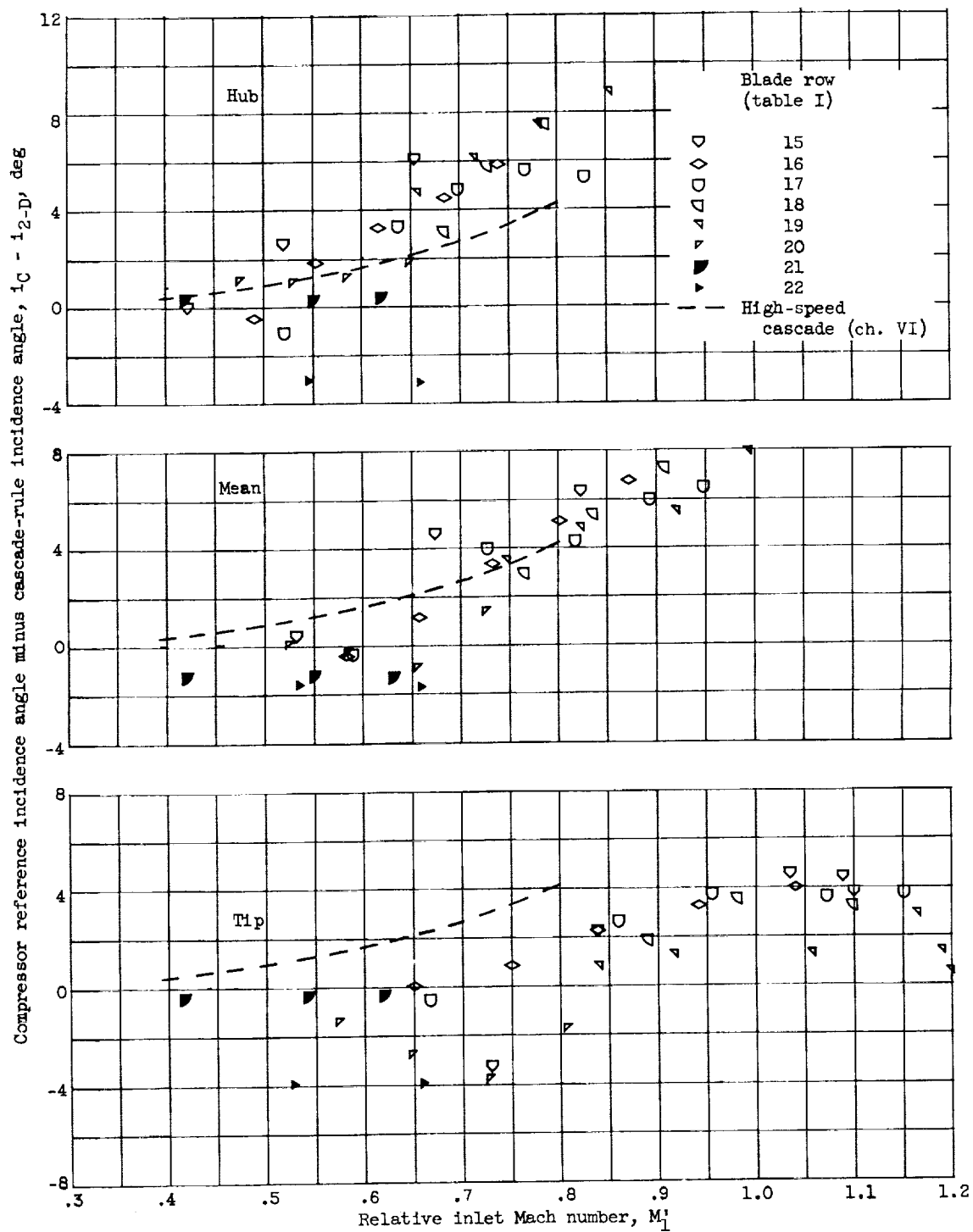


Figure 11. - Variation of compressor reference incidence angle minus two-dimensional-cascade-rule incidence angle with relative inlet Mach number for double-circular-arc blade section.

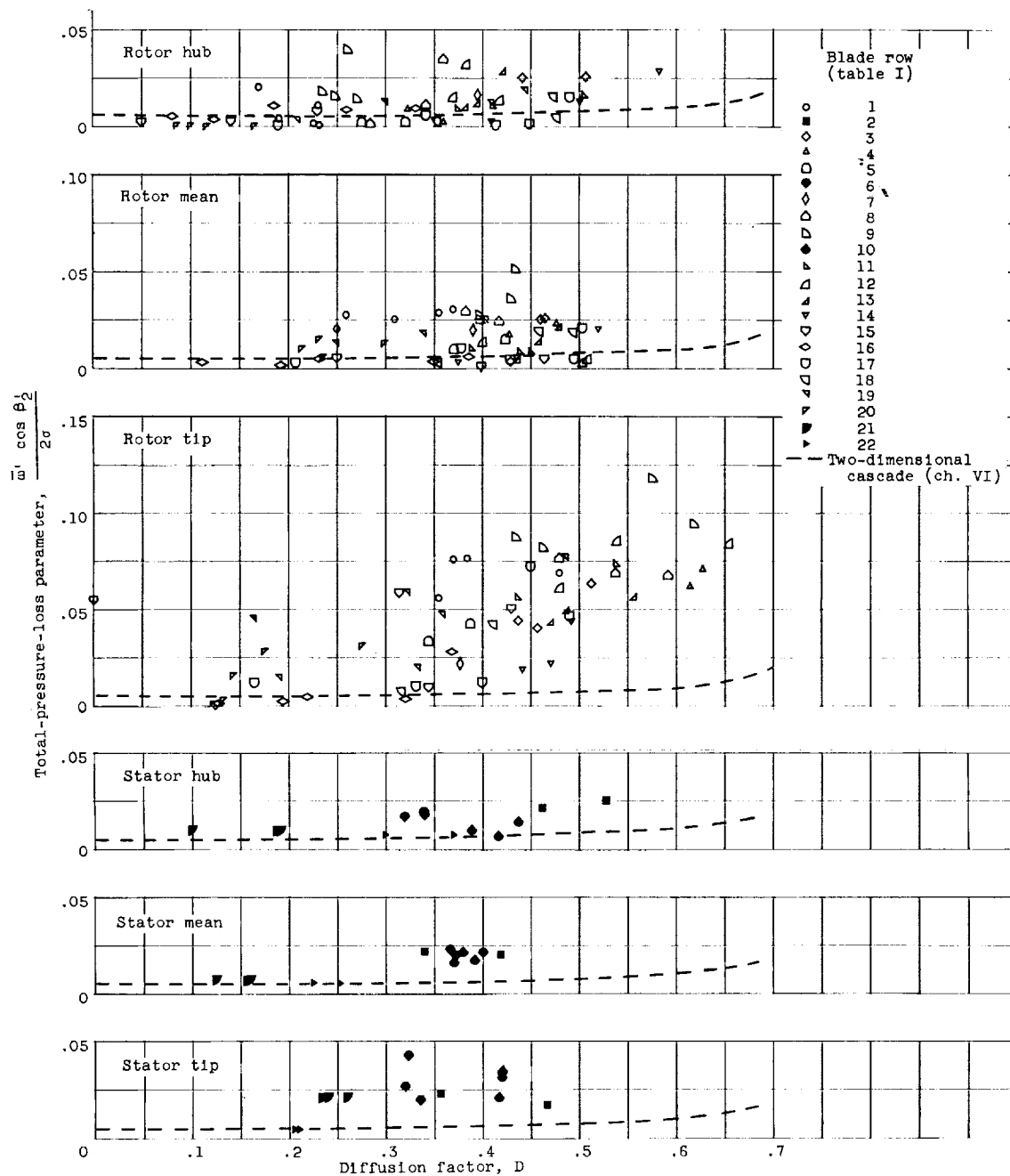


Figure 12. - Variation of total-pressure-loss parameter with diffusion factor at reference incidence angle for NACA 65-(A₁₀)-series and double-circular-arc blade sections.

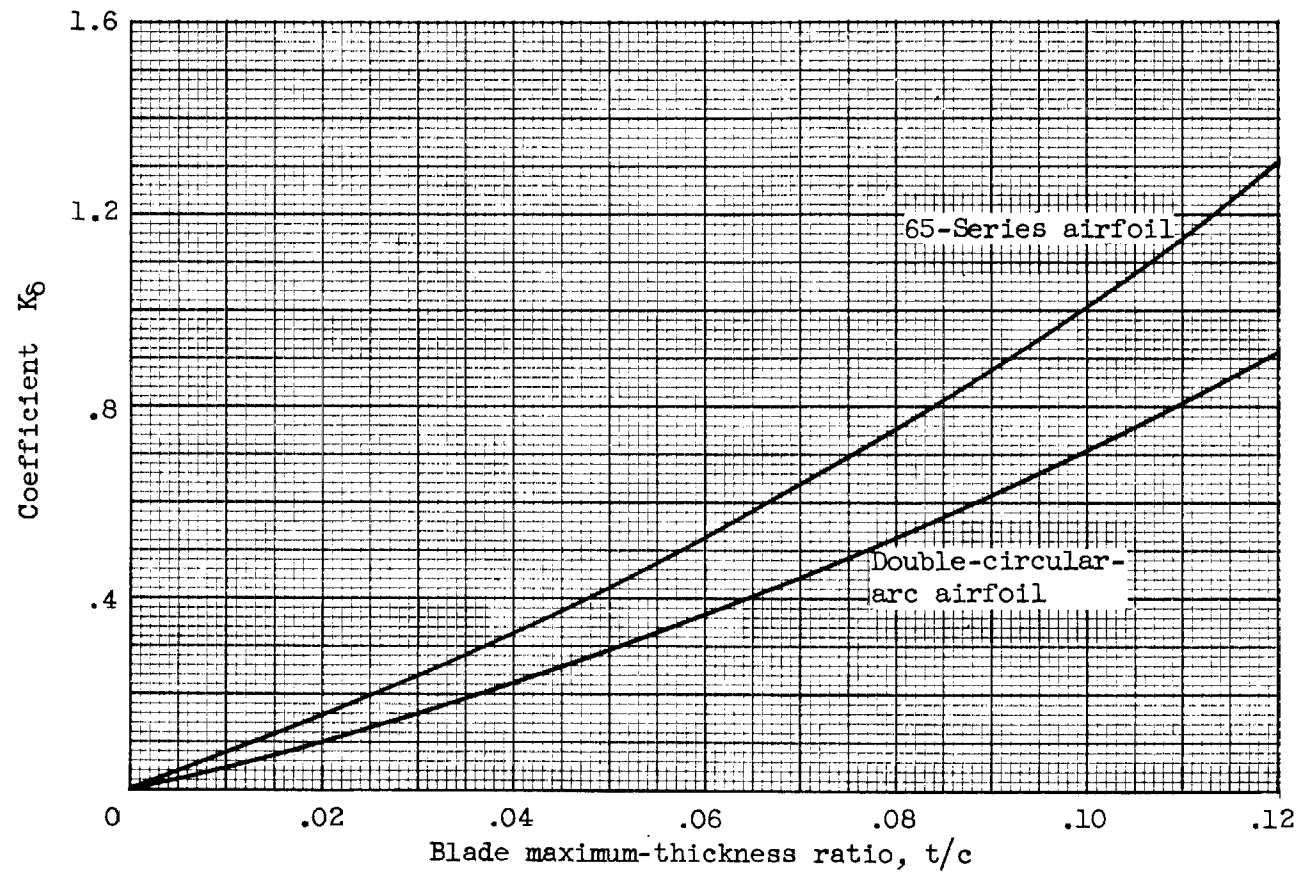


Figure 13. - Thickness correction for zero-camber deviation angle (ch. VI).

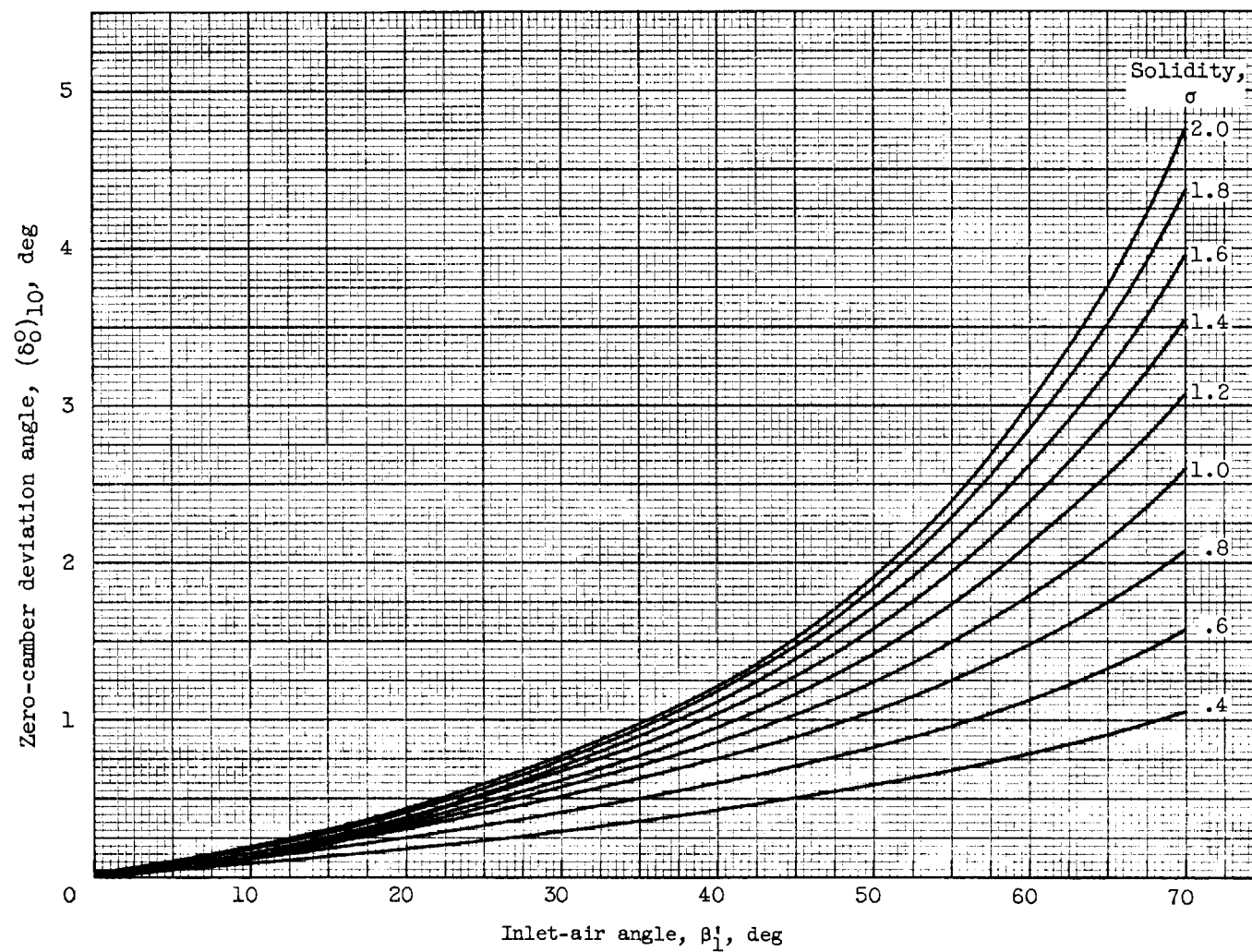


Figure 14. - Zero-camber deviation angle for NACA 65-(A₁₀)-series and true circular-arc blades of 10-percent maximum-thickness ratio (ch. VI).

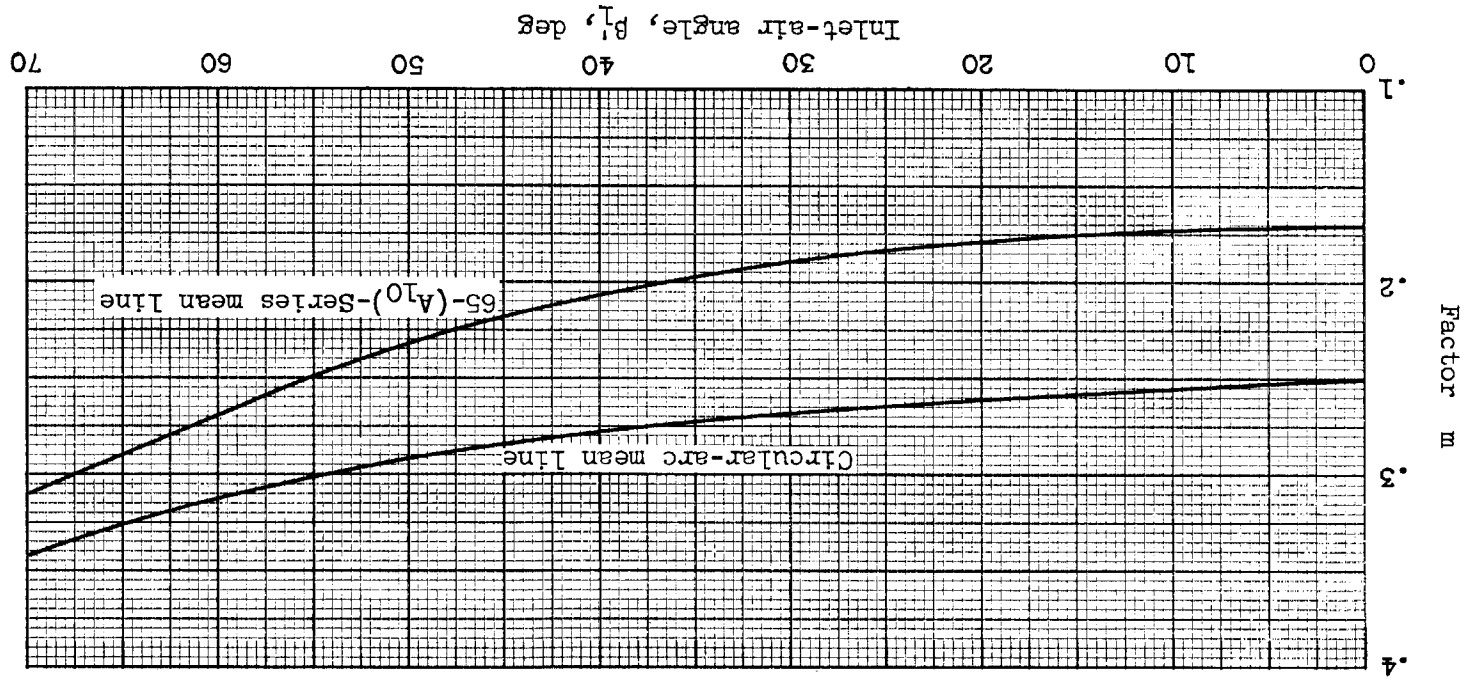


Figure 15. - Factor m in deviation-angle rule (ch. VI).

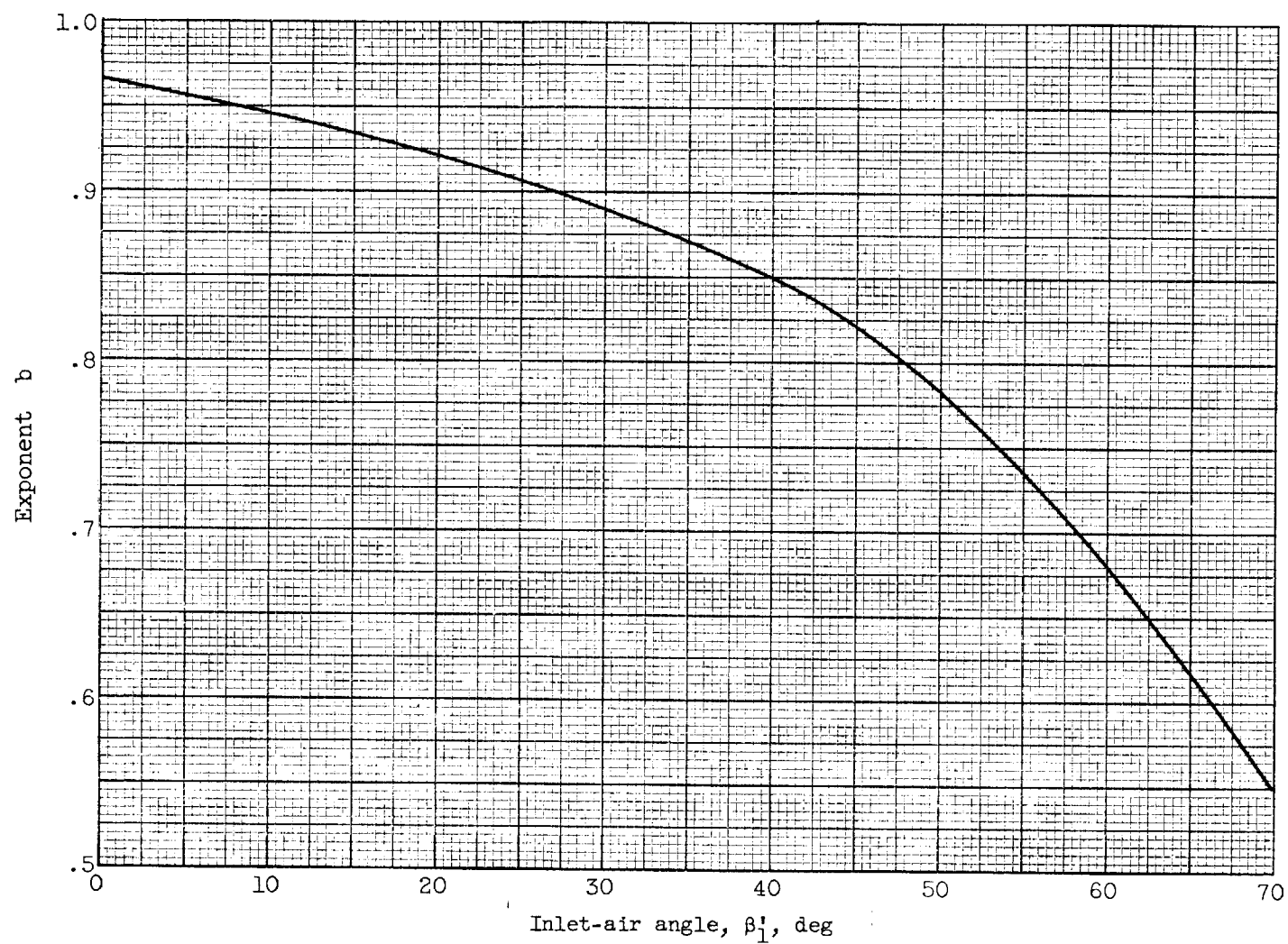


Figure 16. - Solidity exponent b in deviation-angle rule (ch. VI).

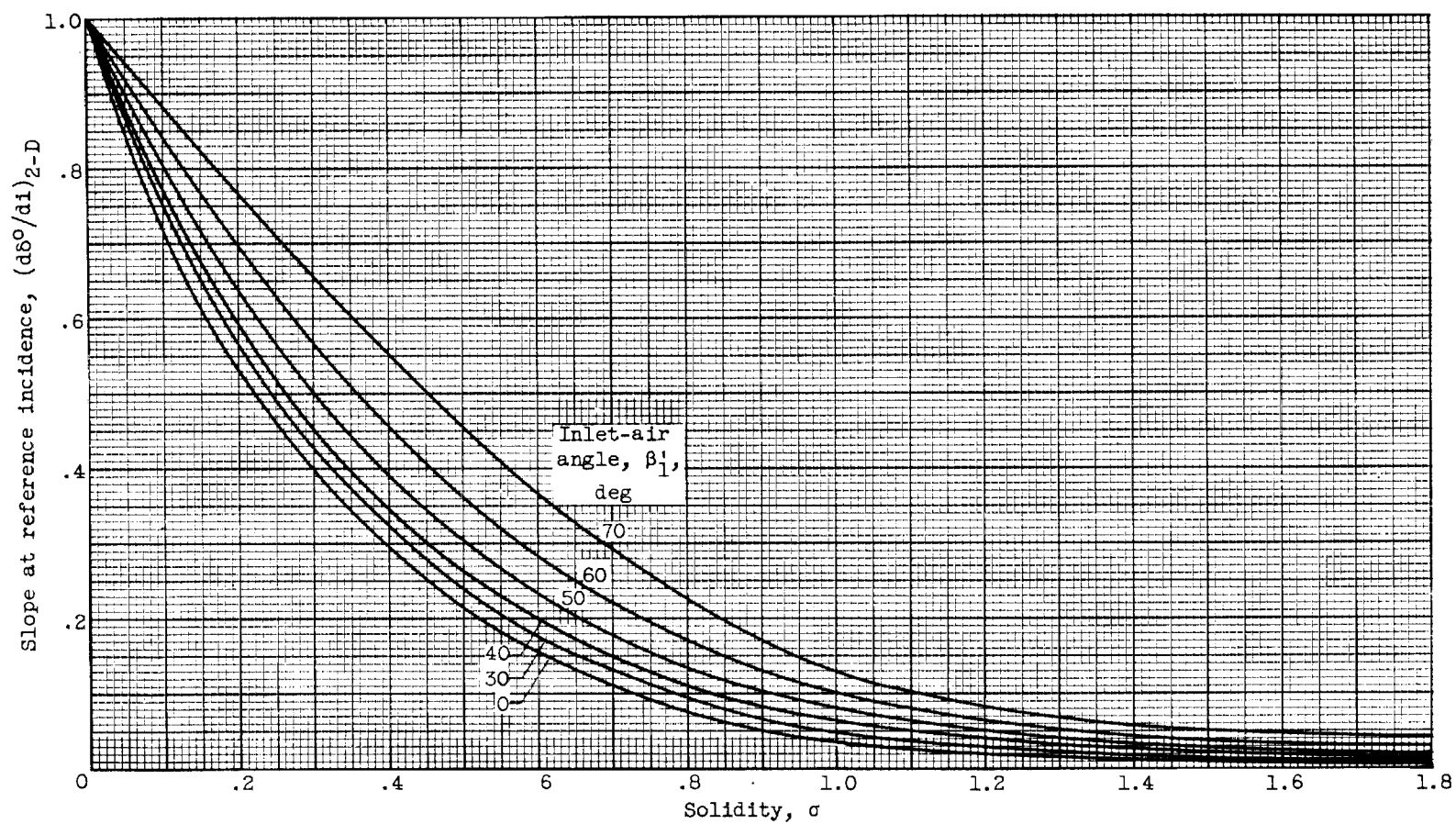


Figure 17. - Deviation-angle slope $(d\delta^0/di)_{2-D}$ at reference incidence angle (ch. VI).

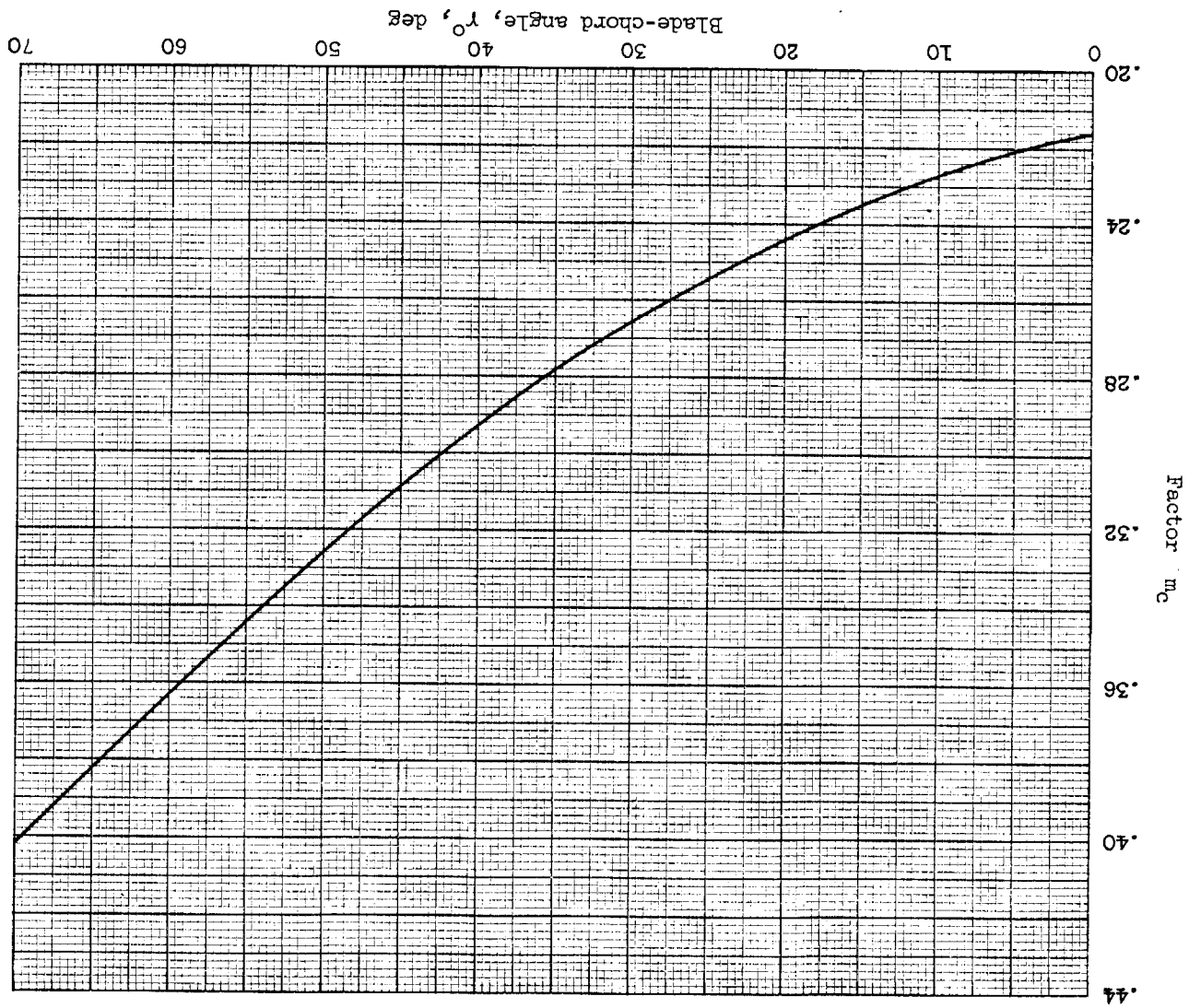


Figure 18. - Variation of m_c for circular-arc compressor cascades (ref. 24).

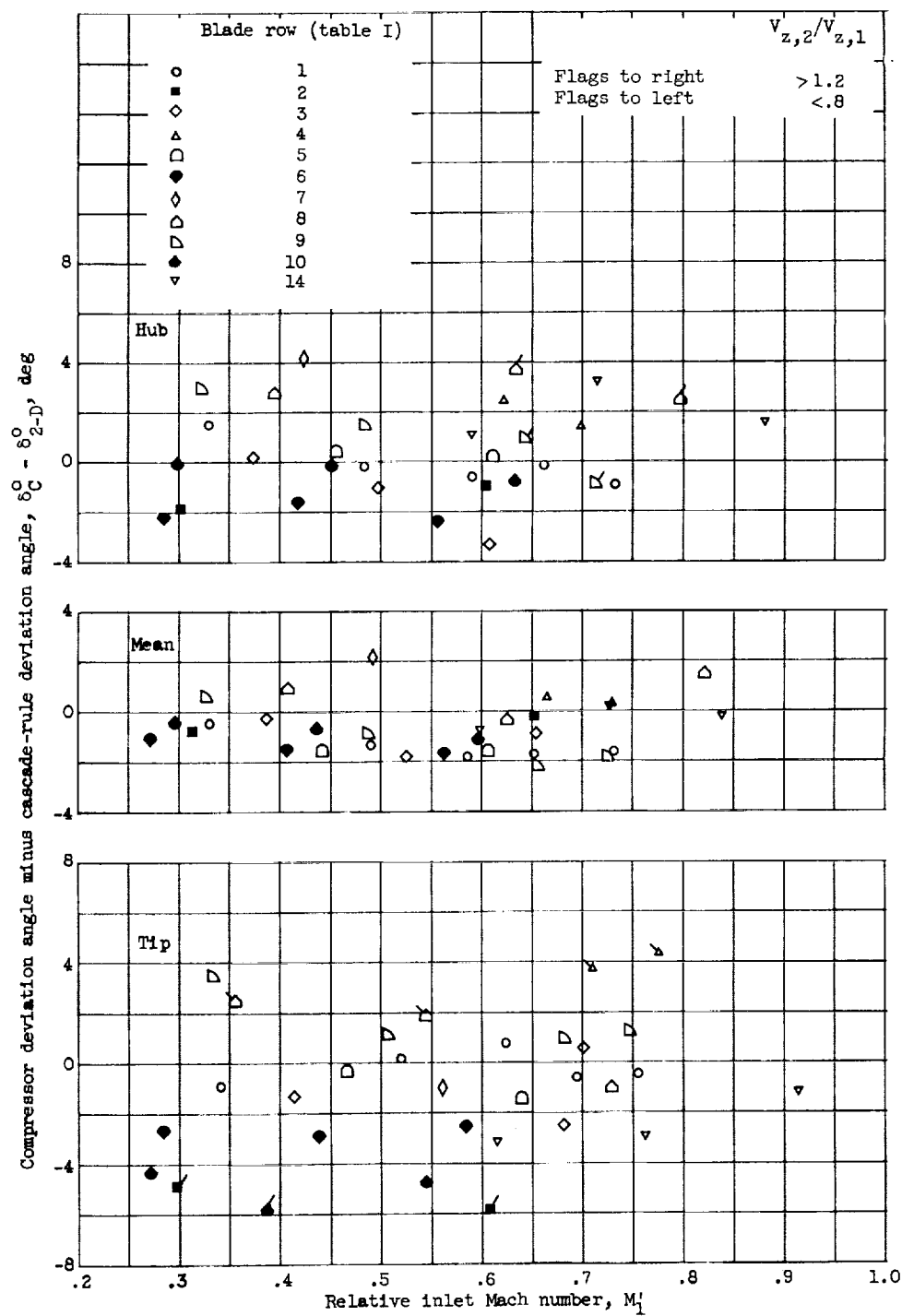
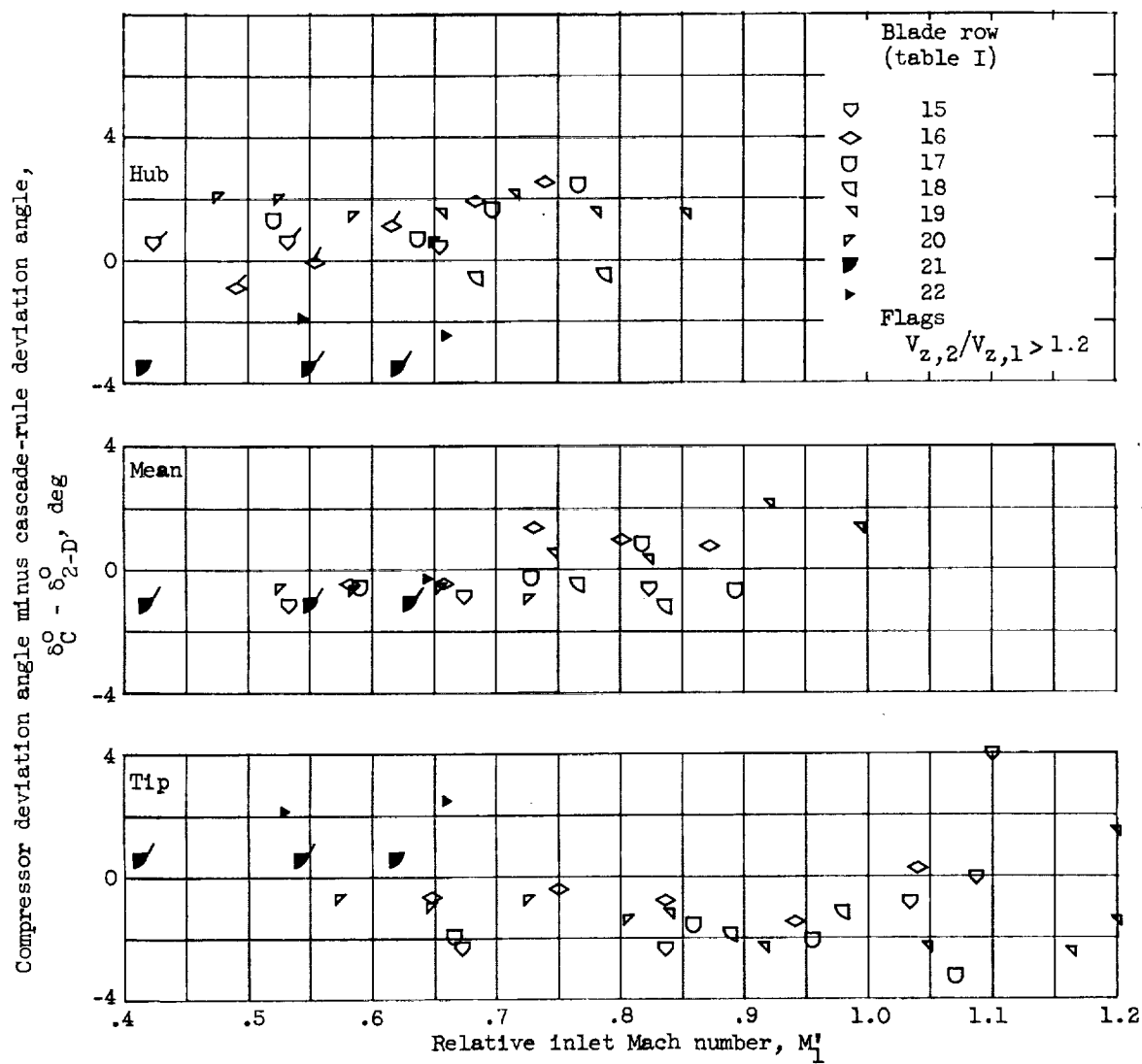
(a) 65-(A₁₀)-Series blade section.

Figure 19. - Variation of compressor deviation angle minus two-dimensional-cascade deviation angle at compressor reference incidence angle with relative inlet Mach number.



(b) Circular-arc blade section.

Figure 19. - Concluded. Variation of compressor deviation angle minus two-dimensional-cascade deviation angle at compressor reference incidence angle with relative inlet Mach number.

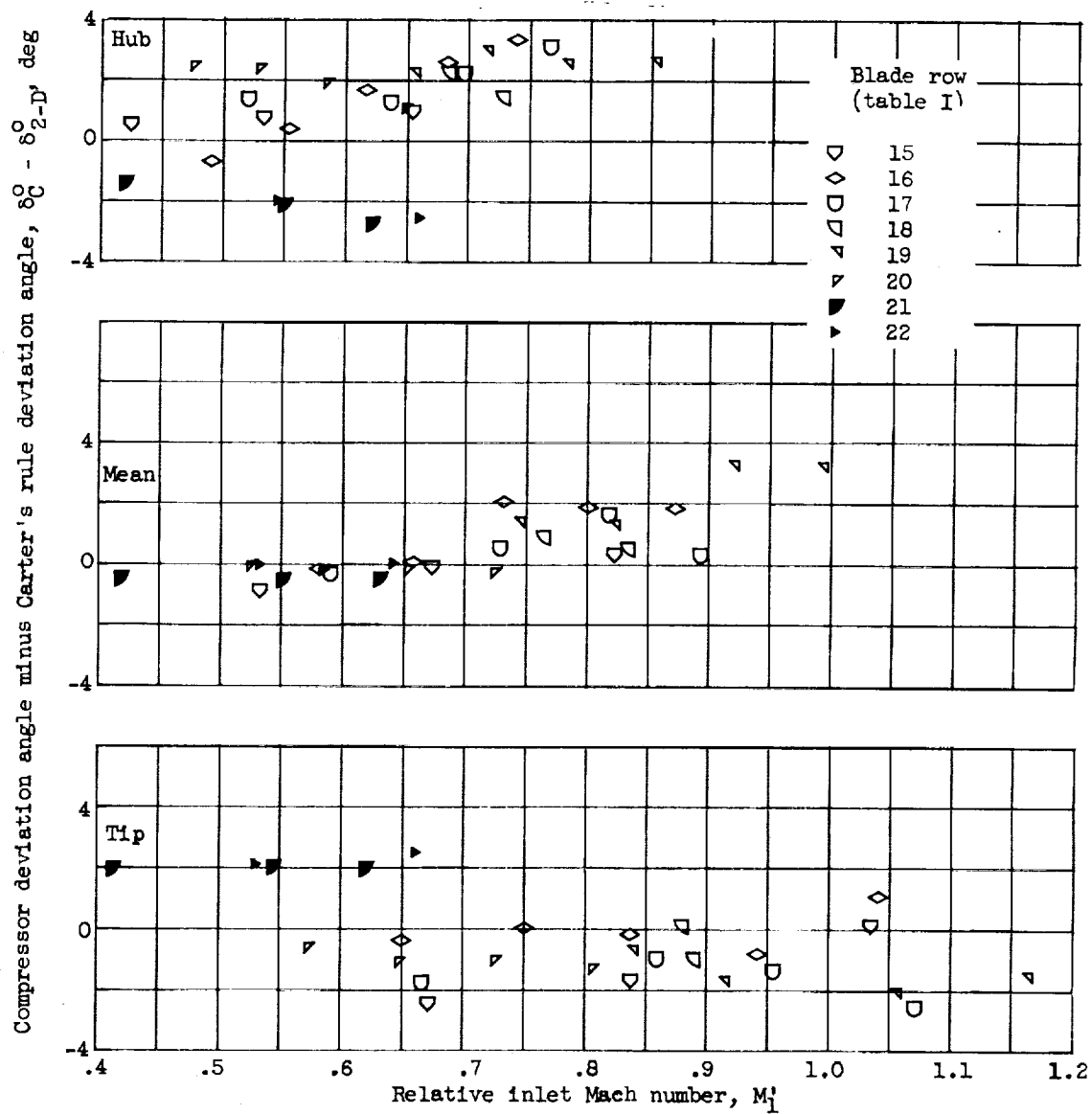


Figure 20. - Variation of compressor deviation angle minus deviation angle predicted by Carter's rule at reference incidence angle with relative inlet Mach number for double-circular-arc blade section.

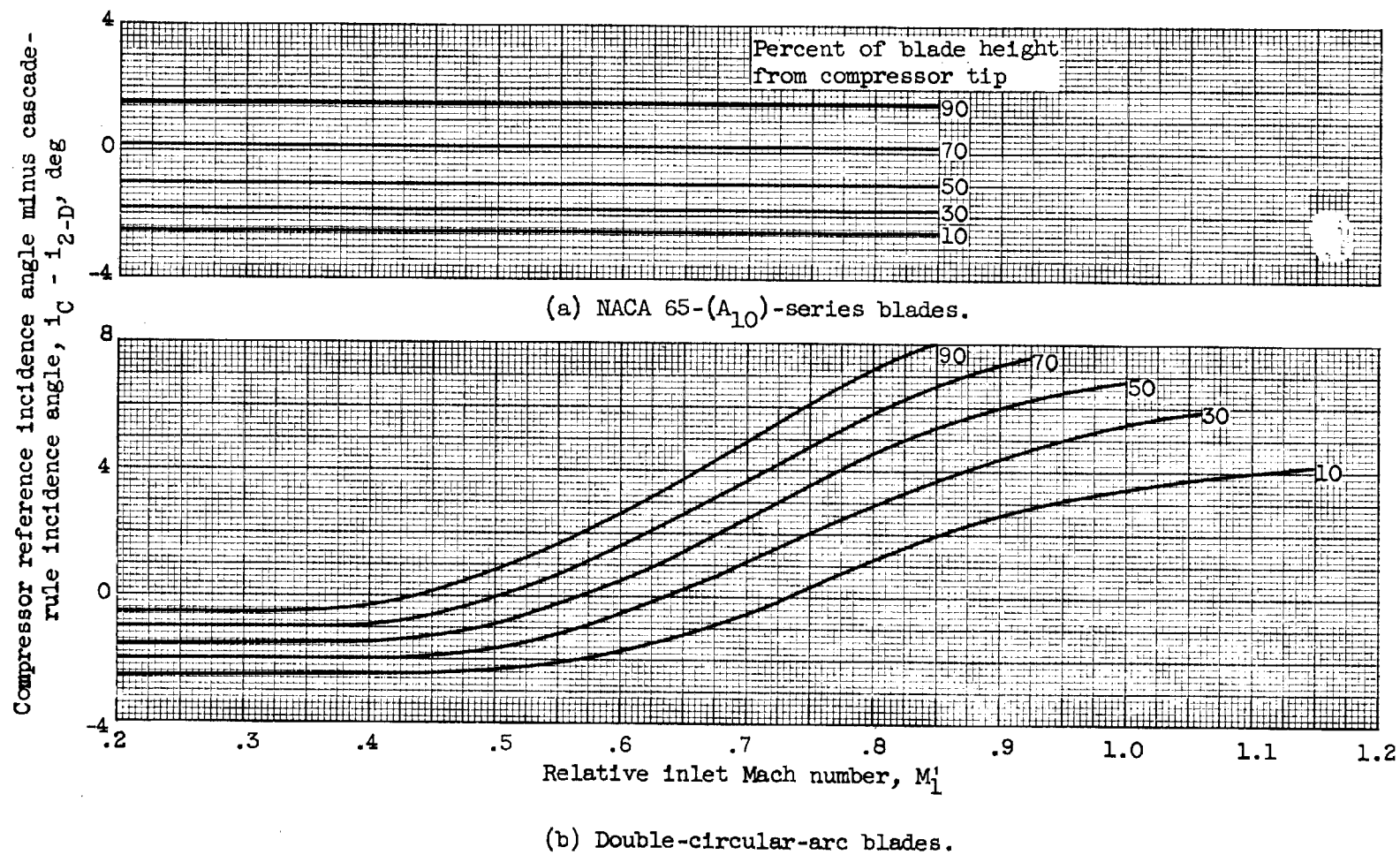


Figure 21. - Deduced variation of average rotor reference incidence angle minus low-speed two-dimensional-cascade-rule reference incidence angle with relative inlet Mach number.

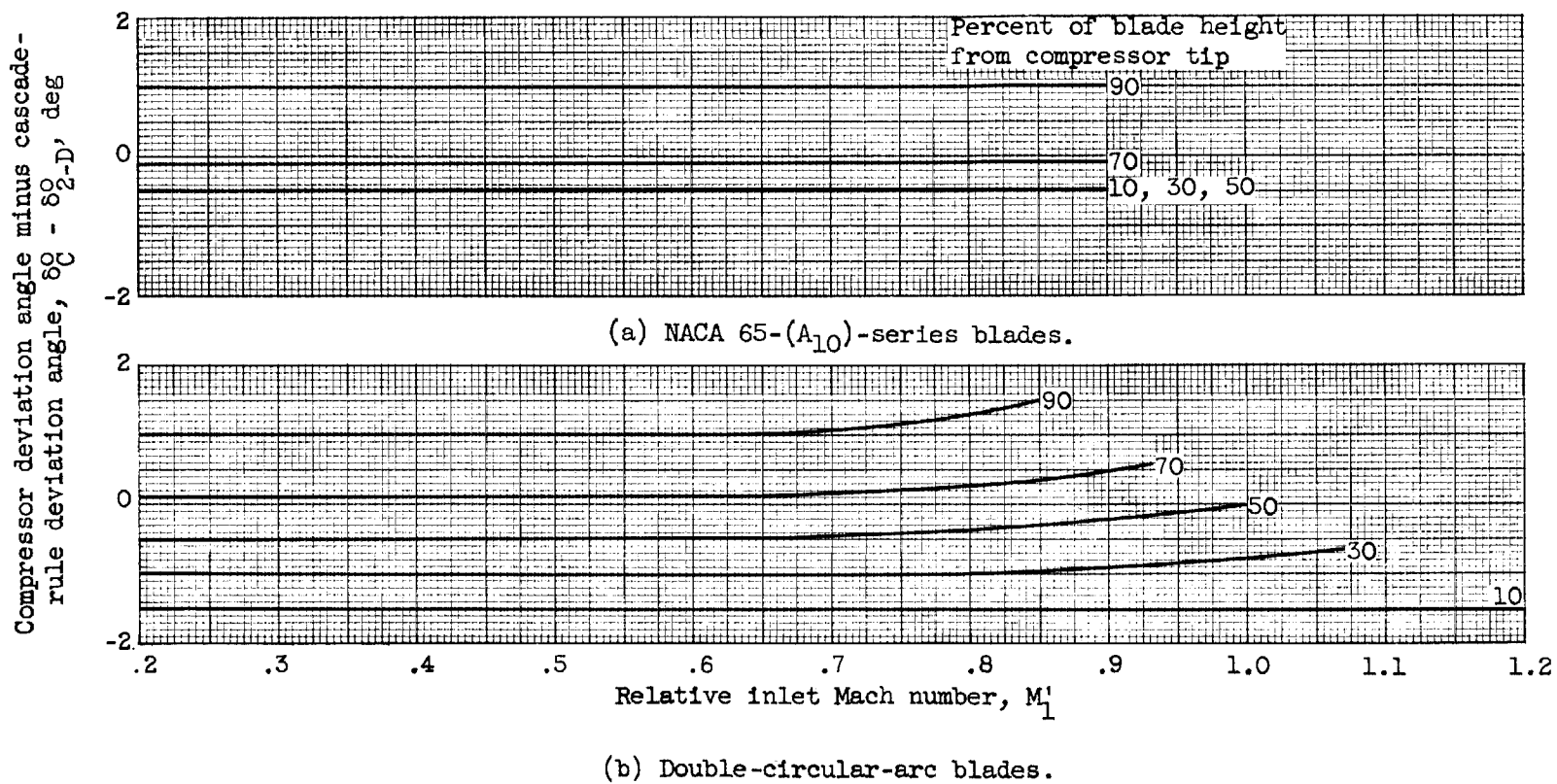


Figure 22. - Deduced variation of average rotor deviation angle minus low-speed two-dimensional cascade-rule deviation angle at compressor reference incidence angle with relative inlet Mach number.

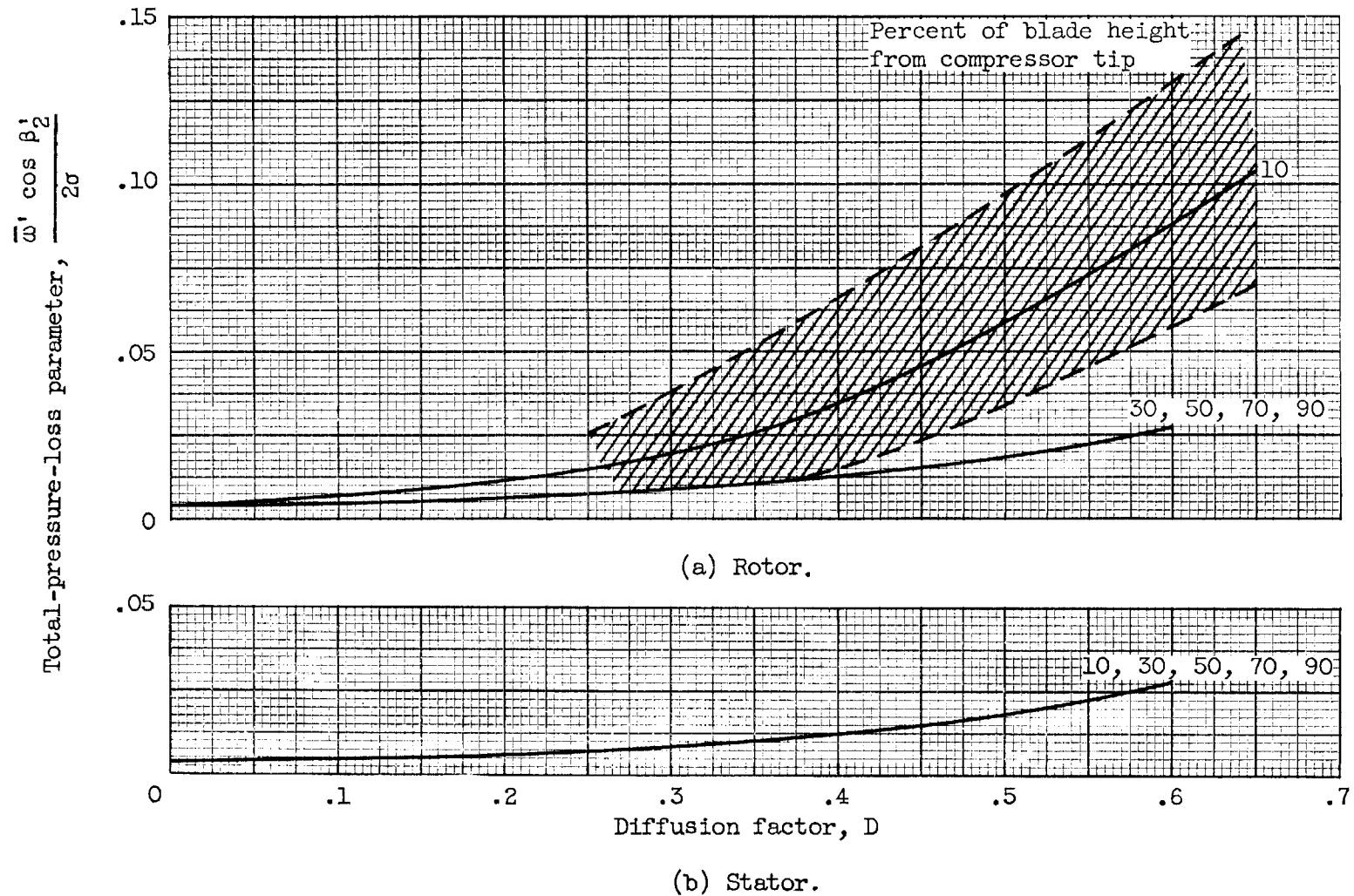


Figure 23. - Deduced variation of total-pressure-loss parameter with diffusion factor at reference incidence angle for NACA 65-(A₁₀)-series and double-circular-arc blades.

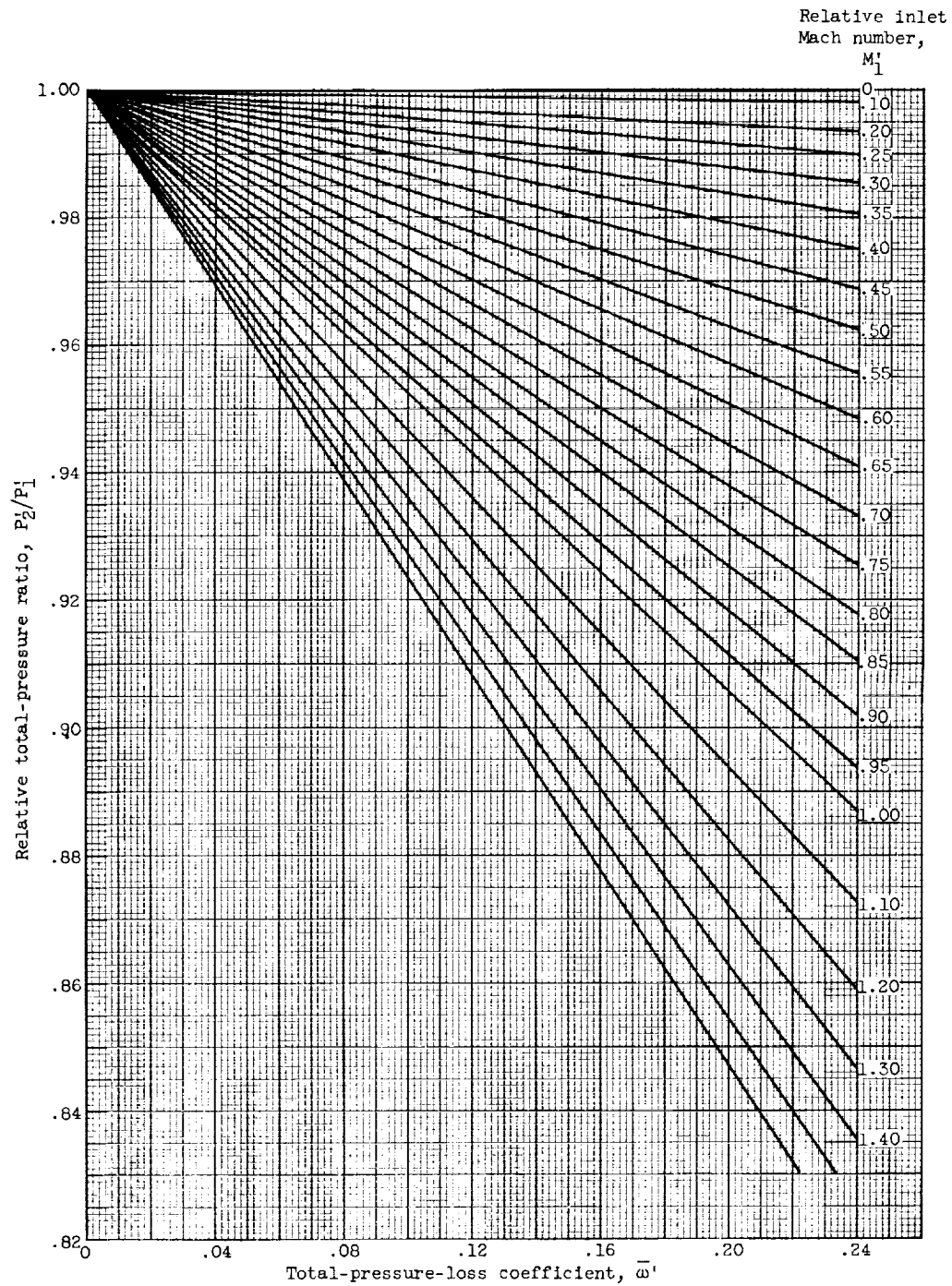


Figure 24. - Variation of rotor relative total-pressure ratio with total-pressure-loss coefficient and inlet Mach number.

$$\bar{w}' = \frac{1 - \frac{P_2'}{P_1'}}{1 - \frac{1}{\left[1 + \frac{\gamma-1}{2} (M_1')^2\right]^{\frac{\gamma}{\gamma-1}}}}$$

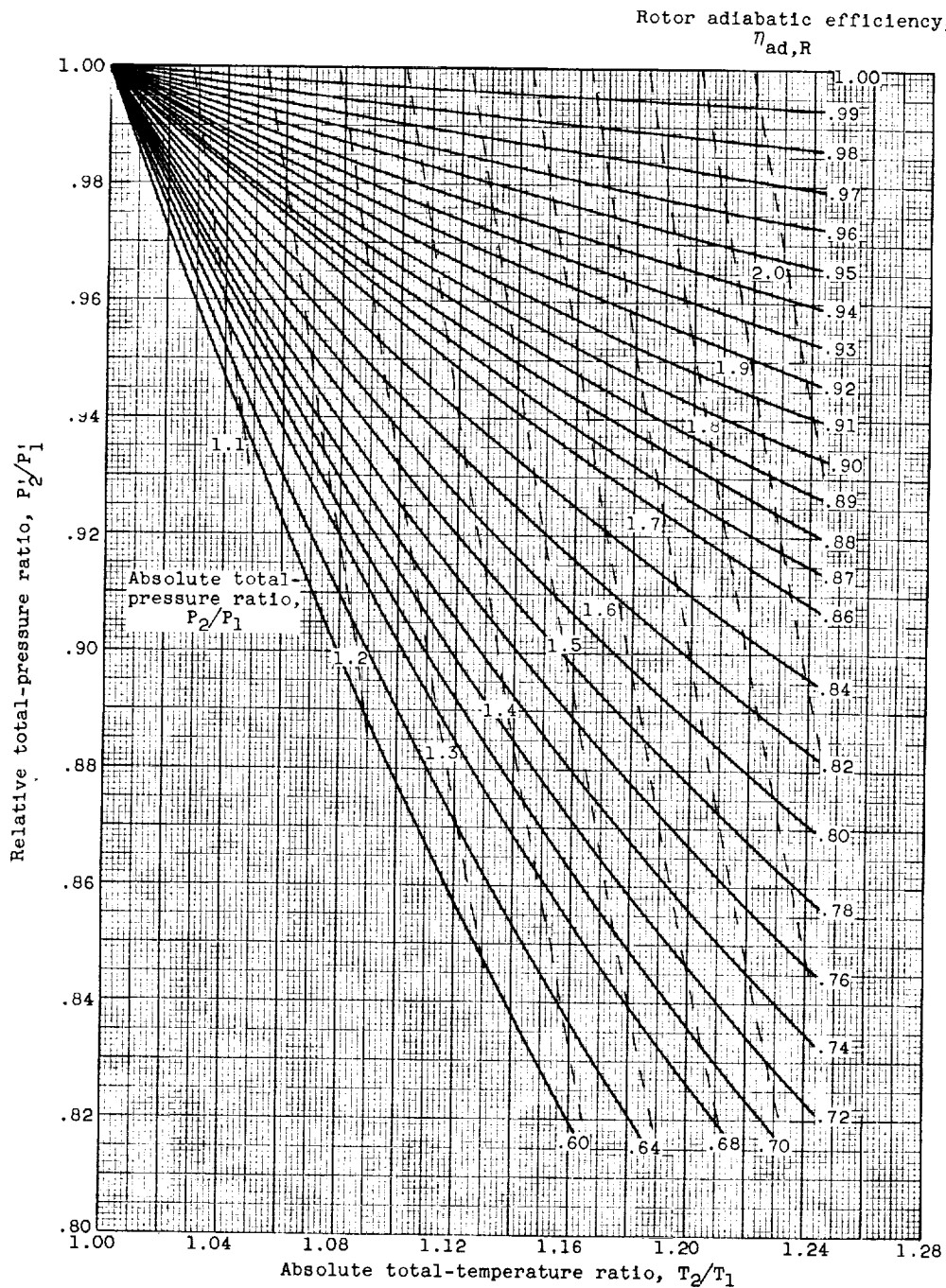
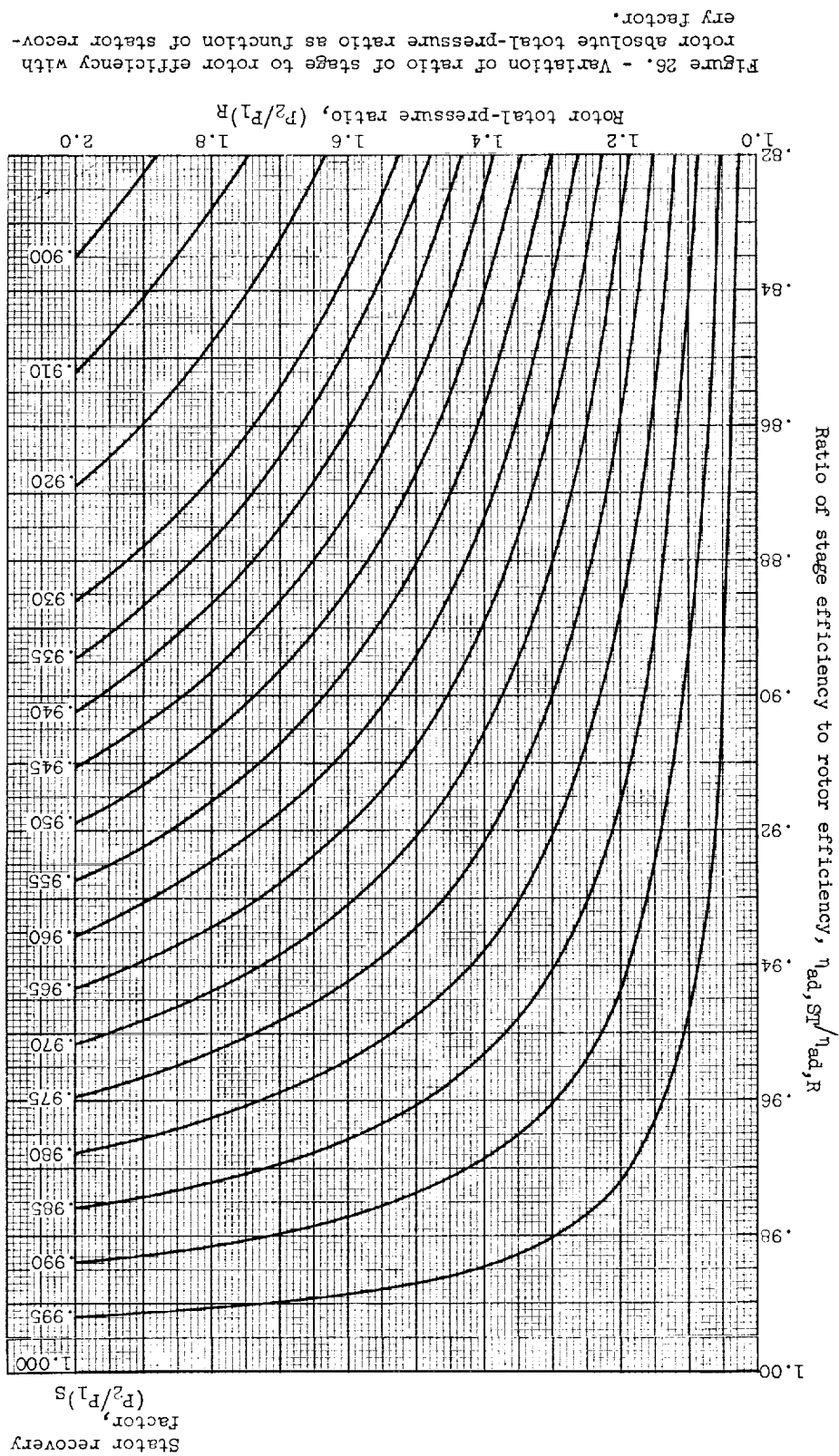


Figure 25. - Variation of relative total-pressure ratio with absolute total-temperature ratio and efficiency for rotor.

$$\eta_{ad} = \frac{\left[\frac{P_2}{P_1} \left(\frac{T_2}{T_1} \right)^{\frac{\gamma}{\gamma-1}} \right]^{\frac{\gamma-1}{\gamma}}}{\frac{T_2}{T_1} - 1.0} - 1.0$$



CHAPTER VIII

DESIGN VELOCITY DISTRIBUTION IN MERIDIONAL PLANE

By Charles C. Giamati, Jr., and Harold B. Finger

SUMMARY

A discussion is presented of the general flow equations and methods to be used in determining the radial distributions of flow in the meridional (hub-to-tip) plane of an axial-flow compressor when the required performance is specified. The problem of determining the radial distributions of flow is simplified by considering conditions at axial stations between blade rows where nonviscous, axisymmetric flow equations are applied. The analysis presumes the availability of blade-element data on deviation angle and on stagnation-pressure loss for all design techniques. Methods for considering the effects of wall boundary layers on required annulus area and mass-averaged stage performance are presented. A sample stage design calculation is given.

INTRODUCTION

The design of a multistage axial-flow compressor consists in the successive design of several individual rotor and stator blade rows which are then compounded to form the multistage compressor. As pointed out in the general compressor design discussion of chapter III (ref. 1), the problem of blade-row design has been simplified by considering the flow in each of two planes, the hub-to-tip or meridional plane and the blade-to-blade or circumferential plane. The meridional-plane solution determines the radial distribution of flow conditions assuming that axial-symmetry conditions apply, and the circumferential-plane solution determines the air-turning characteristics through the blade element. A quasi-three-dimensional description of the actual flow is then obtained by juxtaposition of these two solutions.

The results of experimental blade-to-blade investigations are described in chapters VI and VII. These chapters present circumferentially averaged blade-element performance characteristics as determined from two- and three-dimensional cascades, respectively. The blade-element performance is presented in terms of incidence angle, deviation angle, and

stagnation-pressure loss as functions of cascade geometry, inlet Mach number, and (for three-dimensional cascades) radial position in the blade row.

The present chapter discusses the general flow equations and presents methods to be used in determining the radial distributions of flow in the meridional plane. The problem of determining the radial distributions of flow is simplified by considering conditions only at axial stations between blade rows. In these regions, equations for nonviscous axisymmetric flow are applied to determine the design flow distributions when the required performance (weight flow and turning or energy addition) of the blade row is specified.

Since the calculation involves the determination of the velocities from the inner wall to the outer wall of the annular flow area, it is apparent that some consideration must be given to the boundary-layer accumulation on these walls. The most accurate and complete procedure requires a knowledge of the distribution of entropy from wall to wall as well as a knowledge of the rotor energy input across the entire annulus area including the boundary-layer region. Since complete data for this type of calculation are not currently available, simpler design techniques are required. Essentially, these simpler techniques involve computing the flow variables as if no wall boundary layer existed. Boundary-layer correction factors are then applied to determine the required geometric annulus area and mass-averaged stage performance (efficiency, temperature rise, and pressure ratio).

Since the determination of the flow conditions and annulus area configuration after each blade row in the compressor requires solution of the fundamental flow equations, the first part of this chapter is concerned with the development of the general flow equations. The assumptions and simplifications that are made to permit solution of the equations are then discussed. The equations are applied to determine the design velocity distribution in the meridional plane after a blade row. The necessary boundary-layer correction factors are indicated. In addition, the selection of design variables is discussed. A numerical example is then carried out with the equations and methods presented.

SYMBOLS

The following symbols are used in this chapter:

A_F frontal area, sq ft

a speed of sound, ft/sec

\mathcal{C}	curvature of meridional streamline, ft^{-1}
c_p	specific heat at constant pressure, $\text{Btu}/(\text{lb})(^{\circ}\text{R})$
D	diffusion factor
\mathcal{F}	blade force acting on gas, lb/lb
g	acceleration due to gravity, $32.17 \text{ ft}/\text{sec}^2$
H	total or stagnation enthalpy, Btu/lb
J	mechanical equivalent of heat, $778.2 \text{ ft-lb}/\text{Btu}$
K_{bk}	weight-flow blockage factor
K_e	energy-addition-correction factor
K_p	pressure-correction factor
K_{η}	efficiency-correction factor
M	Mach number
n	polytropic compression exponent
P	total or stagnation pressure, $\text{lb}/\text{sq ft}$
p	static or stream pressure, $\text{lb}/\text{sq ft}$
Q	external heat added to gas, $\text{Btu}/(\text{lb})(\text{sec})$
R	gas constant, $53.35 \text{ ft-lb}/(\text{lb})(^{\circ}\text{R})$
r	radius, ft
$r_{\mathcal{C}}$	radius of curvature of streamline in meridional plane, ft
S	entropy, $\text{Btu}/(\text{lb})(^{\circ}\text{R})$
T	total or stagnation temperature, $^{\circ}\text{R}$
t	static or stream temperature, $^{\circ}\text{R}$
U	rotor speed, ft/sec
u	internal energy, Btu/lb

V	air velocity, ft/sec
w	weight flow, lb/sec
z	coordinate along axis, ft
β	air angle, angle between air velocity and axial direction, deg
γ	ratio of specific heats
δ	ratio of total pressure to NACA standard sea-level pressure of 2116 lb/sq ft
δ^*	boundary-layer displacement thickness, ft
ϵ	angle between tangent to streamline projected on meridional plane and axial direction, deg
η	efficiency
θ	ratio of total temperature to NACA standard sea-level tempera- ture of 518.7° R
ν	kinematic viscosity, sq ft/sec
ρ	density, lb-sec ² /ft ⁴
σ	solidity, ratio of chord to spacing
τ	time
Φ	viscous dissipation of energy, Btu/(cu ft)(sec)
Ω	work-done factor
ω	angular velocity of rotor, radians/sec
$\bar{\omega}$	total-pressure-loss coefficient

Subscripts:

a	stagnation conditions
ad	adiabatic
av	average
d	design value neglecting wall boundary layer

h	hub
i	reference position, radial station where variables are known
id	ideal
m	meridional
m.a.	mass-averaged value
p	polytropic
R	rotor
r	radial direction
S	stator
ST	stage
t	tip
z	axial direction
$\alpha, \beta, \gamma, \delta, \epsilon$	radial design stations at 10, 30, 50, 70, and 90 percent of blade height from tip, respectively
θ	tangential direction
0	station ahead of guide vanes
1	station at rotor inlet
2	station at stator inlet
3	station at stator exit
Superscript:	
'	relative to rotor

STATEMENT OF DESIGN PROBLEM

Specification of Compressor Performance and Configuration Requirements

The design of the axial-flow compressor begins with the determination of the over-all performance specifications obtained from the over-all

3374

CG-21

engine and airplane requirements. In general, the engine inlet-air conditions (pressure, temperature, and density), engine thrust, engine air flow, turbine-inlet temperature, and compressor pressure ratio are fixed by cycle and flight-plan analyses such as are discussed in chapter II (ref. 1). The compressor-inlet hub-tip diameter ratio, the component tip diameters, the compressor rotational speed, the compressor-inlet axial velocity, and the compressor-discharge velocity are then determined considering the compressor efficiency, turbine stresses, compressor stresses, performance of the various components, engine weight, and engine space limitations in the airplane. The interrelation of some of these factors (compressor air flow per unit frontal area, compressor pressure ratio, rotational speed, turbine size, and turbine stresses) is discussed in reference 2. It should be emphasized that a large number of compressor configurations are possible for given over-all performance requirements. The choice of a given configuration is based on a compromise among the various performance and geometric parameters. This compromise depends in turn on the intended use of the engine.

Flow and Geometry Conditions to Be Determined

The design procedure involves an iterative solution of the flow equations after each blade row. Thus, the flow conditions and hub and tip diameter after the first blade row must be calculated from the known inlet and the specified design conditions. The blade-element loadings and Mach numbers selected must be consistent with the attainment of low loss as indicated by the loss data presented in chapters VI and VII. The resulting flow must also be acceptable to the following blade row. After a satisfactory solution for these conditions has been found, the resulting flow distribution after the blade row becomes the inlet condition for the following row. The flow conditions and geometry of the second blade row are then determined. The same procedure is repeated all through the machine until the desired over-all pressure ratio and discharge velocity are obtained.

When the flow conditions have been calculated after a given blade row, the blade sections may be selected to give the desired air turning or the desired blade work. The incidence- and deviation-angle data correlated in chapter VII may be used to assist in this selection. Some consideration of off-design performance may be required in the selection of blading. In addition, the loss correlations that are presented in chapter VII enable the designer to reestimate the originally assumed blade-element losses for the particular blade configuration selected. These reestimated loss data are then used to recalculate the flow distribution after the blade row by the methods of the present chapter.

GENERAL EQUATIONS

The basic equations that apply to the general case of the flow of a real compressible fluid through a turbomachine can be formulated from the conservation laws of matter, momentum, and energy, along with the thermodynamic equation of state. As pointed out in reference 3, these general basic equations of the flow can be stated as follows:

The equation of state for a perfect gas:

$$p = g\rho R t \quad (1)$$

The energy equation:

$$\frac{Du}{D\tau} + p \frac{Dp^{-1}}{D\tau} = Q + \frac{\Phi}{\rho} \quad (2)$$

The continuity equation:

$$\frac{\partial \rho}{\partial \tau} + \nabla \cdot (\rho \bar{V}) = 0 \quad (3)$$

The Navier-Stokes equation:

$$\frac{D(\bar{V})}{D\tau} = g\bar{F} - \frac{1}{\rho} \nabla p + \nu \left[\nabla^2(\bar{V}) + \frac{1}{3} \nabla(\nabla \cdot \bar{V}) \right] \quad (4)$$

Basic Assumptions

The simplifying assumptions usually made in the treatment of the problem of flow through axial-flow compressors are as follows:

(1) The general flow equations are applied only to compute flow distributions between blade rows where blade forces are nonexistent.

(2) The flow is assumed to be steady and axially symmetric. The theoretical significance of this assumption is discussed in chapter XIV (ref. 4). However, when blade-element data including some of the effects of unsteady asymmetric flow conditions are used in calculating the velocity distributions, the errors introduced by this assumption are expected to be small.

(3) The local shearing effects of viscosity (between blade rows) are neglected by dropping the viscosity terms in the flow equations. However, the accumulated effects of upstream viscous action in increasing entropy are considered by use of experimentally determined blade-element

performance. Empirical corrections are also made when required for wall boundary-layer effects on required flow area and mass-averaged energy addition and efficiency.

(4) Heat transfer is neglected.

Simplified Flow Equations

As a result of the preceding assumptions and the use of the definition of entropy, the general flow equations may be combined and restated as follows:

$$Jg(H_2 - H_1) = \omega [(rV_\theta)_2 - (rV_\theta)_1] = (UV_\theta)_2 - (UV_\theta)_1 = Jgc_p(T_2 - T_1) \quad (5)$$

$$\nabla(\rho \bar{V}) = 0 \quad (6)$$

$$Jg\bar{V}H = Jgt\bar{V}S + \bar{V} \times (\nabla \times \bar{V}) \quad (7)$$

Equation (5) relates the change in stagnation enthalpy along a streamline at axial stations ahead of and behind a rotor blade row to the change in angular momentum and the angular velocity of the wheel. Of course, the stagnation enthalpy is constant along a streamline passing through a stator blade row if it is assumed that the heat transfer from streamline to streamline is negligible.

Equation (6) states the law of conservation of matter, which, for application to compressor design, may be expressed as

$$w_1 = 2\pi g \int_{r_{h,1}}^{r_{t,1}} \rho_1 V_{z,1} r_1 dr_1 = w_2 \quad (8)$$

This equation will be discussed in detail in a later section with reference to boundary-layer blockage corrections and with reference to application of the flow equations in the design procedure.

Equation (7) is referred to as the equilibrium equation for the fluid between the blade rows.

SOLUTIONS OF EQUILIBRIUM EQUATIONS

The equations presented in the preceding section may be solved in several ways within the assumptions stated. Most of these solutions differ only in the simplifications made in the equilibrium equation (eq. (7)).

Since the design methods presented here are concerned with finding the radial variation of flow at a specified axial station, the radial component of equation (7) is applicable. For the assumed axially symmetric flow between blade rows, this component equation is

$$Jgc_p \frac{\partial T}{\partial r} = Jgt \frac{\partial S}{\partial r} + V_\theta \frac{\partial V_\theta}{\partial r} + \frac{V_\theta^2}{r} + V_z \frac{\partial V_z}{\partial r} - V_z \frac{\partial V_r}{\partial z} \quad (9)$$

As in the method of reference 5, it has generally been assumed in design applications that the meridional velocity $V_m = \sqrt{V_z^2 + V_r^2}$ is given by the axial velocity V_z and that $\partial V_r / \partial z = 0$. Such a condition (generally referred to as the "simplified-radial-equilibrium" condition) has been successfully used in low-aspect-ratio and lightly loaded blade-row designs. However, a less restricted design solution may be necessary for high Mach number, highly loaded designs. Several analyses (refs. 3 and 6 to 9) have been made to determine the factors influencing the meridional velocity distribution. The analysis of reference 3 considers the effect of the radial motion resulting from velocity-distribution changes through a blade row and evaluates the magnitude of this effect for several cases by assuming that the air flows through the compressor along sinusoidal streamlines. The analyses of references 6 and 7 for incompressible flow also consider the effects of radial motion due to velocity-distribution changes through the compressor. These analyses consider the effects of the velocity induced by the gradients in circulation or vorticity along the blade on the velocity distribution ahead of and behind the blade row. The procedure permits evaluation of the mutual interference effects of blade rows in the multistage compressor. These analyses neglect the radial motion due to the blade blockage resulting from blade thickness variations. Reference 8 presents a simplified analysis of the effect of the radial variation of blade thickness on inlet velocity and incidence-angle distributions. This analysis also assumes axial symmetry but makes a correction in the flow continuity relation for blade thickness. In general, the higher the inlet Mach number, the greater the variation in the axial velocity from hub to tip.

All the preceding investigations neglect the effects of gradients of entropy on radial distributions of velocity and therefore are not directly applicable in regions of high loss. Reference 9 applies experimental data to determine the relative magnitudes of the effects on velocity distributions of the entropy-gradient term for a wide variety of axial-flow-compressor blade rows. Although vast differences generally exist in the shapes of the velocity distributions in the inlet and the outlet stages of the multistage compressor, essentially the same techniques (assuming a knowledge of the entropy distribution across the annulus) can be used to calculate the velocities. Consideration of the entropy gradients was particularly necessary in the rear stages, where the accumulated effects

of viscosity noticeably affected the velocity distribution. On the other hand, the complete radial acceleration term appeared to be significant for the highly loaded inlet stages investigated, where the wall curvatures were large.

The following discussion presents the various forms of the radial-equilibrium equation that may be used in the compressor design procedure.

Simple-Radial-Equilibrium Equation Neglecting Entropy Gradients

The simplest solution of the radial-equilibrium equation (eq. (9)), usually referred to as the "simple-radial-equilibrium solution," has been widely used in compressor design. It is arrived at by assuming (1) that the derivative of V_r with respect to z is zero, and (2) that the derivative of S with respect to r is zero. These assumptions are made, of course, only at the fixed value of z . The resulting equation is

$$Jgc_p \frac{\partial T}{\partial r} = V_\theta \frac{\partial V_\theta}{\partial r} + \frac{V_\theta^2}{r} + V_z \frac{\partial V_z}{\partial r} \quad (10)$$

which is referred to herein as the "isentropic-simple-radial-equilibrium" or "isre" equation. In this case, "isentropic" refers simply to the condition of radially constant circumferentially averaged entropy within the space between blade rows outside the boundary layers. Thus, the entropy of the flow may still change through the blade row.

Equation (10) may be integrated between any two radial positions in the free-stream region of the annular flow area at an axial station between blade rows. For purposes of a design procedure, it is most convenient to integrate between some reference radius, at which the dependent variables are known or assumed, and the other radial positions. The resulting integrated form of the isre equation is

$$V_z^2 - V_{z,i}^2 = 2gJc_p (T - T_i) - (V_\theta^2 - V_{\theta,i}^2) - \int_{r_i}^r \frac{2V_\theta^2}{r} dr \quad (11)$$

The radial variation of axial velocity or $V_z^2 - V_{z,i}^2$ at the blade-row outlet is obtained by prescribing either the stagnation-temperature or tangential velocity distribution after the blade row. These two parameters (stagnation temperature and tangential velocity) are related by equation (5) for the known flow conditions at the inlet of the blade row. As will be shown later, the value of the reference axial velocity $V_{z,i}$

is assigned and the mass continuity condition is applied to determine the required annulus area. For those cases in which the annulus area is specified, the reference velocity is determined by application of the continuity relation.

A series of charts is presented in chapter IX to permit rapid solution of equation (11).

Simple-Radial-Equilibrium Equation Considering

Radial Gradients of Entropy

The major effect of upstream viscous action is manifested by an increase in the entropy of the flow. The major effects of viscosity on the axial velocity distribution are, therefore, accounted for in the radial-equilibrium equation through the use of the term involving the radial gradients of entropy. Thus, the equation presented here is obtained from equation (9) by assuming only that the derivative of the radial velocity V_r with respect to the axial distance z is zero. Equation (9) then becomes

$$Jgc_p \frac{\partial T}{\partial r} = Jgt \frac{\partial S}{\partial r} + V_\theta \frac{\partial V_\theta}{\partial r} + \frac{V_\theta^2}{r} + V_z \frac{\partial V_z}{\partial r} \quad (12)$$

Equation (12), hereinafter referred to as the "nonisentropic-simple-radial-equilibrium" or "nisre" equation, may be integrated between two radial positions at an axial station between blade rows to give

$$V_z^2 - V_{z,i}^2 = 2gJc_p (T - T_i) - (V_\theta^2 - V_{\theta,i}^2) - 2 \int_{r_i}^r \frac{V_\theta^2}{r} dr - 2JgR \int_{r_i}^r t \frac{\partial \left(\frac{S}{R} \right)}{\partial r} dr \quad (13)$$

The nisre equation can be solved in the same manner as the isre equation, except that the entropy term must be evaluated. By the definition of stagnation conditions, stagnation entropy is identically equal to static entropy at any given point. Therefore, the change in the entropy along a streamline from the inlet to the outlet of a blade row may be

expressed as

$$J\left(\frac{S}{R}\right)_2 - J\left(\frac{S}{R}\right)_1 = \ln \left[\frac{\left(\frac{T_2}{T_1}\right)^{\frac{\gamma}{\gamma-1}}}{\frac{P_2}{P_1}} \right] \quad (14)$$

In the design procedure, the temperature ratio is assumed or is determined from a specified variation in tangential velocity by use of equation (5). The stagnation-pressure ratio may be related to the stagnation-temperature ratio in terms of either a polytropic blade-element efficiency η_p , or a stagnation-pressure-loss coefficient $\bar{\omega}$.

When the polytropic efficiency or polytropic compression exponent is used, the stagnation-pressure ratio is given by

$$\frac{P_2}{P_1} = \left(\frac{T_2}{T_1}\right)^{\frac{\eta_p \gamma}{\gamma-1}} = \left(\frac{T_2}{T_1}\right)^{\frac{n}{n-1}} \quad (15)$$

The blade-element data of chapters VI and VII present the blade-element loss in terms of $\bar{\omega}$. When these data are used, it is more convenient to express the stagnation-pressure ratio across the blade element in terms of $\bar{\omega}'$, stagnation-temperature ratio, and inlet-air Mach number relative to the blade element. The expression for pressure ratio is restated from chapter VII as

$$\frac{P_2'}{P_1'} = \left(\frac{P_2'}{P_1'}\right)_{id} - \bar{\omega}' \left\{ 1 - \left[1 + \frac{\gamma-1}{2} (M_1')^2 \right]^{\frac{-\gamma}{\gamma-1}} \right\} \quad (16)$$

where

$$\left(\frac{P_2'}{P_1'}\right)_{id} = \left[1 + \frac{\gamma-1}{2} \frac{(\omega r_2)^2}{\gamma g R T_1'} \left(1 - \frac{r_1^2}{r_2^2} \right) \right]^{\frac{\gamma}{\gamma-1}}$$

This equation holds for both rotor and stator when the appropriate indices are used.

The ideal relative pressure ratio $(P'_2/P'_1)_{id}$ can be taken equal to 1.0 for those cases in which the variation in the streamline radius across the rotor is negligible, a condition obtained in high hub-tip ratio or lightly loaded blade rows.

For convenience in the design procedure, any upstream station at which the entropy is essentially constant radially - for example, the compressor-inlet station 0 - is used as the reference station. Therefore, the radial variation of entropy is, from equation (14),

$$J \frac{\partial \left(\frac{s}{R} \right)_2}{\partial r_2} = \frac{\partial}{\partial r_2} \left\{ \ln \left[\frac{\left(\frac{T_2}{T_0} \right)^{\frac{\gamma}{\gamma-1}}}{\frac{P_2}{P_0}} \right] \right\} \quad (17)$$

The static temperature appearing in the second integral of equation (13) can be expressed in terms of the velocity components and stagnation temperature as follows:

$$Jgc_p t = Jgc_p T - \frac{v_\theta^2}{2} - \frac{v_z^2}{2} - \frac{v_r^2}{2} \quad (18)$$

For the simplified-radial-equilibrium solutions, the radial velocity term is neglected in equation (18). In general, this V_r component can be neglected in the stages with high hub-tip ratio without introducing significant errors in static temperature. In the stages with low hub-tip ratio (where wall slopes may be large), however, V_r may have to be considered in this equation by estimating a streamline slope in the meridional plane and expressing V_r as a function of V_z and this slope.

Radial-Equilibrium Equation Considering Radial Accelerations

As pointed out in the previous discussions on the simple-radial-equilibrium equations, high hub-tip radius ratio and lightly loaded blade rows have been successfully designed by assuming that the meridional velocity V_m is equal to the axial velocity V_z and that the gradient of radial velocity V_r along the axial direction is zero. In this case, the radial gradient of static pressure is

$$\frac{dp}{dr} = \rho \frac{v_\theta^2}{r}$$

However, for high-aspect-ratio, highly loaded stages, the effects of streamline curvature become significant. In this case, the contribution of the radial acceleration of the meridional velocity to the pressure gradient in the radial direction must be considered. The radial gradient of static pressure for this general case of curved streamline flow may be stated as

$$\frac{dp}{dr} = \rho \left(\frac{v_\theta^2}{r} \pm \frac{v_m^2 \cos \epsilon}{r_c} \right)$$

where the angle ϵ is the angle of the streamline with respect to the axial direction, and r_c is the radius of curvature of the streamline.

An accurate determination of the radius of curvature of the streamline and the slope of the streamline (which determines the angle ϵ) requires a knowledge of the shape of the streamline through the blade row. The streamline configuration is a function of the annular-passage area variation, the camber and thickness distribution of the blades in the radial and axial directions, the blade forces existing within the blade row, and the flow angles at inlet and discharge of the blade row. Because the effects of radial acceleration have been small in conventional subsonic-compressor designs, very little information is available concerning the relative importance of each of these variables in determining the effects of radial accelerations in the highly loaded designs now being studied. The usefulness of several methods that have been proposed for evaluating these radial accelerations has, therefore, not yet been established.

Several analyses, such as the work of references 10 and 11, have been applied to determine velocity distributions throughout the flow field in high-solidity mixed-flow compressors and axial-flow turbines. These procedures require estimation of a streamline-orthogonal flow system through the blade row. The distribution of velocity along the orthogonal is then determined from the known inlet conditions, a mean air-turning variation along each streamline, and a blade thickness variation along each streamline. Since this method requires estimation of the streamlines as well as a knowledge of the blade configuration, it is apparent that it becomes an iterative solution.

An approximate evaluation of the radial acceleration term is also made in reference 3 by assuming the streamline shape to be sinusoidal. A similar technique for evaluating the effect of radial accelerations is applied in reference 12. The analysis of reference 3 further assumes that the product of the radial velocity at a given axial station between blade rows and the axial gradient of axial velocity is negligible and that the slope of the streamlines at this axial station is zero. Therefore, for the assumptions of reference 3, the last term (the radial-flow

term) of equation (9) may be expressed as

$$V_z \frac{\partial v_r}{\partial z} = \mathcal{C} V_z^2$$

Results obtained with this procedure are shown in reference 13 to agree with results obtained from the general three-dimensional-flow solution described in reference 14 for a single-stage nontapered-passage compressor.

In addition to the preceding analyses, which attempt to consider the effects of the blades on the streamline configuration through the blade row, several analyses, such as the work of references 15 to 17, present methods of estimating the effects of radial velocity and curvature terms from simplified calculations of the flow only between blade rows. In these solutions, a set of smooth streamlines is estimated through the compressor stage on the basis of the velocities calculated between blade rows. It is apparent that these methods do not consider the effects of the blade thickness and camber distributions and the effects of the blade forces on the streamline curvature.

In view of the present meager knowledge of the effects of the various design parameters on the radial acceleration terms in the general flow equations, it seems reasonable to use the simpler methods of accounting for these effects as stop-gap design measures. In addition, it may be desirable at the present time to try to alleviate the conditions leading to large radial accelerations. In the case of highly loaded designs having high aspect ratios, one technique for reducing the effects of radial accelerations is to taper the tip of the compressor inward so that the hub curvature is reduced. Definitive experimental and analytical work is still required to evaluate the various techniques that have been suggested for computing velocity distributions including the effects of radial accelerations.

CONSIDERATION OF WALL BOUNDARY-LAYER EFFECTS

The equilibrium equations that must be solved in determining the meridional distribution of flow conditions between blade rows in the axial-flow machine were discussed in the preceding section. When the simple-radial-equilibrium equations are suitable, a procedure similar to the following is required to execute a blade-row design if the inlet conditions are given:

- (1) The tip radius at the blade-row discharge is specified.

(2) The axial and tangential velocities at the tip radius after the blade row are assumed. These values must be consistent with the considerations for low losses and compatible with the requirements of the following blade row.

(3) The radial distribution of tangential velocity after the blade row is specified.

(4) The radial distribution of energy addition in the blade row is determined from the known inlet conditions and the specified distribution of tangential velocity by use of equation (5).

(5) The radial distribution of loss and, therefore, entropy is assumed based on blade-element data taken in a similar flow environment.

(6) The radial distribution of axial velocity is calculated.

(7) The radial distributions of all other flow properties are calculated.

(8) The continuity condition is used to calculate the hub radius from the known tip radius and mass flow and the calculated distributions of axial velocity and density.

When the radial acceleration terms associated with streamline curvature become significant, this procedure may be considered as an initial step in the design system. It then becomes necessary to recalculate the radial distributions of axial velocity and other flow properties (items (6) and (7)) and to determine a new hub radius (item (8)).

This technique is referred to as method I. The critical information in this solution is the radial distribution of loss or entropy from wall to wall. Figure 1 illustrates a form of the entropy distribution that might be encountered after a blade row in a compressor. The large rise in entropy at the end walls results from the losses in the wall boundary layers. Across the major portion of the flow passage, the entropy variation is illustrated as being relatively small. It must be emphasized that (as indicated in ref. 9) some cases have been encountered where the variation of entropy is large even in the main stream. In any case, the "nonisentropic" equations can be applied to determine the velocity distribution even into the boundary layers if means of predicting the entropy distribution are available. This procedure would be a direct process near the tip, since the tip radius is specified. Near the hub, however, the entropy and other flow properties could not be determined until after the hub radius is known. Therefore, iteration procedures must be used near the hub for this complete solution. The distribution of flow properties and the annulus area determined from these procedures then permit calculation of the mass-averaged energy addition, pressure ratio, and efficiency for the stage.

It is, of course, apparent that the determination of the entropy distribution from wall to wall for all the possible design velocity diagrams, blade-row geometries, and locations in the multistage compressor would require very extensive tests of many different compressors. Such detailed information requires the analysis of much more multistage-compressor data than are currently available. Substitute techniques for the determination of the annulus area after the blade row and the mass-averaged efficiency, energy addition, and pressure ratio have therefore been used.

One such technique (referred to in this report as method II) involves dividing the flow passage into three parts, the tip boundary layer, the mainstream region, and the hub boundary layer. In the process of solution of the equations, the wall boundary-layer regions are actually treated as one region. The velocities across the annulus are computed by the previously itemized procedure assuming that no wall boundary layer exists. The entropy distribution used in the determination of the velocities is obtained from the blade-element loss data presented in chapter VII. If, as is illustrated in figure 1, the entropy gradient is small in the main stream, then the velocity distribution may be computed using the isre equation (eq. (10) or (11)). If the blade-element loss data indicate a large variation of entropy in the main stream, then the nisre equation (eq. (12) or (13)) must be used to determine the velocity distributions.

The effects of the wall boundary layers on the required annulus area and on the mass-averaged energy addition, pressure ratio, and efficiency are determined in method II from the velocity distributions calculated assuming appropriate "gross" correction factors and the absence of wall boundary layers. Although the evaluation of these gross correction factors will also require extensive compressor testing and analysis, it is anticipated that the general correlations with velocity-diagram parameters and environment may be more readily attainable than those for the detailed entropy distributions in the boundary layers. In addition, indications of the magnitudes of these gross correction factors may be obtained from comparisons of design and measured velocities in the mainstream region.

The general effects of wall boundary layers on rotor performance are indicated in figure 2. This figure is an example of a design that has been worked out for constant mass flow (fig. 2(a)) and energy addition (fig. 2(b)) along the radius without considering the effect of the end-wall boundary layers. The isre solution was used to determine the velocities across the annulus from the specified energy addition (fig. 2(b)), assuming that the stagnation-pressure loss was constant along the radius (fig. 2(c)) and that the effects of the wall boundary layers could be neglected. For such a design, the conditions that might be measured in the flow annulus when the mainstream flow conditions are the same as

the design conditions are indicated by the dashed curves. It is apparent that the integrated weight flow is less than the design weight flow and the mass-averaged energy addition or temperature rise and the mass-averaged pressure ratio may differ from the design value. The average values of mass flow, temperature rise, and pressure ratio are indicated on the figure as the dot-dash lines. Therefore, three correction factors are required in method II to account for the presence of the wall boundary layers. An annulus-area correction must be applied to account for the blockage effect of the wall boundary layer so as to ensure the attainment of the design weight flow; a temperature-rise factor must be applied to calculate the mass-averaged energy addition for the blade row at this design weight flow; and a pressure-ratio factor must be applied to permit calculation of the mass-averaged pressure ratio.

Another system of correction that has been used extensively involves specifying the annulus area and adjusting the axial velocity level across the mainstream region by the continuity equation to ensure the attainment of the design weight flow. This method of design and correction involves principally a rearrangement of the previously enumerated design steps. Other correction factors are still necessary to permit calculation of the mass-averaged energy addition and pressure ratio.

It must be emphasized that, in all the techniques described, the velocities across the mainstream region of the annulus area and the annulus area geometry are calculated with blade-element loss or efficiency data obtained from stages operating in environmental conditions similar to those of the stage being designed. Such blade-element data, principally for inlet stages, are presented in chapter VII.

For those cases where blade-element loss data are not available or where a general design review of a large number of multistage compressors is required, a blade-row and stage mass-averaged efficiency may be assumed to determine the total pressure at each blade element from the specified energy addition. It is assumed in this approach that the blade-element efficiency is equal to the blade-row mass-averaged efficiency. Although this is admittedly not an exact approach, it has been found to give reasonable design accuracy and serves as an extremely useful tool, especially as a first roughing-out step in the design procedure. This method is referred to in the present report as method III. It is described in detail and applied through the use of charts in chapter IX. The method usually assumes that the correction for determining mass-averaged energy addition is negligible. A correction is required for wall boundary-layer blockage in determining the annulus area.

The following discussion is concerned with the boundary-layer correction factors required in method II for the calculation of the annulus geometry and the mass-averaged temperature rise and pressure ratio.

Although only very limited amounts of blade-element data and boundary-layer correction data are available, it is felt that this method offers the basis for an accurate design system.

Correction for Weight-Flow Blockage Factor

The correction for weight-flow blockage factor is intended to ensure the attainment of the design weight flow with the design velocity distribution over the major portion of the annulus area. Because of the lack of extensive data on the boundary-layer characteristics in the compressor, an empirically obtained correction factor that is applied as a gross boundary-layer blockage factor has usually been applied. Although this empirical correction factor leaves much to be desired, it has been used successfully in design. This gross blockage factor is designated by K_{bk} and is defined by the following continuity equation:

$$w = \pi g \int_{r_h}^{r_t} \rho V_z d(r^2) = K_{bk} \pi g \int_{r_h}^{r_t} [\rho V_z d(r^2)]_d = \pi g \int_{r_h + \delta_h^*}^{r_t - \delta_t^*} [\rho V_z d(r^2)]_d \quad (19)$$

The subscript d refers to design values calculated across the annulus as if no wall boundary layer were present. In essence, this gross blockage factor involves the determination of the ideal (no boundary layer) velocity distribution required to pass a flow greater than the design flow. For a given value of tip radius, the hub radius is thus decreased as K_{bk} is decreased (or boundary-layer allowance is increased).

Very little useful data regarding the best values of blockage factor are currently available from multistage-compressor investigations. Reference 15 suggests values of 0.98 for inlet stages and 0.96 for all others. Some single-stage data indicate blockage factors of 0.96 after both rotor and stator. These blockage factors are not expected to be the same for compressors differing in size, axial velocity diffusion, chord length, and so forth.

Correction Factor for Stagnation-Temperature Rise

Besides occupying space and thereby affecting the weight flow, the wall boundary layer causes the mass-averaged energy addition or stagnation-temperature rise to differ from the design value when the main-stream velocities are equal to the design values. Application of the blockage-factor correction does not eliminate the need for the temperature-rise or energy-addition factor in computing the mass-averaged temperature

rise for the stage from the design velocities. This temperature-rise or energy-addition factor K_e can be defined by the following equation:

$$\begin{aligned}
 \left(\frac{T_2}{T_1}\right)_{m.a.} - 1.0 &= \frac{\int_{r_{h,2}}^{r_{t,2}} \left(\frac{T_2}{T_1} - 1\right) [\rho V_z d(r^2)]_2}{\int_{r_{h,2}}^{r_{t,2}} [\rho V_z d(r^2)]_2} \\
 &= \frac{K_e K_{bk} \int_{r_{h,2}}^{r_{t,2}} \left[\left(\frac{T_2}{T_1} - 1\right) \rho V_z d(r^2)\right]_{2,d}}{K_{bk} \int_{r_{h,2}}^{r_{t,2}} [\rho V_z d(r^2)]_{2,d}} \\
 &= K_e \frac{\int_{r_{h,2}}^{r_{t,2}} \left[\left(\frac{T_2}{T_1} - 1\right) \rho V_z d(r^2)\right]_{2,d}}{\int_{r_{h,2}}^{r_{t,2}} [\rho V_z d(r^2)]_{2,d}} \quad (20)
 \end{aligned}$$

It should be emphasized that the temperature-correction factor is used only in calculating the mass-averaged energy addition once the design velocity distributions and the annulus area geometry have been determined in the design process. It does not influence the design velocity diagram or the hub radius.

In most cases, the temperature-rise-correction factor is assumed equal to 1.0. However, analysis of limited data taken on the single-stage rotor of reference 18 indicates that a value of 1.03 for the temperature-rise-correction factor may be more reasonable. More extensive and precise data are still required.

Correction Factor for Stagnation Pressure

In the design procedure, the value of the stagnation-pressure loss $\bar{\omega}$ at any blade element in the mainstream region can be estimated from

the velocity diagram by using the correlation of diffusion factor with $\bar{\omega}$ presented in chapter VII. This method tends to give a higher mass-averaged value of stagnation pressure at a blade-row outlet and higher mass-averaged efficiency than are actually achieved, since consideration of the wall boundary layer is not completely included in the blade-element data. Hence, a correction for the wall boundary layer must be applied in determining the mass-averaged pressure ratio. This pressure-ratio correction factor K_P can be defined by the following equation:

$$\left(\frac{P_2}{P_1}\right)_{m.a.} = \left\{ \frac{K_P K_{bk} \int_{r_{h,2}}^{r_{t,2}} \left[\left(\frac{P_2}{P_1}\right)^{\frac{\gamma-1}{\gamma}} - 1 \right] [\rho V_z d(r^2)]_{2,d}}{K_{bk} \int_{r_{h,2}}^{r_{t,2}} [\rho V_z d(r^2)]_{2,d}} + 1.0 \right\}^{\frac{\gamma}{\gamma-1}}$$

$$= \left\{ K_P \frac{\int_{r_{h,2}}^{r_{t,2}} \left[\left(\frac{P_2}{P_1}\right)^{\frac{\gamma-1}{\gamma}} - 1 \right] [\rho V_z d(r^2)]_{2,d}}{\int_{r_{h,2}}^{r_{t,2}} [\rho V_z d(r^2)]_{2,d}} + 1.0 \right\}^{\frac{\gamma}{\gamma-1}} \quad (21)$$

Limited data on the rotor with 0.4 hub-tip diameter ratio described in reference 18 indicate that the value of K_P may be approximately 1.0 after a rotor. These data were taken from an inlet-stage rotor where wall boundary layers were small. Detailed data after stators are not yet available.

A knowledge of the mass-averaged temperature rise and the mass-averaged pressure ratio permits calculation of the mass-averaged

efficiency by the following equation:

$$\eta_{m.a.} = \frac{\left(\frac{P_2}{P_1}\right)_{m.a.}^{\frac{\gamma-1}{\gamma}} - 1}{\left(\frac{T_2}{T_1}\right)_{m.a.} - 1} \quad (22)$$

It is apparent that an efficiency correction similar to the temperature-rise- and pressure-ratio-correction factors may also be applied to determine the mass-averaged efficiency of a stage if the average efficiency based on the mainstream velocities and blade-element losses is known. Thus, the average rotor efficiency is obtained by multiplying the efficiency calculated from the mainstream flow conditions by the efficiency-correction factor. As a result of the correction factors determined from the data of reference 18 for the temperature rise and the pressure ratio, the efficiency correction K_η for the rotor was found to be approximately equal to 0.97.

Work-Done-Factor System

A boundary-layer correction procedure that has been widely used by British designers (refs. 19 to 21) includes the "work-done" factor, which is used to estimate stage temperature rise from design values of axial velocity and air angles. In this case, the hub and tip radii of the blade row are prescribed. For a given weight flow through the blade row, the effect of the wall boundary layers is to increase the axial velocities above the design values across the mainstream portion of the annulus and to decrease the axial velocity near the end walls as shown in figure 3. Because of the high values of velocity over the major portion of the annulus, the mass-averaged energy addition at the design flow is lower than the design value (i.e., the low mass flow at the end walls does not weight the temperature rise in this region enough to compensate for the central-portion deficit in work), resulting in less "work done." Thus, the actual stage temperature rise is lower than that predicted on the basis of the design values of velocity and air angles. The work-done factor Ω is defined in reference 19 by the following relation:

$$c_p J g \Delta T = \Omega (U_2 V_{z,2} \tan \beta_2 - U_1 V_{z,1} \tan \beta_1)_d$$

where the flow parameters are the ideal values calculated assuming that wall boundary layers do not exist.

Although it was developed for designs with free-vortex velocity diagrams, the work-done factor has since been applied to other types of diagrams. It is necessary in this system to set the blades (on the basis of the design velocities) at an incidence angle higher than the optimum value. The higher velocities actually obtained across the main stream will then produce incidence angles close to the optimum values.

Thus, the design velocity and blade-angle distributions are set so as to ensure that application of the work-done factor will result in the desired energy addition. It is then usually assumed that the major part of the correction for boundary-layer blockage has been considered by application of the work-done factor.

SELECTION OF DESIGN VARIABLES

The design calculation of the multistage-compressor blade rows requires first the specification of certain aerodynamic and geometric characteristics. Among these are the inlet values of hub-tip radius ratio, weight flow, and wheel speed; the variation through the compressor of blade loading, axial velocity, and tip diameters; and an additional parameter specifying the radial distribution of work or velocity in each stage. Since the emphasis in aircraft compressors is for high mass flow per unit frontal area and high pressure ratio per stage, the discussion of the selection of design variables is slanted toward achieving these goals.

The selection of design variables and the entire design procedure involve an iterative process in which compromises are necessary at each step. The process can be shortened by using a quick approximate method for the initial parts of the design and, after a rough outline of the compressor is determined, using the more accurate methods to fix the details of the compressor blading. Thus, a trial hub and tip contour for the entire compressor can be obtained from the method that uses the isre equation along with an assumed efficiency for the blade rows. The majority of the necessary compromises can be made in this step, so that the required performance is reasonably assured without exceeding specified limitations on diverse flow variables.

Velocity Diagrams

A general velocity diagram for a fixed radius is shown in figure 4. In the past, many compressors have been designed to achieve a specific type of velocity diagram at a given radius or given radii. A discussion of the commonly used velocity diagrams and their application in the design procedure is given in references 3 and 22. The free-vortex diagram has been widely used because of its simplicity and the accuracy with

which flow distributions could be calculated for this type flow. Two-dimensional blade-element considerations (which are now known to be insufficient) showed that the symmetrical velocity diagram gave maximum blade-element-profile efficiency as well as high flow and stage pressure ratio for a subsonic Mach number limit. Therefore, this type of diagram also has been used extensively. As the various limitations of compressors became better known, more freedom was taken in the type of velocity diagram. With the advent of the transonic compressor and the removal of the subsonic Mach number limit, the free-vortex design returned to prominence for inlet stages. The absence of large gradients in outlet axial velocity with this type design facilitates the maintenance of recently established loading limits and the achievement of high pressure ratio.

Experimental tests of axial-flow compressors show that satisfactory performance can be obtained for a wide range of velocity-diagram types if the blade-loading and Mach number limits are not exceeded. Therefore, present design philosophy emphasizes the limitations as determined by Mach number and diffusion factor rather than the specific velocity diagram used. In general, an iterative procedure of specifying radial distribution of work (ΔH or ΔT) and checking all radial sections for extremes in diffusion factor or Mach number is satisfactory. A specification of a velocity diagram may in some cases be desirable to systematize the procedure or to utilize past experience.

Compressor-Inlet Conditions

Inlet hub-tip radius ratio and axial velocity must be specified to satisfy the design weight-flow requirement, which is fixed by an engine analysis. Figure 5 presents curves of compressor weight flow per unit frontal area against axial Mach number for constant values of hub-tip radius ratio. It is apparent from this figure that weight flow per unit frontal area increases with decreasing hub-tip radius ratio and with increasing axial velocity (or Mach number). Reduction in hub-tip ratio below approximately 0.4 may be expected to result in aggravated aerodynamic as well as mechanical problems, thus giving diminishing returns. For instance, the blade-element-flow choking problem ($M = 1.0$ at throat) at the compressor hub becomes more acute because of large fillets and blade thicknesses, while blade fastening may become difficult and blade stresses may become high.

Figure 5 also illustrates that the value of weight flow per unit frontal area depends on the value of inlet axial Mach number. However, design values of axial Mach number are fixed (for any desired blade speed and air prerotation) by the limiting relative inlet Mach number of the blade sections used in the inlet row. Thus, the relative inlet Mach number becomes the important variable and will be considered here.

The limiting relative Mach number for conventional subsonic blade shapes and designs is usually set at 0.7 to 0.8; while, for transonic blade shapes (thin blades with thin leading edges and solidity of the order of 1.0), good efficiencies have been obtained at Mach numbers up to 1.1 (ref. 23) and even higher. These limits are determined from loss and efficiency considerations, which in turn may be affected by blade-row choking considerations, particularly at the compressor hub. An analysis of the choking problem is presented for two-dimensional cascades in reference 24. If a cascade analysis is applied to a compressor rotor and does not indicate choking, there will probably be a built-in safety factor because of the advantage of the energy rise through the rotor.

In the past, inlet corotation has been used to reduce the relative Mach number at the rotor inlet. Since compressors have been operated efficiently at high values of relative inlet Mach number, the role of inlet guide vanes has become decreasingly important in compressor design. However, the use of counterrotation inlet guide vanes to increase Mach number at a given wheel speed for the attainment of high stage pressure ratio should not be overlooked when blade speed is otherwise limited.

Variation of Design Parameters through Compressor

Axial velocity. - In any compressor, values of axial velocity are fixed at two axial stations: at the compressor inlet by the weight flow and hub-tip ratio, and at the compressor exit by compressor-discharge diffuser and combustor-inlet requirements. With the trend toward higher compressor-inlet velocities, fixed combustor requirements will necessitate appreciable decreases in axial velocity through the unit. Care must also be taken that blade heights in the latter stages do not become so small that end-wall boundary layers and blade tip clearances occupy a large percentage of the passage and thus deteriorate performance. The exact scheduling of axial velocity through the compressor will depend largely on the individual blade-row requirements. Large axial velocity reductions across any blade element are to be avoided if high efficiency is desired.

Diffusion factor. - The diffusion factor, a blade-loading criterion discussed in reference 25, is given by

$$D = 1 - \frac{V_2^1}{V_1^1} + \frac{\Delta V_\theta^1}{2\sigma V_1^1} \quad (23)$$

The analysis of single-stage-compressor data in reference 25 indicates the following diffusion-factor limits for inlet stages: for the rotor tip, D less than 0.4; for the rotor hub, D less than 0.6; for the stator, D less than 0.6. The variation of limiting diffusion factor through the compressor is not yet known. Although this blade-loading

parameter (eq. (23)) is a good stop-gap, a more complete and general loading criterion and a better correlation of loss with loading is still required.

Efficiency. - The stage or blade-row efficiency, rather than the blade-element loss, may be used as a design parameter in certain design procedures (e.g., method III). Experimental investigations of axial-flow compressors indicate that, where blade-loading limits are not exceeded, the stage efficiencies remain at a relatively constant high value. A slight decrease in efficiency in the rear stages of the compressor has usually been attributed to distortions of the radial distributions of velocity in these blade rows. Also, the ratio of wetted area to flow area is greater in the latter stages than in the inlet stage, so that boundary-layer effects become more prominent. The design-speed peak adiabatic efficiency for an inlet stage operating as a single-stage unit is about 0.92. Of course, the assumed design efficiency will vary with the performance requirements of pressure ratio and weight flow and perhaps with axial position in the compressor.

Boundary-layer characteristics. - Unfortunately, there is very little information from which the boundary-layer growth through a compressor can be determined accurately beyond that mentioned in reference 15. Values of correction factors used to account for boundary-layer growth have been given and discussed in the section on weight-flow blockage. Data obtained from an 8-stage axial-flow compressor (ref. 26) indicate that the boundary-layer thickness (expressed as a percent of blade height) remained approximately constant through the last four stages near the design weight flow. Although the boundary layer in the compressor of reference 26 was thicker than might be generally expected, these results support the choice of a constant value of K_{bk} through the latter stages of an axial-flow compressor.

Physical Aspects

Physical considerations limit some compressor variables that affect the aerodynamics of the flow. The shape of the compressor outer casing is limited by restrictions on over-all size of the engine and accessories, and a constant-tip-radius configuration has been used in the past as a good compromise between aerodynamic and weight considerations. The required decrease in annular area from inlet to outlet is then obtained by gradually increasing the hub radius. Of course, other combinations of hub and tip shapes may be desirable for specific applications; for example, the section on radial-flow accelerations indicates that tapering the tip casing at the compressor inlet may be desirable to reduce hub-wall curvature effects, if these are otherwise detrimental.

The value of the solidity used in each blade row may be varied slightly to keep the blade loading (expressed for the present by the diffusion factor) within certain limits. Reasonable values of solidity for the transonic compressors appear to be in the order of 1.0 at the tip section. Extremely low solidities lead to poor guidance and high losses, while extremely high solidities lead to hub choking problems and high losses.

Although the tip clearance used in a compressor design is usually set by mechanical considerations, large effects of tip clearance on aerodynamic performance have been noted in various compressor investigations. Some effects of blade tip clearance are discussed in reference 27, which reports that the smallest clearance used in the series of tests gave the best rotor efficiency.

Off-Design Performance

In regard to compressor weight, it is desirable to select a design for the minimum number of stages consistent with good aerodynamic efficiency to achieve a specified over-all pressure ratio. Inasmuch as the compressor must also have good acceleration characteristics, good high flight Mach number performance, and a reasonable overspeed margin as well as satisfactory design-point operation, the off-design operating characteristics should be considered when the stagewise variation of blade loading is chosen. Possible means of determining the off-design operating characteristics are given in chapter X. At compressor speeds above and below design speed, the front and rear stages deviate considerably from design angle of incidence, operating over a range from choked flow to stall (ref. 28). Therefore, it is important to prescribe blading and velocity diagrams in the front and rear stages that will permit the attainment of a large stall-free range of operation.

Consideration of compressor-inlet flow distortions resulting from inlet-diffuser boundary layers, aircraft flight at angle of attack, and so forth, may also influence the stage design selection, especially in the inlet stages of the compressor.

APPLICATION OF EQUATIONS

Design Equations

The equations to be used in a design are grouped in table I for ease of reference. They are either repeated or are directly derived from equations in the previous sections. Additional relations are obtained from the velocity diagram such as is shown in figure 4.

Equations (D2b) (the isre solution) and (D3b) (the nisre solution) for determining the axial velocity variation along the radius are obtained from equations (D2a) and (D3a) by evaluating the integrals by the trapezoidal rule. [In addition, eqs. (17) and (18) or eqs. (D12) and (D13) (with the radial velocity equal to zero) are applied to derive eq. (D3b) from eq. (D3a).] An accurate evaluation of the axial velocity distribution by use of equations (D2b) and (D3b) requires that the reference radius be shifted from point to point. That is, the integration is first carried out from the initial reference radius to an adjacent radial station. The computed values of velocity at this adjacent radial station are then used as the reference-point values to compute conditions at the following radial station. Thus, the effect of any variation of entropy, temperature, and tangential velocity on the axial velocity distribution may be accurately considered if enough radial stations are specified across the annulus area.

Equation (D11) is a form of (D2a) for the special case of inlet guide vanes where the stagnation temperature is constant. This equation is derived in reference 29. Equation (D10b) is an alternate form of the diffusion-factor relation (eq. (D10a)). A graphical solution of equation (D10b) is presented in chapter IX.

General Determination of Axial Velocity Distribution

The design of the multistage compressor requires the solution of the general flow equations after each blade row in the compressor. This section is concerned with the methods of determining the velocity distributions after the inlet guide vanes and rotor and stator blade rows.

For the case of no inlet guide vanes or for guide vanes that impose a vortex turning distribution, it may be assumed for the initial design trial that the axial velocity is constant along the radius at the inlet to the first rotor row. For the case of compressors having inlet guide vanes imparting a nonvortex turning distribution to the flow, the axial velocities at the outlet of the guide vanes or at the inlet to the first rotor will vary with radius and must be computed. As indicated in the previous discussion, the effects of streamline curvature may be sufficiently large in certain cases to necessitate consideration of these effects in the calculation procedure. In the design procedure, corrections for these curvature effects may be applied after the preliminary velocity distributions and passage geometry have been specified.

After the flow conditions at the inlet to the rotor are determined, the steps previously enumerated in the section on CONSIDERATION OF WALL BOUNDARY-LAYER EFFECTS are used to determine the velocity distribution and annulus area geometry after the rotor. The design variables that

3374 must be specified for the first rotor are the tip radius at the rotor discharge, the tangential and axial velocity changes (based on blade-loading considerations) across the critical blade element (usually the tip) of the rotor, and the radial distributions of energy addition and blade-element loss. The specification of these quantities completely determines the flow parameters at the discharge of the blade row. Application of the blockage correction K_{bk} in the continuity equation then permits the determination of the hub radius of the annular flow passage after the rotor. A similar procedure is used to determine the flow conditions after the following stator.

It is then necessary to review completely the preliminary design in order to determine its critical and undesirable features with respect to both the compressor performance and the performance of the other engine components. For instance, it will be necessary to go through the design procedure again in order to correct for streamline-curvature effects, or to improve the shape of the hub contour, or to revise the loss assumptions made originally. A recalculation may also be required to change the loading or Mach number level because certain blade elements appear to be too critically loaded. The blade sections may then be determined from the two-dimensional and annular-cascade data of chapters VI and VII and the calculated design flow conditions.

Three methods discussed generally in the section on CONSIDERATION OF WALL BOUNDARY-LAYER EFFECTS for determining the flow conditions in the compressor are presented here to indicate the possible uses of the available equations and data. In discussing these methods, it is assumed that the compressor tip geometry and aerodynamic conditions are known (i.e., inlet and outlet tip radii, wheel speed, limiting-loading parameter, and axial velocity ratio) and that inlet values for pressure, temperature, weight flow, and velocity are known. It is assumed that the radial velocity terms may be neglected. The tangential velocity distribution is taken to be the prescribed outlet variable. The values selected are not to be considered as uniquely desirable values. They are chosen merely to illustrate the methods of solution of the design equations. It should be emphasized that, once the preliminary flow and geometry conditions are determined, it will be necessary to review the design procedure to ensure the attainment of satisfactory performance.

Method I

As pointed out previously, the solution of the flow equations by method I assumes a complete knowledge of the radial variations of energy addition or tangential velocity after the rotor as well as the radial variation of entropy even into the wall boundary layers. Because of the lack of sufficient data of this type, this method may not be generally usable at the present time.

The steps itemized in the following sections for application of method I follow as closely as possible the procedure enumerated in the previous section.

Inlet guide vanes. -

(1) Tip radius and hub-tip radius ratio at the discharge of the inlet guide vanes are specified.

(2) The desired weight flow is specified. This weight flow will be used in the continuity equation to determine the magnitude of axial velocity required.

(3) The radial distribution of tangential velocity is specified. (Some restrictions on this are given in ref. 30.)

(4) The outlet stagnation temperature is equal to the inlet stagnation temperature and is constant radially.

(5) The radial distribution of loss $\bar{\omega}$ is assumed from wall to wall on the basis of data obtained from similar blade sections. The radial distribution of outlet stagnation pressure is computed from equation (D5b).

(6) The radial variation of axial velocity is computed from equation (D3b).

(7) The density variation along the radius is computed from equation (D7).

(8) The magnitude of the axial velocity is determined by trial-and-error application of the continuity equation (eq. (D8)) with the blockage factor K_{bk} equal to 1.0. It should be emphasized that in this method the velocities are calculated into the wall boundary layer so that additional boundary-layer corrections are unnecessary.

Rotor. -

(1) The tip radius at the rotor discharge is specified.

(2) The axial velocity at the tip radius after the rotor is specified. The tip tangential velocity after the rotor is then calculated from equation (D10a) for a specified value of diffusion factor (consistent with low loss or high efficiency) and an assumed tip solidity.

(3) The radial distribution of tangential velocity after the rotor is specified.

(4) The radial distribution of stagnation temperature after the rotor is computed from equation (D1).

(5) The radial distribution of loss from wall to wall is assumed from the diffusion-factor - loss correlation of figure 6 (which is re-plotted from ch. VII) and from data taken in the wall boundary layers. The radial distribution of stagnation pressure after the rotor is calculated from equation (D5a).

(6) The radial distribution of axial velocity is calculated from equation (D3b) using the specified tip axial velocity as the initial reference velocity $V_{z,i}$.

(7) The radial distribution of density is computed from equation (D7).

(8) The hub radius after the rotor is determined from equation (D8) with the blockage factor K_{bk} equal to 1.0. If this hub radius causes a shift in the streamline configuration from that used in the initial calculation, it may be necessary to repeat this procedure using the modified streamline locations.

Stator. -

(1) The tip radius at the discharge of the stator blade row is specified.

(2) The axial velocity and tangential velocity at the tip radius after the stator are specified considering the effect of these values on the losses and on the characteristics that are desirable for the following rotor row.

(3) The radial distribution of tangential velocity after the stator is specified.

(4) The radial variation of stagnation temperature is assumed to be the same after the stator as at the inlet to the stator.

(5) The radial distribution of loss from wall to wall is assumed from boundary-layer data of similar stators and from the diffusion-factor - loss correlation of chapter VII. The radial distribution of stagnation pressure is computed from equation (D5b).

(6) The radial distribution of axial velocity is computed from equation (D3b).

(7) The density variation along the radius is computed from equation (D7).

(8) The hub radius after the stator is determined from equation (D8) with the blockage factor K_{bk} equal to 1.0.

Method II

The essential difference between solution of the flow equations by this method and solution by method I is that the flow distributions are computed using available blade-element data as if no wall boundary layers were present. Appropriate correction factors for the effects of the wall boundary layers are then applied. Specifically, the principal differences are in the evaluation of the loss distribution along the radius (step (5) of method I) and in consideration of the wall boundary-layer blockage factor in the flow-continuity condition (step (8) of method I). The radial variation of loss for method II is determined from blade-element considerations alone and does not go into the wall boundary-layer effects. The blockage factor K_{bk} used in applying the continuity equation (D8) in method II is some value less than 1.0. As pointed out in reference 15, it may vary from 0.98 to 0.96 through the compressor.

The isre equation can also be used in this method for an initial approximation of the flow or for cases in which the radial gradients of entropy are negligible. In these cases, equation (D2a) or (D2b) is used in step (6) of method I. Equation (D11) may be used to compute the axial velocity distribution for the case of blade rows having negligible radial gradients of stagnation temperature and pressure. In applying equation (D11), however, it is necessary to specify the flow-angle distribution after the blade row rather than the tangential velocity distribution.

Method III

The principal difference between the solution by this method and that by method II is in consideration of the blade-element loss. Rather than estimating a blade-element loss $\bar{\omega}'$, an average rotor row efficiency is assigned in this method. It is then assumed that the rotor blade-element efficiency is equal to this average rotor efficiency. The stator losses may then be considered by specifying an average stage efficiency. The stagnation pressure after the rotor and stator blades may then be determined from the rotor and stage temperature ratios and the appropriate efficiencies. The isre equation ((D2a) or (D2b)) is then used in calculating the velocity distribution after the blade row. A method very similar to this one is presented in chapter IX, in which the solution is accomplished by the use of charts.

Remarks

It must be emphasized that the previously outlined calculations are to be considered as preliminary calculations. After the annulus area geometry is determined, it will be necessary to review and probably recalculate the design to determine the final flow conditions through the compressor.

Naturally, other forms of these equations can lead to variations in the design procedure. It should be noted, however, that any variations must use self-consistent boundary-layer correction factors. Indiscriminate use of correction factors can lead to a design that is as poor as or worse than one in which boundary-layer corrections are completely neglected.

The radial velocity terms may be included in the methods presented if the streamline slope in the meridional plane is estimated. Thus, the radial velocity is related to the axial velocity. This necessitates retaining the radial velocity terms in equations (D7) and (D13).

Some secondary-flow effects may also be considered for certain specific cases in the design system. For instance, reference 30 presents a method of considering the induced effects of the trailing vortex system on the inlet-guide-vane turning angle. Research on secondary-flow effects in annular cascades will no doubt eventually lead to corrections in the design system.

NUMERICAL EXAMPLE

As an illustration of the design procedure of method II discussed previously, the design calculations for an inlet stage consisting of inlet rotor and stator are presented here. The given inlet conditions are as follows:

$$\begin{aligned} P_1 &= 2116 \text{ lb/sq ft} & a_{a,1} &= 1116 \text{ ft/sec} \\ T_1 &= 518.7^\circ \text{ R} & r_{1,t} &= 1.5 \text{ ft} \\ V_{\theta,1} &= 0 & \frac{w\sqrt{\theta}}{\delta A_F} &= 35.0 \text{ (lb/sec)/sq ft} \end{aligned}$$

The following design variables are selected:

Radial stations $r_\alpha, r_\beta, r_\gamma, r_\delta, r_\epsilon$ at 10, 30, 50, 70, 90 percent of passage depth.

$$M_{z,1} = 0.6 \quad V_{\theta,3} = 0 \quad D_{R,\epsilon} \leq 0.6$$

$$M_{1,\alpha} = 1.1 \quad D_{R,\alpha} = 0.35 \quad D_S \leq 0.6$$

$$K_{bk} = 0.98 \quad K_P, K_e, \text{ and } K_\eta \text{ are not used.}$$

$$\left(\frac{V_{z,2}}{V_{z,1}}\right)_\alpha = 1.0$$

$$r_{2,t} = 1.44 \text{ ft}$$

$$r_{3,t} = 1.44 \text{ ft}$$

$$\left(\frac{V_{z,3}}{V_{z,2}}\right)_\alpha = 1.0$$

$$\sigma_{R,\alpha} = 1.0$$

$$\sigma_{S,\alpha} = 0.7$$

Values used for various constants are

$$g = 32.17 \text{ ft/sec}^2$$

$$c_p = 0.243 \text{ Btu/(lb)}(^{\circ}\text{R})$$

$$J = 778.2 \text{ ft-lb/Btu}$$

$$R = 53.35 \text{ ft-lb/(lb)}(^{\circ}\text{R})$$

$$\gamma = 1.4$$

The value of inlet hub-tip radius ratio is computed from the flow per unit frontal area, axial Mach number, and tip radius, as follows:

$$\frac{w\sqrt{\theta}}{\delta A_F} \frac{1}{K_{bk}} = \frac{35}{0.98} = 35.7 \text{ (lb/sec)/sq ft}$$

From $M_{z,1}$, $w\sqrt{\theta}/\delta A_F$, and figure 5, $r_h/r_t = 0.377$.

The actual weight flow is obtained from

$$A_{F,1} = \pi r_{1,t}^2 = 7.069 \text{ sq ft}$$

$$\frac{w\sqrt{\theta}}{\delta A_F} A_{F,1} = \frac{w\sqrt{\theta}}{\delta} = w = 247 \text{ lb/sec}$$

The conditions at the rotor tip design station α (10 percent of passage depth) are computed next. From $M_{z,1}$ and reference 31,

$$\frac{a_1}{a_{a,1}} = 0.9658$$

$$a_1 = 1078 \text{ ft/sec}$$

$$V_{z,1} = a_1 M_{z,1} = (1078)(0.6) = 647 \text{ ft/sec}$$

$$V'_{1,\alpha} = a_1 M'_{1,\alpha} = (1078)(1.1) = 1186 \text{ ft/sec}$$

$$U_{1,\alpha} = V_{\theta,1,\alpha} = \left[(V'_{1,\alpha})^2 - V_{z,1,\alpha}^2 \right]^{1/2} = 994 \text{ ft/sec}$$

$$\beta'_{1,\alpha} = \tan^{-1} \left(\frac{U_1}{V_{z,1,\alpha}} \right) = 56.9^\circ$$

$$V_{z,2,\alpha} = 1.0 V_{z,1,\alpha} = 647 \text{ ft/sec}$$

The value of $\beta'_{2,\alpha}$ is computed from equation (D10b) by application of the appropriate chart (fig. 5 of ch. IX):

$$\beta'_{2,\alpha} = 46.0^\circ$$

$$V'_{\theta,2,\alpha} = V_{z,2,\alpha} \tan \beta'_{2,\alpha} = 670 \text{ ft/sec}$$

$$V_{\theta,2,\alpha} = U_{2,\alpha} - V'_{\theta,2,\alpha} = 297 \text{ ft/sec}$$

The iteration procedure for the computation of the radial variation of gas state is started by selecting the inlet radial stations. The computation lineups and results for the velocity calculations using the isre and nisre equations are shown in tables II(a) and (b), respectively, where only the final results and final calculation lineups of the iteration procedure are presented.

In these designs the variation of outlet tangential velocity is prescribed as a function of r_2 , so that an analytical integration of the isre equation is possible. Of course, graphical or numerical procedures may also be used. This velocity distribution is

$$V_{\theta,2} = V_{\theta,2,t} \left(2 - \frac{r_2}{r_{2,t}} \right)$$

It should be emphasized that this distribution is chosen only to illustrate the design procedure for the general case where radial temperature gradients are present and does not necessarily represent an optimum design condition. The isre equation (D2a) can then be directly integrated, with the following result:

$$\begin{aligned} V_{z,2}^2 = & V_{z,2,i}^2 + 2gJc_p(T_2 - T_{2,i}) - (V_{\theta,2}^2 - V_{\theta,2,i}^2) - \\ & 8V_{\theta,2,t}^2 \left[\ln \frac{r_2}{r_{2,i}} - \frac{1}{r_{2,t}} (r_2 - r_{2,i}) + \frac{1}{8} \left(\frac{1}{r_{2,t}^2} \right) (r_2^2 - r_{2,i}^2) \right] \end{aligned}$$

(24)

where the α station is used as the initial reference station. All the terms on the right side of equation (24) are known as functions of the trial values of r_2 (r_2 depends on the selection of $r_{2,t}$ and $r_{2,h}$, since in this procedure the radial stations were chosen at stated percentages of the passage depth). The final value of $r_{2,h}$ is obtained by the iteration procedure of steps 6 to 23 in table II(a). The weight flow is computed numerically (e.g., by plotting $(2\pi K_{bk} \rho V_z r_t r)_2$ against $(r/r_t)_2$ and carrying out a graphical integration).

In order to compute weight flow, density and, hence, stagnation pressure must be calculated at the blade-row outlet. Stagnation pressure can be computed from stagnation temperature and the loss - velocity-diagram correlations presented in chapters VI and VII. The design chart (from data presented in ch. VII) used here to relate stagnation-pressure loss to velocity diagram is shown in figure 6. This chart is used in the design procedure shown in table II, while an explanation of its significance is given in chapter VII. Here $(P_2'/P_1')_{id}$ is taken equal to 1.0, which is exact for a constant-radius blade element.

The stator design is simpler than that for the rotor in this case, since $V_{\theta,3}$ is chosen to be zero; however, the basic approach is the same. The isre equation becomes

$$V_{z,3}^2 = V_{z,3,i}^2 + 2gJc_p(T_3 - T_{3,i})$$

where again the α station is used as the initial reference station. The stator curve in figure 6 is used for all radial stations.

The rotor and stator design using the nisre equation is carried out with the same design conditions as prescribed for the design using the isre equation. Thus steps 36 to 44 of table II(b) are the same as those from 1 to 9. The method of computing the outlet axial velocity is now changed, since data from a previous approximation are used in the solution. Here the final results of the isre solution are used to obtain the loss data for the initial nisre solution for outlet axial velocity. This is an intermediate step for which the data are not presented in the tables. The nisre equation for outlet axial velocity

for the assumed conditions is

$$\begin{aligned}
 v_{z,2}^2 \left[1 + \frac{\gamma-1}{2\gamma} \frac{J}{R} (s_{2,i} - s_2) \right] &= v_{z,2,i}^2 + 2gJc_p(T_2 - T_{2,i}) - \\
 (v_{\theta,2}^2 - v_{\theta,2,i}^2) - 8v_{\theta,2,t}^2 \left[\ln \frac{r_2}{r_{2,i}} - \frac{r_2 - r_{2,i}}{r_{2,t}} + \frac{1}{8r_{2,t}^2} (r_2^2 - r_{2,i}^2) \right] &+ \\
 \frac{J}{R} \left[gR(T_{2,i} + T_2) - \frac{\gamma-1}{2\gamma} (v_{\theta,2,i}^2 + v_{\theta,2}^2 + v_{z,2,i}^2) \right] (s_{2,i} - s_2) & \\
 & \quad (25)
 \end{aligned}$$

where

$$s_{2,i} - s_2 = \frac{R}{J} \ln \frac{\left(\frac{T_{2,i}}{T_2} \right)^{\frac{\gamma}{\gamma-1}}}{\frac{P_{2,i}}{P_2}}$$

Equation (25) was obtained under the following restrictions: (1) that $V_r = 0$, and (2) that entropy and static temperature vary linearly with radius in the interval of integration and thus the reference radius is shifted from point to point, starting at α near the tip. This solution illustrates a numerical solution of the equilibrium equation. The remainder of this calculation for the rotor is the same as that for the isre case.

The loss estimates for the stator are made initially from the isre solution for the stator, and the entropy variation is computed from these values. The stator velocity-diagram calculations then proceed as do the rotor isre calculations, using the equation

$$\begin{aligned}
 v_{z,3}^2 \left[1 + \frac{\gamma-1}{2\gamma} \frac{J}{R} (s_{3,i} - s_3) \right] &= v_{z,3,i}^2 + 2gJc_p(T_3 - T_{3,i}) + \\
 \frac{J}{R} \left[gR(T_{3,i} + T_3) - \frac{\gamma-1}{2\gamma} v_{z,2,i}^2 \right] (s_{3,i} - s_3) & \\
 & \quad (26)
 \end{aligned}$$

CONCLUDING REMARKS

The general flow equations that must be solved in the determination of design velocity distributions and flow passage configuration in compressors have been presented. In general, it is felt that more data are required to accurately establish the boundary-layer effects and correction factors on weight flow or annulus area and average stage pressure ratio and efficiency. It is expected, however, that the boundary-layer correction system discussed in this chapter will lead to a satisfactory design approximation. The need for concentrated analytical and experimental work is indicated by the lack of satisfactorily evaluated calculation procedures for determination of velocity distributions where streamline-curvature effects are large. In the high-performance compressors being considered at the present time, accurate prediction of design-point performance may not be possible until these curvature effects can be considered in the design procedure. For the time being, these three-dimensional-flow problems may be alleviated by geometric modifications of the hub and casing profile. It should be reemphasized here that the compressor design procedure is a trial-and-error compromise procedure. It is generally necessary to go through the design calculations a number of times before all elements of the compressor may be considered to be satisfactorily designed with respect to aerodynamic and mechanical considerations.

REFERENCES

1. Compressor and Turbine Research Division: Aerodynamic Design of Axial-Flow Compressors. Vol. I. NACA RM E56B03, 1956.
2. Cavicchi, Richard H., and English, Robert E.: Analysis of Limitations Imposed on One-Spool Turbojet-Engine Designs by Compressors and Turbines at Flight Mach Numbers of 0, 2.0, and 2.8. NACA RM E54F21a, 1954.
3. Wu, Chung-Hua, and Wolfenstein, Lincoln: Application of Radial-Equilibrium Condition to Axial-Flow Compressor and Turbine Design. NACA Rep. 955, 1950. (Supersedes NACA TN 1795.)
4. Compressor and Turbine Research Division: Aerodynamic Design of Axial-Flow Compressors. Vol. III. NACA RM E56B03b, 1956.
5. Eckert, and Korbacher: The Flow through Axial Turbine Stages of Large Radial Blade Length. NACA TM 1118, 1947.
6. Marble, Frank E.: The Flow of a Perfect Fluid through an Axial Turbomachine with Prescribed Blade Loading. Jour. Aero. Sci., vol. 15, no. 8, Aug. 1948, pp. 473-485.
7. Marble, Frank E., and Michelson, Irving: Analytical Investigation of Some Three-Dimensional Flow Problems in Turbo-Machines. NACA TN 2614, 1952.
8. Stanitz, John D.: Effect of Blade-Thickness Taper on Axial-Velocity Distribution at the Leading Edge of an Entrance Rotor-Blade Row with Axial Inlet, and the Influence of This Distribution on Alignment of the Rotor Blade for Zero Angle of Attack. NACA TN 2986, 1953.
9. Hatch, James E., Giamati, Charles C., and Jackson, Robert J.: Application of Radial-Equilibrium Condition to Axial-Flow Turbomachine Design Including Consideration of Change of Entropy with Radius Downstream of Blade Row. NACA RM E54A20, 1954.
10. Hamrick, Joseph T., Ginsburg, Ambrose, and Osborn, Walter M.: Method of Analysis for Compressible Flow through Mixed-Flow Centrifugal Impellers of Arbitrary Design. NACA Rep. 1082, 1952. (Supersedes NACA TN 2165.)
11. Stewart, Warner L.: Analytical Investigation of Flow through High-Speed Mixed-Flow Turbine. NACA RM E51H06, 1951.

12. Eckert, B.: Axialkompressoren und Radialkompressoren. Springer-Verlag (Berlin), 1953.
13. Wu, Chung-Hua: Subsonic Flow of Air through a Single-Stage and a Seven-Stage Compressor. NACA TN 2961, 1953.
14. Wu, Chung-Hua: A General Theory of Three-Dimensional Flow in Subsonic and Supersonic Turbomachines of Axial-, Radial-, and Mixed-Flow Types. NACA TN 2604, 1952.
15. Novak, R. A.: Notes on the Fundamentals of the Design of Multi-Stage Axial Compressors. Lecture No. 6, Gas Turbine Lectures, Dept. Mech. and Ind. Eng., Univ. Mich., June 29-July 10, 1953.
16. Smith, L. H., Jr., Traugott, S. C., and Wislicenus, G. F.: A Practical Solution of a Three-Dimensional Flow Problem of Axial-Flow Turbomachinery. Trans. A.S.M.E., vol. 75, no. 5, July 1953, pp. 789-803.
17. Holmquist, Carl O., and Rannie, W. Duncan: An Approximate Method of Calculating Three-Dimensional Flow in Axial Turbomachines. Paper presented at meeting Inst. Aero. Sci., New York (N.Y.), Jan. 24-28, 1955.
18. Montgomery, John C., and Glaser, Frederick W.: Experimental Investigation of a 0.4 Hub-Tip Diameter Ratio Axial-Flow Compressor Inlet Stage at Transonic Inlet Relative Mach Numbers. II - Stage and Blade-Element Performance. NACA RM E54I29, 1955.
19. Howell, A. R.: The Present Basis of Axial Flow Compressor Design. Pt. II - Compressor Theory and Performance. Rep. No. E.3961, British R.A.E., Dec. 1942.
20. Howell, A. R.: Fluid Dynamics of Axial Compressors. Proc. Inst. Mech. Eng., vol. 153, 1945, p. 441.
21. Carter, A. D. S., Andrews, S. J., and Fielder, E. A.: The Design and Testing of an Axial Compressor Having a Mean Stage Temperature Rise of 30° C. Rep. R.148, British N.G.T.E., Nov. 1953.
22. Sinnette, John T., Jr.: Analysis of Effect of Basic Design Variables on Subsonic Axial-Flow-Compressor Performance. NACA Rep. 901, 1948. (Supersedes NACA RM E7D28.)
23. Klapproth, John F.: General Considerations of Mach Number Effects on Compressor-Blade Design. NACA RM E53L23a, 1954.

24. Howell, A. R.: The Present Basis of Axial Flow Compressor Design. Pt. I - Cascade Theory and Performance. R. & M. No. 2095, British A.R.C., June 1942.
25. Lieblein, Seymour, Schwenk, Francis C., and Broderick, Robert L.: Diffusion Factor for Estimating Losses and Limiting Blade Loadings in Axial-Flow-Compressor Blade Elements. NACA RM E53D01, 1953.
26. Briggs, William B., and Giamati, Charles C.: Interstage Surveys and Analysis of Viscous Action in Latter Stages of a Multistage Axial-Flow Compressor. NACA RM E52I12, 1953.
27. Ruden, P.: Investigation of Single Stage Axial Fans. NACA TM 1062, 1944.
28. Finger, Harold B., and Dugan, James F., Jr.: Analysis of Stage Matching and Off-Design Performance of Multistage Axial-Flow Compressors. NACA RM E52D07, 1952.
29. Finger, Harold B.: Method of Experimentally Determining Radial Distributions of Velocity through Axial-Flow Compressor. NACA TN 2059, 1950.
30. Lieblein, Seymour, and Ackley, Richard H.: Secondary Flows in Annular Cascades and Effects on Flow in Inlet Guide Vanes. NACA RM E51G27, 1951.
31. Ames Research Staff: Equations, Tables, and Charts for Compressible Flow. NACA Rep. 1135, 1953. (Supersedes NACA TN 1428.)

TABLE I. - Concluded. DESIGN EQUATIONS

$$\frac{P_3}{P_2} = 1 - \bar{\omega} \left[1 - \left(\frac{1}{1 + \frac{\gamma-1}{2} M_2^2} \right)^{\frac{\gamma}{\gamma-1}} \right] \quad (D5b)$$

$$\left(\frac{P'_2}{P'_1} \right)_{id} = \left[1 + \frac{\gamma-1}{2} \frac{(\omega r_2)^2}{r g R T'_1} \left(1 - \frac{r_1^2}{r_2^2} \right) \right]^{\frac{\gamma}{\gamma-1}} \quad (D6)$$

$$g\rho = \frac{P}{RT} \left(1 - \frac{V^2}{2gJc_p T} \right)^{\frac{1}{\gamma-1}} \quad (D7)$$

$$w = K_{bk} 2\pi g \int_{r_h}^{r_t} (\rho V_z r dr)_d \quad (D8)$$

$$\eta_{ad} = \frac{\left(\frac{P_2}{P_1} \right)^{\frac{\gamma-1}{\gamma}} - 1}{\frac{T_2}{T_1} - 1} \quad (D9)$$

$$D = 1 - \frac{V'_2}{V'_1} + \frac{\Delta V'_\theta}{2\sigma V'_1} \quad (D10a)$$

$$\frac{2\sigma}{\cos \beta'_2} + \tan \beta'_2 = \frac{V_{z,1}}{V_{z,2}} \left[\frac{2\sigma (1-D)}{\cos \beta'_1} + \tan \beta'_1 \right] \quad (D10b)$$

$$V_z = V_{z,i} \frac{\cos \beta}{\cos \beta_1} \exp \left(- \int_{r_1}^r \frac{\sin^2 \beta}{r} dr \right) \quad (D11)$$

$$J\left(\frac{S}{R}\right)_2 - J\left(\frac{S}{R}\right)_1 = \ln \left[\frac{\left(\frac{T_2}{T_1} \right)^{\frac{\gamma}{\gamma-1}}}{\frac{P_2}{P_1}} \right] \quad (D12)$$

$$Jgc_p t = Jgc_p T - \frac{V^2}{2} \quad (D13)$$

TABLE II. - CALCULATION PROCEDURES

(a) Using isre equations

Step	Parameter	Known design condition	Procedure	Radial position				
				α	β	γ	δ	ϵ
1	$r_1/r_{1,t}$	$r_{1,h}/r_{1,t} = 0.577$	Choose 10, 30, 50, 70, 90 percent of passage depth	0.938	0.813	0.688	0.564	0.439
2	$U_1 = V_{\theta,1}$	$U_{1,t} = 1060$	$U_{1,t}(r_1/r_{1,t})$	994	862	729	598	465
3	β_1	$V_{z,1} = 647$	$\tan^{-1}(V_{\theta,1}/V_{z,1})$	56.9	53.1	48.4	42.8	35.7
4	V_1		$[V_{z,1}^2 + (V_{\theta,1})^2]^{1/2}$	1186	1078	975	881	797
5	M_1	$a_1 = 1078$	V_1/a_1	1.100	0.999	0.904	0.817	0.739
6	$r_2/r_{2,t}$	$r_{2,t} = 1.44$	$r_{2,h}$ known from preliminary design (step 1)	0.950	0.832	0.720	0.608	0.496
7	$V_{\theta,2}$	$V_{\theta,2,t} = 283$	$V_{\theta,2,t}[2 - (r/r_{t,2})]$	297	331	362	394	426
8	U_2	$U_{2,t} = 1018$	$U_{2,t}(r/r_{t,2})$	967	847	733	619	505
9	$T_2 = T_3$	$T_1 = 518.7$	$T_1 + [(U_{2,t}V_{\theta,2} - U_1V_{\theta,1})/gJc_p]$	566	565	562	559	554
10	$V_{z,2}$	$V_{z,2,a} = 647$	Eq. (24)	647	640	627	612	600
11	$V_{\theta,2}$		$U_2 - V_{\theta,2}$	670	516	371	225	79
12	β_2		$\tan^{-1}(V_{\theta,2}/V_{z,2})$	46.0	38.9	30.6	20.2	7.5
13	V_2		$V_{z,2}/\cos \beta_2$	932	822	728	652	605
14	$a_{a,2}$	$a_{a,1} = 1116$	$a_{a,1}(T_2/T_1)^{1/2}$	1166	1165	1162	1158	1153
15	M_2		$V_2/a_{a,2}$ and ref. 31	0.635	0.644	0.649	0.655	0.666
16	M_2'		$M_2 V_2/V_1$	0.830	0.735	0.653	0.587	0.548
17	σ	$\sigma_a = 1.0$	$\sigma_t(r_{1,t} + r_{2,t})/(r_1 + r_2)$	1.00	1.15	1.34	1.61	2.02
18	D'		$1 - (V_2/V_1) + (\Delta V_{\theta}/2\sigma V_1)$	0.351	0.377	0.390	0.391	0.360
19	\bar{w}'		$D', \cos \beta_2/2\sigma$, and fig. 6	0.0734	0.0369	0.0405	0.0446	0.0489
20	$(p/P)_2$		M_2 and ref. 31	0.636	0.699	0.751	0.792	0.816
21	P_2/P_1		$\left(\frac{T_2}{T_1}\right)^{\frac{\gamma}{\gamma-1}} \left[1 - \bar{w}' \left(1 - \frac{P_2}{P_1}\right)\right]$	1.320	1.333	1.313	1.284	1.248
22	ϵP_2		$\frac{P_2}{RT_2} \left(1 - \frac{V_{z,2}^2 + V_{\theta,2}^2}{2gJc_p T_2}\right)^{\frac{1}{\gamma-1}}$	0.0764	0.0769	0.0759	0.0744	0.0724
23	w	$K_{bk} = 0.98$	$2\pi K_{bk} r_{2,t} \int_{r_h/r_{t,2}}^{1.0} (\rho V_{z,2})_2 d(r_2/r_{2,t})$			247		
24	$r_3/r_{3,t}$	$r_{3,t} = 1.44$	$r_{3,h}$ known from preliminary design (step 1)	0.950	0.838	0.730	0.622	0.514
25	$V_{z,3} = V_3$	$V_{z,3,a} = V_{z,2,a}$	$[V_{z,3,1}^2 + 2gJc_p(T_3 - T_{3,1})]^{1/2}$	647	637	612	576	524
26	M_3	$a_{a,2} = a_{a,3}$	$V_3/a_{a,3}$ and ref. 31	0.573	0.564	0.527	0.498	0.455
27	σ	$\sigma_a = 0.7$	$\sigma_t(r_{2,t} + r_{3,t})/(r_2 + r_3)$	0.700	0.796	0.917	1.08	1.32
28	D		$1 - (V_3/V_2) + (\Delta V_{\theta}/2\sigma V_2)$	0.389	0.405	0.427	0.458	0.507
29	\bar{w}		$D, 2\sigma$, and fig. 6	0.0182	0.0223	0.0275	0.0346	0.0501
30	$(p/P)_3$		M_3 and ref. 31	0.800	0.806	0.819	0.837	0.862
31	P_3/P_2		$1 - \bar{w} \left(1 - \frac{P_3}{P_2}\right)$	0.996	0.996	0.995	0.994	0.993
32	ϵP_3		$\frac{P_3}{RT_3} \left(1 - \frac{V_3^2}{2gJc_p T_3}\right)^{\frac{1}{\gamma-1}}$	0.0788	0.0800	0.0800	0.0799	0.0799
33	w		$2\pi K_{bk} r_{3,t} \int_{r_h/r_{t,3}}^{1.0} (\rho V_{z,3})_3 d(r_3/r_{3,t})$			247		
34	P_3/P_1			1.32	1.33	1.31	1.28	1.24
35	$\eta_{ad,ST}$		$\left[\left(\frac{P_3}{P_1}\right)^{\frac{\gamma-1}{\gamma}} - 1\right] / \left[\left(\frac{T_3}{T_1}\right) - 1\right]$	0.895	0.946	0.944	0.940	0.928
	$(T_3/T_1)_{av}$		Mass-average T_3/T_1			1.083		
	$(P_3/P_1)_{av}$		Mass-average P_3/P_1			1.29		
	$\eta_{ad,av}$		Mass-average $\eta_{ad,ST}$			0.932		

TABLE II. - Concluded. CALCULATION PROCEDURES

(b) Using nisre equations

Step	Parameter	Known design condition	Procedure	Radial position				
				α	β	γ	δ	ϵ
36	$r_1/r_{1,t}$	$r_{1,h}/r_{1,t}$	(Step 1)	0.938	0.913	0.688	0.564	0.439
37	$U_1 = V_{\theta,1}$	$U_{1,t} = 1060$	$U_{1,t}(r_1/r_{1,t})$	994	862	729	598	465
38	β_1	$V_{z,1} = 647$	$\tan^{-1}(V_{\theta,1}/V_{z,1})$	56.9	53.1	48.4	42.8	35.7
39	V_1		$[V_{z,1}^2 + (V_{\theta,1})^2]^{1/2}$	1186	1078	975	881	797
40	M_1	$a_1 = 1078$	V_1/a_1	1.100	0.999	0.904	0.817	0.739
41	$r_2/r_{2,t}$	$r_{2,t} = 1.44$	$r_{2,h}$ known from preliminary design	0.950	0.838	0.730	0.622	0.514
42	$V_{\theta,2}$	$V_{\theta,2,t} = 283$	$V_{\theta,2,t} \left[2 - \left(\frac{r}{r_t} \right)^2 \right]$	297	329	359	390	420
43	U_2	$U_{2,t} = 1018$	$U_{2,t}(r_2/r_{2,t})$	967	853	743	633	523
44	$T_2 = T_3$	$T_1 = 518.7$	$T_1 + [(U_2 V_{\theta,2} - U_1 V_{\theta,1})/gJc_p]$	566	565	563	553	555
45	$\frac{S_{2,1} - S_2}{RJ^{-1}}$	P_2 known from previous trial	$\ln \left[\frac{\left(\frac{T_{2,1}}{T_2} \right)^{\frac{\gamma}{\gamma-1}}}{P_{2,1}/P_2} \right]$	-----	1.009	0.988	0.981	0.974
46	$V_{z,2}$	$V_{z,2,\alpha} = 647$	Eq. (25)	647	662	652	640	628
47	$V_{\theta,2}$		$U_2 - V_{\theta,2}$	670	524	384	243	103
48	β_2		$\tan^{-1}(V_{\theta,2}/V_{z,2})$	46.0	38.4	30.5	20.8	9.3
49	$a_{a,2}$	$a_{a,1} = 1116$	$a_{a,1}(T_2/T_1)^{1/2}$	1166	1165	1162	1159	1154
50	M_2		$V_2/a_{a,2}$ and ref. 31	0.635	0.662	0.669	0.675	0.685
51	M_2		$M_2 V_2 / V_2$	0.830	0.756	0.680	0.617	0.577
52	σ	$\sigma_a = 1.0$	$\sigma_t(r_{1,t} + r_{2,t})/(r_1 + r_2)$	1.0	1.14	1.33	1.59	1.98
53	D'		$1 - (V_2/V_1) + (\Delta V_{\theta}/2\sigma V_1)$	0.351	0.353	0.356	0.350	0.316
54	\bar{w}		$D', \cos \beta_2/2\sigma$, and fig. 6	0.0734	0.0350	0.0371	0.0409	0.0422
55	$(p/P')_2$		M_2' and ref. 31	0.636	0.685	0.734	0.774	0.798
56	P_2/P_1		$\left(\frac{T_2}{T_1} \right)^{\frac{\gamma}{\gamma-1}} \left[1 - \bar{w} \left(1 - \frac{P_2}{P_1} \right) \right]$	1.320	1.332	1.316	1.290	1.256
57	gP_2		$\frac{P_2}{RT_2} \left(1 - \frac{V_{z,2}^2 + V_{\theta,2}^2}{2gJc_p T_2} \right)^{\frac{1}{\gamma-1}}$	0.0764	0.0761	0.0750	0.0738	0.0719
58	w	$K_{bk} = 0.98$	$2\pi K_{bk} r_{2,t} \int_{r_h/r_t}^{1.0} (\rho V_z r) d(r_2/r_{2,t})$			247		
59	$r_3/r_{3,t}$	$r_{3,t} = 1.44$	$r_{3,h}$ known from preliminary design (step 1)	0.950	0.844	0.740	0.636	0.532
60	$\frac{S_{3,1} - S_3}{RJ^{-1}}$	P_3 known from previous trial	$\ln \left[\frac{\left(\frac{T_{3,1}}{T_3} \right)^{\frac{\gamma}{\gamma-1}}}{P_{3,1}/P_3} \right]$	-----	0.0152	0.0005	0.0000	-0.0004
61	$V_{z,3} = V_3$	$V_{z,3,\alpha} = 647$	Eq. (26)	647	658	638	606	559
62	M_3	$a_{a,2} = a_{a,3}$	$V_3/a_{a,3}$ and ref. 31	0.573	0.584	0.566	0.538	0.496
63	σ	$\sigma_a = 0.7$	$\sigma_t(r_{2,t} + r_{3,t})/(r_2 + r_3)$	0.700	0.791	0.905	1.057	1.272
64	D		$1 - (V_3/V_2) + (\Delta V_{\theta}/2\sigma V_2)$	0.390	0.391	0.410	0.438	0.480
65	\bar{w}		$D, 2\sigma$, and fig. 6	0.0182	0.0206	0.0253	0.0317	0.0445
66	$(p/P)_3$		M_3 and ref. 31	0.8005	0.794	0.804	0.822	0.845
67	P_3/P_2		$1 - \bar{w} \left(1 - \frac{P_3}{P_2} \right)$	0.9964	0.9958	0.9951	0.9941	0.9931
68	gP_3		$\frac{P_3}{RT_3} \left(1 - \frac{V_3^2}{2gJc_p T_3} \right)^{\frac{1}{\gamma-1}}$	0.0788	0.0792	0.0791	0.0792	0.0791
69	w		$2\pi K_{bk} r_{3,t} \int_{r_{3,h}/r_{3,t}}^{1.0} \rho_3 V_{z,3} r_3 d(r_3/r_{3,t})$			247		
70	P_3/P_1		$\left[\frac{P_3}{P_1} \right]^{\frac{\gamma-1}{\gamma}} \left[\frac{T_3}{T_1} - 1 \right]$	1.315	1.327	1.309	1.282	1.247
71	$\eta_{ad,ST}$		Mass-average T_3/T_1	0.895	0.947	0.946	0.940	0.932
	$(T_3/T_1)_{av}$		Mass-average P_3/P_1			1.090		
	$(P_3/P_1)_{av}$		Mass-average $\eta_{ad,ST}$			1.30		
	$\eta_{ad,av}$					0.936		

3374

CG-26

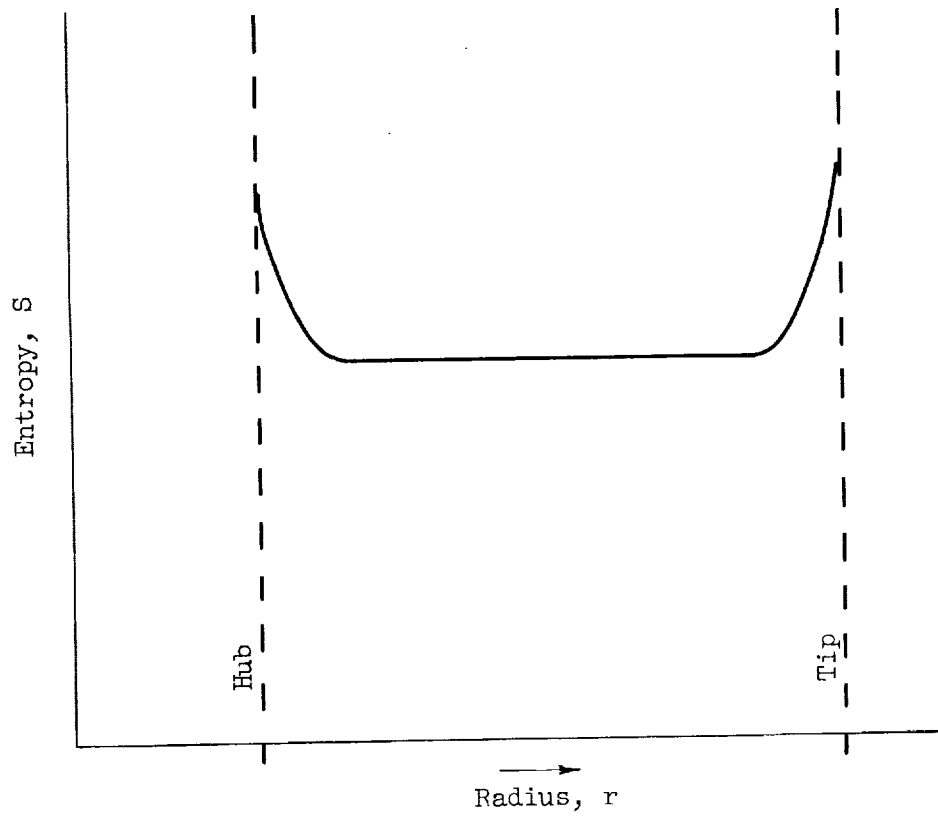


Figure 1. - Typical entropy distribution after compressor blade row.

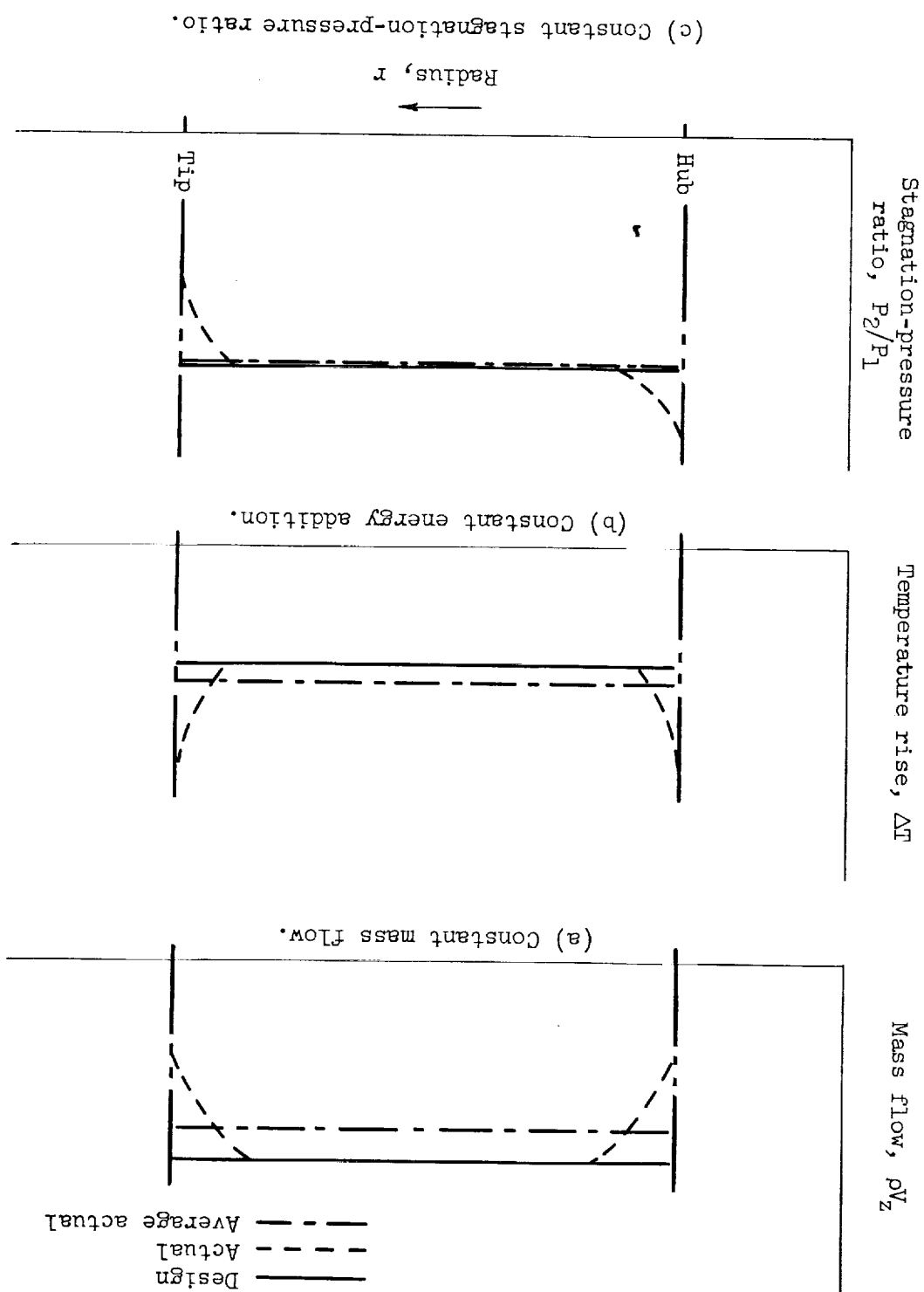


Figure 2. - General effects of wall boundary layer.

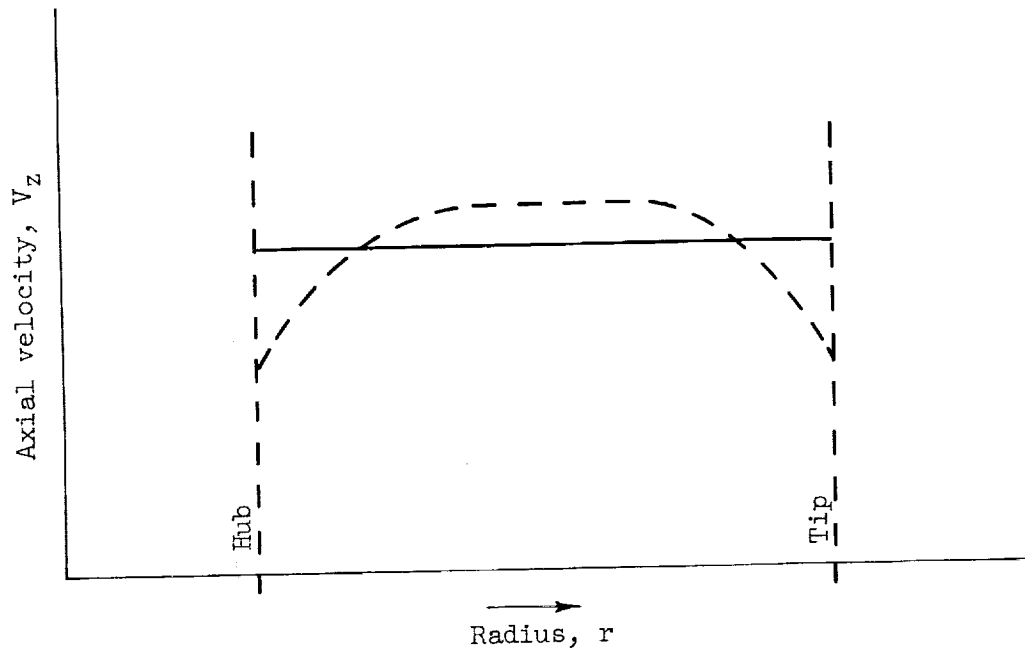


Figure 3. - Effect of wall boundary layer on axial velocity.

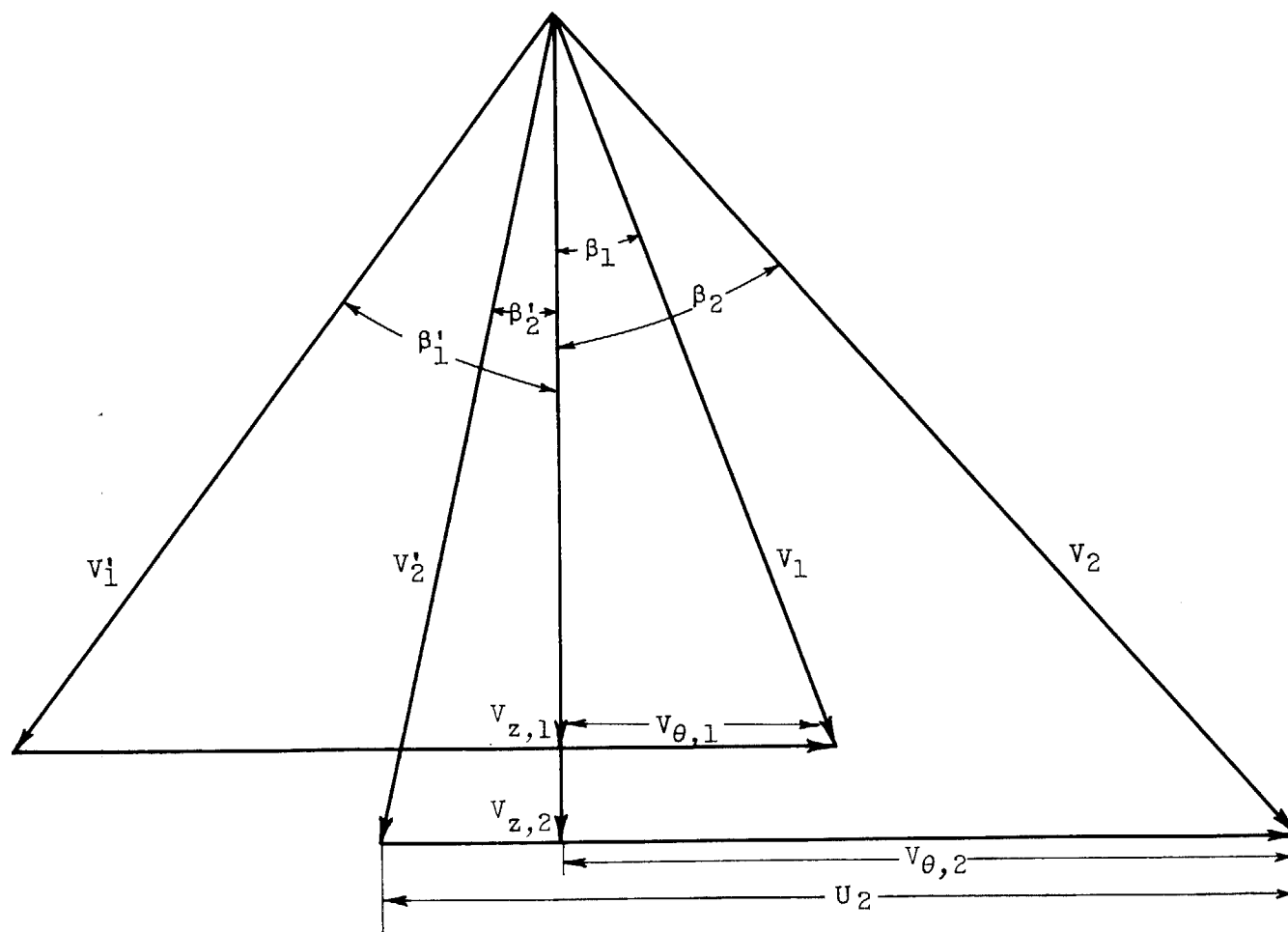


Figure 4. - General velocity diagram.

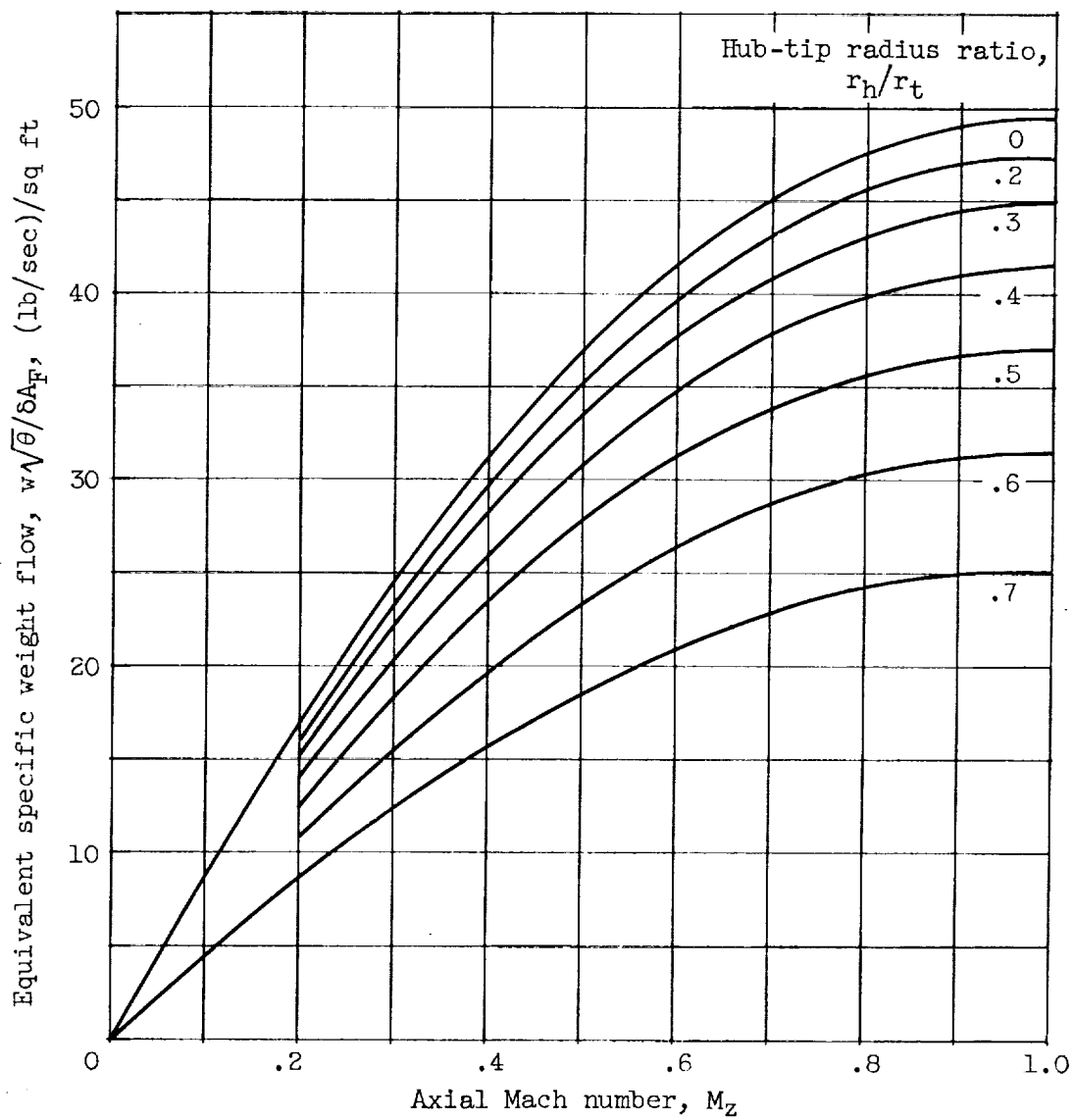


Figure 5. - Weight-flow - Mach number characteristics for various values of hub-tip radius ratio.

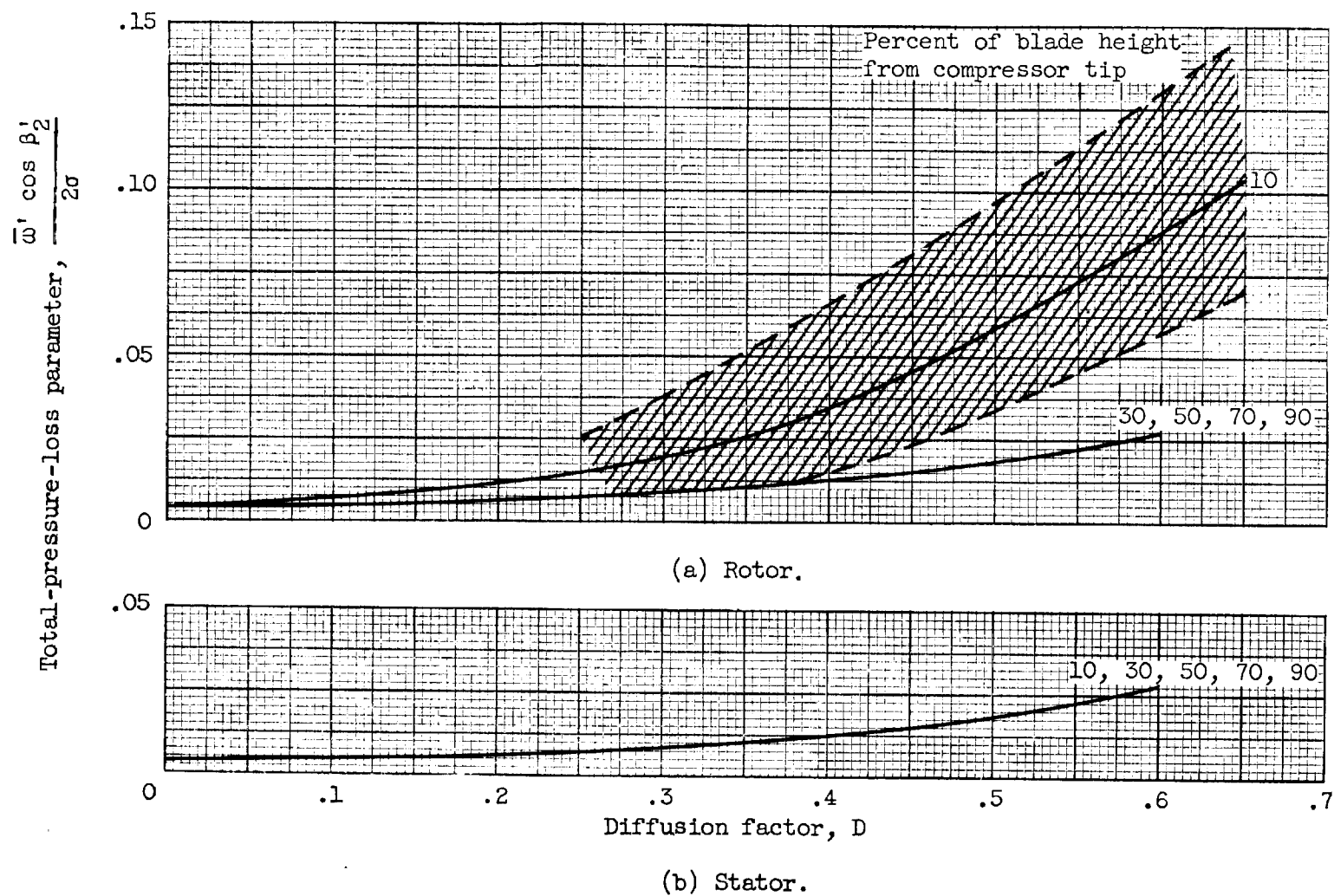


Figure 6. - Design chart relating $\bar{\omega}' \cos \beta_2' / 2\sigma$ to diffusion factor (from ch. VII).

CHAPTER IX

CHART PROCEDURES FOR DESIGN VELOCITY DISTRIBUTION

By Arthur A. Medeiros and Betty Jane Hood

SUMMARY

A series of charts for the solution of the flow equations used in the design of axial-flow compressors is developed. The equations, which are presented in chart form, are radial equilibrium (in a simplified form), continuity of flow, energy addition, efficiency, vector relations, and diffusion factor.

Because the charts are based on general flow equations, they can be used in the design of any axial-flow compressor. An example of the use of the charts in the design of a stage consisting of a rotor and stator blade row is presented. Comparison of the pertinent design values obtained by the chart procedure with analytically calculated values indicates that good accuracy can be attained by careful use of the charts.

INTRODUCTION

The over-all design requirements of air flow and pressure ratio for the compressor component of a gas-turbine engine are generally determined on the basis of a cycle analysis for the particular application of the engine. For many present-day aircraft applications, an axial-flow compressor is selected because of its high efficiency and high flow per unit frontal area.

The general geometry of the compressor, such as the tip diameter, blade speed, inlet and discharge axial velocities, and inlet and discharge areas, is determined by consideration not only of the compressor but also of the combustor and turbine components of the engine. The selection of inlet axial velocity, compressor blade speed, and inlet hub and tip diameters involves a compromise among high weight flow per unit frontal area (low hub-tip diameter ratio and high axial velocity), high stage pressure ratio (high blade speed), and reasonable turbine blade stresses (low blade speed, low axial velocity, and high hub-tip diameter ratio).

The magnitudes of the axial velocity and blade speed must also be compromised on the basis of the effects of the resultant Mach number on blade-section efficiency. Compressor blade stresses, other than vibratory stresses, play only a small part in this compromise. The factors affecting these considerations are discussed more completely in chapter II (ref. 1) and in reference 2.

Other compromises must be made in the compressor design in addition to the inlet configuration. The compressor-discharge velocity must be adjusted on the basis of compressor diffuser and combustor-inlet requirements. Low compressor-discharge axial velocities are favorable with respect to combustor efficiency; however, high axial velocities are desirable through the compressor for attaining high stage pressure ratios and hence decreasing compressor weight. With the inlet and discharge axial velocities selected, it is then necessary to prescribe a stagewise variation in the axial velocities and blade-loading limits such that a reasonable hub shape is obtained.

Another variable that must be dealt with is the radial distribution of tangential velocities. Not a great deal of information is available on the over-all desirability of the various radial distributions of velocity diagrams, so that, for the most part, the choice is a matter of experience with some particular distribution.

It is obvious, then, that, with this wide selection of combinations of axial and radial distributions of velocities and the compromises required because of the factors affecting aerodynamic performance, weight, and mechanical reliability of the various components, many compressor configurations are possible to meet the given over-all design requirements. Some preliminary design calculations are therefore necessary before a final compressor configuration is selected.

Each of these preliminary design calculations requires the solution of the fundamental flow equations after each blade row. The application of the fundamental flow equations to compressor design is discussed in detail in chapter VIII. However, the complete design procedure presented in chapter VIII would be very time-consuming if used for the purpose of design evaluations. It is desirable to put the fundamental flow equations applicable to compressor design in simple and easily used chart form.

Another reason for simplifying the compressor design procedure for certain applications is the iterative nature of the complete design procedure. The iteration is a result of the mutual interrelation between the calculation of the radial distribution of velocities, the passage shape of the compressor, and the selection of blading to achieve the radial distributions of velocity. For example, the axial velocity distribution after any blade row is a function not only of the radial distribution of tangential velocities but also of the energy gradient and the gradient

of losses. However, the tangential velocities (or energy) and losses are functions of the blading and the angular setting of the blading with respect to the flow. The general procedure is to prescribe the desired radial distribution of tangential velocity or energy and assume a loss at each radial station at which the axial velocity is to be calculated. The calculation of the axial velocity to satisfy the radial-equilibrium condition completes the vector diagram, and it is then possible to select blading on the basis of data such as that presented in chapters VI and VII. At this point, the losses for the selected blade section can be obtained from blade-element data and checked against the assumed losses. If the assumed and calculated losses are sufficiently different, the entire calculation must be repeated with new assumed values of losses.

Streamline curvature, particularly in stages with low hub-tip diameter ratios and high pressure ratios, will affect the radial distribution of axial velocity. Some of the factors that control the streamline curvature and methods of analytically correcting for the effect on axial velocity are discussed in chapter VIII and in references 3 to 7. It is obvious that the hub and tip diameter variation through the compressor will greatly influence the streamline shape. Therefore, a preliminary design calculation is necessary to determine the approximate passage shape variation before streamline-curvature corrections to the axial velocity can be made. For this reason, also, it is advantageous to have the preliminary design procedure in easily used chart form.

This chapter develops and presents a chart procedure for the design of axial-flow compressors using any consistent set of assumed design values and velocity distributions. The radial-equilibrium equation (in simplified form), the continuity equation, the energy-addition and efficiency equations, vector relations, and the diffusion-factor equation (see ref. 8) are presented in graph form.

The method can be used for making preliminary design calculations to determine the compressor configuration to meet given over-all performance requirements with any given set of aerodynamic limitations such as Mach number and blade-loading levels. It can also be used as the first step in a complete design procedure to determine initial velocity diagrams and passage shape variations. An intelligent estimate of losses in the blading and streamline curvatures due to the walls can then be made, so that iterations in the complete design procedure can be minimized or eliminated. When the corrections to the design due to entropy gradients and streamline curvatures are expected to be small, the charts can be used for final design calculations, provided, of course, that they are used with care and judgment. An example of the use of the charts in the design of an axial-flow compressor stage is presented herein, and the results of the graphical procedure are compared for accuracy with analytically calculated values.

3384

CG-27 back

SYMBOLS

The following symbols are used in this chapter:

A	area, sq ft
a	speed of sound, ft/sec
a_a	speed of sound based on stagnation conditions, ft/sec
B	$C + V_z^2 - V_{z,i}^2$, (ft/sec) ²
C	$2gJc_p(T_i - T)$, (ft/sec) ²
c_p	specific heat at constant pressure, 0.243 Btu/(lb)(°R)
D	diffusion factor
\mathcal{F}	blade force acting on gas, lb
g	acceleration due to gravity, 32.17 ft/sec ²
H	total or stagnation enthalpy, Btu/lb
J	mechanical equivalent of heat, 778.2 ft-lb/Btu
K_{bk}	weight-flow blockage factor
M	Mach number
P	total or stagnation pressure, lb/sq ft
p	static or stream pressure, lb/sq ft
R	gas constant, 53.35 ft-lb/(lb)(°R)
r	radius, ft
S	entropy, Btu/(lb)(°R)
T	total or stagnation temperature, °R
t	static or stream temperature, °R
U	rotor speed, ft/sec
V	air velocity, ft/sec

w	weight flow, lb/sec
z	coordinate along axis, ft
β	air angle, angle between air velocity and axial direction, deg
γ	ratio of specific heats, 1.4
δ	ratio of total pressure to NACA standard sea-level pressure of 2116 lb/sq ft
η_{ad}	adiabatic efficiency
θ	ratio of total temperature to NACA standard sea-level temperature of 518.7° R
ρ	density, lb-sec ² /ft ⁴
σ	solidity, ratio of chord to spacing
ω	angular velocity of rotor, radians/sec
$\bar{\omega}$	total-pressure-loss coefficient

Subscripts:

an	annulus
av	average
b	radial station midway between tip and mean
c	radial station midway between mean and hub
F	frontal
h	hub
i	reference position, radial station where variables are known
k	continuity value, value corrected for boundary-layer blockage
l	local value of flow per unit annulus area
m	mean
R	rotor

- r radial direction
- S stator
- s_l NACA standard sea-level conditions
- t tip
- z axial direction
- θ tangential direction
- 1 station at inlet to rotor blade row at equispaced distances across annulus
- 2 station at exit of rotor blade row at equispaced distances from tip to assumed hub
- 2a station at exit of rotor blade row at equispaced distances across annulus
- 3a station at exit of stator blade row at equispaced distances across annulus

Superscript:

- ' relative to rotor

DESIGN EQUATIONS

The flow equations applicable to compressor design are discussed in detail in chapters III (ref. 1) and VIII. These equations, in the form usually used in compressor design, are as follows:

Radial equilibrium:

$$gJ \frac{\partial H}{\partial r} = \mathcal{F}_r + gJt \frac{\partial S}{\partial r} + \frac{V_\theta}{r} \frac{\partial(rV_\theta)}{\partial r} + V_z \frac{\partial V_z}{\partial r} - V_z \frac{\partial V_r}{\partial z} \quad (1)$$

Continuity:

$$w_k = 2\pi K_{bk} \int_{r_h}^{r_t} \rho g V r \cos \beta \, dr \quad (2)$$

Energy addition:

$$gJc_p(T_2 - T_1) = \omega(r_2 V_{\theta,2} - r_1 V_{\theta,1}) = U_2 V_{\theta,2} - U_1 V_{\theta,1} \quad (3)$$

Adiabatic temperature-rise efficiency:

$$\eta_{ad} = \frac{\left(\frac{P_2}{P_1}\right)^{\frac{\gamma-1}{\gamma}} - 1.0}{\frac{T_2}{T_1} - 1.0} \quad (4)$$

Diffusion factor:

$$D = 1 - \frac{V'_2}{V'_1} + \frac{\Delta V'_\theta}{2\sigma V'_1} \quad (5)$$

State:

$$p = \rho g R t \quad (6)$$

Mach number:

$$M = \frac{V}{\sqrt{\gamma g R t}} \quad (7)$$

In addition to these are the trigonometric relations equating velocities and flow angles, and the adiabatic relations equating the static and stagnation values of pressure and temperature. The adiabatic relations, as function of Mach number, are presented in tabular form in reference 9.

Equations (6) and (7) can be handled conveniently by using readily computed stagnation conditions, instead of static conditions, and using the tables of reference 9; therefore, no charts are deemed necessary to determine state conditions and Mach numbers. Charts for the solution of equations (1) to (5) and the vector relations are presented herein.

FORMULATION OF CHARTS

Radial Equilibrium

In order to calculate the vector diagrams for an axial-flow turbo-machine, it is necessary to satisfy the radial-equilibrium condition given as equation (1). For the purpose of preliminary design analyses and, in some instances, even for the final design procedure, it is possible to simplify the equation.

Inasmuch as the equation is usually applied between blade rows, the blade force term \mathcal{F} is zero. If the entropy gradient $\partial S/\partial r$ is assumed zero and the streamline curvature is assumed small so that the change in radial velocity in the axial direction $\partial V_r/\partial z$ can be neglected, equation (1) can be written

$$gJ \frac{\partial H}{\partial r} = \frac{V_\theta^2}{r} + \frac{V_\theta \partial V_\theta}{\partial r} + \frac{V_z \partial V_z}{\partial r} \quad (8)$$

Equation (8) is the isentropic simplified-radial-equilibrium equation that is widely used in the design of axial-flow compressors and will be put in chart form.

Integration of equation (8) between any radius r and the radius at which all values are known r_i gives the following:

$$gJ(H_i - H) = \int_r^{r_i} \frac{V_\theta^2}{r} \partial r + \frac{V_{\theta,i}^2 - V_\theta^2}{2} + \frac{V_{z,i}^2 - V_z^2}{2} \quad (9)$$

If the absolute tangential velocity V_θ is expressed analytically as a function of radius r , the integral in equation (9) can be evaluated analytically and the equation solved for any desired variable. However, it is sometimes impossible or undesirable to use a distribution of tangential velocity that makes equation (9) convenient to apply.

If it is assumed that V_θ^2/r is linear with respect to r over the interval $r_i - r$, equation (9) can be written

$$2gJc_p(T_i - T) + V_z^2 - V_{z,i}^2 = \left[\left(\frac{V_\theta^2}{r} \right)_i + \frac{V_\theta^2}{r} \right] (r_i - r) + V_{\theta,i}^2 - V_\theta^2 \quad (10)$$

With a rearrangement of terms, equation (10) becomes

$$\frac{2gJc_p(T_i - T) + V_z^2 - V_{z,i}^2}{V_{\theta,i}^2} = 2 \left(1 - \frac{V_{\theta}^2}{V_{\theta,i}^2} \right) + \frac{r_i}{r} \left(\frac{V_{\theta}^2}{V_{\theta,i}^2} \right) - \frac{r}{r_i} \quad (11)$$

Equation (11) is presented in graph form in figure 1. In the first quadrant, the tangential velocity ratio $V_{\theta}/V_{\theta,i}$ is plotted against the right side of equation (11) with the radius ratio r/r_i as a parameter. Then, with $V_{\theta,i}$ as a parameter in the second quadrant, the numerator of the left side of equation (11) appears as the abscissa. Therefore, if the tangential velocities are known at two radii, use of the first two quadrants of figure 1 will give a value for

$$2gJc_p(T_i - T) + V_z^2 - V_{z,i}^2 = B$$

If the radial interval is sufficiently close for the approximation of linearity between V_{θ}^2/r and r , the value of B will be that required to satisfy isentropic simplified radial equilibrium between radial stations r_i and r . For convenience, let

$$2gJc_p(T_i - T) = 12,170(T_i - T) = C \quad (12)$$

Then

$$V_z^2 - V_{z,i}^2 = B - C \quad (13)$$

The third quadrant of figure 1 is a plot of $B - C$ against V_z with $V_{z,i}$ as the parameter. The abscissa of quadrants II and III, then, represents two values, depending on which quadrant is being used. When used with the second quadrant, its value is B ; when used with the third quadrant, its value is $B - C$. If the temperature gradient is known, C can be calculated by the use of equation (12). This value is subtracted from the value of B , determined by use of the first two quadrants of figure 1, and the difference ($B - C$) is used as the abscissa of the third quadrant together with the known value of axial velocity $V_{z,i}$ to determine the value of axial velocity V_z at radius r .

Although the use of figure 1 has been discussed on the basis of known tangential velocities and temperatures at all radii and solving for the axial velocities, it is obvious that the chart can also be used

with other assumptions. For example, the axial velocities and temperatures can be assumed at all radii and the tangential velocity assumed at one radius. The tangential velocity required to satisfy radial equilibrium at all other radii can then be obtained from the chart. In other words, figure 1 may be used to determine any independent variable of equation (11).

The accuracy of the method of utilizing figure 1 is limited only by the assumption of linearity of V_θ^2/r with respect to radius. For wheel-type rotation, for example, V_θ^2/r is linear with radius; therefore, good accuracy can be expected regardless of the size of the interval $r_1 - r$. However, with nonlinear radial variations of V_θ^2/r , the accuracy of the results obtained from figure 1 will depend on the interval used. For this reason, a small radial interval is recommended.

In order to illustrate the effect of the radial interval on the accuracy of the results of figure 1, axial velocities were read using 3 and 7 radial positions. An arbitrary, nonlinear radial distribution of V_θ^2/r was assumed. The distribution of tangential velocity is a combination of constant, wheel, and vortex rotations. The assumptions and results are as follows:

$$V_\theta = 2400 - 900 \frac{r}{r_t} - 900 \frac{r_t}{r}$$

$$\frac{r_h}{r_t} = 0.5; \quad V_{z,t} = 450; \quad \frac{dT}{dr} = 0$$

$\frac{r}{r_t}$	V_θ	Calculated V_z	3-Point chart procedure		7-Point chart procedure	
			V_z	Percent error	V_z	Percent error
1.0	600	450	450	---	450	---
.9	590	538	---	---	536	0.4
.8	555	638	---	---	636	.3
.75	525	691	683	1.2	691	0
.7	484	744	---	---	743	.1
.6	360	846	---	---	844	.2
.5	150	921	910	1.2	921	0

As the table shows, even with the larger radial interval the errors in axial velocity are only 1.2 percent; however, with the 7-radial-position procedure, the error is reduced to a maximum of 0.4 percent. It should be noted that the radial intervals used in the 7-position procedure are not all equispaced; an extra position was used at $r/r_t = 0.75$. The error in the region of this smallest interval was 0.1 percent. Thus, extremely good accuracy can be obtained by the use of the radial-equilibrium chart, even with nonlinear distributions of V_θ^2/r , if small radial intervals are used.

Continuity

Another condition that must be satisfied, in addition to the radial-equilibrium condition, is continuity of flow:

$$w_k = 2\pi K_{bk} \int_{r_h}^{r_t} \rho g V r \cos \beta \, dr \quad (2)$$

The use of the boundary-layer blockage factor K_{bk} in compressor design is discussed in chapter VIII. From the equations of state and Mach number and the adiabatic relations, the following equations can be obtained:

$$\rho g = \frac{P}{RT} \left(1 + \frac{\gamma-1}{2} M^2 \right)^{-\frac{1}{\gamma-1}} \quad (14)$$

and

$$V = a_a \left(\frac{V}{a_a} \right) = \frac{M \sqrt{\gamma g R T}}{\sqrt{1 + \frac{\gamma-1}{2} M^2}} \quad (15)$$

Substituting equations (14) and (15) into the continuity equation (2) produces the following expression:

$$w_k = 2\pi K_{bk} \int_{r_h}^{r_t} \frac{\sqrt{\gamma g} P M \cos \beta}{\sqrt{RT} \left(1 + \frac{\gamma-1}{2} M^2 \right)^{\frac{\gamma+1}{2(\gamma-1)}}} r \, dr \quad (16)$$

Writing equation (16) in terms of equivalent weight flow,

$$\left(\frac{w\sqrt{\theta}}{\delta}\right)_k = 2\pi K_{bk} \int_{r_h}^{r_t} \left[\frac{\gamma g P_{sl} M \cos \beta}{a_{sl} \left(1 + \frac{\gamma-1}{2} M^2\right)^{\frac{\gamma+1}{2(\gamma-1)}}} \right] r \, dr \quad (17)$$

The part of the integrand in brackets is the local value (value at radius r) of equivalent weight flow per unit annulus area:

$$\left(\frac{w\sqrt{\theta}}{\delta A_{an}}\right)_l = \frac{\gamma g P_{sl} M \cos \beta}{a_{sl} \left(1 + \frac{\gamma-1}{2} M^2\right)^{\frac{\gamma+1}{2(\gamma-1)}}} \quad (18)$$

The first quadrant of figure 2 is a plot of equation (18). The local value of equivalent flow per unit annulus area is plotted against absolute resultant Mach number for constant values of absolute flow angle. Local values of equivalent flow per unit annulus area can be determined from figure 2 for all radii at which the vector diagrams have been determined; then, the continuity value of equation (17) becomes

$$\left(\frac{w\sqrt{\theta}}{\delta}\right)_k = 2\pi K_{bk} \int_{r_h}^{r_t} \left(\frac{w\sqrt{\theta}}{\delta A_{an}}\right)_l r \, dr \quad (19)$$

The integral can be evaluated by a graphical or mathematical procedure, and either the continuity value of equivalent flow, the tip radius, or the hub radius can be calculated, depending on which conditions are given.

If the radial gradient of $(w\sqrt{\theta}/\delta A_{an})_l$ is small, sufficient accuracy in evaluating the integral can be attained by using either an arithmetic average or the mean-radius value of local equivalent flow per unit annulus areas. This, of course, means that the hub and tip diameters must either be known or assumed. The continuity value of the flow per unit annulus area then becomes

$$\left(\frac{w\sqrt{\theta}}{\delta A_{an}}\right)_k = K_{bk} \left(\frac{w\sqrt{\theta}}{\delta A_{an}}\right)_{l,av} \quad (20)$$

The annulus area of the compressor in terms of the frontal area and hub-tip radius ratio is given by

$$A_{an} = A_F \left[1 - \left(\frac{r_h}{r_t} \right)^2 \right] \quad (21)$$

Combining equations (20) and (21) gives

$$\frac{w\sqrt{\theta}}{\delta A_F \left[1 - \left(\frac{r_h}{r_t} \right)^2 \right]} = K_{bk} \left(\frac{w\sqrt{\theta}}{\delta A_{an}} \right)_{l,av}$$

or

$$\frac{w\sqrt{\theta}}{\delta A_F \left[1 - \left(\frac{r_h}{r_t} \right)^2 \right]} = \left(\frac{w\sqrt{\theta}}{\delta A_{an}} \right)_k \quad (22)$$

Equation (22) is plotted in the second quadrant of figure 2, with $w\sqrt{\theta}/\delta A_{an}$ as the ordinate, $w\sqrt{\theta}/\delta A_F$ as the abscissa, and r_h/r_t as the parameter. After determining values of $(w\sqrt{\theta}/\delta A_{an})_l$ at all radii at which the vector diagrams have been calculated, $(w\sqrt{\theta}/\delta A_{an})_k$ is computed from equation (20). Then this value is used in the second quadrant to find the value of r_h/r_t for a given value of $w\sqrt{\theta}/\delta A_F$. If the specific weight flow $w\sqrt{\theta}/\delta A_F$ is specified at one axial station (1), the value at any other axial station (2) is obtained as follows:

$$\left(\frac{w\sqrt{\theta}}{\delta A_F} \right)_2 = \left(\frac{w\sqrt{\theta}}{\delta A_F} \right)_1 \frac{\sqrt{\left(\frac{T_2}{T_1} \right)_{av}}}{\left(\frac{P_2}{P_1} \right)_{av} \left(\frac{r_{t,2}}{r_{t,1}} \right)^2} \quad (23)$$

where $(T_2/T_1)_{av}$ and $(P_2/P_1)_{av}$ are arithmetically averaged values across the annulus.

If the value of hub-tip radius ratio determined by this procedure is greatly different from the value assumed for the purpose of averaging the local values of flow per unit annulus area in equation (20) and the temperature and pressure ratio in equation (23), it will be necessary to repeat the procedure with a new assumed radius ratio.

By proper use of figure 2 and equations (20) and (23), the continuity requirement, with any consistent set of assumptions, can be met. Use of the charts and equations is shown in a specific example later in this chapter.

Energy Addition and Efficiency

The energy addition across a rotor blade element is a function of both the change in tangential velocity and in blade speed across the blade row. The magnitude of the energy addition is given by Euler's equation as

$$gJc_p(T_2 - T_1) = U_2 V_{\theta,2} - U_1 V_{\theta,1} \quad (3)$$

or

$$gJc_p(T_2 - T_1) = U_1(V_{\theta,2} - V_{\theta,1}) + V_{\theta,2}(U_2 - U_1) \quad (24)$$

Solving equation (24) for the temperature ratio T_2/T_1 across the blade element gives

$$\frac{T_2}{T_1} = 1.0 + \frac{U_1(V_{\theta,2} - V_{\theta,1}) + V_{\theta,2}(U_2 - U_1)}{gJc_p T_1}$$

or, by using equivalent velocities,

$$\frac{T_2}{T_1} = 1.0 + \frac{\left(\frac{U_1}{\sqrt{\theta_1}}\right)\left(\frac{\Delta V_{\theta}}{\sqrt{\theta_1}}\right)}{gJc_p T_{s1}} + \frac{\left(\frac{V_{\theta,2}}{\sqrt{\theta_1}}\right)\left(\frac{\Delta U}{\sqrt{\theta_1}}\right)}{gJc_p T_{s1}} \quad (25)$$

where

$$\Delta V_{\theta} = V_{\theta,2} - V_{\theta,1}$$

and

$$\Delta U = U_2 - U_1 = \omega(r_2 - r_1)$$

The last term on the right side of equation (25) is the contribution to the temperature ratio of the change in radius across the blade element; therefore, if the design is carried out on cylindrical stream surfaces ($r_1 = r_2$), equation (25) can be used in the following form:

$$\frac{T_2}{T_1} = 1.0 + \frac{\left(\frac{U_1}{\sqrt{\theta_1}}\right)\left(\frac{\Delta V_\theta}{\sqrt{\theta_1}}\right)}{gJc_p T_{sl}} \quad (26)$$

Equation (26) is plotted in quadrant I of figure 3 with T_2/T_1 as a function of $\Delta V_\theta/\sqrt{\theta_1}$ for constant values of $U_1/\sqrt{\theta_1}$.

If there is a change in streamline radius across the blade element, figure 3 can still be used directly to determine the temperature ratio because of the change in tangential velocity. The contribution to the temperature ratio of the change in radius across the blade element can be obtained either by calculating the last term of equation (25) or by obtaining it from the chart, and adding this value to the temperature ratio previously obtained from the chart result based on $U_1/\sqrt{\theta_1}$ and $\Delta V_\theta/\sqrt{\theta_1}$. In order to use the chart for obtaining the last term of equation (25) the abscissa is considered as $\Delta U/\sqrt{\theta_1}$ and the parameter as $V_{\theta,2}/\sqrt{\theta_1}$. The ordinate will then be the value of the last term of equation (25) plus 1; therefore, 1 should be subtracted from this value before it is added to the first two terms of equation (25).

The chart can also be used for any change in radius if either $V_{\theta,1}$ or $V_{\theta,2}$ is zero. If $V_{\theta,1} = 0$, then $U = U_2$ and $\Delta V_\theta = V_{\theta,2}$; and, if $V_{\theta,2} = 0$, then $U = U_1$ and $\Delta V_\theta = V_{\theta,1}$.

The second quadrant of figure 3 gives pressure ratio as a function of temperature ratio and adiabatic temperature-rise efficiency. The relation is as follows:

$$\frac{P_2}{P_1} = \left[\eta_{ad} \left(\frac{T_2}{T_1} - 1.0 \right) + 1.0 \right]^{\frac{\gamma}{\gamma-1}} \quad (27)$$

In compressor design it may be more desirable to specify a value of relative pressure-loss coefficient $\bar{\omega}$ instead of a blade-element efficiency. A discussion of the relative pressure-loss coefficient and its use in compressor design can be found in chapters VI and VII. If a relative

pressure-loss coefficient is used, the adiabatic temperature-rise efficiency can be obtained from the following expression:

$$\eta_{ad} = \frac{\frac{T_2}{T_1} \left(1.0 - \frac{\bar{\omega}_R \left\{ 1.0 - \left[\frac{1.0}{1.0 + \frac{\gamma-1}{2} (M_1')^2} \right]^{\frac{\gamma}{\gamma-1}} \right\}^{\frac{\gamma-1}{\gamma}}}{\left\{ 1.0 + \frac{\gamma-1}{2} \left(\frac{U_2}{a_{a,1}} \right)^2 \left[1.0 - \left(\frac{r_1}{r_2} \right)^2 \right]^{\frac{\gamma}{\gamma-1}} \right\}^{\frac{\gamma-1}{\gamma}}} \right) - 1.0}{\frac{T_2}{T_1} - 1.0} \quad (28)$$

Vector Relations

The constant use of the relations between velocities and angles in the compressor velocity diagram warrants a chart regardless of the simplicity of application. Construction of the chart can be illustrated by inspecting the following two relations:

$$V_z^2 + V_\theta^2 = V^2 \quad (29)$$

and

$$V_\theta = V_z \tan \beta \quad (30)$$

From equation (29) it can be seen that, if V_z and V_θ are used as rectilinear coordinates, constant values of V will be concentric circles with $V_\theta = V_z = 0$ as a center. Using the same coordinates, a plot of equation (30) would produce a family of straight lines going through the origin ($V_\theta = V_z = 0$). The angle between these lines and the V_z axis would be equal to the value of β .

Such a vector chart is shown in figure 4 with V_z as the abscissa and V_θ as the ordinate. Obviously, relative values of the velocities and flow angle can also be used in the chart. Further, the coordinates can represent Mach numbers if the decimal point is changed for the values appearing in both axes.

Diffusion Factor

A blade-element-loading criterion for axial-flow compressors is developed in reference 8. The application of this loading criterion to

blade elements in cascades and in compressors is presented in chapters VI and VII. The loading criterion, or diffusion factor, in the form usually applied is given by the following expressions:

$$D = 1 - \frac{V_2'}{V_1'} + \frac{\Delta V_\theta'}{2\sigma V_1'} \quad (31)$$

The diffusion factor can be used in two ways in compressor design: (1) With the vector diagrams known, the diffusion factor is computed and the energy losses across the blade element are estimated from data such as presented in chapters VI and VII; or (2) a limiting value of diffusion factor is prescribed and the conditions required to satisfy the assumed diffusion factor for given inlet or outlet conditions are calculated.

Although equation (31) is in satisfactory form for the first of these purposes, it is not directly applicable for the second purpose. In order to put equation (31) in a form that can be used to determine conditions for a prescribed diffusion factor, it can be written in terms of flow angles and axial velocities:

$$1 - D = \left(\frac{V_{z,2}}{V_{z,1}} \right) \left(\frac{\cos \beta_1}{\cos \beta_2} \right) - \left(\frac{V_{z,1} \tan \beta_1 - V_{z,2} \tan \beta_2}{2\sigma V_{z,1}} \right) \cos \beta_1$$

In the application of this equation, flow angles are always taken relative to the blade row under consideration.

A rearrangement of terms produces the following expression:

$$\left[\frac{\sigma(1 - D)}{\cos \beta_1} + \frac{\tan \beta_1}{2} \right] = \frac{V_{z,2}}{V_{z,1}} \left[\frac{\sigma}{\cos \beta_2} + \frac{\tan \beta_2}{2} \right] \quad (32)$$

Equation (32) is readily adaptable to chart form. The terms in brackets on both sides of the equation are identical with β_1 substituted for β_2 and $\sigma(1 - D)$ substituted for σ ; therefore, a single family of curves can be used to represent each function inside the brackets. The ratio of the two functions will be equal to the axial velocity ratio across the blade row. In order to simplify the expression, let

$$X = \frac{\sigma(1 - D)}{\cos \beta_1} + \frac{\tan \beta_1}{2} \quad (33)$$

and

$$Y = \frac{\sigma}{\cos \beta_2} + \frac{\tan \beta_2}{2} \quad (34)$$

Then,

$$\frac{V_{z,2}}{V_{z,1}} = \frac{X}{Y} \quad (35)$$

Figure 5 is a plot of X as a function of β_1 for constant values of $\sigma(1 - D)$. The same family of curves represents Y as a function of β_2 for constant values of σ . Figure 5 and equation (35) can be used for the solution of equation (32) for any desired parameter. The use of figure 5 to compute diffusion factor with the velocity diagrams known and to compute the discharge flow angle for given diffusion factor, inlet conditions, and axial velocity ratio, is shown in the following example.

EXAMPLE

The procedure in using the charts is best illustrated by an example of the design of an axial-flow-compressor stage. The stage design assumptions were made so that they would provide a stringent case for the charts and also to illustrate as many uses of the charts as possible. The axial and radial station designations and a typical vector diagram are shown in figures 6 and 7, respectively. The design assumptions and calculation procedure are as follows.

Compute the vector diagrams, pressure ratio, temperature ratio, Mach number, and diffusion factor at five equispaced radial positions and the passage shape for an axial-flow-compressor stage consisting of rotor and stator blade row to meet the following specifications:

Assumed design parameters:

Parameter	Design value	Parameter	Design value
$(w\sqrt{\theta}/8A_F)_1$	35.0 (lb/sec)/sq ft	dT/dr	12° R/ft
$M_{z,1}$	0.6	$D_{R,t}$	0.35
$M'_{t,1}$	1.2	$D_{R,h}$	≤ 0.6
$r_{t,1}$	1.50 ft	$D_{S,h}$	≤ 0.6
$r_{t,2} = r_{t,2a}$	1.42 ft	$\sigma_{R,t}$	1.0
$r_{t,3a}$	1.41 ft	$\sigma_{S,t}$	0.7
$(V_{z,2}/V_{z,1})_t$	1.1	K_{bk}	0.98
$(V_{z,3a}/V_{z,2a})_t$	1.0	$\bar{\omega}_S$	0.02
$V_{\theta,1} = V_{\theta,3a}$	0	$T_1 = T_{s1}$	518.7° R
$\eta_{ad,R}$	0.92	$P_1 = P_{s1}$	2116 lb/sq ft

Blade chords constant from hub to tip

Calculated design parameters:

Parameter	Procedure	Value
$A_{F,1}$	$\pi r_{t,1}^2 = \pi(1.5)^2$	7.069 sq ft
$\left(\frac{w\sqrt{\theta}}{\delta}\right)_1$	$\left(\frac{w\sqrt{\theta}}{\delta A_F}\right)_1 A_{F,1} = (35)(7.069)$	247 lb/sec
$\left(\frac{w\sqrt{\theta}}{\delta A_{an}}\right)_{l,1}$	$M_{z,1} = 0.6$, $\beta_1 = 0$, and fig. 2	41.6 (lb/sec)/sq ft
$\left(\frac{w\sqrt{\theta}}{\delta A_{an}}\right)_{k,1}$	$K_{bk} \left(\frac{w\sqrt{\theta}}{\delta A_{an}}\right)_{l,1} = (0.92)(41.6)$	40.8 (lb/sec)/sq ft
$\left(\frac{r_h}{r_t}\right)_1$	$\left(\frac{w\sqrt{\theta}}{\delta A_{an}}\right)_{k,1} = 40.8$, $\left(\frac{w\sqrt{\theta}}{\delta A_F}\right)_1 = 35.0$, and fig. 2	0.378
$r_{h,1}$	$r_{t,1} \left(\frac{r_h}{r_t}\right)_1 = (1.5)(0.378)$	0.567 ft
$(a/a_a)_1$	$M_{z,1} = 0.6$ and ref. 9	0.9658
a_1	$a_{a,1} \left(\frac{a}{a_a}\right)_1 = (1116)(0.9658)$	1078 ft/sec
$V_{z,1}$	$a_1 M_{z,1} = (1078)(0.6)$	647 ft/sec
$V'_{t,1}$	$a_1 M'_{t,1} = (1078)(1.2)$	1294 ft/sec
$\left. \begin{matrix} V'_{\theta,t,1} = U_{t,1} \\ \beta'_{t,1} \end{matrix} \right\}$	$V_{z,1} = 647$, $V'_{t,1} = 1294$, and fig. 4	$\left\{ \begin{matrix} 1120 \text{ ft/sec} \\ 60^\circ \end{matrix} \right.$
$\sigma_{R,t} (1 - D_{R,t})$	1.0 (1.00 - 0.35)	0.65
X	$\sigma_{R,t} (1 - D_{R,t}) = 0.65$, $\beta'_{t,1} = 60$, and fig. 5	2.16
Y	$X / \left(\frac{V_{z,2}}{V_{z,1}}\right)_t = \frac{2.16}{1.1}$	1.96

Calculated design parameters - concluded:

Parameter	Procedure	Value
$\beta'_{t,2}$	$Y = 1.96, \sigma_{R,t} = 1.0, \text{ and fig. 5}$	46.3°
$V_{z,t,2}$	$V_{z,1} \left(\frac{V_{z,2}}{V_{z,1}} \right)_t = (647)(1.1)$	712 ft/sec
$\left. \begin{matrix} V'_{\theta,t,2} \\ V'_{t,2} \end{matrix} \right\}$	$V'_{z,t,2} = 712, \beta'_{t,2} = 46.3,$ and fig. 4	$\left\{ \begin{matrix} 744 \text{ ft/sec} \\ 1028 \text{ ft/sec} \end{matrix} \right.$
$U_{t,2}$	$U_{t,1} \left(\frac{r_2}{r_1} \right)_t = (1120) \left(\frac{1.42}{1.50} \right)$	1060 ft/sec
$V_{\theta,t,2} = \Delta V_{\theta,t} = \Delta V'_{\theta,t}$	$U_{t,2} - V'_{\theta,t,2} = 1060 - 744$	316 ft/sec
$\left(\frac{T_2}{T_1} \right)_t$	$\frac{U_{t,2}}{\sqrt{\theta_1}} = 1060, \frac{\Delta V_{\theta,t}}{\sqrt{\theta_1}} = 316, \sqrt{\theta_1} = 1.0,$ and fig. 3	1.1061
$\left(\frac{P_2}{P_1} \right)_t$	$\left(\frac{T_2}{T_1} \right)_t = 1.1061, \eta_{ad,R} = 0.92,$ and fig. 3	1.386
ΔT_t	$T_{t,2} - T_{t,1} = T_1 \left[\left(\frac{T_2}{T_1} \right)_t - 1.0 \right]$ $= 518.7 (1.1061 - 1.0)$	55.03° R

Vector-diagram calculation:

Step	Parameter	Known design condition	Procedure	Radial position				
				Tip	b	Mean	c	Hub
1	r_1	$r_{t,1} = 1.50$ $r_{h,1} = 0.567$		1.500	1.267	1.034	0.800	0.567
2	$U_1 = V_{\theta,1}$	$U_{t,1} = 1120$ $r_{t,1} = 1.50$	$\left(\frac{rU_t}{r_t}\right)_1$	1120	946	772	597	423
3	V'_1	$V_{z,1} = 647$	$V_{z,1}, U_1, \text{ and fig. 4}$	1294	1144	1006	879	772
4	β'_1			60.0	55.6	50.0	42.7	33.1
5	M'_1	$a_1 = 1078$	$\left(\frac{V'}{a}\right)_1$	1.200	1.061	0.933	0.815	0.716
6	r_2	$r_{t,2} = 1.42$ $r_{h,2} = r_{h,1} = 0.567$		1.420	1.207	0.994	0.780	0.567
7	ΔT	$\Delta T_t = 55.03$ $\left(\frac{dT}{dr}\right) = 12$	$\Delta T_t - \left(\frac{dT}{dr}\right)(r_{t,2} - r_2)$	55.03	52.47	49.92	47.35	44.79
8	$\frac{T_2}{T_1}$	$T_1 = 518.7$	$\frac{\Delta T}{T_1} + 1.0$	1.1061	1.1012	1.0962	1.0913	1.0864
9	U_2	$U_{t,2} = 1060$ $r_{t,2} = 1.42$	$\left(\frac{rU_t}{r_t}\right)_2$	1060	901	742	582	423
10	$\frac{\Delta V_{\theta}}{\sqrt{\theta_1}} = V_{\theta,2}$	$\theta_1 = 1.0$	$\frac{U_2}{\sqrt{\theta_1}}, \frac{T_2}{T_1}, \text{ and fig. 3}$	316	355	409	496	645
11	$\frac{P_2}{P_1}$	$\eta_{ad,R} = 0.92$	$\frac{T_2}{T_1}, \eta_{ad,R}, \text{ and fig. 3}$	1.386	1.366	1.346	1.326	1.308

Step	Parameter	Known design condition	Procedure	Radial position				
				Tip	b	Mean	c	Hub
12	$\left(\frac{r}{r_i}\right)_2$	$V_{z,t,2} = 712$	Example at mean $\left(\frac{r}{r_i}\right)_2 = \left(\frac{r_m}{r_b}\right)_2$	-----	0.85	0.82	0.78	0.73
13	$\left(\frac{V_\theta}{V_{\theta,i}}\right)_2$		Example at hub $\left(\frac{V_\theta}{V_{\theta,i}}\right)_2 = \left(\frac{V_{\theta,h}}{V_{\theta,c}}\right)_2$	-----	1.123	1.152	1.213	1.300
14	B_2		$\left(\frac{V_\theta}{V_{\theta,i}}\right)_2$, $\left(\frac{r}{r_i}\right)_2$, $V_{\theta,2,i}$, and fig. 1	-----	0.012×10^6	0.021×10^6	0.025×10^6	0.050×10^6
15	C_2		$12,170 (\Delta T_i - \Delta T)$	-----	0.031×10^6	0.031×10^6	0.031×10^6	0.031×10^6
16	$(V_z^2 - V_{z,i}^2)_2$		$(B - C)_2$	-----	-0.019×10^6	-0.010×10^6	-0.006×10^6	0.019×10^6
17	$V_{z,2}$		$(V_z^2 - V_{z,i}^2)_2$, $V_{z,2,i}$, and fig. 1	712	696	688	683	698
18	$V'_{\theta,2}$		$(U - V_\theta)_2$	744	546	333	86	-222
19	V'_2		$V_{z,2}$, $V'_{\theta,2}$, and fig. 4	1028	883	763	689	732
20	β'_2			46.3	38.2	25.8	7.0	-17.6
21	V_2	$a_{a,1} = 1116$	$V_{z,2}$, $V_{\theta,2}$, and fig. 4	778	780	800	843	949
22	β_2			23.8	27.0	30.6	36.0	42.7
23	$\left(\frac{V}{a_a}\right)_2$		$\frac{V_2}{a_{a,1} \sqrt{\frac{T_2}{T_1}}}$	0.6629	0.6661	0.6847	0.7231	0.8159
24	M_2		$\left(\frac{V}{a_a}\right)_2$ and ref. 9	0.694	0.698	0.719	0.764	0.876

Step	Parameter	Known design condition	Procedure	Radial position				
				Tip	b	Mean	c	Hub
25	$\left(\frac{w\sqrt{\theta}}{\delta A_{an}}\right)_{l,2}$		M_2, β_2 , and fig. 2	41.2	40.2	39.3	37.8	35.8
26	$\left(\frac{w\sqrt{\theta}}{\delta A_{an}}\right)_{k,2}$	$K_{bk} = 0.98$	$K_{bk}\left(\frac{w\sqrt{\theta}}{\delta A_{an}}\right)_{l,2}$	40.4	39.4	38.5	37.0	35.1
27	$\left(\frac{w\sqrt{\theta}}{\delta A_F}\right)_2$	$\left(\frac{w\sqrt{\theta}}{\delta A_F}\right)_1 = 35$ $r_{t,1} = 1.50$ $r_{t,2} = 1.42$	$\left(\frac{w\sqrt{\theta}}{\delta A_F}\right)_1 \sqrt{\frac{T_2}{T_1}}$ $\frac{(P_2)(r_{t,2})^2}{(P_1)(r_{t,1})^2}$	29.6	30.0	30.4	30.8	31.1
28	$\left(\frac{r_h}{r_t}\right)_2$		$\left(\frac{w\sqrt{\theta}}{\delta A_{an}}\right)_{k,2,av}, \left(\frac{w\sqrt{\theta}}{\delta A_F}\right)_{2,av}$, and fig. 2	0.450				
29	r_{2a}	$r_{t,2a} = r_{t,2} = 1.42$		1.420	1.225	1.030	0.834	0.639
30	$\left(\frac{w\sqrt{\theta}}{\delta A_{an}}\right)_{k,2a}$		From plot of $\left(\frac{w\sqrt{\theta}}{\delta A_{an}}\right)_{k,2}$ (step 26) against r_2 (step 6) read at r_{2a} (step 29)	40.4	39.7	38.7	37.5	35.8
31	$\left(\frac{w\sqrt{\theta}}{\delta A_F}\right)_{2a}$		From plot of $\left(\frac{w\sqrt{\theta}}{\delta A_F}\right)_2$ (step 27) against r_2 read at r_{2a}	29.6	30.0	30.3	30.7	31.0
32	$\left(\frac{r_h}{r_t}\right)_{2a}$		$\left(\frac{w\sqrt{\theta}}{\delta A_{an}}\right)_{k,2a,av}, \left(\frac{w\sqrt{\theta}}{\delta A_F}\right)_{2a,av}$, and fig. 2	0.460				
33	r_{2a}	$r_{t,2a} = 1.42$		1.420	1.228	1.037	0.845	0.653

Step	Parameter	Known design condition	Procedure	Radial position				
				Tip	b	Mean	c	Hub
			Using value of r_{2a} from step 33 repeat steps 30 to 33 until consecutive values of $\left(\frac{r_h}{r_t}\right)_{2a}$ in step 32 agree					
34	$\frac{T_{2a}}{T_1} = \frac{T_{3a}}{T_1}$		From plots of $\frac{T_2}{T_1}$, $\frac{P_2}{P_1}$, $V_{\theta,2}$, $V_{z,2}$, β'_2 and M_2 against r_2 read at r_{2a} (final)	1.1061	1.1017	1.0973	1.0929	1.0885
35	$\frac{P_{2a}}{P_1}$			1.386	1.368	1.350	1.332	1.315
36	$V_{\theta,2a}$			316	350	397	463	579
37	$V_{z,2a}$			712	697	689	684	689
38	β'_{2a}			46.3	39.2	28.5	13.1	-6.7
39	M_{2a}			0.694	0.697	0.712	0.744	0.822
40	V_{2a}		$V_{z,2a}$, $V_{\theta,2a}$, and fig. 4	778	780	794	824	900
41	β_{2a}			23.8	26.6	30.0	34.0	40.0
42	$\sigma_{R,av}$	$\sigma_{R,t} = 1.0$ $r_{t,1} = 1.50$ $r_{t,2a} = 1.42$	$\sigma_{R,t} \left(\frac{r_{t,1} + r_{t,2a}}{r_1 + r_{2a}} \right)$	1.00	1.17	1.41	1.78	2.39
43	Y		$\sigma_{R,av}$, β'_{2a} , and fig. 5	1.96	1.91	1.89	1.94	2.34
44	X	$V_{z,1} = 647$	$Y \left(\frac{V_{z,2a}}{V_{z,1}} \right)$	2.16	2.06	2.01	2.05	2.49

Step	Parameter	Known design condition	Procedure	Radial position				
				Tip	b	Mean	c	Hub
45	$\sigma_{R,av}(1 - D_R)$		$X, \beta_1',$ and fig. 5	0.65	0.76	0.91	1.17	1.80
46	D_R		$1.0 - \left[\frac{\sigma_{R,av}(1 - D_R)}{\sigma_{R,av}} \right]$	0.35	0.35	0.35	0.34	0.25
47	C_{3a}	$T_1 = 518.7$	$12,170 T_1 \left[\left(\frac{T_{3a}}{T_1} \right)_i - \left(\frac{T_{3a}}{T_1} \right) \right]$	-----	0.028×10^6	0.028×10^6	0.028×10^6	0.028×10^6
48	$(V_z^2 - V_{z,i}^2)_{3a}$	$V_{\theta,3a} = 0$ $\therefore B_{3a} = 0$	$(B - C)_{3a}$	-----	-0.028×10^6	-0.028×10^6	-0.028×10^6	-0.028×10^6
49	$V_{z,3a} = V_{3a}$	$\left(\frac{V_{z,3a}}{V_{z,2a,t}} \right) = 1.0$	$(V_z^2 - V_{z,i}^2)_{3a}, V_{z,3a,i},$ and fig. 1	712	691	670	650	629
50	$\left(\frac{V}{a_a} \right)_{3a}$	$a_{a,1} = 1116$	$\frac{V_{3a}}{a_{a,1} \sqrt{\frac{T_{3a}}{T_1}}}$	0.6067	0.5899	0.5732	0.5572	0.5402
51	M_{3a}		$\left(\frac{V}{a_a} \right)_{3a}$ and ref. 9	0.630	0.612	0.593	0.575	0.557
52	$\left(\frac{p}{P} \right)_{2a}$		M_{2a} and ref. 9	0.7248	0.7229	0.7132	0.6925	0.6417
53	$\frac{P_{3a}}{P_1}$	$\bar{\omega}_S = 0.02$	$\frac{P_{2a}}{P_1} \left[1.0 - \bar{\omega}_S \left(1.0 - \frac{P_{2a}}{P_{2a}} \right) \right]$	1.378	1.360	1.342	1.324	1.306
54	$\left(\frac{w \sqrt{\vartheta}}{\delta A_{an} l} \right)_{3a}$	$\beta_{3a} = 0$	$M_{3a}, \beta_{3a},$ and fig. 2	42.8	42.0	41.3	40.5	39.7

Step	Parameter	Known design condition	Procedure	Radial position				
				Tip	b	Mean	c	Hub
55	$\left(\frac{w\sqrt{\theta}}{\delta A_{an}}\right)_{k,3a}$	$K_{bk} = 0.98$	$K \left(\frac{w\sqrt{\theta}}{\delta A_{an}}\right)_{l,3a}$	41.9	41.2	40.5	39.7	38.9
56	$\left(\frac{w\sqrt{\theta}}{\delta A_F}\right)_{3a}$	$\left(\frac{w\sqrt{\theta}}{\delta A_F}\right)_1 = 35$ $r_{t,1} = 1.50$ $r_{t,3a} = 1.41$	$\frac{\left(\frac{w\sqrt{\theta}}{\delta A_F}\right)_1 \left(\sqrt{\frac{T_{3a}}{T_1}}\right)}{\left(\frac{P_{3a}}{P_1}\right) \left(\frac{r_{t,3a}}{r_{t,1}}\right)^2}$	30.2	30.6	30.9	31.3	31.6
57	$\left(\frac{r_h}{r_t}\right)_{3a}$		$\left(\frac{w\sqrt{\theta}}{\delta A_{an}}\right)_{k,3a,av}, \left(\frac{w\sqrt{\theta}}{\delta A_F}\right)_{3a,av}$, and fig. 2	0.484				
58	r_{3a}	$r_{t,3a} = 1.41$		1.410	1.228	1.046	0.864	0.682
59	$\sigma_{S,av}$	$\sigma_{S,t} = 0.7$ $r_{t,2a} = 1.42$ $r_{t,3a} = 1.41$	$\sigma_{S,t} \left(\frac{r_{t,2a} + r_{t,3a}}{r_{2a} + r_{3a}}\right)$	0.70	0.81	0.95	1.16	1.48
60	Y	$\beta_{3a} = 0$	$\sigma_{S,av}$, β_{3a} , and fig. 5	0.70	0.81	0.95	1.16	1.48
61	X		$Y \left(\frac{V_{z,3a}}{V_{z,2a}}\right)$	0.70	0.80	0.92	1.10	1.35
62	$\sigma_{S,av}(1 - D_S)$		X, β_{2a} , and fig. 5	0.44	0.49	0.54	0.63	0.72
63	D_S		$1.0 - \left[\frac{\sigma_{S,av}(1 - D_S)}{\sigma_{S,av}}\right]$	0.37	0.40	0.43	0.46	0.51
64	η_{ad}		$\frac{P_{3a}}{P_1}, \frac{T_{3a}}{T_1}$, and fig. 3	0.904	0.902	0.900	0.899	0.896

COMPARISON OF CHART AND CALCULATED VALUES

The more important parameters obtained by use of the chart procedures are summarized in the following table. The analytically calculated values of the parameters are also given for comparison and an indication of accuracy:

Parameter	Chart procedure					Analytical calculation					Parameter
	Radial position					Radial position					
	Tip	b	Mean	c	Hub	Tip	b	Mean	c	Hub	
M ₁ [']	1.200	1.061	0.933	0.815	0.716	1.200	1.064	0.934	0.817	0.717	M ₁ [']
β ₁ [']	60.0	55.6	50.0	42.7	33.1	60.0	55.7	50.0	42.7	33.2	β ₁ [']
β _{2a} [']	46.3	39.2	28.5	13.1	-6.7	46.3	39.8	29.1	15.4	-5.1	β _{2a} [']
β _{2a}	23.8	26.6	30.0	34.0	40.0	24.0	26.6	29.9	34.1	39.7	β _{2a}
V _{z,2a}	712	697	689	684	689	712	697	686	679	678	V _{z,2a}
M _{2a}	.694	.697	.712	.744	.822	.695	.697	.710	.740	.804	M _{2a}
D _R	.35	.35	.35	.34	.25	.35	.35	.35	.33	.25	D _R
V _{z,3a}	712	691	670	650	629	712	692	671	648	625	V _{z,3a}
M _{3a}	.630	.612	.593	.575	.557	.630	.612	.594	.574	.553	M _{3a}
D _S	.37	.40	.43	.46	.51	.38	.39	.42	.45	.51	D _S
T _{3a} /T ₁	1.1061	1.1017	1.0973	1.0929	1.0885	1.1066	1.1021	1.0976	1.0928	1.0882	T _{3a} /T ₁
P _{3a} /P ₁	1.378	1.360	1.342	1.324	1.306	1.380	1.360	1.342	1.324	1.305	P _{3a} /P ₁

$$(r_h/r_t)_1 = 0.378$$

$$(r_h/r_t)_{2a} = 0.460$$

$$(r_h/r_t)_{3a} = 0.484$$

$$(r_h/r_t)_1 = 0.377$$

$$(r_h/r_t)_{2a} = 0.471$$

$$(r_h/r_t)_{3a} = 0.495$$

Comparison of the values in the table indicates that good accuracy can be obtained with the charts. The largest differences in axial velocities and resultant Mach numbers were about 2 percent, occurring at the hub of the rotor-discharge station. At all other stations the differences were less than 0.7 percent. The flow angles agreed within 0.6° at all stations except the hub and c positions at the rotor discharge, where the chart values of the relative flow angles varied 1.6° and 2.3° , respectively, from the analytically calculated values. The passage areas obtained by the chart procedure were within 1.4 percent of the analytically calculated areas.

REFERENCES

1. Compressor and Turbine Research Division: Aerodynamic Design of Axial-Flow Compressors. Vol. I. NACA RM E56B03, 1956.
2. Cavicchi, Richard H., and English, Robert E.: Analysis of Limitations Imposed on One-Spool Turbojet-Engine Designs by Compressors and Turbines at Flight Mach Numbers of 0, 2.0, and 2.8. NACA RM E54F21a, 1954.
3. Hatch, James E., Giamati, Charles C., and Jackson, Robert J.: Application of Radial-Equilibrium Condition to Axial-Flow Turbomachine Design Including Consideration of Change of Entropy with Radius Downstream of Blade Row. NACA RM E54A20, 1954.
4. Wu, Chung-Hua, and Wolfenstein, Lincoln: Application of Radial-Equilibrium Condition to Axial-Flow Compressor and Turbine Design. NACA Rep. 955, 1950. (Supersedes NACA TN 1795.)
5. Marble, Frank E.: The Flow of a Perfect Fluid through an Axial Turbomachine with Prescribed Blade Loading. Jour. Aero. Sci., vol. 15, no. 8, Aug. 1948, pp. 473-485.
6. Marble, Frank E., and Michelson, Irving: Analytical Investigation of Some Three Dimensional Flow Problems in Turbo-Machines. NACA TN 2614, 1952.
7. Stanitz, John D.: Effect of Blade-Thickness Taper on Axial-Velocity Distribution at the Leading Edge of an Entrance Rotor-Blade Row with Axial Inlet, and the Influence of This Distribution on Alinement of the Rotor Blade for Zero Angle of Attack. NACA TN 2986, 1953.
8. Lieblein, Seymour, Schwenk, Francis C., and Broderick, Robert L.: Diffusion Factor for Estimating Losses and Limiting Blade Loadings in Axial-Flow-Compressor Blade Elements. NACA RM E53D01, 1953.
9. The Staff of the Ames 1- by 3-Foot Supersonic Wind-Tunnel Section: Notes and Tables for Use in the Analysis of Supersonic Flow. NACA TN 1428, 1947.

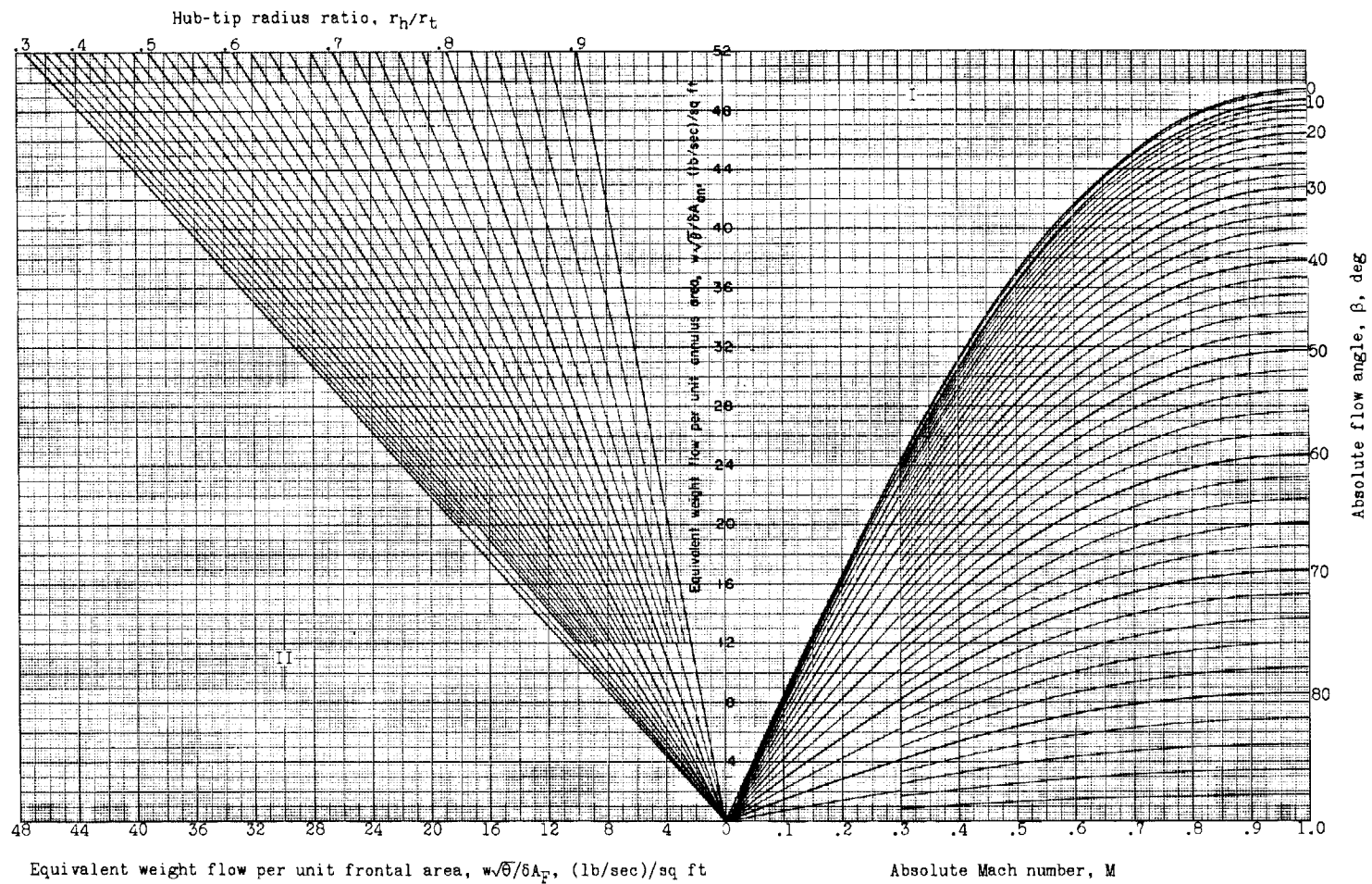


Figure 2. - Chart for satisfying continuity of flow.

(A large copy of this chart may be obtained by using the request card bound in the back of the report.)

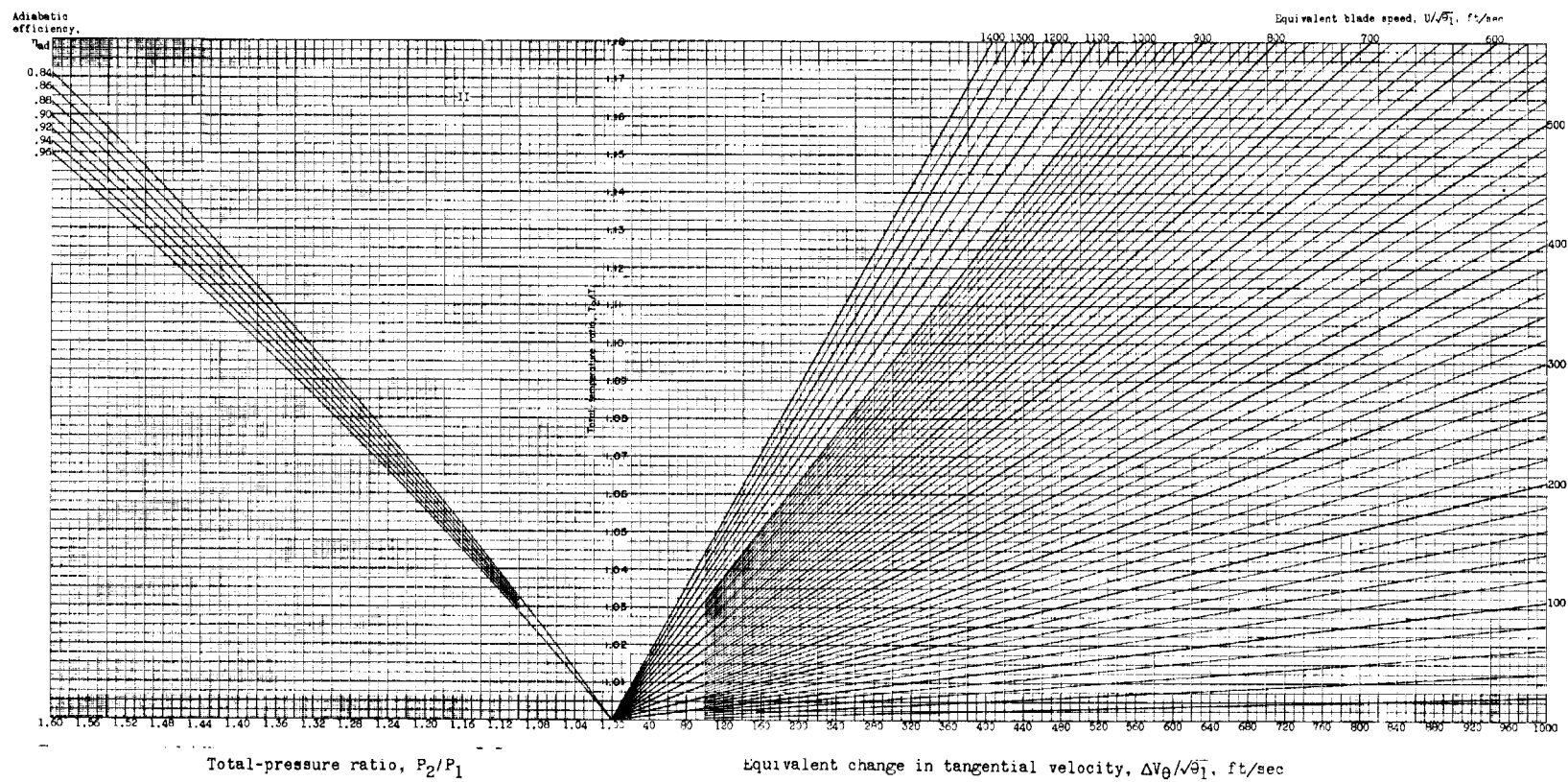


Figure 3. - Total-pressure ratio and total-temperature ratio as functions of equivalent change in tangential velocity, equivalent blade speed, and efficiency.

(A large copy of this chart may be obtained by using the request card bound in back of the report.)

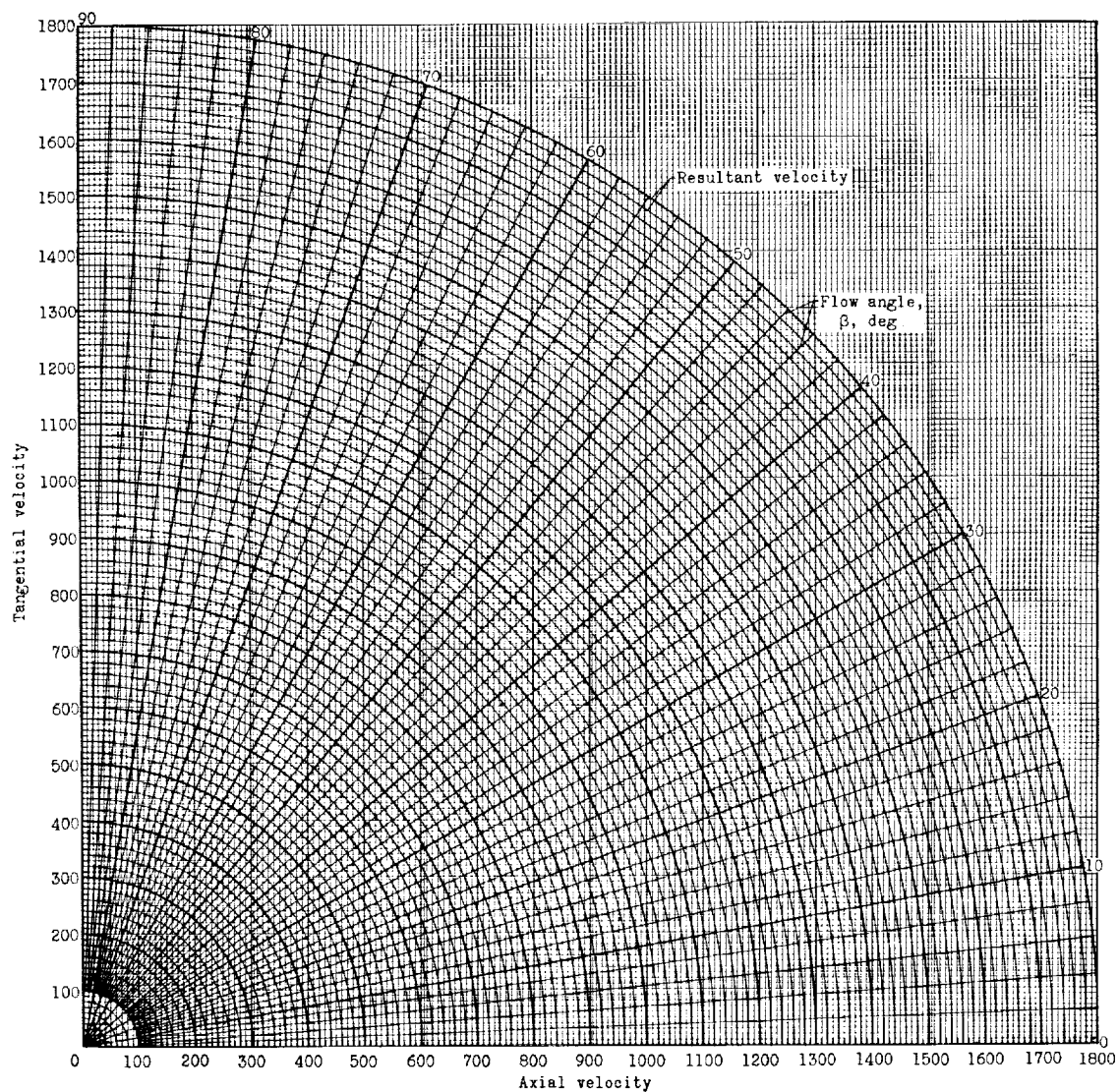
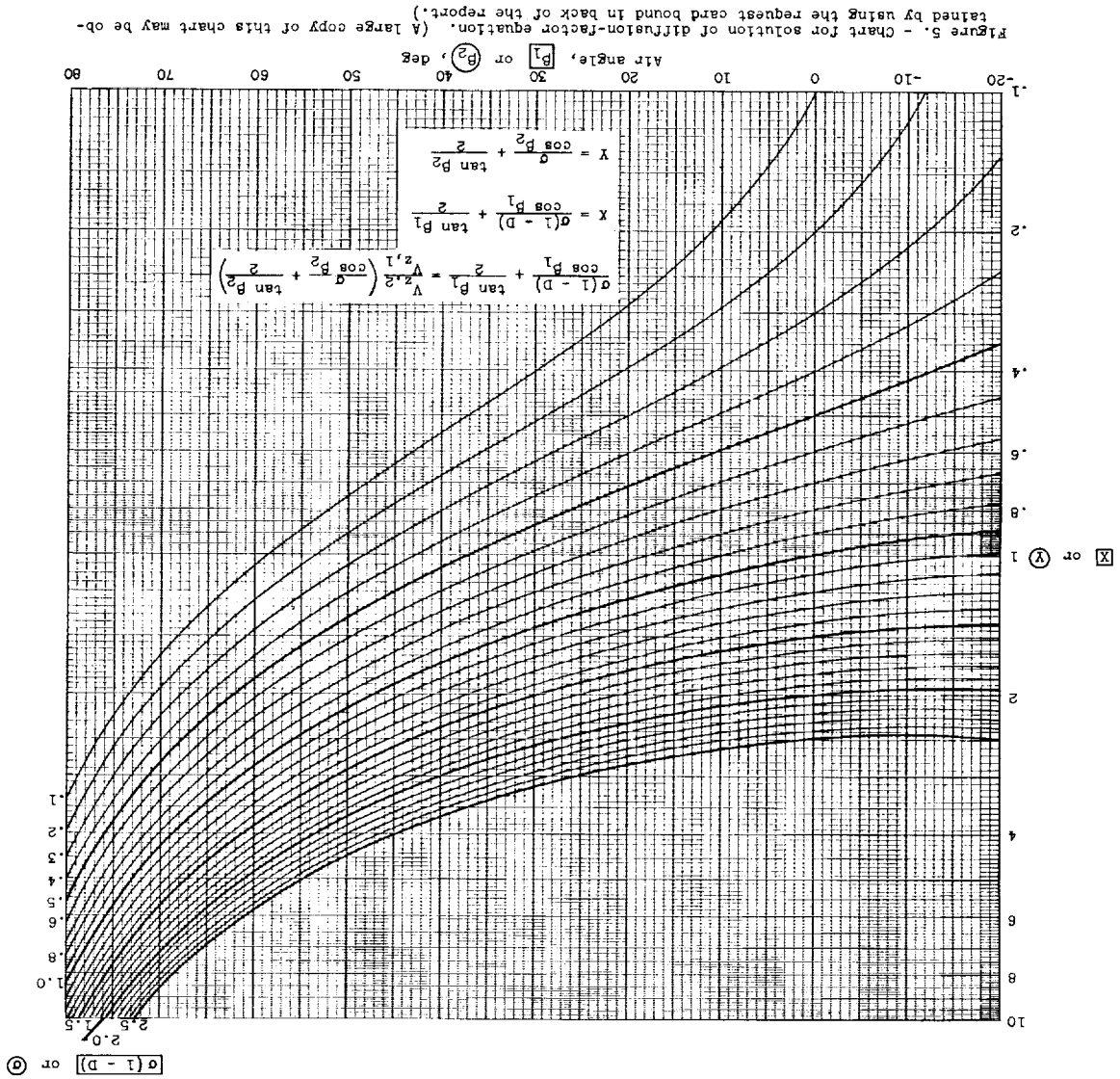
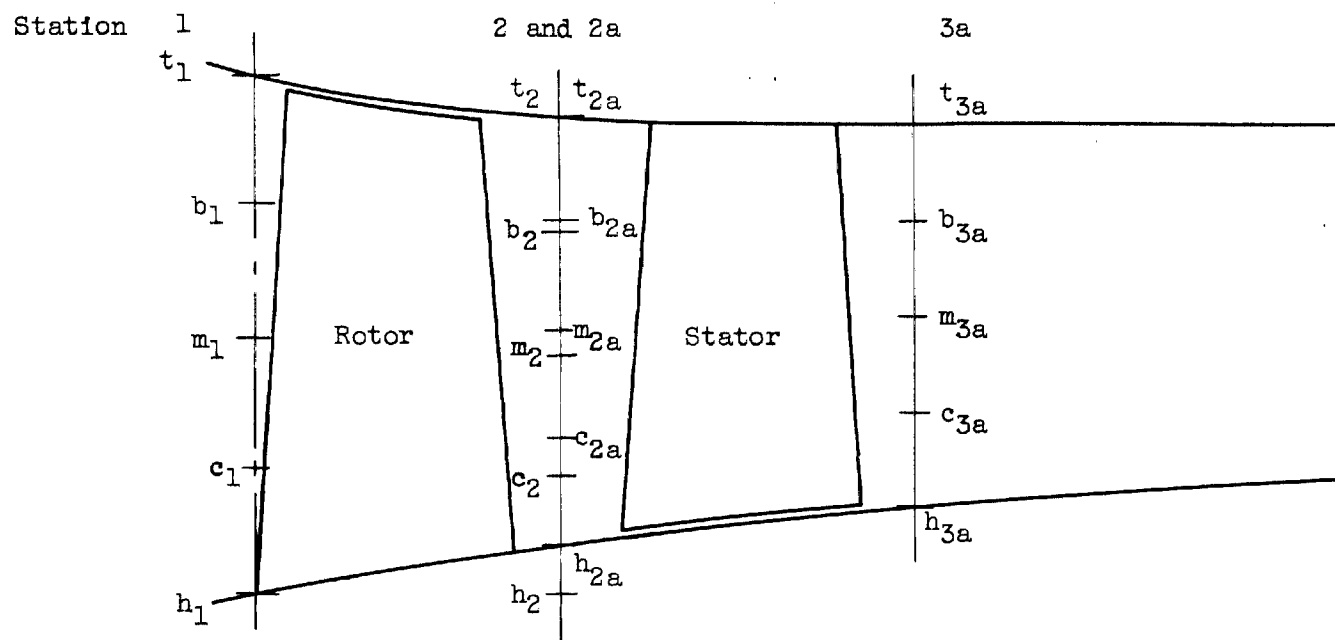


Figure 4. - Chart for vector relations.
 (A large copy of this chart may be obtained by using the request card bound in the back of the report.)





Q_L

Figure 6. - Cross section of typical stage showing axial and radial stations.

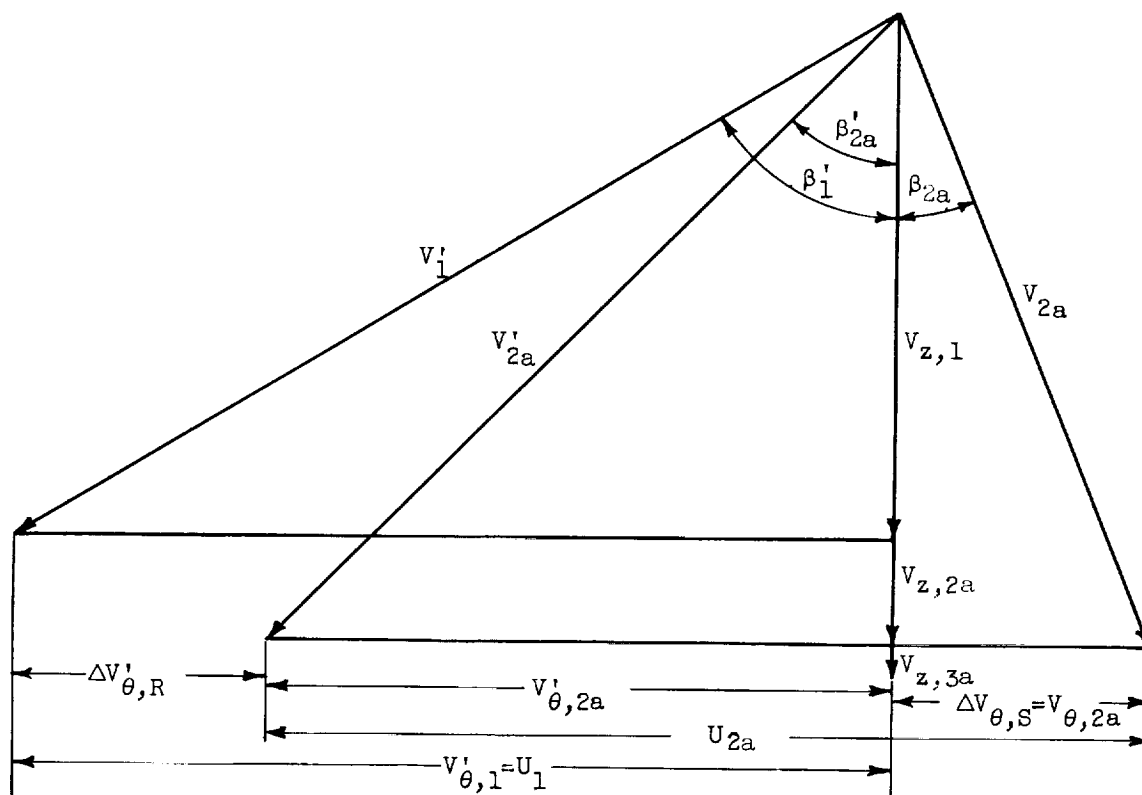


Figure 7. - Vector diagram for typical stage. $\beta_1 = \beta_{3a} = 0$.

CHAPTER X

PREDICTION OF OFF-DESIGN PERFORMANCE OF MULTISTAGE COMPRESSORS

By William H. Robbins and James F. Dugan, Jr.

SUMMARY

Three techniques are presented for estimating compressor off-design performance. The first method, which is based on blade-element theory, is useful for obtaining only a small part of the compressor map over which all blade elements in the compressor operate unstalled. The second method, which involves individual stage performance curves and a stage-by-stage calculation, is useful for estimating the performance of a compressor for which reliable stage performance curves are available. The third method, which is based on over-all performance data of existing compressors, may be used to estimate the complete performance map of a new compressor if the compressor design conditions are specified.

INTRODUCTION

The availability of good analytical techniques for predicting performance maps of designed compressors reduces costly and time-consuming testing and development and in addition aids in selecting the best compressor for a given application. Specific information that is required to achieve these goals is the relation between the stall-limit line and the operating line and the variation of efficiency and pressure ratio along the operating line. Therefore, one of the goals of compressor research is to obtain reliable performance prediction methods. This problem, which can be considered as an analysis of off-design compressor performance, is one of the most difficult tasks facing the compressor designer.

Off-design performance is defined as the performance of the compressor at flow conditions and speeds other than those for which the compressor was specifically designed. The off-design analysis differs from the design case in that the compressor geometry is given and the object is to find the compressor-outlet conditions for a range of speeds and weight flows. It is sometimes referred to as the "direct compressor problem," whereas the original design is called the "inverse" or "design problem." The design problem is discussed in detail in chapter VIII.

Prediction of off-design performance is considered in this chapter. A typical compressor performance map is shown in figure 1 with the design point and the stall-limit or surge line indicated. The regions of the performance map that are discussed herein are those to the right of the stall-limit line along lines of constant speed; in other words, the complete compressor map. Three techniques for predicting off-design performance are presented.

In the first method, compressor performance is obtained by first radially integrating compressor blade-element data to obtain blade-row performance. The performance of successive blade rows is determined by utilizing the computed outlet conditions of one blade row as the inlet conditions to the following blade row until complete compressor performance is obtained. This type of solution for compressor off-design performance, of course, requires a rather complete knowledge of compressor blade-element flow, radial integration techniques, boundary-layer growth, blade-row interactions, and the radial mixing process. Some of this information is currently available; although it is limited in many cases, the amount is steadily increasing. For example, the axial-flow-compressor blade-element theory and correlation results are given in chapters VI and VII for cascades and single-stage compressors. By utilizing this type of data, the performance of a compressor blade element can be determined. Furthermore, the results of chapter VIII provide a means for radial stacking of blade elements to estimate blade-row performance and axial stacking of blade rows to determine design-point performance, provided adequate blade-element performance data are available. This information can be applied to the off-design problem and is discussed in detail herein.

The second method is somewhat more simplified than the first, in that the average performance of each stage is obtained and the stages are axially stacked to acquire the compressor map. Therefore, neither blade-element data nor radial integration is necessary to obtain a performance map by this method. The success or failure of the technique depends upon the accuracy of the individual stage performance curves used for the computation of over-all performance. This method is used in the analyses of multistage-compressor performance in references 1 to 6 and in chapter XIII (ref. 7).

The final method of predicting multistage-compressor performance that is discussed in this chapter is based on data obtained from over-all performance maps of previously designed compressors. It is considerably more simplified than the first two methods, because there are no integration procedures or stage-stacking techniques involved in the computation of performance maps. This method was first proposed in reference 8 and was subsequently used in the analysis of two-spool compressor performance in reference 9. In the present chapter, data from several multistage compressors are correlated, so that it is possible to obtain a complete performance map from known compressor design conditions by means of a few simple and short numerical calculations.

Essentially, the purpose of this chapter is to review the methods currently available for predicting multistage-compressor performance. Although the techniques apply primarily to fixed-geometry compressors, they may be adapted to study operation with variable geometry and bleed. The advantages, disadvantages, limitations, and applicability of each method are discussed.

SYMBOLS

The following symbols are used in this chapter:

A	area, sq ft
a	speed of sound, ft/sec
c_p	specific heat at constant pressure, Btu/(lb)(°R)
g	acceleration due to gravity, 32.17 ft/sec ²
H	total or stagnation enthalpy, Btu/lb
J	mechanical equivalent of heat, 778.2 ft-lb/Btu
K_{bk}	weight-flow blockage factor
M	Mach number
N	rotational speed, rpm
P	total or stagnation pressure, lb/sq ft
R	gas constant, 53.35 ft-lb/(lb)(°R)
r	radius, ft
S	entropy, Btu/(lb)(°R)
T	total or stagnation temperature, °R
t	static or stream temperature, °R
U	rotor speed, ft/sec
V	air velocity, ft/sec
w	weight flow, lb/sec
Y	$\left(\frac{P_3}{P_1}\right)^{\frac{\gamma-1}{\gamma}} - 1$
z	coordinate along axis, ft

β	air angle, angle between air velocity and axial direction, deg
γ	ratio of specific heats
δ	ratio of total pressure to NACA standard sea-level pressure of 2116 lb/sq ft
δ^*	boundary-layer displacement thickness
η	efficiency
θ	ratio of total temperature to NACA standard sea-level temperature of 518.7° R
ρ	density, lb-sec ² /ft ⁴
ϕ	flow coefficient
ψ	pressure coefficient

Subscripts:

a	stagnation conditions
ac	actual conditions
ad	adiabatic
an	annulus
b	backbone
d	design
h	hub
i	reference position, radial station where variables are known
id	ideal
in	compressor inlet
m	mean
out	compressor outlet
r	radial direction
ref	reference
s	stall limit
sl	NACA standard sea-level conditions

t tip
z axial direction
 θ tangential direction
0,1, station numbers (fig. 2)
2,3

Superscript:

' denotes conditions relative to rotor blade row

METHODS OF PREDICTING OFF-DESIGN PERFORMANCE

Blade-Element Method

Blade-element theory is used extensively in the compressor design technique (ch. VIII). Compressor blades are evolved by a radial stacking of a series of blade sections or blade elements to form the complete blade. The theory proposes, therefore, that the blade-row characteristics can be determined if the performance of each blade element is known and that over-all compressor performance can then be obtained by an integration of the performance of each blade row. In this section, blade-element theory is applied to solve the off-design problem.

Basically, the solution for the off-design compressor performance proceeds as follows: From specified inlet conditions and blade geometry, the outlet conditions are computed from a knowledge of the flow about blade elements and with the conditions that continuity and radial equilibrium must be satisfied. Allowances must be made for boundary-layer growth, blade-row interaction effects, and radial mixing of blade wakes. The approach is admittedly an idealized one at present, since much of the information (blade-element losses at off-design operating conditions, boundary-layer growth, interactions, and radial mixing of blade wakes) required to carry out this calculation is not currently available. The general method is presented, because it has the greatest potentiality for providing a picture of the internal-flow mechanism through a compressor at off-design operating conditions. A method for computing the performance of a complete compressor stage (inlet guide vanes, rotors, and stators) is outlined; recourse is made to the equations and techniques for radial stacking of blade elements presented in chapter VIII. The performance of successive stages can be determined by utilizing the computed outlet conditions of one stage as the inlet conditions to the following stage.

Performance of inlet guide vanes. - Guide vanes are utilized to establish a specified prerotation at the design condition (ch. VIII). For the off-design problem, it is necessary to determine the effect of changes in weight flow and speed on guide-vane performance.

Experimental evidence indicates that the effect of variations of inlet Mach number and secondary flows (caused by variations in weight flow) on guide-vane turning angle is very small over the range of inlet Mach numbers usually encountered in axial-flow-compressor guide vanes (0.3 to 0.5). Also, changes in rotor speed have very little effect on turning angle. Therefore, for the purpose of this analysis it can be assumed that, for fixed-geometry guide vanes, the guide-vane-outlet angle remains constant (the design value) for all values of speed and weight flow if the subsequent rotor is operating unstalled.

With the guide-vane-outlet angle fixed, the outlet velocity distribution may be computed. The radial variation of axial and tangential velocity leaving an annular row of blades for steady axially symmetric flow, neglecting terms involving viscosity, is expressed in chapter VIII as follows:

$$Jg \frac{\partial H}{\partial r} = Jgt \frac{\partial S}{\partial r} + V_\theta \frac{\partial V_\theta}{\partial r} + V_z \frac{\partial V_z}{\partial r} + \frac{V_\theta^2}{r} - V_z \frac{\partial V_r}{\partial z} \quad (1)$$

For flow across inlet guide vanes, the total enthalpy is constant and entropy variations along the radial height can be considered negligible in most cases, making $\partial H / \partial r = 0$ and $t \frac{\partial S}{\partial r} = 0$. In addition, experimental data for guide vanes with small wall taper and relatively low-aspect-ratio blading indicate that the effect of radial accelerations and the radial velocity component can be neglected with little error. Therefore, when equation (1) is integrated with respect to r , the following equation results:

$$\left(\frac{V_z}{V_{z,i}} \right)_1 = \left(\frac{\cos \beta}{\cos \beta_i} \right)_1 \exp \left(- \int_{r_i}^r \frac{\sin^2 \beta_1}{r} dr \right) \quad (2)$$

Equation (2) can be utilized to express the axial velocity in terms of outlet angle and radial position for zero radial gradients of enthalpy and entropy and no radial velocity component. (Subscripts 0, 1, 2, and 3 denote axial stations and are indicated in figure 2 on a schematic diagram of a compressor stage. A typical velocity diagram is shown in figure 3.) In order to solve for values of axial velocity at all radial positions, a value of reference axial velocity must be assumed.

The assumption of the reference axial velocity can be checked by means of the continuity equation, since the condition that the inlet weight flow equals the outlet weight flow must be satisfied. The continuity equation can be expressed as follows:

$$w_0 = w_1 = K_{bk} 2\pi \rho_{a,0} g \int_{r_h}^{r_t} \frac{\rho_1}{\rho_{a,0}} V_{z,1} r dr = 2\pi \rho_{a,0} g \int_{r_h+\delta^*}^{r_t-\delta^*} \frac{\rho_1}{\rho_{a,0}} V_{z,1} r dr \quad (3)$$

where

$$\frac{\rho_1}{\rho_{a,0}} = \left[1 - \frac{\gamma-1}{2} \left(\frac{V_1}{a_{a,0}} \right)^2 \right]^{\frac{1}{\gamma-1}}$$

for the case of inlet guide vanes.

From equations (2) and (3) an iteration solution is necessary to solve for the correct axial velocity to satisfy weight flow. The area blockage caused by boundary-layer growth is taken into account by the limits of integration of equation (3), so that values of $(r_h+\delta^*)$ and $(r_t-\delta^*)$ correspond to the effective passage area rather than to the geometric area, or by the use of the blockage factor K_{bk} described in chapter VIII. Experimental results indicate that the ratio of effective area to actual passage area is approximately 0.98 at station 1. Equations (1) to (3) do not consider guide-vane losses. Since little data are available for estimating guide-vane losses, it is difficult to obtain a complete loss picture. However, if at all possible, it is desirable that a reasonable estimate of the losses be made. In some cases a guide-vane over-all efficiency is assumed. Some information that may be helpful in estimating losses is presented in reference 10.

Rotor and stator analysis. - With the guide-vane-outlet (rotor-inlet) conditions fixed, the rotor-outlet calculations can proceed. The procedure for determining the performance of the rotor is more complicated than that for the guide vanes, and the following information must be provided:

- | | |
|--------------------------------|------------------------------------|
| (1) Blade camber | } determined from blade geometry |
| (2) Blade angle | |
| (3) Solidity | |
| (4) Relative inlet-air angle | } determined from inlet conditions |
| (5) Relative inlet Mach number | |
| (6) Rotor speed | |

With this information available, blade-element results similar to those in chapters VI and VII are required to determine the turning angle and therefore the variation of rotor-outlet air angle.

In order to obtain an approximate velocity distribution at the rotor exit, zero losses are assumed between stations 1 and 2 and simple radial equilibrium with no radial entropy gradient is assumed at station 2. The simple-radial-equilibrium equation can be expressed as follows:

$$v_{z,2}^2 - v_{z,2,i}^2 = \left[(U - v_z \tan \beta')_{2,i}^2 - (U - v_z \tan \beta')_2^2 \right] + 2Jgc_p (T_2 - T_{2,i}) + 2 \int_r^{r_i} \frac{(U - v_z \tan \beta')_2^2}{r} dr \quad (4)$$

where

$$Jgc_p T_2 = Jgc_p T_1 - U_1 V_{\theta,1} + U_2 (U - v_z \tan \beta')_2$$

As in the case of the inlet guide vanes, the variation of outlet axial velocity v_z can be determined by assuming a reference value of outlet axial velocity $v_{z,i}$. The assumption of $v_{z,i}$ can be verified by means of the continuity equation (eq. (3)), where

$$\frac{\rho_2}{\rho_{a,1}} = \left(\frac{Jgc_p T_1 + U_2 V_{\theta,2} - U_1 V_{\theta,1} - \frac{v_{z,2}^2}{2}}{Jgc_p T_1} \right)^{\frac{1}{\gamma-1}} \quad (5)$$

for the rotor blade row with no losses. The simultaneous solutions of equations (3) and (4) for the rotor require a double iteration for axial velocity. Solutions of equations of this type are readily adaptable to high-speed electronic computing equipment.

The solution of equations (3) and (4) provides only a first approximation to the rotor-outlet velocity distribution, because no allowance for losses is included in the calculation. One way of refining this calculation to account for losses is by the use of the equilibrium equation with the entropy-gradient term included. The equilibrium equation with entropy gradient is given in chapter VIII and can be expressed as follows:

$$v_{z,2}^2 - v_{z,2,1}^2 = \left[(U - v_z \tan \beta')_{2,1}^2 - (U - v_z \tan \beta')_2^2 \right] + 2Jg_c p (T_2 - T_{2,1}) + 2 \int_r^{r_1} \frac{(U - v_z \tan \beta')_2^2}{r} dr + 2JgR \int_r^{r_1} t \frac{\partial \left(\frac{S}{R} \right)}{\partial r} dr \quad (6)$$

A detailed discussion of the solution of equations (6) and (3) for the design case is presented in chapter VIII. A solution of these equations to satisfy the off-design problem is similar and requires detailed knowledge of boundary-layer growth and blade-element losses over the complete range of operating conditions. Although complete loss information is not readily available at the present time, the relations between the diffusion factor and blade-element losses (chs. VI and VII) might be used for operating points in the vicinity of the design point. If a solution of these equations is obtained, mass-averaged values of rotor over-all pressure ratio and efficiency can be calculated.

The blade-element calculations for the stator blade performance are similar to those for the rotor. Values of outlet axial velocity can be determined by an iteration solution of equation (6) where the subscript 1 becomes 2, the subscript 2 becomes 3, and the term $(U - v_z \tan \beta')$ becomes $(v_z \tan \beta)$. Continuing this iteration process blade row by blade row through the compressor will ultimately provide the compressor-outlet conditions.

Remarks on blade-element method. - Unfortunately, at present the complete blade-element-flow picture is unknown. In the region near the compressor design point, adequate blade-element data are available for entrance stages. However, the variations of loss and turning angle have not been established as compressor stall is approached. In addition, boundary-layer theory does not as yet provide a means of calculating the boundary-layer growth through a multistage compressor, and there are no unsteady-flow results, blade-row interaction effects, nor data concerning radial mixing of blade wakes that can be applied directly to compressor design.

The preceding analysis reveals the gaps in our knowledge (particularly off-design blade-element data) that must be bridged by future research programs. In view of the length of the preceding calculation, it probably is not justified at present unless a good estimate can be made of the blade-element flow at off-design operating conditions. As stated previously, the method is presented because it has the greatest potentiality for providing a complete picture of the internal-flow mechanism

through a compressor at off-design operating conditions. Of course, one obvious way of simplifying the calculation would be to carry it out at only one radius of the compressor. This procedure would not be exact; however, a qualitative picture could be obtained of the compressor operating characteristics.

Stage-Stacking Method

Over-all compressor performance for a range of speeds and weight flows may be estimated by a stage-stacking method. The performance of each stage of the multistage compressor is obtained and presented so that its performance is a function only of its inlet equivalent weight flow and wheel speed. For assigned values of compressor weight flow and speed, the first-stage performance yields the inlet equivalent flow and wheel speed to the second stage. A stage-by-stage calculation through the compressor gives the individual stage pressure and temperature ratios, so that over-all compressor pressure ratio and efficiency can be calculated for the assigned values of compressor weight flow and wheel speed.

Stage performance. - Single-stage performance tests are conveniently made at constant speed, so that performance is very often presented as plots of pressure ratio and adiabatic efficiency against equivalent weight flow for constant values of equivalent speed. Such plots, however, are not convenient to use in applying the stage-stacking method, and stage performance for this use is presented as plots of efficiency and pressure coefficient against a flow coefficient. These dimensionless quantities are defined by the following equations:

$$\eta_{ad} = \frac{\Delta H_{id}}{\Delta H_{ac}} \quad (7)$$

$$\psi = \frac{\frac{\Delta H_{id}}{\theta}}{\left(\frac{U_m}{\sqrt{\theta}}\right)^2} = \frac{Jgc_p T_{s1} Y}{\left(\frac{U_m}{\sqrt{\theta}}\right)^2} \quad (8)$$

$$\phi = \left(\frac{V_z}{U}\right)_m \quad (9)$$

Representative single-stage performance curves are shown in figure 4. These curves may vary in the multistage environment (ch. XIII (ref. 7)); however, for undistorted inlet flow, stage performance generalizes quite well for a considerable range of Reynolds and Mach numbers. The stage characteristics at different speeds may be presented as a single line (fig. 4) for relative stage-inlet Mach numbers up to approximately 0.75. An exception is made for stage operation at low angles of attack.

Even for relatively low values of relative stage-inlet Mach number, the flow coefficient denoting a choked condition changes with wheel speed, so that a family of curves is required in the high-flow-coefficient range. Stage performance for relative stage-inlet Mach numbers higher than about 0.75 may be presented as a family of curves for the different wheel speeds. Stage performance is influenced by flow distortion at its inlet, but very little quantitative information is available.

3486 Sources of stage performance. - The stage performance curves needed for the stage-stacking method may be obtained from single-stage and multi-stage testing or from theoretical calculations. The chief shortcoming of the single-stage test data available to date is the lack of information concerning radial maldistribution of flow and unsteady flow. Such information is needed to estimate over-all compressor performance by the stage-stacking method; for example, at low wheel speeds, the inlet stage of a multistage compressor operates stalled so that the inlet flow to the second stage often is far from uniform.

Stage performance obtained from interstage data on multistage compressors (see refs. 4, 11, and 12) includes specific amounts of radial maldistribution of flow; for example, the stalled portions of the second-stage curves are obtained for inlet flow affected by stall in the first stage.

The difficulty in estimating stage performance from theoretical calculations is concerned with the fact that the flow in a compressor is three-dimensional, while the basic data normally used are based on two-dimensional flow. Employing blade-element theory to obtain stage performance involves all the difficulties discussed in the section entitled Blade-Element Method. As before, the calculation breaks down when a blade element stalls. A theoretical method of estimating stage performance along the mean line is presented in reference 8. Conditions at the mean diameter are taken as representative for the stage. For stages having hub-tip radius ratios lower than 0.6, reference 8 indicates that some form of integration of the individual blade-element characteristics (possibly by means of the blade-element method) along the blade height should be attempted. An example of stage performance calculated from mean diameter conditions is presented in appendix I of reference 8.

Stacking procedure. - In order to estimate the performance of a multistage axial-flow compressor with a stacking procedure, the following must be known:

- (1) Stage performance curves of each stage
- (2) Annulus area at inlet to each stage
- (3) Mean radius at inlet to each stage
- (4) Design value of absolute flow angle at inlet to each stage

The over-all compressor performance can be calculated for assigned values of compressor-inlet equivalent weight flow $w\sqrt{\theta_1}/\delta_1$ and rotative speed $U_{m,1}/\sqrt{\theta_1}$. The value of flow coefficient into the first stage is found from

$$\phi_1 = \frac{\frac{V_{z,1}}{\sqrt{\theta_1}}}{\frac{U_{m,1}}{\sqrt{\theta_1}}} \quad (10)$$

where the value of $V_{z,1}/\sqrt{\theta_1}$ is read from curves representing the following equation:

$$\frac{w\sqrt{\theta}}{\delta A_{an}} = \frac{V_z}{\sqrt{\theta}} \left[1 - \left(\frac{V_z}{\sqrt{\theta}} \right)^2 \frac{1}{2Jgc_p T_{s1} \cos^2 \beta} \right]^{\frac{1}{\gamma-1}} g \rho_{s1} \quad (11)$$

The area term A_{an} in equation (11) is commonly taken as the geometrical annulus area. However, experience has shown that more realistic values of axial velocity are obtained from equation (11) if effective annulus area is used. In order to determine effective annulus area, the boundary-layer growth through the compressor must be known (ch. VIII). Again, information concerning the growth and behavior of the boundary layer in an axial-flow compressor is required for the off-design case.

The first-stage performance curves yield values of ψ_1 and η_1 that permit calculation of the first-stage pressure ratio and temperature ratio from the following equations:

$$\frac{P_3}{P_1} = \left[1 + \frac{\psi_1 \left(\frac{U_{m,1}}{\sqrt{\theta_1}} \right)^2}{Jgc_p T_{s1}} \right]^{\frac{\gamma}{\gamma-1}} \quad (12)$$

$$\frac{T_3}{T_1} = \left[1 + \frac{\psi_1 \left(\frac{U_{m,1}}{\sqrt{\theta_1}} \right)^2}{\eta_1 Jgc_p T_{s1}} \right] \quad (13)$$

The values of equivalent flow and speed at the inlet to the second stage are calculated from

$$\frac{w \sqrt{\theta_3}}{\delta_3} = \frac{w \sqrt{\theta_1}}{\delta_1} \frac{\sqrt{\frac{T_3}{T_1}}}{\frac{P_3}{P_1}} \quad (14)$$

$$\frac{U_{m,3}}{\sqrt{\theta_3}} = \frac{U_{m,1}}{\sqrt{\theta_1}} \frac{r_{m,3}}{r_{m,1}} \frac{1}{\sqrt{\frac{T_3}{T_1}}} \quad (15)$$

The values of equivalent weight flow and equivalent wheel speed at the second-stage inlet determine the value of the flow coefficient Φ_3 , so that the second-stage pressure and temperature ratios may be calculated from the values of ψ_3 and η_3 . The stage-by-stage calculation is continued throughout the compressor, and over-all pressure ratio and efficiency are calculated from the compressor-inlet and -outlet pressures and temperatures. Thus, for any wheel speed, the over-all compressor pressure ratio and efficiency can be calculated for each assigned value of compressor weight flow.

In calculating a compressor performance map, some means must be employed for estimating the surge line, which influences starting, acceleration, and control problems. One scheme is to draw the surge line through the peak-pressure-ratio points of the over-all performance map. If the stage performance curves exhibit discontinuities, surge at any compressor speed may be taken to correspond to flow conditions for which a discontinuity is encountered in the performance curve of any stage.

Remarks on stage-stacking method. - The stage-stacking method may be used as a research tool to investigate compressor off-design problems or to estimate the performance of an untested compressor. In reference 3, the stage-stacking method was employed to indicate qualitatively the operation of each stage in a high-pressure-ratio multistage compressor over a full range of operating flows and speeds, the effect of stage performance on off-design performance, the effect of designing for different stage-matching points, and the effect on over-all performance of loading exit stages and unloading inlet stages by resetting stator blade angles. The part-speed operation for high-pressure-ratio multistage axial-flow compressors is analyzed in chapter XIII (ref. 7) with regard to the surge-line dip and the multiple performance curves that exist in the intermediate-speed range. In both these references, stage performance curves were assumed.

3487C

CG-33

The difficulty in estimating the performance of an actual compressor lies in obtaining reliable stage performance curves. Use of stage curves obtained from a given multistage compressor results in good performance estimation of a compressor having similar stages and only a slightly different over-all design pressure ratio. This is illustrated in reference 5, where the performance of a modified compressor is predicted from the stage curves of the original version of the compressor. The results of this performance-map prediction by the stage-stacking method are illustrated in figure 5. Calculated and measured values agreed particularly well at the higher compressor speeds.

This method is also useful for determining the effects of interstage bleed and variable geometry on compressor performance. In the interstage bleed calculation, the flow coefficient ϕ can be adjusted for the amount of air bled from the compressor. The effect of variable geometry can be accounted for in the calculation procedure if the variation of the stage curves is known as the compressor geometry is varied.

Simplified Method

A drawback common to the blade-element and stage-stacking methods of estimating over-all compressor performance is the length of time required for the calculations. A simplified method requiring much less calculating time is discussed herein. This method provides a means of obtaining the performance map of a new compressor from the results of previously designed compressors. Correlation curves are provided to facilitate the calculation.

Background information. - In reference 8 a method for predicting multistage-compressor performance is outlined. It was used to estimate the performance map of a newly designed compressor having blading similar to an existing compressor but slightly different design values of weight flow, pressure ratio, wheel speed, and number of stages. The application of this method to new compressor designs is, of course, restricted to cases where a compressor map of a similar existing compressor is available.

In this report, an attempt is made to extend the method presented in reference 8 to a more general case. Therefore, experimental data on eight multistage compressors were collected, correlated, and plotted in curve form, so that multistage-compressor performance maps of new compressors could be obtained easily from a knowledge of the design conditions alone. The method presented herein is similar to that used in reference 9 to obtain multistage performance maps. There are three phases of the calculation procedure. First, points of maximum efficiency at each speed are calculated. The line of maximum efficiency is called the backbone of the compressor map, and values along this line are termed backbone values. Second, the stall-limit line is determined, and values along the stall-limit line are referred to as stall-limit values or

stall-limit points. Finally, points along lines of constant speed are calculated from the stall limit to maximum flow. The integration of these phases results in a complete compressor performance map.

Calculation of compressor backbone. - Experimental over-all performance maps (similar to fig. 1) of eight compressors (listed in table I) were obtained. For the condition of maximum adiabatic efficiency at each speed, values of pressure ratio, weight flow, and efficiency were tabulated. From these backbone values, the reference-point values of speed, pressure ratio, weight flow, and adiabatic efficiency were found. The reference point of a compressor map, which is not necessarily the design point, is defined as the point of maximum polytropic efficiency of the compressor backbone.

The effect of reference-point pressure ratio on backbone characteristics is shown in figure 6, where each backbone value is plotted as a percentage of its reference-point value. In figure 6(a), values of backbone pressure ratio are plotted against reference pressure ratio with equivalent rotor speed as a parameter. Similar plots of backbone weight flow and adiabatic efficiency are shown in figures 6(b) and (c), respectively.

The backbone of a new compressor may be calculated from figure 6 and known reference-point values of pressure ratio, weight flow, adiabatic efficiency, and rotor speed. For the reference pressure ratio, the backbone values of pressure ratio, weight flow, and efficiency at various speeds are read from figure 6. Absolute backbone values are obtained by multiplying the values read from figure 6 by appropriate reference-point values.

Calculation of stall-limit line. - The effect of reference pressure ratio on stall-limit or surge-line characteristics is shown in figure 7, in which stall-limit pressure ratio is plotted against reference pressure ratio with stall-limit weight flow as a parameter. The values of stall-limit weight flow and pressure ratio are plotted as percent of the reference values. The stall-limit line of a new compressor may be calculated by multiplying the stall-limit values of pressure ratio and weight flow read from figure 7 for the known reference pressure ratio by their respective reference values. Stall-limit lines estimated in this manner are single-valued; whereas, the stall-limit lines of some actual compressors are multivalued (ch. XIII (ref. 7)).

Constant-speed characteristics. - The constant-speed characteristics of an existing compressor may be obtained from its performance map. For several points along each speed line, values of temperature rise $(T_{out} - T_{in})/\theta_1$, adiabatic efficiency η_{ad} , and flow parameter $(w_{in} \sqrt{\theta_{in}/\delta_{in}}) (\sqrt{T_{out}/T_{in}}/\sqrt{P_{out}/P_{in}})$ are calculated and divided by their respective backbone values to yield relative values of temperature rise, efficiency, and flow parameter. Values from the entire compressor

map tend to give a single curve of relative temperature rise against relative flow parameter and a single curve of relative efficiency against relative flow parameter. These two curves define the constant-speed characteristics of a compressor. Plots of this type are illustrated in figure 8. The data points represent seven different compressor speeds, and in general the correlation of data at all speeds is relatively good.

In figure 9 faired curves are plotted representing the constant-speed characteristics of four compressors designed according to the basic principles outlined in chapter VIII. When specific data are lacking on the constant-speed characteristics of a newly designed compressor, an average of the curves of figure 9 could probably be used successfully for the compressor constant-speed characteristics, if the design system is similar to that presented in chapter VIII.

The lines of constant speed for a desired compressor performance map may be calculated from a given set of constant-speed characteristic curves and the calculated backbone values. For each speed, relative values of flow parameter are assigned and relative values of temperature rise and efficiency are read from the constant-speed curves. Absolute values are calculated from these relative values and the appropriate backbone values. In the use of these curves, one end is limited by the stall-limit line and the other end by the maximum-weight-flow value. Compressor pressure ratio is calculated from the values of temperature rise and efficiency, and compressor weight flow is calculated from values of temperature ratio, pressure ratio, and flow parameter.

Comments on reference point. - As stated previously, the reference point is defined as the point of maximum polytropic efficiency of the compressor map. Experimental data indicate that the reference point is usually found at values of compressor speed somewhat below the actual design speed. Unfortunately, attempts to obtain an exact relation between the actual compressor design point and the reference point were unsuccessful. In the case of the four NACA compressors that utilized the design principles of chapter VIII, the reference speed varied from 90 to 100 percent of the actual design speed. This fact may be helpful in establishing the relation of these two points.

The following procedure may be used to compute reference conditions from design conditions for a particular ratio of design speed to reference speed $(N/\sqrt{\theta})_d/(N/\sqrt{\theta})_{ref}$:

- (1) A trial value of reference pressure ratio is selected $(P_{out}/P_{in})_{ref}$.

(2) A value of backbone total-pressure ratio $\frac{(P_{out}/P_{in})_b}{(P_{out}/P_{in})_{ref}} 100$ is read from figure 6(a) for the values of $(P_{out}/P_{in})_{ref}$ and $\frac{(N/\sqrt{\theta})_d}{(N/\sqrt{\theta})_{ref}} 100$.

(3) A value of $(P_{out}/P_{in})_{ref}$ is calculated from

$$\left(\frac{P_{out}}{P_{in}}\right)_{ref} = \frac{\left(\frac{P_{out}}{P_{in}}\right)_d}{\frac{\left(\frac{P_{out}}{P_{in}}\right)_b}{\left(\frac{P_{out}}{P_{in}}\right)_{ref}}} \quad (16)$$

If this calculated value does not equal the trial value from step (1), steps (1) to (3) are repeated until the two values do agree.

(4) A value of $\frac{(w\sqrt{\theta}/\delta)_b}{(w\sqrt{\theta}/\delta)_{ref}} 100$ is read from figure 6(b) for the values of $\left(\frac{P_{out}}{P_{in}}\right)_{ref}$ and $\frac{(N/\sqrt{\theta})_d}{(N/\sqrt{\theta})_{ref}} 100$.

(5) The value of $(w\sqrt{\theta}/\delta)_{ref}$ is calculated from

$$\left(\frac{w\sqrt{\theta}}{\delta}\right)_{ref} = \frac{\left(\frac{w\sqrt{\theta}}{\delta}\right)_d}{\frac{\left(\frac{w\sqrt{\theta}}{\delta}\right)_b}{\left(\frac{w\sqrt{\theta}}{\delta}\right)_{ref}}} \quad (17)$$

(6) A value of $\frac{\eta_{ad,b}}{\eta_{ad,ref}} 100$ is read from figure 6(c) for the values of $\left(\frac{P_{out}}{P_{in}}\right)_{ref}$ and $\frac{(N/\sqrt{\theta})_d}{(N/\sqrt{\theta})_{ref}} 100$.

(7) The value of $\eta_{ad,ref}$ is calculated from

$$\eta_{ad,ref} = \frac{\eta_{ad,d}}{\frac{\eta_{ad,b}}{\eta_{ad,ref}}} \quad (18)$$

Remarks on simplified method. - How closely the performance map calculated by the simplified method will conform with the actual performance map depends on each phase of the calculation. The agreement depends on (1) how well the available compressor performance maps generalize to backbone, stall-limit, and constant-speed curves, (2) how closely design conditions are realized in the new compressor, and (3) how accurately reference-point conditions are calculated from design conditions. The performance maps of the limited number of compressors designed along the lines suggested in this volume have had some affinity in shape. As previously noted, however, double-valued stall lines cannot be anticipated by this method.

CONCLUDING REMARKS

Three techniques have been presented for estimating compressor off-design performance. The first method, which is based on blade-element theory, is useful for obtaining only a small part of the compressor map over which all blade elements in the compressor remain unstalled. This technique is restricted at present because of the limited amount of available information concerning off-design blade-element data, boundary-layer growth, blade-row interaction effects, and radial mixing of blade wakes. This method has the greatest potential for providing a complete picture of the internal-flow mechanism through a compressor.

The second method, which involves individual stage performance curves and a stage-by-stage calculation, is useful for estimating the performance of a compressor for which reliable stage performance curves are available. In addition, this method has been used effectively as a research tool to determine the effects of interstage bleed and variable geometry on compressor performance.

The third method, which is based on over-all performance data of existing compressors, may be used to estimate the complete performance map of a new compressor if the compressor design conditions are specified. At present, it is as effective as the other methods and has the advantages of simplicity and short calculating time.

REFERENCES

1. Hagen, H.: Compressor Characteristics and Starting Powers of Jet Propulsion Power Plants. BuShips 338, vol. 8, pt. A, May 1946, pp. 1-20.
2. Bogdonoff, Seymour M.: The Performance of Axial-Flow Compressors As Affected by Single-Stage Characteristics. Jour. Aero. Sci., vol. 18, no. 5, May 1951, pp. 319-328.
3. Finger, Harold B., and Dugan, James F., Jr.: Analysis of Stage Matching and Off-Design Performance of Multistage Axial-Flow Compressors. NACA RM E52D07, 1952.
4. Medeiros, Arthur A., Benser, William A., and Hatch, James E.: Analysis of Off-Design Performance of a 16-Stage Axial-Flow Compressor with Various Blade Modifications. NACA RM E52L03, 1953.
5. Geye, Richard P., and Voit, Charles H.: Investigation of a High-Pressure-Ratio Eight-Stage Axial-Flow Research Compressor with Two Transonic Inlet Stages. IV - Modification of Aerodynamic Design and Prediction of Performance. NACA RM E55B28, 1955.
6. Standahar, Raymond M., and Geye, Richard P.: Investigation of a High-Pressure-Ratio Eight-Stage Axial-Flow Research Compressor with Two Transonic Inlet Stages. V - Preliminary Analysis of Over-All Performance of Modified Compressor. NACA RM E55A03, 1955.
7. Compressor and Turbine Research Division: Aerodynamic Design of Axial-Flow Compressors. Vol. III. NACA RM E56B03b, 1956.
8. Howell, A. R., and Bonham, R. P.: Over-All and Stage Characteristics of Axial-Flow Compressors. Proc. Inst. Mech. Eng., vol. 163, 1950, pp. 235-248.
9. Dugan, James F., Jr.: Effect of Design Over-All Compressor Pressure Ratio Division on Two-Spool Turbojet-Engine Performance and Geometry. NACA RM E54F24a, 1954.
10. Dunavant, James C.: Cascade Investigation of a Related Series of 6-Percent-Thick Guide-Vane Profiles and Design Charts. NACA RM L54I02, 1954.
11. Budinger, Ray E., and Serovy, George K.: Investigation of a 10-Stage Subsonic Axial-Flow Research Compressor. IV - Individual Stage Performance Characteristics. NACA RM E53C11, 1953.

12. Voit, Charles H., and Geye, Richard P.: Investigation of a High-Pressure-Ratio Eight-Stage Axial-Flow Research Compressor with Two Transonic Inlet Stages. III - Individual Stage Performance Characteristics. NACA RM E54H17, 1954.
13. Kovach, Karl, and Sandercock, Donald M.: Experimental Investigation of a Five-Stage Axial-Flow Research Compressor with Transonic Rotors in All Stages. II - Compressor Over-All Performance. NACA RM E54G01, 1954.
14. Budinger, Ray E., and Thomson, Arthur R.: Investigation of a 10-Stage Subsonic Axial-Flow Research Compressor. II - Preliminary Analysis of Over-All Performance. NACA RM E52C04, 1952.
15. Geye, Richard P., Budinger, Ray E., and Voit, Charles H.: Investigation of a High-Pressure-Ratio Eight-Stage Axial-Flow Research Compressor with Two Transonic Inlet Stages. II - Preliminary Analysis of Over-All Performance. NACA RM E53J06, 1953.

TABLE I. - EXPERIMENTAL COMPRESSOR DATA

Compressor	Inlet guide vanes	Reference pressure ratio	Stages	Outer diam- eter, in.	Inlet hub- tip ratio	Refer- ence
1. Subsonic	Yes	2.08	6	15.75	0.575	--
2. Subsonic	Yes	3.00	10	19	0.5	--
3. Subsonic	Yes	3.48	12	Vari- able	0.6	--
4. Transonic	No	4.02	5	20	0.50	13
5. Subsonic	Yes	5.53	10	20	0.55	14
6. Transonic	No	7.35	8	20	0.48	15
7. Subsonic	Yes	9.20	16	33.5	0.55	4
8. Transonic	No	10.26	8	Vari- able	0.46	6

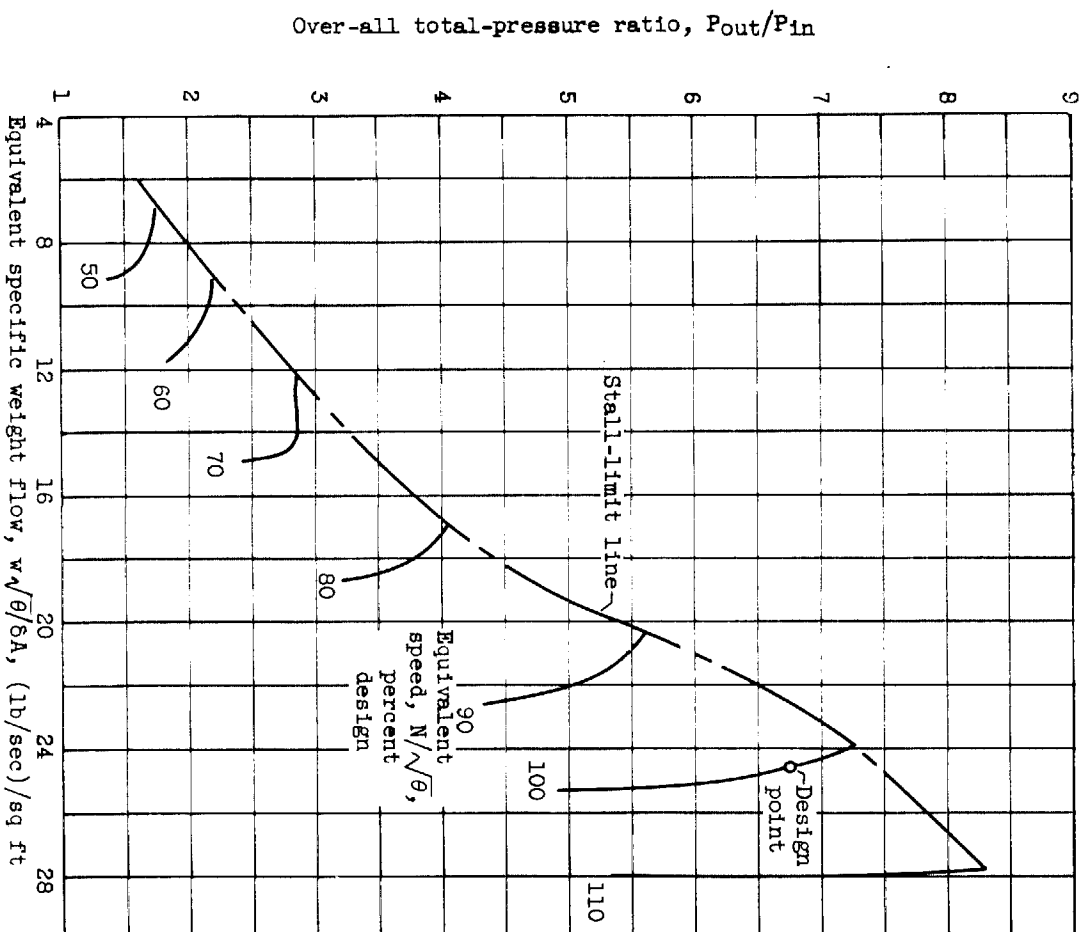
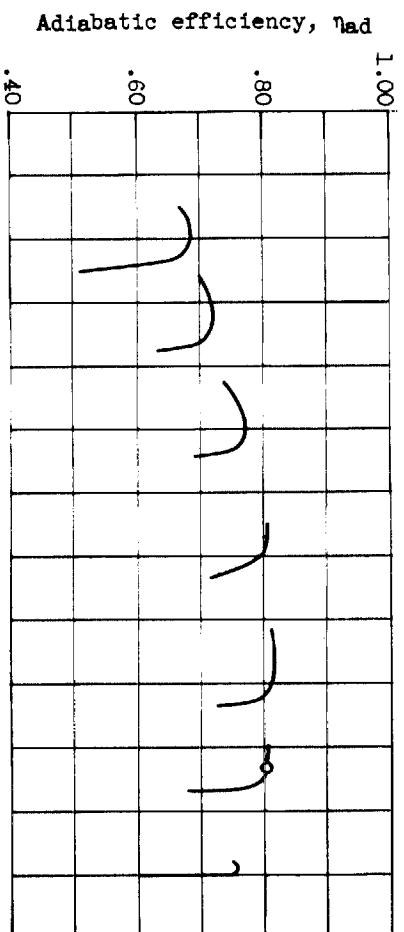


Figure 1. - Typical axial-flow-compressor over-all performance map.

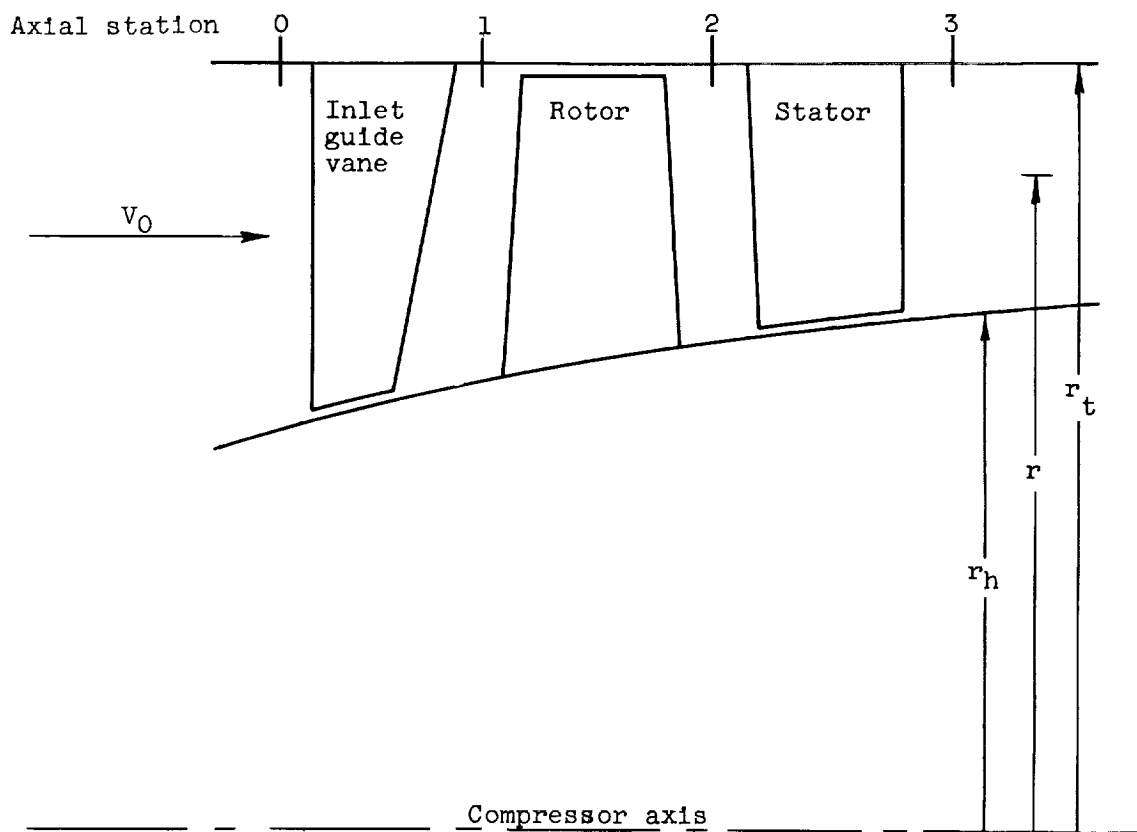


Figure 2. - Schematic diagram of compressor stage.

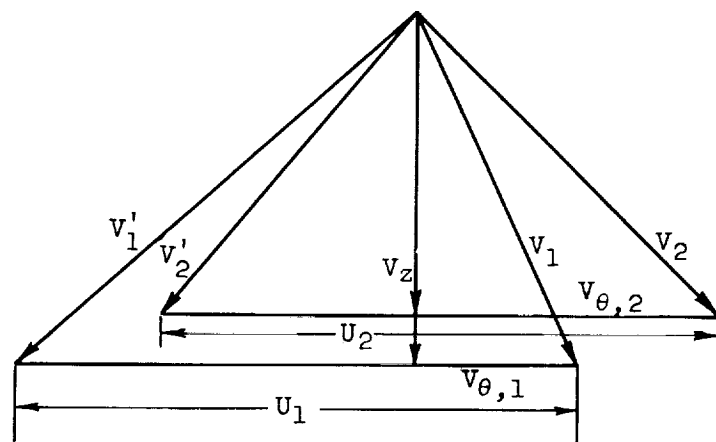


Figure 3. - Typical velocity diagram.

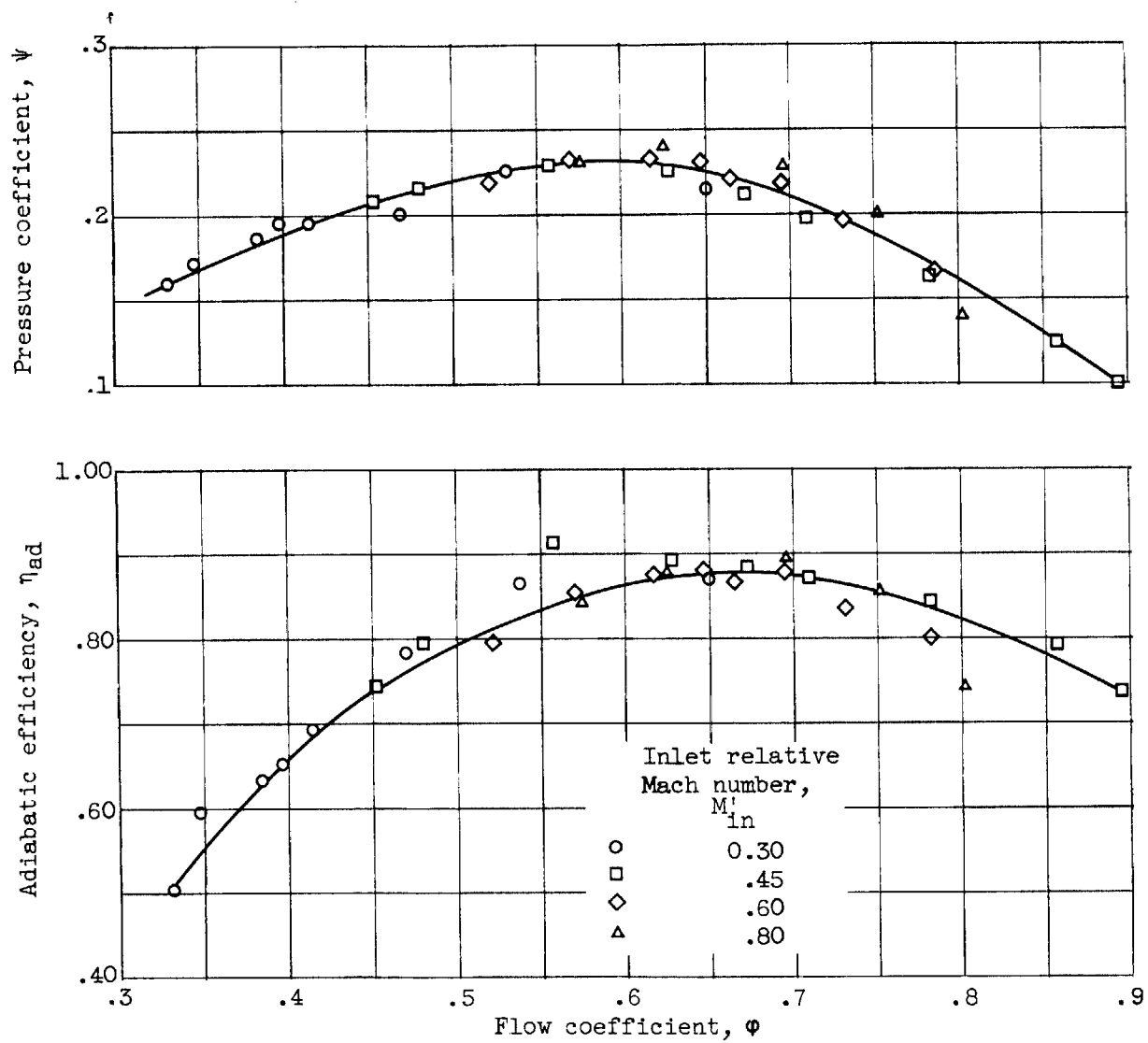


Figure 4. - Typical stage characteristic curves.

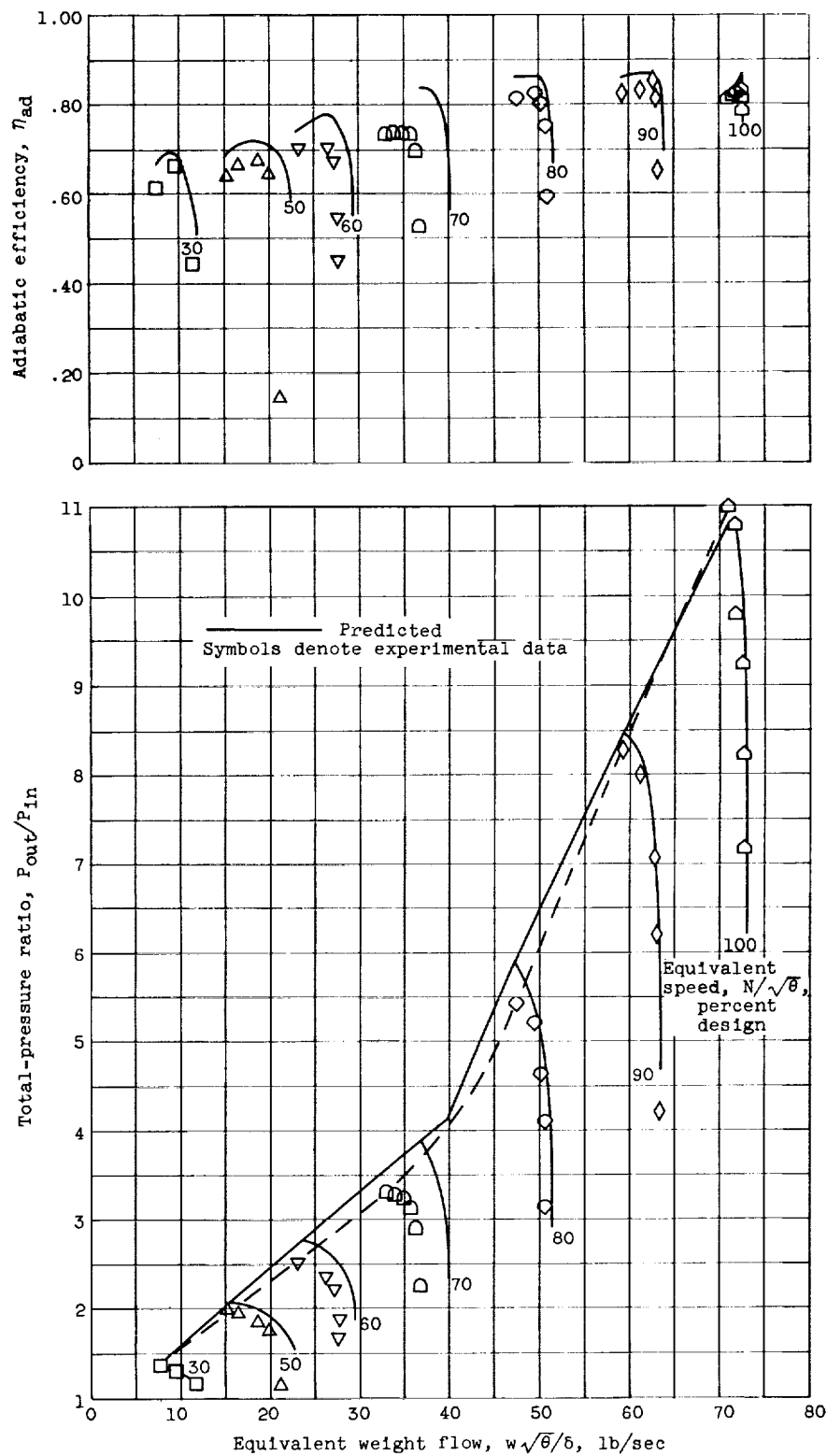
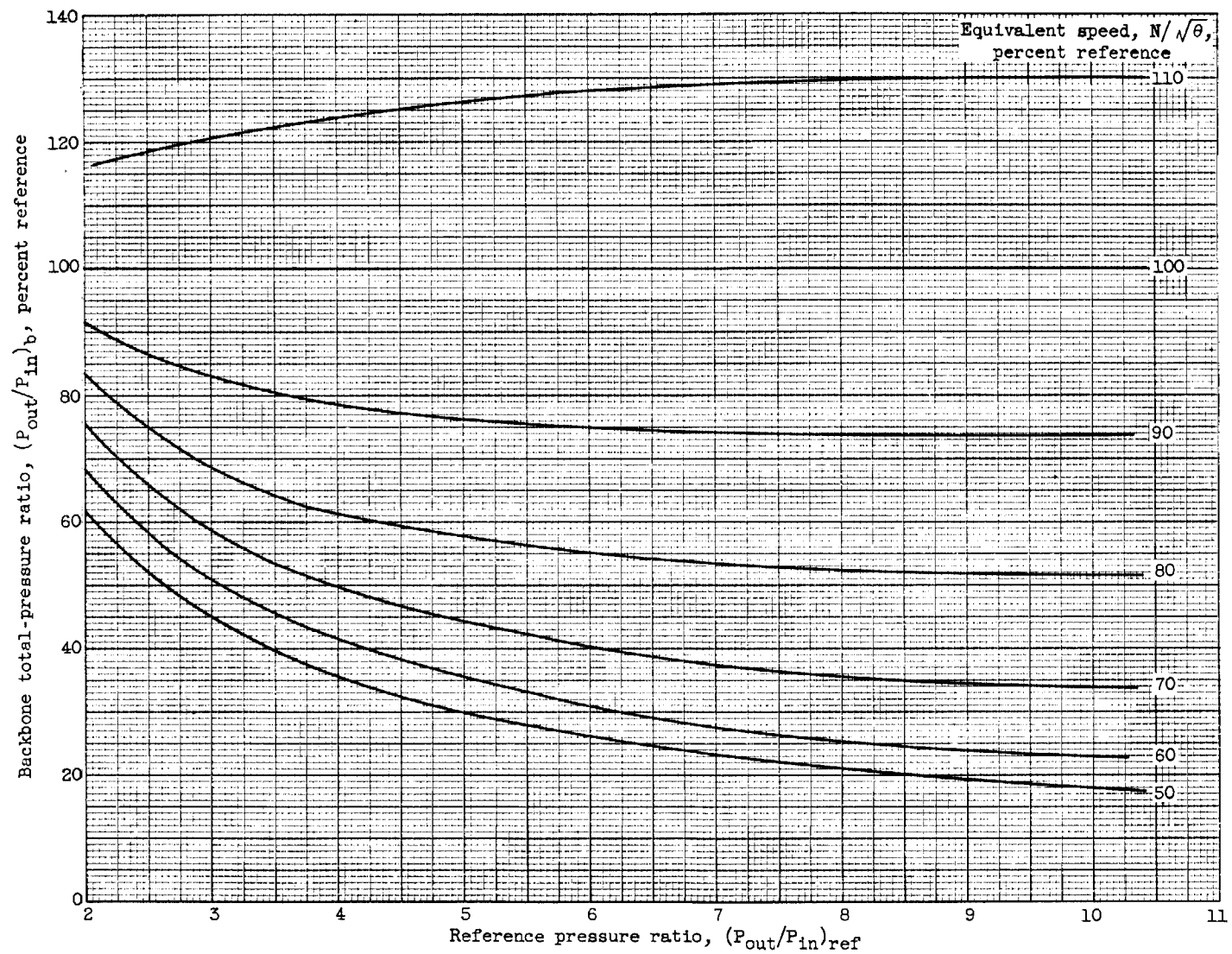
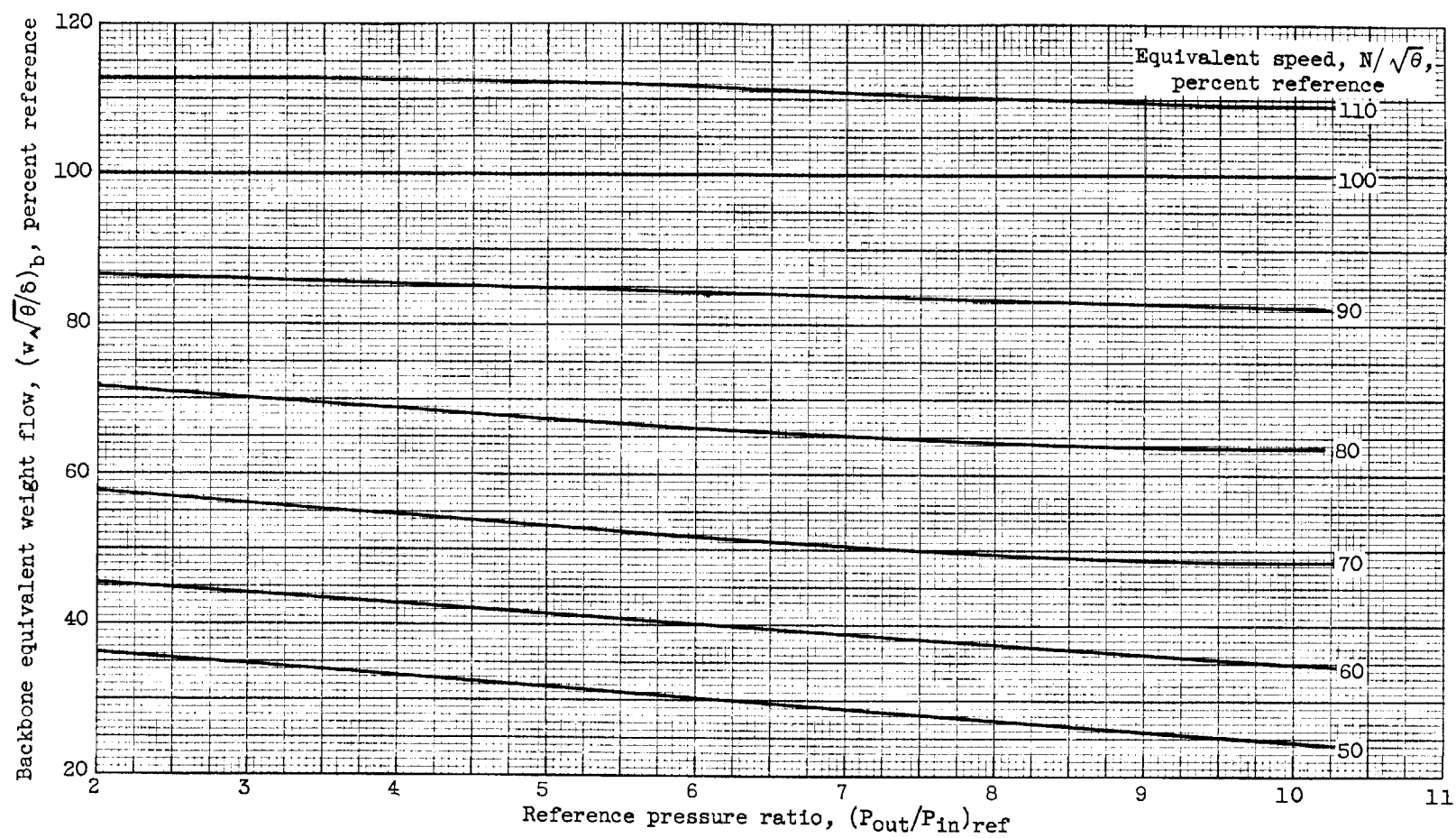


Figure 5. - Comparison of predicted and experimental over-all performance for modified eight-stage compressor.



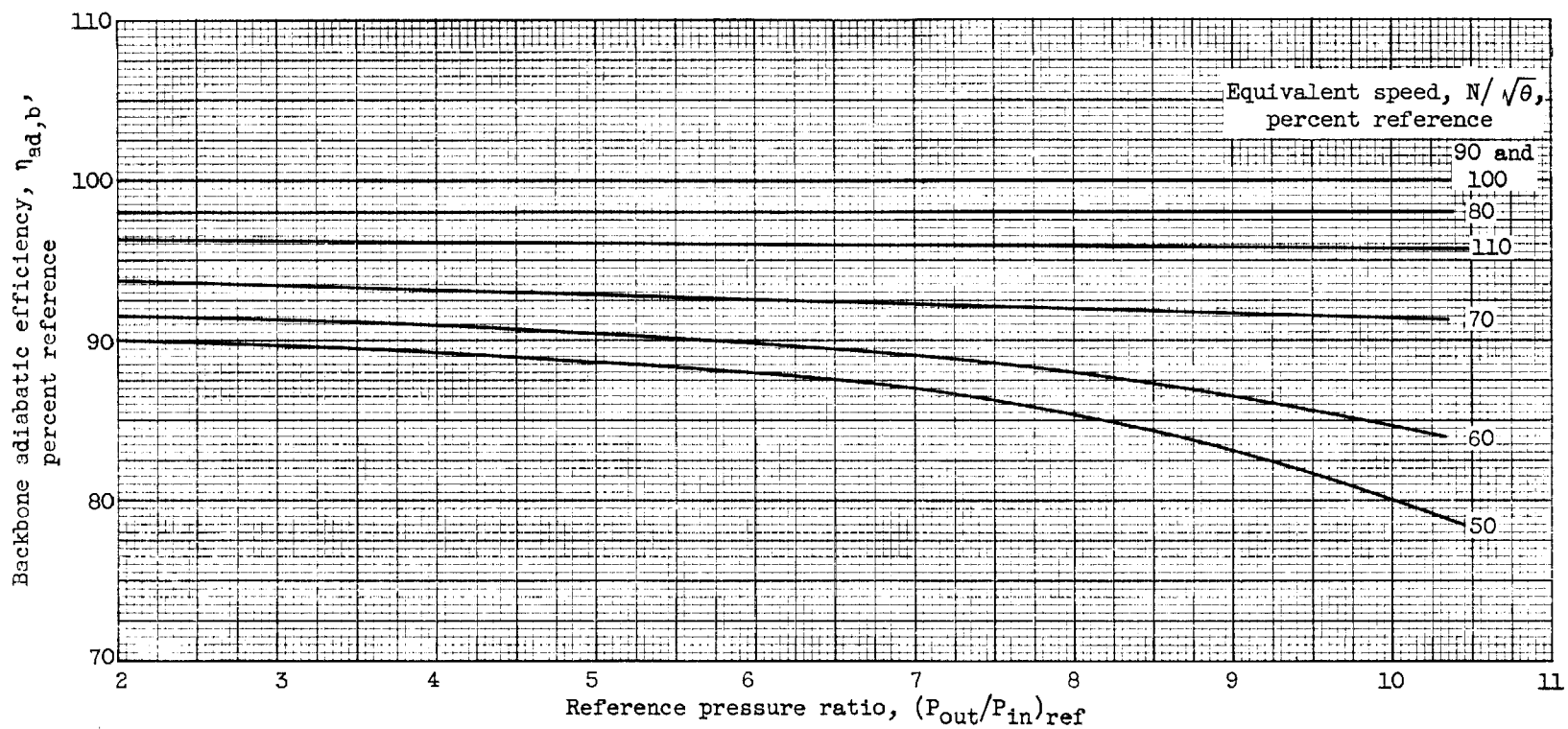
(a) Pressure ratio.

Figure 6. - Effect of reference pressure ratio on backbone characteristics.



(b) Weight flow.

Figure 6. - Continued. Effect of reference pressure ratio on backbone characteristics.



(c) Efficiency.

Figure 6. - Concluded. Effect of reference pressure ratio on backbone characteristics.

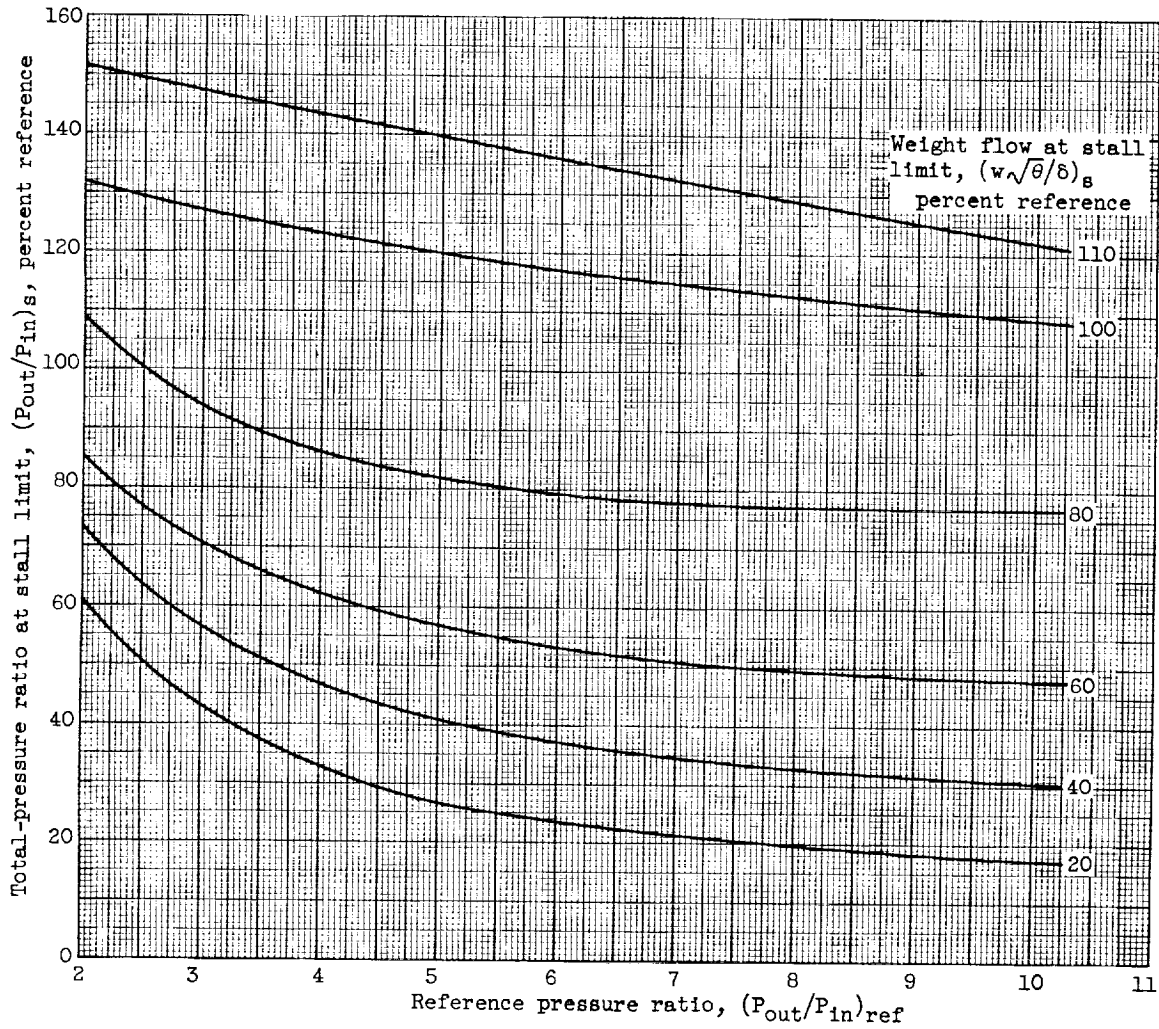
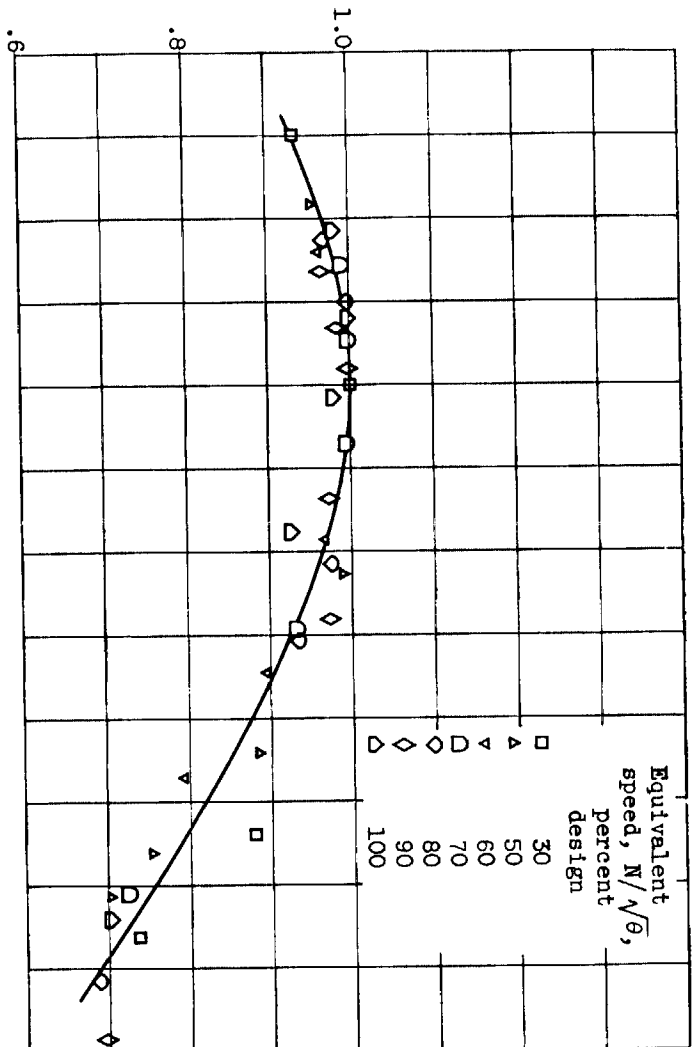


Figure 7. - Effect of reference pressure ratio on stall-limit line.

Relative adiabatic efficiency



Relative temperature rise

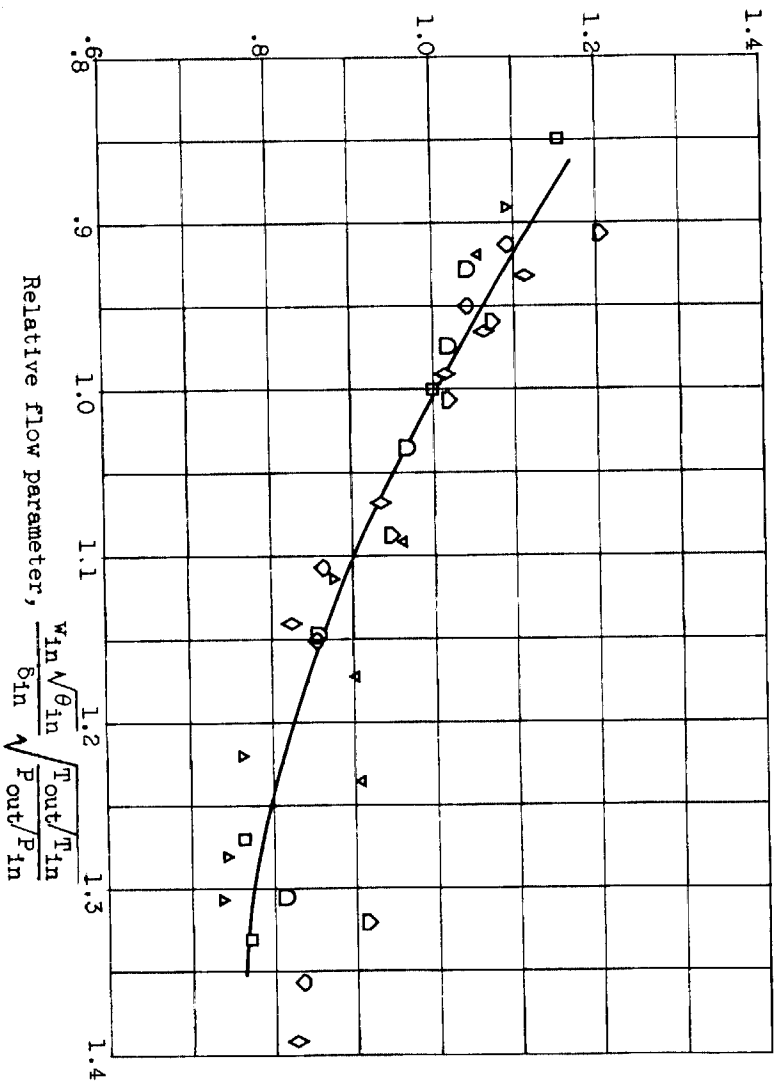


Figure 8. - Generalized performance parameters at several speeds for typical axial-flow compressor.

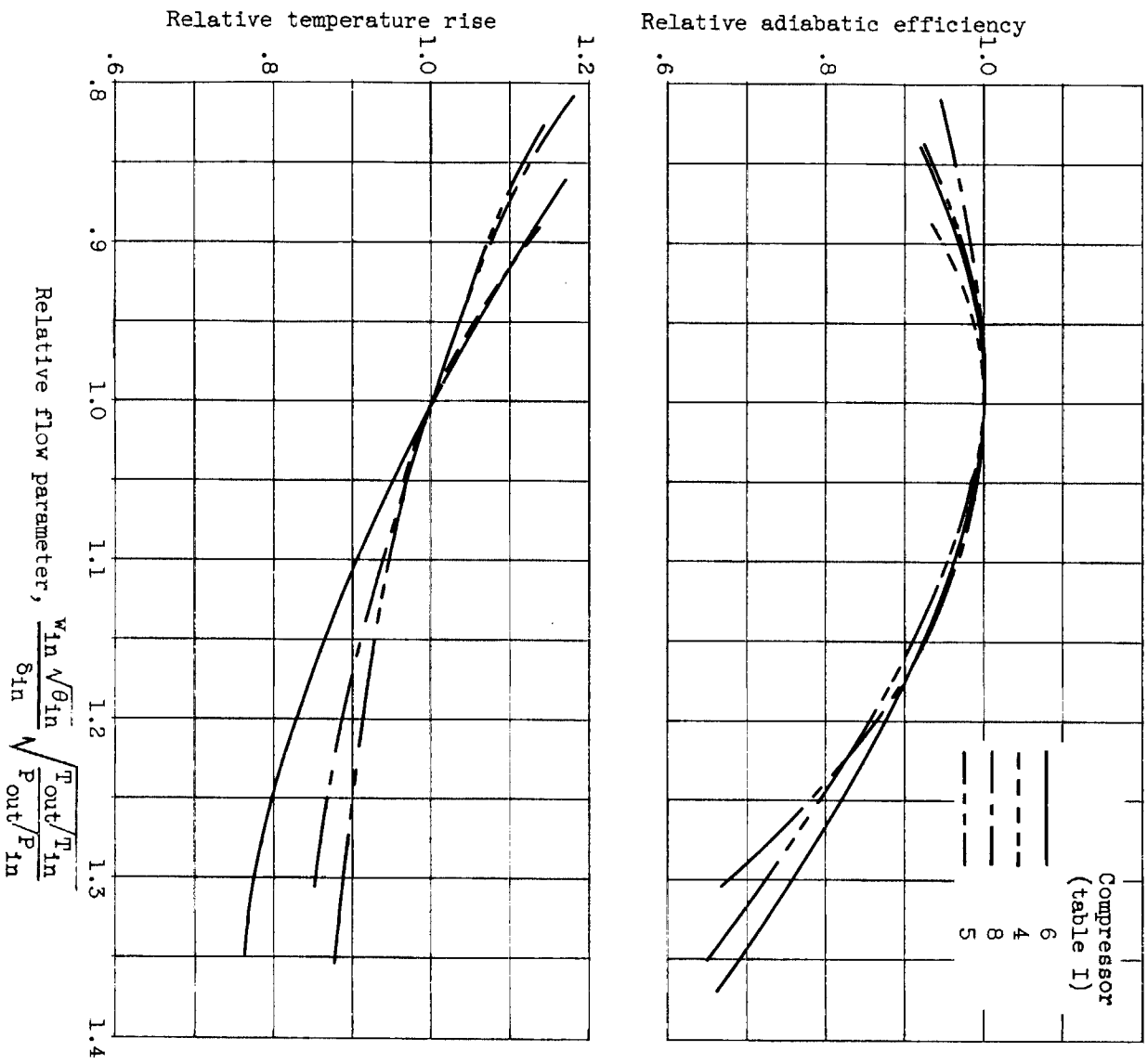


Figure 9. - Generalized performance curves of four multistage compressors.

NACA RM E56B03a

National Advisory Committee for Aeronautics.
AERODYNAMIC DESIGN OF AXIAL-FLOW COMPRESSORS. VOLUME II. Compressor and Turbine Research Division. Edited by Irving A. Johnsen and Robert O. Bullock. Chapter VI: EXPERIMENTAL FLOW IN TWO-DIMENSIONAL CASCADES. Seymour Lieblein. Chapter VII: BLADE-ELEMENT FLOW IN ANNULAR CASCADES. William H. Robbins, Robert J. Jackson, and Seymour Lieblein. Chapter VIII: DESIGN VELOCITY DISTRIBUTION IN MERIDIONAL PLANE. Charles C. Giamati, Jr., and Harold B. Finger. Chapter IX: CHART PROCEDURES FOR DESIGN VELOCITY DISTRIBUTION. Arthur A. Medeiros and Betty Jane Hood. Chapter X: PREDICTION OF OFF-DESIGN PERFORMANCE OF MULTISTAGE COMPRESSORS. William H. Robbins and James F. Dugan, Jr. August 1956. x, 275p. diagrs., tabs. (NACA RM E56B03a)

1. Cascades, Theory (1.4.5.1)
2. Cascades, Experiment (1.4.5.2)
3. Compressor Flow Theory and Experiment (3.6.1)
4. Compressors - Axial-Flow (3.6.1.1)
5. Compressors - Matching (3.6.3)
 - I. Johnsen, Irving A.
 - II. Bullock, Robert O.
 - III. Lieblein, Seymour
 - IV. Robbins, William H.
 - V. Jackson, Robert J.
 - VI. Giamati, Charles C., Jr.



NACA RM E56B03a

National Advisory Committee for Aeronautics.
AERODYNAMIC DESIGN OF AXIAL-FLOW COMPRESSORS. VOLUME II. Compressor and Turbine Research Division. Edited by Irving A. Johnsen and Robert O. Bullock. Chapter VI: EXPERIMENTAL FLOW IN TWO-DIMENSIONAL CASCADES. Seymour Lieblein. Chapter VII: BLADE-ELEMENT FLOW IN ANNULAR CASCADES. William H. Robbins, Robert J. Jackson, and Seymour Lieblein. Chapter VIII: DESIGN VELOCITY DISTRIBUTION IN MERIDIONAL PLANE. Charles C. Giamati, Jr., and Harold B. Finger. Chapter IX: CHART PROCEDURES FOR DESIGN VELOCITY DISTRIBUTION. Arthur A. Medeiros and Betty Jane Hood. Chapter X: PREDICTION OF OFF-DESIGN PERFORMANCE OF MULTISTAGE COMPRESSORS. William H. Robbins and James F. Dugan, Jr. August 1956. x, 275p. diagrs., tabs. (NACA RM E56B03a)

1. Cascades, Theory (1.4.5.1)
2. Cascades, Experiment (1.4.5.2)
3. Compressor Flow Theory and Experiment (3.6.1)
4. Compressors - Axial-Flow (3.6.1.1)
5. Compressors - Matching (3.6.3)
 - I. Johnsen, Irving A.
 - II. Bullock, Robert O.
 - III. Lieblein, Seymour
 - IV. Robbins, William H.
 - V. Jackson, Robert J.
 - VI. Giamati, Charles C., Jr.



NACA RM E56B03a

National Advisory Committee for Aeronautics.
AERODYNAMIC DESIGN OF AXIAL-FLOW COMPRESSORS. VOLUME II. Compressor and Turbine Research Division. Edited by Irving A. Johnsen and Robert O. Bullock. Chapter VI: EXPERIMENTAL FLOW IN TWO-DIMENSIONAL CASCADES. Seymour Lieblein. Chapter VII: BLADE-ELEMENT FLOW IN ANNULAR CASCADES. William H. Robbins, Robert J. Jackson, and Seymour Lieblein. Chapter VIII: DESIGN VELOCITY DISTRIBUTION IN MERIDIONAL PLANE. Charles C. Giamati, Jr., and Harold B. Finger. Chapter IX: CHART PROCEDURES FOR DESIGN VELOCITY DISTRIBUTION. Arthur A. Medeiros and Betty Jane Hood. Chapter X: PREDICTION OF OFF-DESIGN PERFORMANCE OF MULTISTAGE COMPRESSORS. William H. Robbins and James F. Dugan, Jr. August 1956. x, 275p. diagrs., tabs. (NACA RM E56B03a)

1. Cascades, Theory (1.4.5.1)
2. Cascades, Experiment (1.4.5.2)
3. Compressor Flow Theory and Experiment (3.6.1)
4. Compressors - Axial-Flow (3.6.1.1)
5. Compressors - Matching (3.6.3)
 - I. Johnsen, Irving A.
 - II. Bullock, Robert O.
 - III. Lieblein, Seymour
 - IV. Robbins, William H.
 - V. Jackson, Robert J.
 - VI. Giamati, Charles C., Jr.



NACA RM E56B03a

National Advisory Committee for Aeronautics.
AERODYNAMIC DESIGN OF AXIAL-FLOW COMPRESSORS. VOLUME II. Compressor and Turbine Research Division. Edited by Irving A. Johnsen and Robert O. Bullock. Chapter VI: EXPERIMENTAL FLOW IN TWO-DIMENSIONAL CASCADES. Seymour Lieblein. Chapter VII: BLADE-ELEMENT FLOW IN ANNULAR CASCADES. William H. Robbins, Robert J. Jackson, and Seymour Lieblein. Chapter VIII: DESIGN VELOCITY DISTRIBUTION IN MERIDIONAL PLANE. Charles C. Giamati, Jr., and Harold B. Finger. Chapter IX: CHART PROCEDURES FOR DESIGN VELOCITY DISTRIBUTION. Arthur A. Medeiros and Betty Jane Hood. Chapter X: PREDICTION OF OFF-DESIGN PERFORMANCE OF MULTISTAGE COMPRESSORS. William H. Robbins and James F. Dugan, Jr. August 1956. x, 275p. diagrs., tabs. (NACA RM E56B03a)

1. Cascades, Theory (1.4.5.1)
2. Cascades, Experiment (1.4.5.2)
3. Compressor Flow Theory and Experiment (3.6.1)
4. Compressors - Axial-Flow (3.6.1.1)
5. Compressors - Matching (3.6.3)
 - I. Johnsen, Irving A.
 - II. Bullock, Robert O.
 - III. Lieblein, Seymour
 - IV. Robbins, William H.
 - V. Jackson, Robert J.
 - VI. Giamati, Charles C., Jr.



NACA RM E56B03a

The first two chapters of vol. II survey and correlate experimentally obtained blade-element data. Ch. VI summarizes the data obtained in two-dimensional cascades, while ch. VII summarizes blade-element data obtained in annular cascades (compressor rotors and stators). Ch. VIII summarizes the design problem and design techniques in the meridional or hub-to-tip plane, and ch. IX provides simple chart procedures for the solution of this meridional-plane design problem. Methods for the prediction of compressor performance over a range of flow conditions and speeds (off-design operation) are presented in ch. X.

- VII. Finger, Harold B.
- VIII. Medeiros, Arthur A.
- IX. Hood, Betty Jane
- X. Dugan, James F., Jr.
- XI. NACA RM E56B03a



NACA RM E56B03a

The first two chapters of vol. II survey and correlate experimentally obtained blade-element data. Ch. VI summarizes the data obtained in two-dimensional cascades, while ch. VII summarizes blade-element data obtained in annular cascades (compressor rotors and stators). Ch. VIII summarizes the design problem and design techniques in the meridional or hub-to-tip plane, and ch. IX provides simple chart procedures for the solution of this meridional-plane design problem. Methods for the prediction of compressor performance over a range of flow conditions and speeds (off-design operation) are presented in ch. X.

- VII. Finger, Harold B.
- VIII. Medeiros, Arthur A.
- IX. Hood, Betty Jane
- X. Dugan, James F., Jr.
- XI. NACA RM E56B03a



NACA RM E56B03a

The first two chapters of vol. II survey and correlate experimentally obtained blade-element data. Ch. VI summarizes the data obtained in two-dimensional cascades, while ch. VII summarizes blade-element data obtained in annular cascades (compressor rotors and stators). Ch. VIII summarizes the design problem and design techniques in the meridional or hub-to-tip plane, and ch. IX provides simple chart procedures for the solution of this meridional-plane design problem. Methods for the prediction of compressor performance over a range of flow conditions and speeds (off-design operation) are presented in ch. X.

- VII. Finger, Harold B.
- VIII. Medeiros, Arthur A.
- IX. Hood, Betty Jane
- X. Dugan, James F., Jr.
- XI. NACA RM E56B03a



NACA RM E56B03a

The first two chapters of vol. II survey and correlate experimentally obtained blade-element data. Ch. VI summarizes the data obtained in two-dimensional cascades, while ch. VII summarizes blade-element data obtained in annular cascades (compressor rotors and stators). Ch. VIII summarizes the design problem and design techniques in the meridional or hub-to-tip plane, and ch. IX provides simple chart procedures for the solution of this meridional-plane design problem. Methods for the prediction of compressor performance over a range of flow conditions and speeds (off-design operation) are presented in ch. X.

- VII. Finger, Harold B.
- VIII. Medeiros, Arthur A.
- IX. Hood, Betty Jane
- X. Dugan, James F., Jr.
- XI. NACA RM E56B03a

